MBE GROWTH AND INVESTIGATION OF (001) GaAs SURFACES USING SIMS

W F CROYDON

MAY 1985

This thesis is submitted in part fulfillment of the requirements of the Council for National Academic Awards for the degree of Doctor of Philosophy, and is sponsored by the City of London Polytechnic in collaboration with the GEC Hirst Research Centre.

CONTENTS

MBE GROWTH AND INVESTIGATION OF (001) GaAs SURFACES USING SIMS

W F CROYDON

MAY 1985

Abstract

An MBE system has been designed and constructed. After identification and elimination of various problems, high mobility, Si-doped, n-type GaAs has been grown with electron concentration from $\sim 5 \times 10^{15}$ cm^{-3} ($\mu_{77} \sim 30{,}000$ cm^2/Vs) to a solubility limit at $\sim 7 \times 10^{18}$ cm^{-3}. Unintentionally doped material is high mobility p-type $\sim 10^{15}$ cm^{-3} ($\mu_{77} \sim 8000$ cm^2/Vs), with carbon acceptors identified as the major impurity. Differently reconstructed surfaces have been grown and transferred under UHV conditions to a separate chamber for SIMS analysis.

The low-dose SIMS measurements also identified various deficiencies in the system and enabled improvements to be made throughout the project. Sampling of selected mass peaks enabled SIMS spectra to be obtained with an ion dose of only 5×10^{11} cm^{-2}. The sensitivity of various secondary ion species to the primary ion dose was also measured. Clean surfaces showed reproducible differences only in higher secondary ion yields from the (2 x 4) As stabilised surface, which correlates with the higher work function of this reconstruction, and a higher relative $GaAs^+$ ion yield from the same surface, associated with a more 'bulk-like' reconstruction. The Ga_2^+ signal sometimes showed a large increase with primary ion dose. This may be due to variable quantities of randomly adsorbed arsenic or to ion induced damage, but also dependent on the incident direction of the primary ion beam. Negative SIMS spectra showed only contaminant species.

No great differences were apparent in oxygen uptake on the differently reconstructed surfaces. There are indications that details of the exposure regime may be important, and of a higher initial sticking coefficient on the (4 x 6) Ga stabilised surface, but the results are not easily interpretable. A tentative deduction is that after initial adsorption, possibly at defect sites, the oxide is formed by a process of nucleation and growth, involving oxidation of both gallium and arsenic atoms, followed by the development of a more highly oxidised surface layer at higher oxygen exposures. Several interesting effects such as mass fractionation, ion-bombardment induced species and primary ion current density effects have also been observed and merit further attention.

Various experiments have been suggested as a continuation of this project, but directed as much towards understanding the basic processes of secondary ion emission as in applying the results to determining the GaAs surface structure.

CHAPTER 1

Introduction

The (001) gallium arsenide surface is of interest because of its technological importance in the construction of microwave and other high frequency electronic devices as well as its intrinsic complexity which has, as yet, prevented an adequate understanding of its physical and chemical properties. The structure and properties of the various gallium arsenide surfaces had been reviewed [Croydon (1979)] shortly before commencing this project, with particular reference to oxidation properties and the growth of dielectrics suitable for fabrication of MOS devices. However, the oxidation properties are also of importance in passivation of surfaces and as a source of unwanted contamination during manufacture of eg Schottky barriers. Most previous investigations had centred on the (110) surface, which may be prepared by cleavage in vacuum, rather than on the more technologically important (001) surface, and many fundamental aspects of these surfaces were, and still are, not fully understood.

The Polytechnic had been active for several years in the field of compound semiconductor growth by molecular beam epitaxy [Grange & Parker (1979)] which was claimed to produce near-perfect surfaces suitable for the study of intrinsic surface properties. Secondary ion mass spectrometry, which can be very sensitive to contaminant species and changes in the local chemistry of surfaces, and may be able to provide direct information on surface bonding configurations through molecular secondary ions [Benninghoven (1973) (1975), Dowsett (1977)] had also been in use for several years. It was, therefore, proposed to combine the two techniques in an investigation of compound semiconductor surfaces and interfaces. Other techniques such as PES and ELS can only provide indirect information on bonding configuration through chemical shifts of energy levels, and their interpretation may be both complex and controversial [see eg Croydon (1979), Croydon & Parker (1981)].

A combined SIMS-MBE system had been designed and the SIMS portion was nearing completion when I commenced work on the project in 1980. The MBE portion was designed only in outline, with the main chamber and vacuum pumps, which were constrained by the

requirements of the combined system, being the only large components already available. The intention was that I should design and construct the remainder of the MBE system which would then be used to produce surfaces for SIMS analysis. The design and construction of this MBE system is described in Chapter 2 of this thesis.

MBE growth was commenced with gallium arsenide, since this is the most extensively studied of the III-V semiconductors, and electrical transport measurements were used to evaluate material quality, as described in Chapter 3. It had been intended to construct some active devices for evaluation at GEC Hirst Research Centre as a further test of material quality but this was not carried out, although photoluminescence measurements were obtained, allowing identification of some of the electrically active residual impurities. However, the investigation and modification of the MBE system found necessary to produce high quality epitaxial gallium arsenide took considerably longer than anticipated, becoming an important part of the work, so that it was not possible to extend the investigation to indium phosphide or other III-V compounds. Further work with gallium arsenide is still, in fact, required to characterise, or eliminate, those defects remaining in the epilayers.

An extensive programme of both static and dynamic SIMS investigations had been proposed for the MBE grown surfaces, together with comparative results from surfaces prepared by UHV cleavage. However, subsequent commitment of the SIMS system to other work meant that the static SIMS results presented in Chapters 4 and 5 comprise the first such results obtained from this system. Various improvements were implemented throughout the course of these measurements to overcome deficiencies in the initial configuration of the system, as they became apparent, but the collection of comparative results from the more extensively studied cleaved surfaces and additional AES, XPS and EID measurements originally proposed did not prove possible. Initial work on the effects of oxygen adsorption on (001) GaAs was carried out and is reported in Chapter 5, but there was insufficient time available to extend this work to hydrogen adsorption or the formation of thicker oxides or Schottky barriers as initially proposed.

The work presented in this thesis forms the initial portion of a more extensive programme involving SIMS and other techniques in the investigation of III-V compounds and their surface reactions. This work is, in that sense, a preliminary investigation, but the demonstration of an ability to optimise a complex analysis and growth system and obtain consistent results must be an essential precursor to more extensive studies on the surface composition and chemistry of the (001) GaAs surface, and is equally important with any novel deductions which may be made from these initial results.

A report on the work carried out was presented at the Third International MBE Conference and has been accepted for publication in the Journal of Vacuum Science and Technology. A copy is included as Appendix II of this thesis.

CHAPTER 2

EVA2000 Combined SIMS-MBE System

2.1 Combined System Components

A photograph of the completed EVA2000 combined SIMS-MBE system together with a schematic diagram of the major features of the combined system is given in Figure 2.1. The SIMS and MBE chambers are normally operated as separate systems and the connecting valve only opened to transfer MBE grown surfaces into the SIMS chamber for surface analysis whilst maintaining UHV conditions. Items specific to the separate chambers are therefore discussed in the separate sections below whilst those items relevant to the combined system are discussed here.

The basic configuration of the combined system had already been decided, and construction of the SIMS section was well advanced when I commenced work on the project. The main MBE chamber was already constructed (although it was soon to be modified) and the main frame of the combined system designed to mount this using an Edwards High Vacuum EO4 oil diffusion pump and Vacuum Generators CCT100 anti-creep liquid nitrogen trap as integral parts of the system. Component parts for the backing line were also available and this was constructed as indicated using an Edwards ED50 oil sealed rotary pump, and suitable brackets made to hold the pipework in place without undue stress on the vacuum connections. When the transfer valve was fitted between the two chambers it was found necessary to swing the MBE system by up to one inch to correctly align it with the SIMS system port, and several minor modifications were made in order to accommodate this movement.

2.1.1 Nitrogen Admittance System

A filtered dry nitrogen supply was connected into the roughing line for filling the system before opening it to atmosphere, and for maintaining a slight overpressure of nitrogen to minimise contamination from the laboratory atmosphere. Since the same dry nitrogen supply is used on both the SIMS and MBE chambers and their associated load locks it is necessary to check before letting either system up to atmospheric pressure that the admittance valve of the

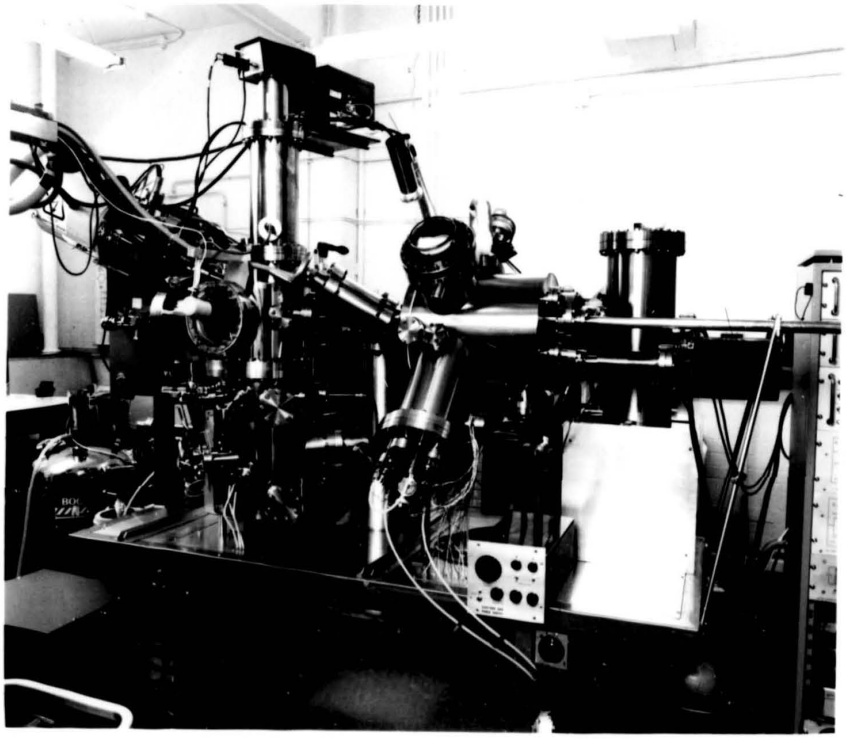

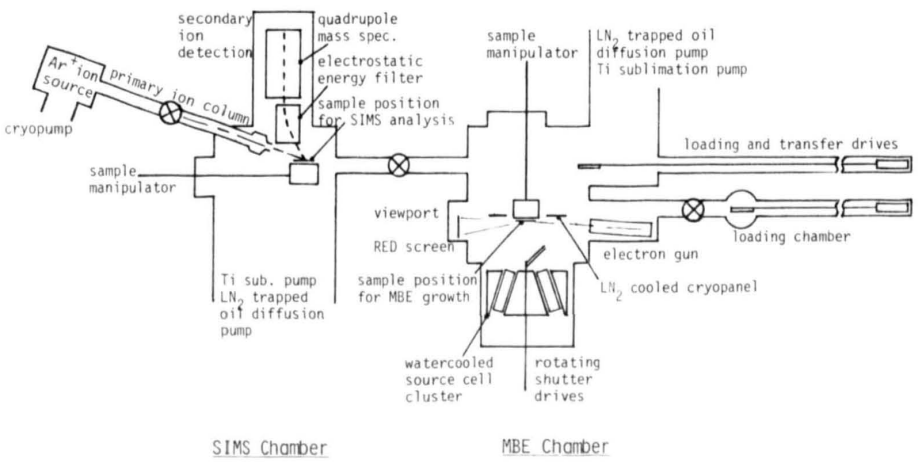

Figure 2.1 EVA 2000 combined SIMS-MBE system.

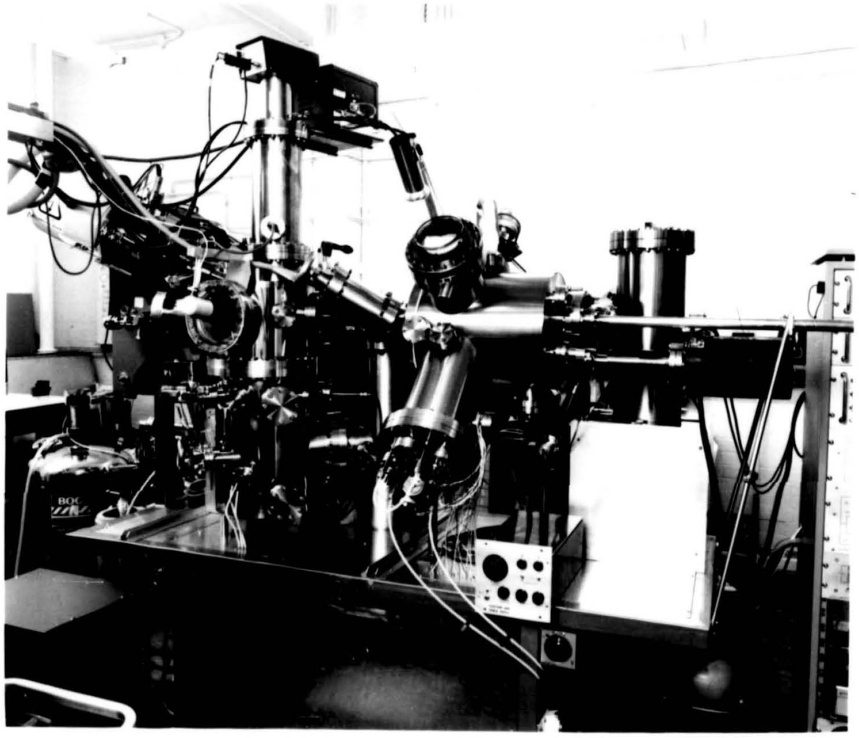

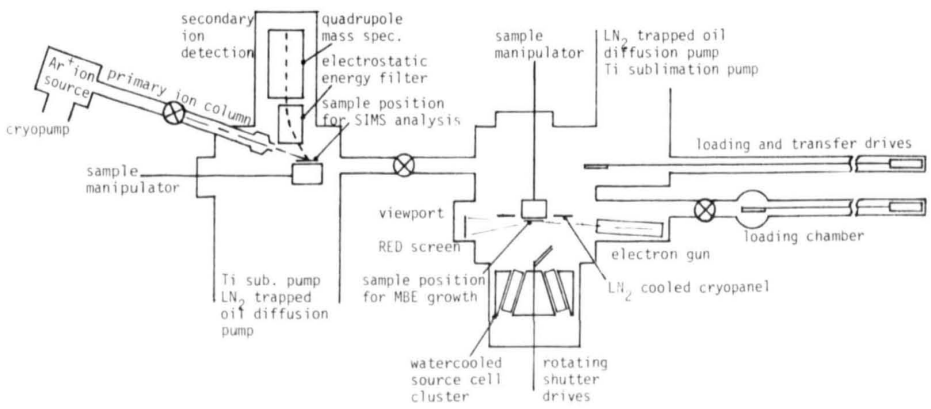

Figure 2.1 EVA 2000 combined SIMS-MBE system.

other system is closed to prevent inadvertant admission of laboratory air via the second system. The dry nitrogen is obtained from a high pressure cylinder and a persistent leak in the line was traced to the use of an incorrect pipe fitting in its original construction. Re-making the connection with a new fitting cured the problem. On the occasions when the nitrogen cylinder was empty the system was brought up to atmospheric pressure using nitrogen gas drawn off from a tube immersed in liquid nitrogen, thus minimising initial adsorption of contaminants but not providing any flow of nitrogen to reduce subsequent atmospheric contamination.

2.1.2 Liquid Nitrogen Supply

The use of liquid nitrogen trapped oil diffusion pumps as the major pumps for both sections of the system entailed a regular replenishment of the liquid nitrogen in these traps. This was accomplished by means of standard BOC electrically powered centrifugal pumps connected to the traps with silicone rubber tubing and operated on a timed basis. An existing timer, already in use on the SIMS system, was modified and fitted with a second timing channel to enable both pumps to be operated independently either manually or by the preset timer. In the latter case, to prevent overloading of the power supply and inefficient operation of the pumps, it was arranged that the pumps did not operate simultaneously but sequentially for their independently set periods. Some difficulties in operation were experienced initially due to the low pressure head capabilities of the centrifugal pumps exacerbated by partial blockage of the silicone rubber tubing with ice. Use of 3/8" bore x 1/8" wall tubing and maintenance of the pumps cured these problems and subsequent operation was generally satisfactory.

2.1.3 System Vibration

The use of rotary pumps to back the oil diffusion pumps transmitted some vibration to the system despite the use of flexible pipe connections and trial of various different configurations to minimise the vibration. Whilst this is not believed to be important for the operation of the MBE system it produced a noticeable vibration of the SIMS sample holder with consequent degradation of crater shapes and resolution in dynamic SIMS depth profiles. The systems were, therefore, often operated for extended periods with the diffusion pumps pumping into their backing volumes. Although the

backing pressure remained < 10^{-1} Torr the MBE system residual pressure was occasionally observed to rise from < 1 to ∿ 3 x 10^{-9} Torr, with no system cryopanelling in use, and this may have caused increased residual impurity levels in some epilayers grown in the system. It is apparent that the EO4 diffusion pump is operating very close to the limit of its differential pressure capability and, to minimise the possibility of backstreaming of contaminants in any future diffusion pumped MBE system, a pump with improved characteristics should be used.

2.1.4 Bakeout Ovens

Bakeout ovens for the SIMS system had already been constructed in the form of insulated flat panels with an aluminium frame and skin as shown in figure 2.2 (a) and (b). It was apparent that this system was much more convenient than the standard box arrangement and material was ordered to construct a similar enclosure for the MBE system. However, by the time construction was started it had become apparent that the insulation provided by the 3/4" thick panels was inadequate and where possible the panels were made thicker as shown in figure 2.2 (c).

The oven was designed to fit the system whether or not the SIMS system was being simultaneously baked; one panel, in the centre of the combined system, being used as a part of both ovens. Whilst the major part of the oven was constructed so that this was the case, the fixing of the lowest panels, to which the bakeout heaters were attached, was not correctly altered with the result that these panels alone could not be simultaneously fixed to their respective ovens. In practice it was not required to bake both systems simultaneously and heating of the laboratory would probably have been excessive had this been done.

Chromel-Alumel thermocouples fixed to the vacuum chamber were used in conjunction with existing temperature controllers to maintain the required bakeout temperature. A total of 6 kW of electrical heating was available in each oven but the MBE system was routinely used with only 4 kW connected, and easily maintained the usual bakeout temperature of 200 °C. On one occasion when the temperature controller failed to operate the temperature rose to 250 °C with no adverse effects. The SIMS system, on the otherhand, required the

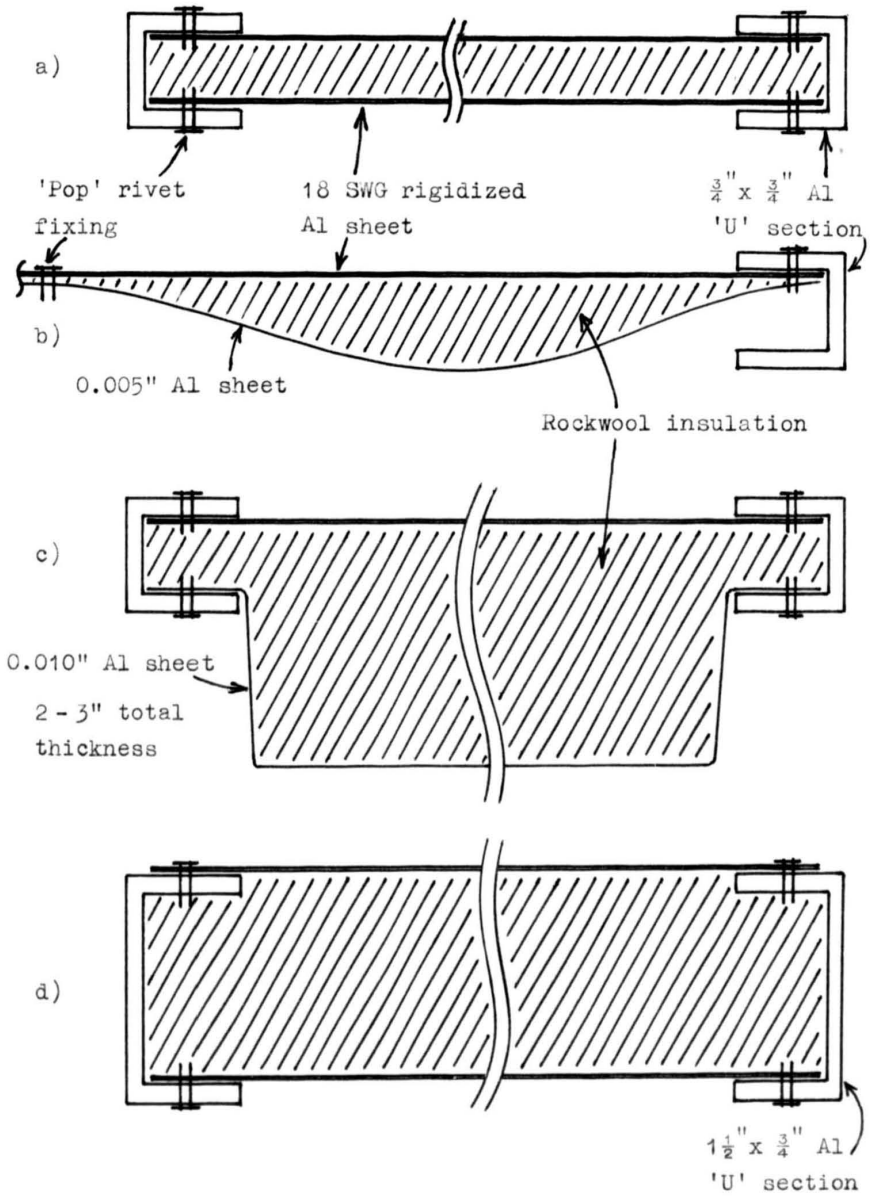

Figure 2.2 Bakeout oven panel cross-sections.
a&b) Initial design.
c) Modified design.
d) Final design.

full 6 kW to reach ∿ 180 °C in an overnight bakeout due to the poorer thermal insulation of this oven.

The design of the MBE system is such that almost all components are enclosed within the cuboid box of the oven, the exceptions being:

(a) the load lock drive tube. This was baked using a 200 W glass fibre insulated heating tape wound around the tube, and being part of the load lock, it is not as important as the main chamber to maintain a uniformly high bakeout temperature.

(b) the transfer drive tube. This was initially baked using a reclaimed, 400 W, silicone rubber insulated heating tape wound around the tube, and which maintained a fairly uniform 200 °C. However, after a period of use the rubber insulation became brittle and started to break up. A separate heating jacket was therefore constructed for this drive based on a thermally insulated tube with a heating element running its full length, and a small box structure to fit around the mechanical support for the transfer drive. The heater was tested using a mains powered variac, found to reach a temperature of 200 °C at ∿ 130 V and therefore connected using a standard mains plug fitted with a single diode rectifier to provide half-wave rectified mains, which produced a temperature of ∿ 190 °C.

(c) the transfer valve. Only the short tube between the valve seat and the MBE chamber is within the MBE system. This was maintained at the baking temperature by wrapping several layers of aluminium foil between the base of the valve and a fixing ring secured to the main oven around the hole cut for the connecting tube.

(d) the substrate manipulator. The inner skin of the top panel had to be 'cut-in' to accommodate this but it did not protrude beyond the outer skin of the panel.

The bakeout oven and heaters for the MBE system are shown in figure 2.3.

From the experience gained in making these bakeout ovens it was concluded that the use of flat insulated panels was beneficial but that they needed wider frames to provide adequate insulation without excessive difficulty in construction. The section shown in figure 2.2 (d) has since been satisfactorily used for the bake-out oven of a new MBE system constructed by the research group.

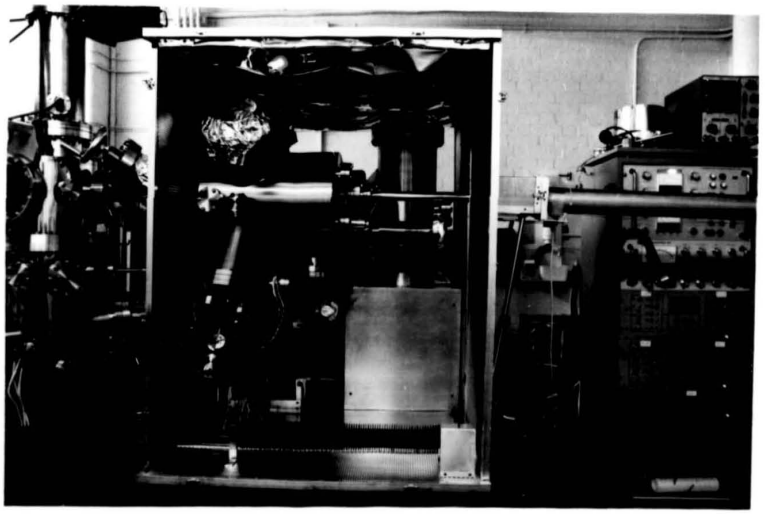

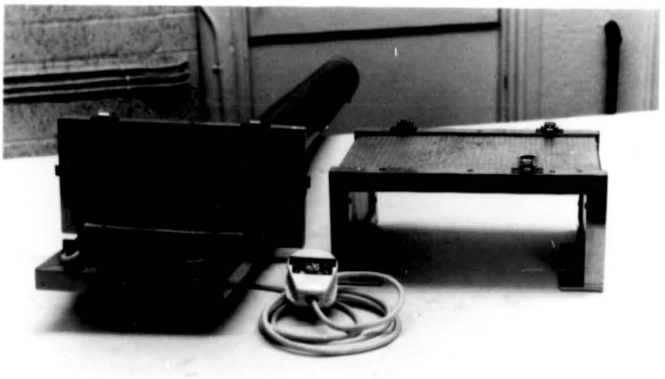

Figure 2.3 MBE system bakeout oven and transfer drive heater.

From the experience gained in making these bakeout ovens it was concluded that the use of flat insulated panels was beneficial but that they needed wider frames to provide adequate insulation without excessive difficulty in construction. The section shown in figure 2.2 (d) has since been satisfactorily used for the bake-out oven of a new MBE system constructed by the research group.

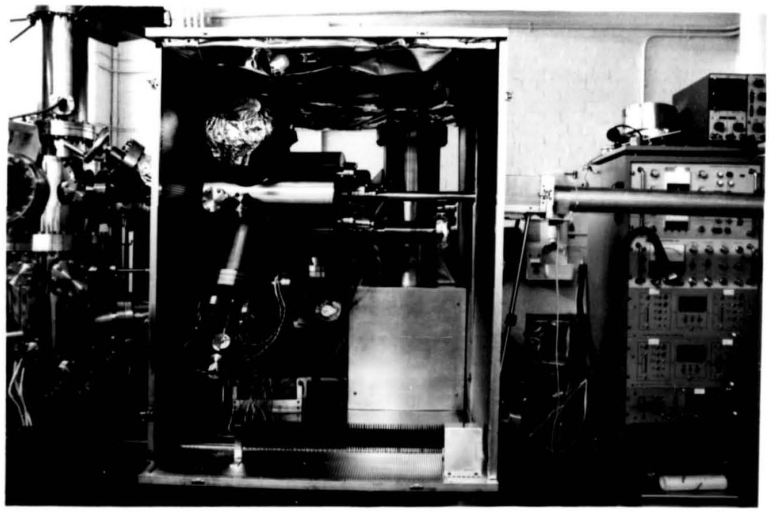

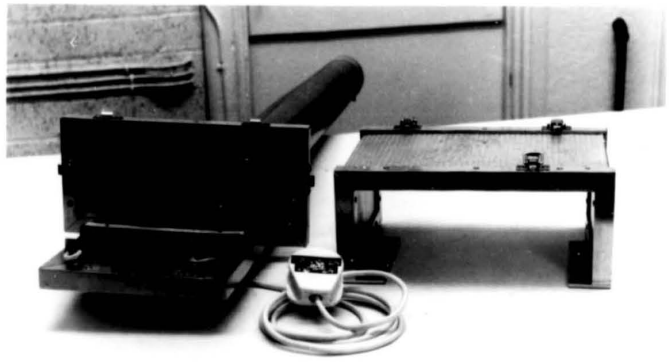

Figure 2.3 MBE system bakeout oven and transfer drive heater.

2.2 MBE System Components

General views of the MBE system are shown in figures 2.4 - 2.6.

2.2.1 Main Chamber and Pumping

A drawing of the main chamber is given in figure 2.7. This chamber was already fabricated when I commenced work on the project but six small additional ports were welded onto the chamber as shown in order to fit various items. When the system was operational three of the ports were in continuous use, one was allocated for an additional cryopanel not fitted but still considered a desirable improvement, and the fifth was used occasionally. Cleaning of the chamber before use proved difficult due to its large overall size and awkward shape. Making one end of the actual chamber a removable flange would have greatly eased matters. A further complication when constructing the system was the absence of any fixing brackets inside the main chamber. This would have simplified the mounting of various baffles and other small items not easily held from their mounting flanges alone.

The major system pumping by a liquid nitrogen trapped oil diffusion pump has already been discussed and a schematic diagram of the complete MBE pumping system is shown in figure 2.8. The viton sealed system isolation valve was constructed as indicated in the diagram to provide the minimum obstruction when fully open. However an additional baffle was necessary where the side arm enters the main chamber to prevent line of sight from both the MBE growth region and the titanium sublimation pump onto the sealing surfaces.

Several all metal UHV compatible valves are incorporated in the pumping arrangement to permit independent evacuation of the main chamber and load lock by the same pumps with a minimum of contamination of the main chamber. All valves fitted required reseating, and knife edges were remachined where possible to attain helium leak free seals. The side port on one non-demountable valve was enlarged to permit replacement of the copper pad, and a Ferranti valve was so well-used that a circlip groove on the operating spindle required remachining to prevent the circlip springing out, in addition to remachining of the knife edge seal.

Due to the relatively high mounting position of the diffusion pump it is actually within the system baking oven, although open to the laboratory on the underside. When the system was first baked the

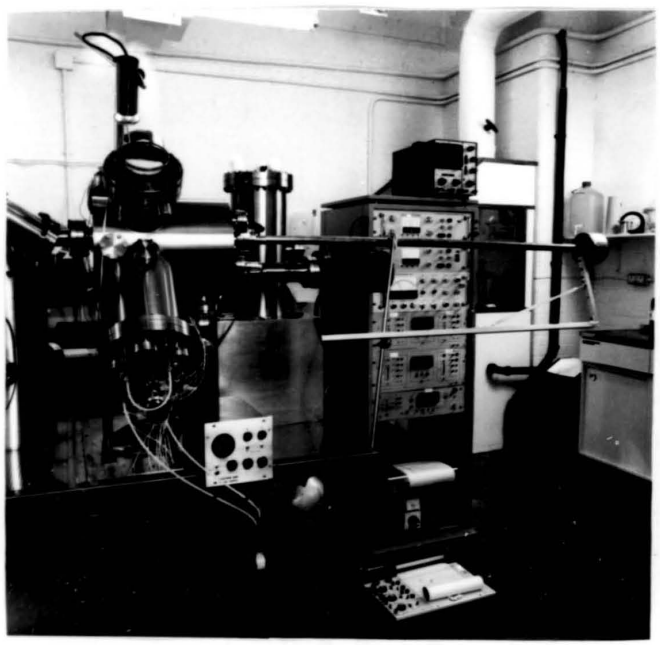

Figure 2.4

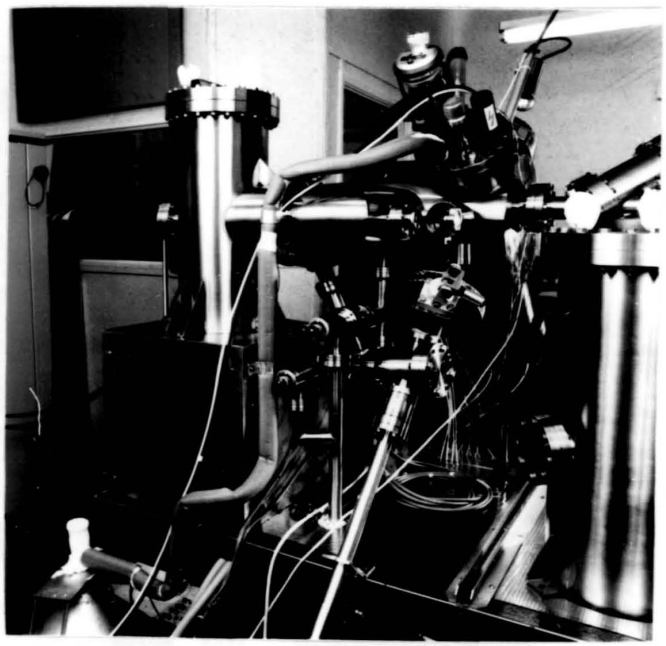

Figure 2.5

Two views of EVA 2000 MBE system showing (2.4) main chamber with source cell cluster, main viewport and RED screen, mass spectrometer, transfer drive and electronics rack; and (2.5) electron gun mounting, load lock and associated components, substrate mounting flange and pressurised LN_2 supply.

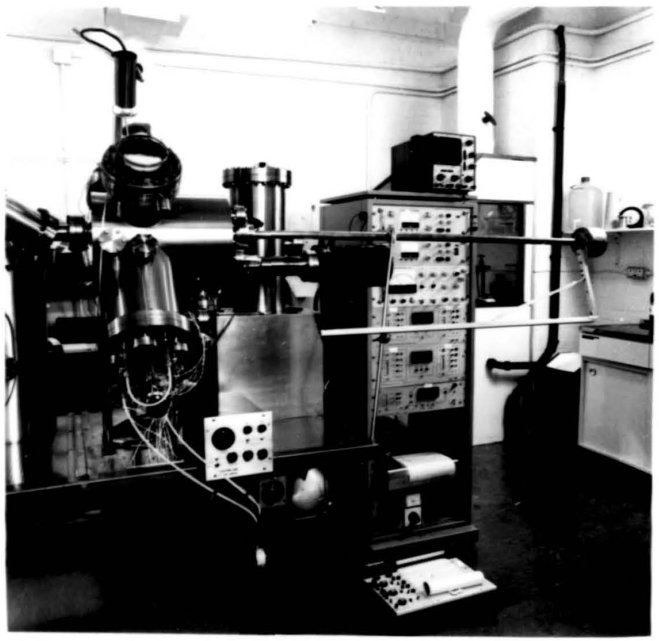

Figure 2.4

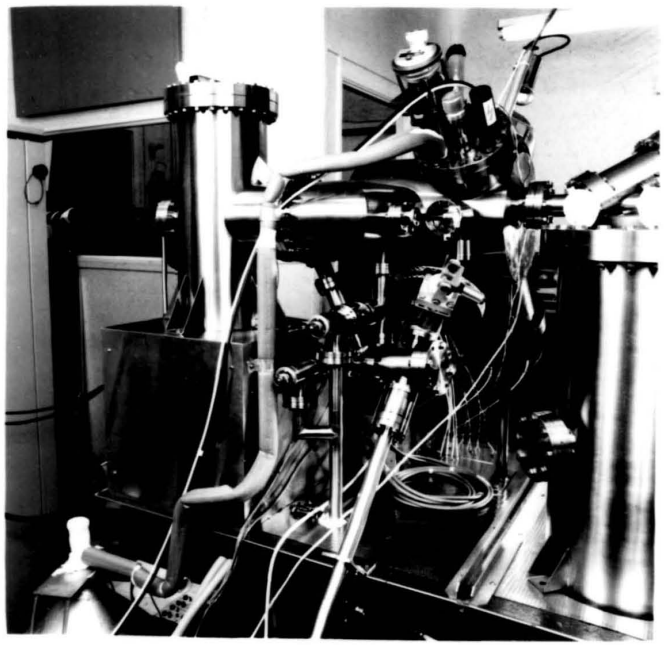

Figure 2.5

Two views of EVA 2000 MBE system showing (2.4) main chamber with source cell cluster, main viewport and RED screen, mass spectrometer, transfer drive and electronics rack; and (2.5) electron gun mounting, load lock and associated components, substrate mounting flange and pressurised LN_2 supply.

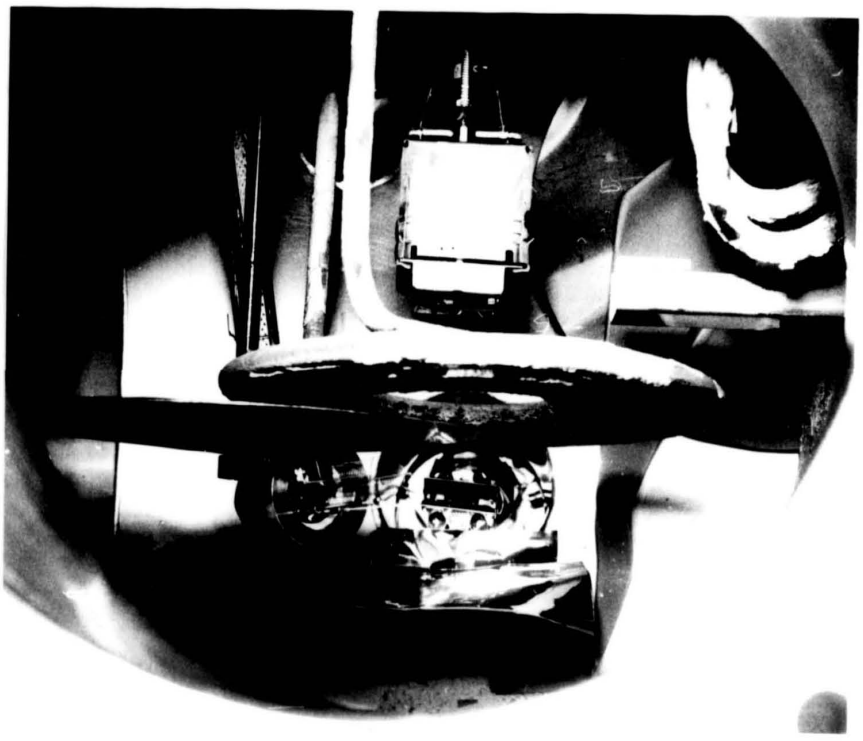

Figure 2.6 Internal view of MBE chamber taken through viewport with window and RED screen removed, and showing substrate heater with substrate in place, substrate shutter and flux monitor, electron gun, transfer tray for moving substrate into SIMS chamber, cryopanels and baffles.

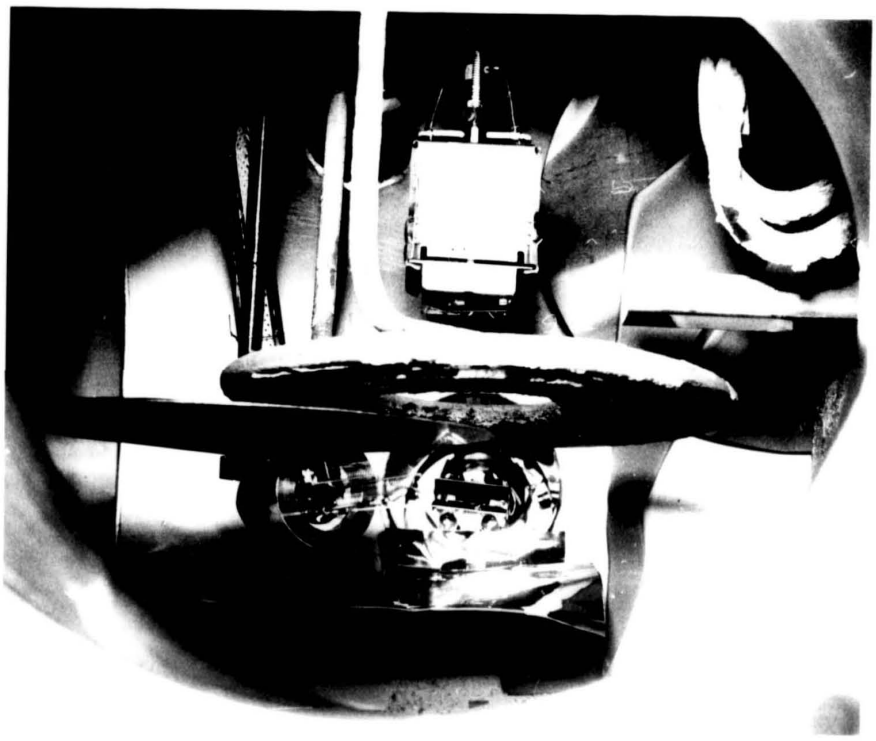

Figure 2.6 Internal view of MBE chamber taken through viewport with window and RED screen removed, and showing substrate heater with substrate in place, substrate shutter and flux monitor, electron gun, transfer tray for moving substrate into SIMS chamber, cryopanels and baffles.

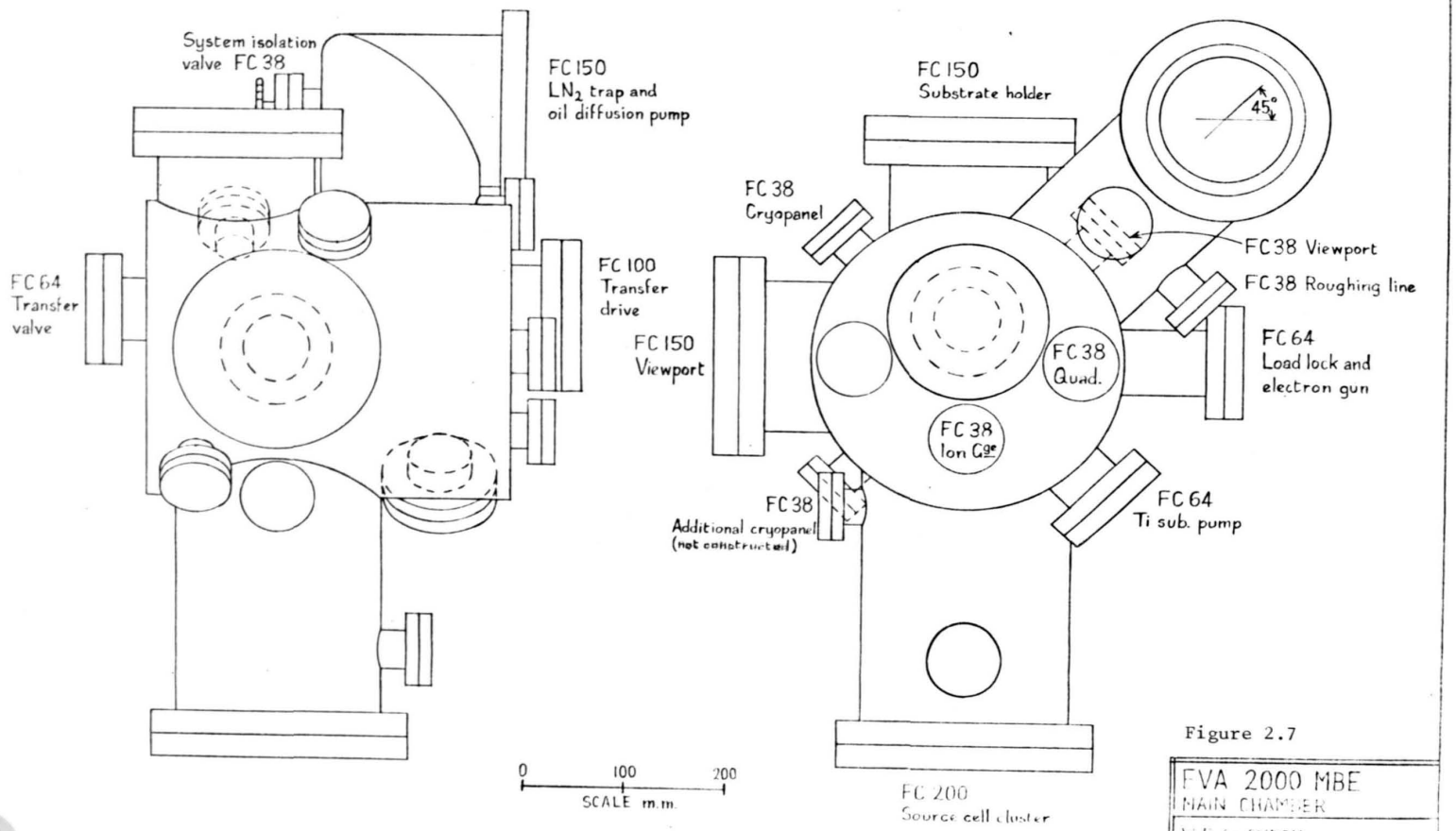

Figure 2.7

FVA 2000 MBE
MAIN CHAMBER
W.F. C. LOYDON
CITY OF LONDON POLYTECHNIC

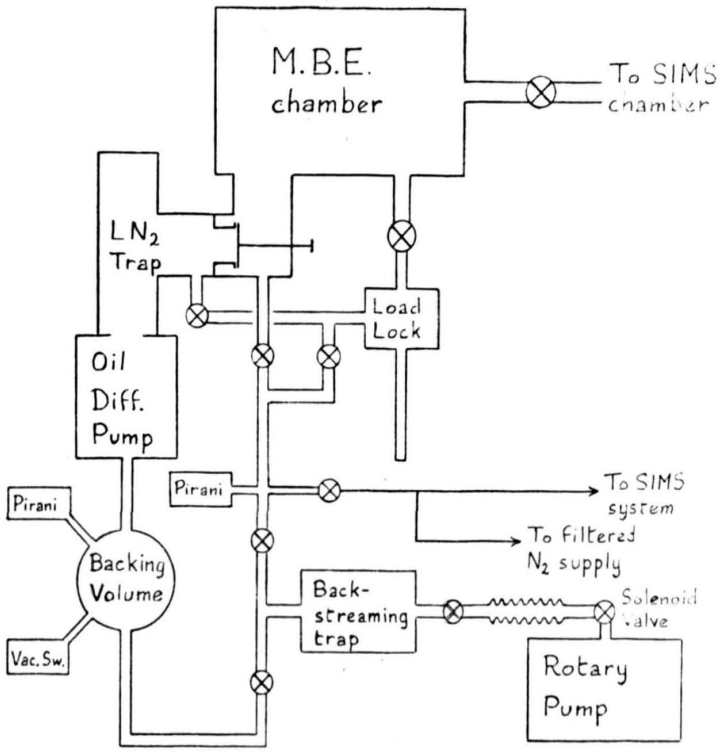

Figure 2.8 MBE system pumping schematic.

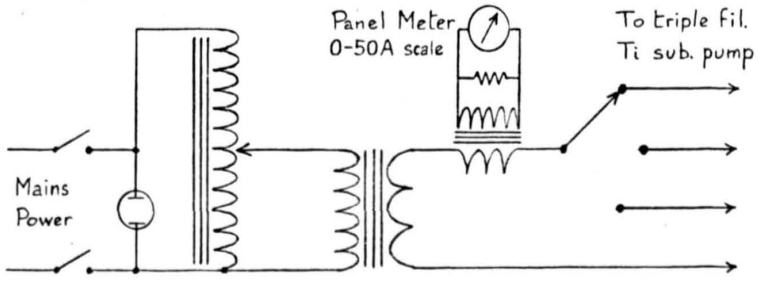

Figure 2.9 Titanium sublimation pump power supply.

the pump did in fact switch off due to overheating of the thermal cutout mounted on the body of the diffusion pump. However this was due to radiant and convective heating of the cutout mechanism from the baking oven rather than actual overheating of the pump body itself, and mounting the cutout in better thermal contact to the pump body prevented reoccurrence of this problem.

On another occasion at an early stage in construction of the system, the motor for the rotary backing pump overheated and cut out. However the power to the isolating solenoid valve was not cut, with the result that the system pressure rose to a few Torr due to leakage of air through the anti suck-back valve in the rotary pump. It was ensured that, on the replacement pump, the solenoid valve was connected after the motor cut-out to prevent a further occurrence. A circuit was also designed, using a non-contacting Hall effect switch, to monitor rotation of the pump spindle and operate the solenoid valve from this, to allow for possible failure of the drive belt. However no further problems were encountered with the rotary pump and this circuit was not constructed.

2.2.2 Titanium Sublimation Pump

The titanium sublimation pump is mounted so that it deposits onto the system cryopanel and a large area of the main chamber wall. Suitable shielding is used to protect nearby components from the titanium flux. Several existing sublimation pumps were tried, but all found to be defective in some way, before constructing a similar triple filament unit using an existing three way 100 Amp electrical feedthrough with common earth return. A power supply was built from existing components and the circuit diagram is shown in figure 2.9. 60 Amp mains cable was used to connect to the terminal block beneath the baked volume and PTFE insulated solid copper wire to connect from here to the vacuum feedthrough.

2.2.3 Cryopanels and Pressurised Liquid Nitrogen Supply

Two major cryopanels were mounted in the system and supplied with a flow of liquid nitrogen from a pressurised dewar. The simplest consists of a coil of copper tube mounted on the substrate flange (see figures 2.12 and 2.13). Initially the copper tube was taken directly through the system wall but this did not provide a

rigid mounting for the Swagelok pipe fittings and built up a dark oxide scale during bakeout. When the knife edge seal on this flange was re-machined the opportunity was taken to replace the copper tube with stainless steel externally and for the vacuum feedthrough, whilst retaining the copper coil as the cryopanel.

The second cryopanel was formed from a copper plate with copper tube silver soldered to one face. This panel is designed to divide the vacuum chamber into two portions - the growth region and a small service region - and has to be inserted through the source cell port with connections to the liquid nitrogen feedthrough made inside the chamber. These connections were made using standard silver plated stainless steel Swagelok pipe fittings, since the specified helium leak rates of less than 5×10^{-9} atm cc/sec are similar to those quoted for other UHV pipe fittings and I was advised that Swagelok fittings were used for this purpose by Philips Research Laboratories. However, considerable difficulty was experienced in obtaining a helium leak tight seal and suitable Cajon UHV pipe fittings were purchased in case the seals had to be broken and remade at any stage. It later transpired that the Swagelok fittings used by Philips Research Laboratories were modified to use a small copper gasket with a seal similar in principle to UHV Conflat seals, in place of the standard olive compression seal. A drawing of the liquid nitrogen feedthrough is provided in figure 2.10. The cryopanel is held in place solely by the liquid nitrogen feed pipes and a nominal half inch clearance was allowed between the cryopanel and system wall to enable it to be correctly positioned without touching the chamber. A 1½" diameter hole was provided in the panel to pass the transfer drive mechanism and a 1½" length of copper tube was fitted in this hole to prevent any direct line of sight from the titanium sublimation pump into the MBE growth region. Six 4BA holes were tapped near the edges of the cryopanel for additional fixings if found necessary, but they were not used.

All silver soldering on both of these cryopanels was carried out with Argo-braze 56. This alloy is free of Zinc, Cadmium and other volatile components which might generate impurities in the MBE epilayers, having a nominal composition of 56% Ag, 27% Cu, 14.5% In, 2.5% Ni (Johnson Matthey Metals Ltd). As a further

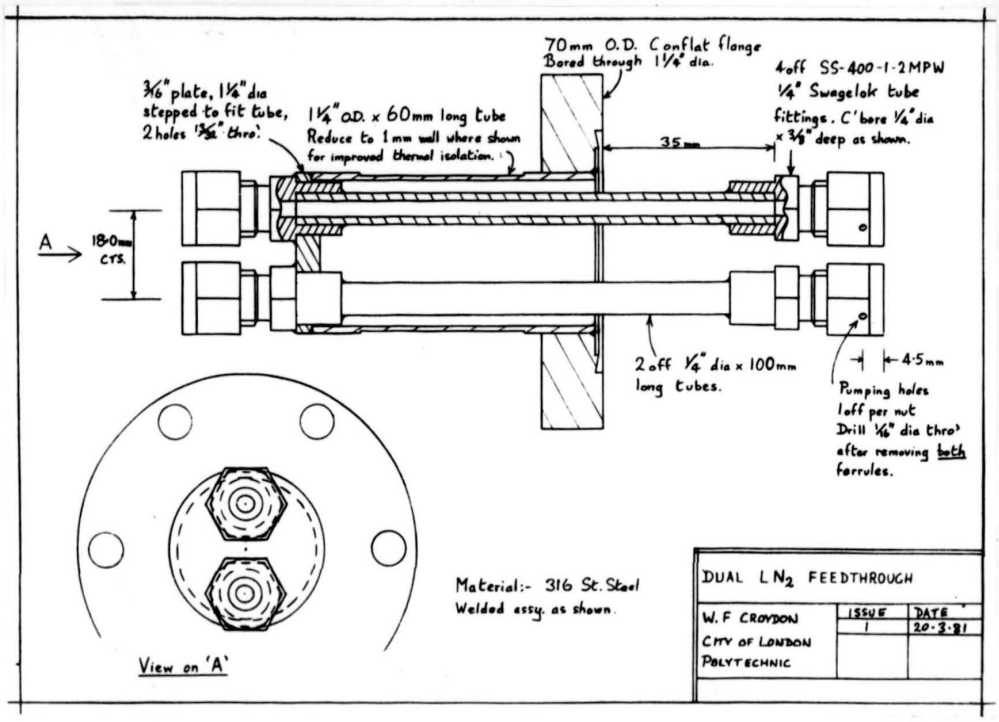

Figure 2.10 Dual LN_2 feedthrough.

Figure 2.11 Counterbalanced viewport shutter.

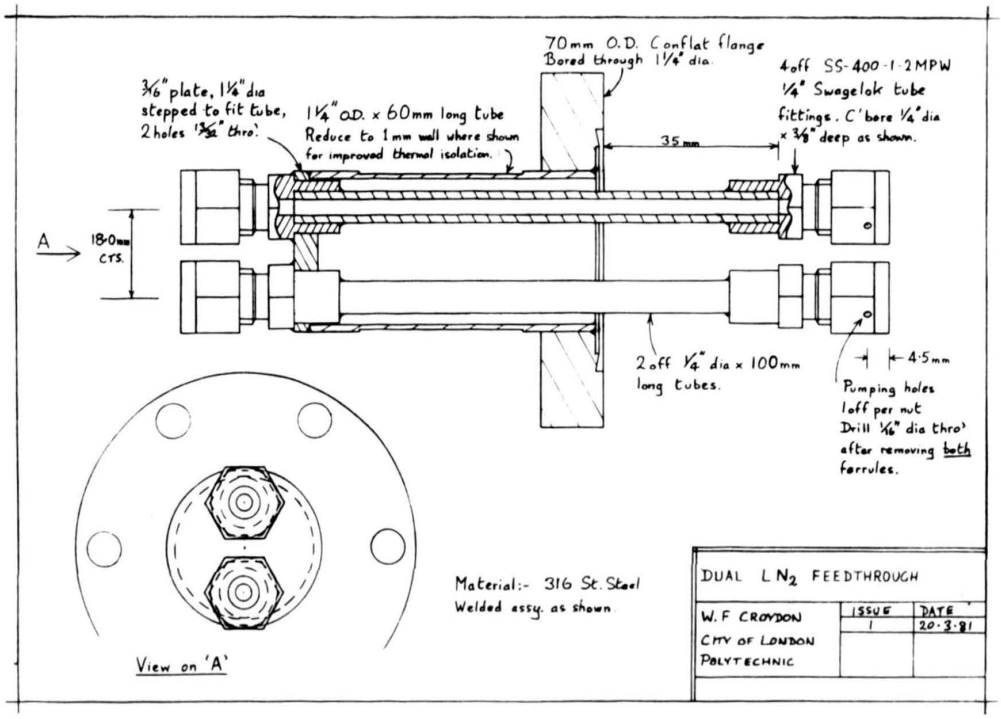

Figure 2.10 Dual LN_2 feedthrough.

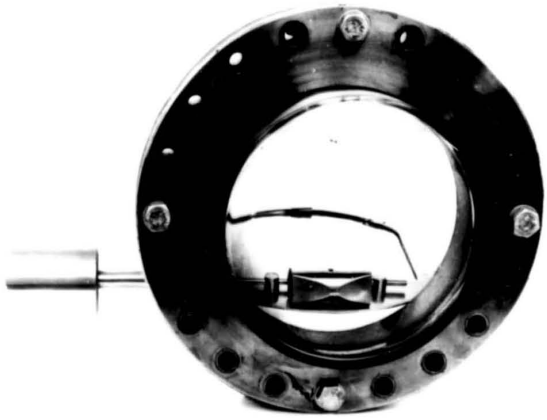

Figure 2.11 Counterbalanced viewport shutter.

precaution silver soldering was carried out such that there was no direct line of sight to the epilayer.

It was intended to fit a third helically wound copper cryopanel between the source cell cluster and the growth plane as indicated in figure 2.16 but this involved further pipe fittings inside the vacuum system and in view of the problems encountered with the second cryopanel described above it was decided not to attempt to fit this initially, and the liquid nitrogen feedthrough constructed for this was used on another vacuum system. However, I now consider that fitting this cryopanel would give a significant improvement to the system both by reducing the residual background pressure, and changes occurring on shuttering the arsenic cell, which would enable more accurate measurement of molecular beam fluxes with the ion gauge fluxmonitor and faster return to UHV conditions after growth of an epilayer, and, perhaps more importantly, by preventing a direct line of sight between the epilayer and the annulus surrounding the source cell cluster, thus minimising exposure of the epilayer to those volatile gases generated by the source cell heaters and which must be pumped through the main growth chamber.

Finally a series of small cooling panels was fitted to the mounting flange of the source cell cluster (see figures 2.16 and 2.17). This was primarily intended to prevent excessive temperature rise due to radiant heating from the source cells and was generally water cooled. However it was designed with the option of liquid nitrogen cooling to provide some pumping behind the source cell cluster and the few occasions when this was done gave some indication of lower impurity levels within the epilayers.

Liquid nitrogen for these cryopanels was provided initially from a simple 25 litre liquid nitrogen dewar. A large rubber bung was bored to take a liquid draw-off fitting which was extended to reach the base of the dewar when the assembly was fitted into the dewar mouth. Pressure was raised and maintained in the dewar by boiling off liquid nitrogen using a small electrical heating element wound around the lower part of the draw-off tube. The nitrogen was piped to the cryopanels, connected in series, using 1/4" diameter copper tube insulated with standard foam rubber pipe insulation. Larger diameter and/or thinner wall tubing would probably be advantageous for both the cryopanels themselves and the connecting

tube to reduce the pressure required to maintain a sufficient flow of nitrogen.

Initially the nitrogen was vented directly from the feedthrough to the second cryopanel as is apparent in the general photographs figure 2.1, 2.4 and 2.5,and the heater power was adjusted to give a minimal outflow of liquid nitrogen. Under these conditions the 25 litre dewar was barely sufficient for 5 hours growth. It then became apparent that residual CO pressure would vary considerably with small changes in cryopanel temperature caused by inadequate liquid nitrogen supply and that the residual gas might also be affected by changes in the chamber wall temperature near the outlet, caused by changes in the excess liquid nitrogen vented. A length of tube was therefore used to direct the excess nitrogen into an insulated container and the dewar pressure increased to give a small, but definite, flow of liquid nitrogen at the outflow to ensure that all cryopanels were maintained at liquid nitrogen temperature.

This increased flow of liquid nitrogen meant that the 25 litre dewar was no longer adequate for many growth runs. A 35 litre dewar was obtained and a suitable adapter made to enable the existing draw-off mechanism to be used on this dewar. However, when it was tested, continuous venting of the dewar was required, rather than power input, due to an excessive thermal leak. The boil-off rate was found to be approximately 1½ litres/hour giving an effective capacity comparable with the original 25 litre dewar. All other 35 litre dewars available were in a similar condition and therefore a 75 litre dewar previously used for long-term storage was obtained. This dewar was fitted with a self pressurising mechanism and pressure gauge, and was a more than adequate supply for a full day's work, however the pressure gauge froze up after a couple of hours continuous use. Use of this large dewar enabled the fourth cryopanel, on the source cell flange, to be liquid nitrogen cooled using the 25 litre dewar and draw off unit.

Although the main source cell cluster was only water cooled throughout this project, as originally intended, I now believe that it would be worthwhile to attempt liquid nitrogen cooling of this tank. Such cooling should reduce considerably any flux of volatile gases generated by the source cell heaters and effusing around the source cell cluster into the growth region of the chamber. Provided

the tank can be adequately dried before filling with liquid nitrogen and maintained full when in use, possibly by continually circulating liquid nitrogen with a pump, it should be a straightforward experiment to see whether the level of background impurities in epilayers is reduced.

2.2.4 Viewport Shutters

Unshuttered viewports in a III-V MBE system are gradually obscured by a deposit of the group V element even if they are not in direct line of sight to any of the source cells. The two viewports used in this system were therefore provided with magnetically operated shutters. The shutter is mounted as a flag at one end of a stainless steel shaft, the other end being fixed to a soft iron plate, enabling the shaft to be rotated by a small magnet to open and close the shutter. That for the main viewport is shown in figure 2.11 before fitting the RED screen. Since this port is inclined at 45° it was necessary to lighten the shutter and fit a counterbalance weight as shown so that the shutter would remain in either the open or closed position as required when the operating magnet was removed.

2.2.5 Substrate Holder

A drawing of the substrate mounting flange and other associated components is provided in figure 2.12. Figure 2.13 shows photographic views of the flange in both initial and final states. The copper cryopanel has already been mentioned and, in addition to this and the substrate holder itself, the flange also carries a rotatable substrate shutter and the ion gauge flux monitor discussed in section 2.2.8 below.

The substrate heater itself is shown diagramatically in figure 2.14 and consists of a tantalum wire heating element wound on a boron nitride former and suspended by its connecting leads inside a molybdenum box constant temperature enclosure. Several layers of crinkled molybdenum foil are fitted inside the box to act as heat reflectors and minimise radiant heat losses whilst the molybdenum substrate mounting plate forms one side of the enclosure. Gaps between the heater enclosure and the substrate mounting plate are kept as small as possible, consistent with reliable loading and removal of substrates, to minimise stray light from the heater which may obscure electron diffraction patterns formed on the fluorescent screen. Initially

Flange Details
A- FC 38 stub flange.
B- adaptor, 70 O.D. Al wire seal to mini-conflat.
C- 70 O.D. Al wire seal - see detail for arrangement of electrical feedthroughs for substrate heater and thermocouple connections.
D- adaptor, 24 O.D. Al wire seal to mini-conflat, EFT 940 elect. feedthrough for flux monitor connections.
E- LN_2 feedthroughs, 8 O.D. tube ½" O.D. mounting, welded assy.

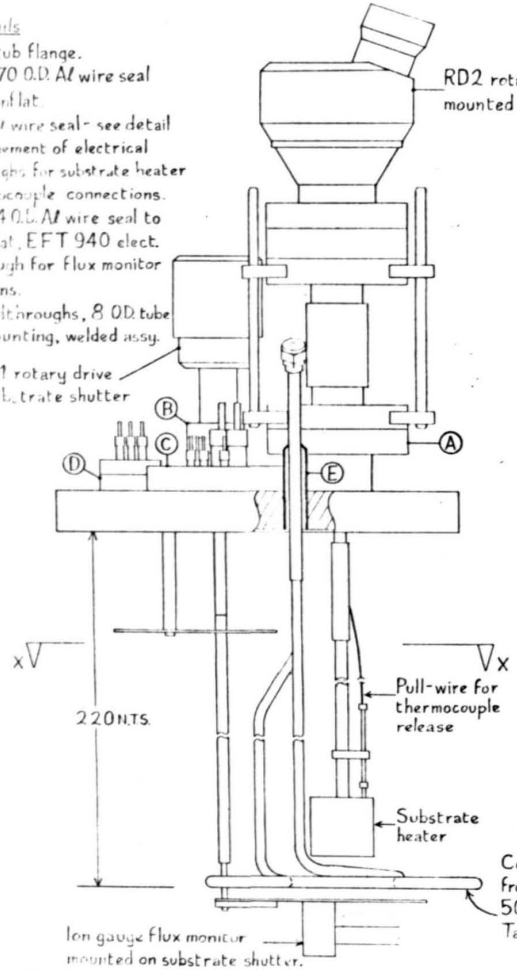

Note: Quartz insulated electrical connecting wires are not shown.

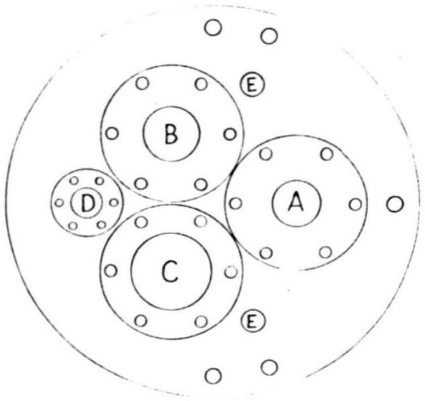

Detail of main flange
(200 O.D. conflat seal)

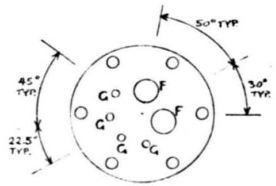

Detail of flange 'C'

Hole Details
A, B & C equi-spaced on 41 rad.
Bolt holes 6.8 thro' (A) or ¼" B.S.F. x 10 deep (B) equi-spaced on 58.7 P.C.D.
A- 26.8 dia to take stub flange.
B- 27 dia thro'. Mcd to suit Al wire seal.
C- 38 dia thro'. Ditto.
D- 16 dia thro'. Ditto. on 62 rad.
Bolt holes M4 x 6 deep equi-spaced on 27.0 P.C.D.
E- 2 off 12.7 dia thro' on 65 rad.
F- 2 off 12.7 dia thro' on 11.0 rad.
G- 4 off 4.5 dia thro' on 15.0 rad.

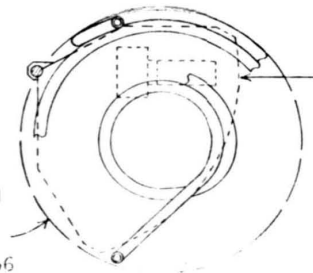

View on X X

Substrate shutter, 0.5 thick Mo sheet plus Ta & Mo foil heat reflectors.

0 100 200

SCALE – ALL DIMENSIONS IN m.m.

Figure 2.12

EVA 2000 MBE
SUBSTRATE FLANGE ASSY.
W.E. CROYDON
CITY OF LONDON POLYTECHNIC

a)

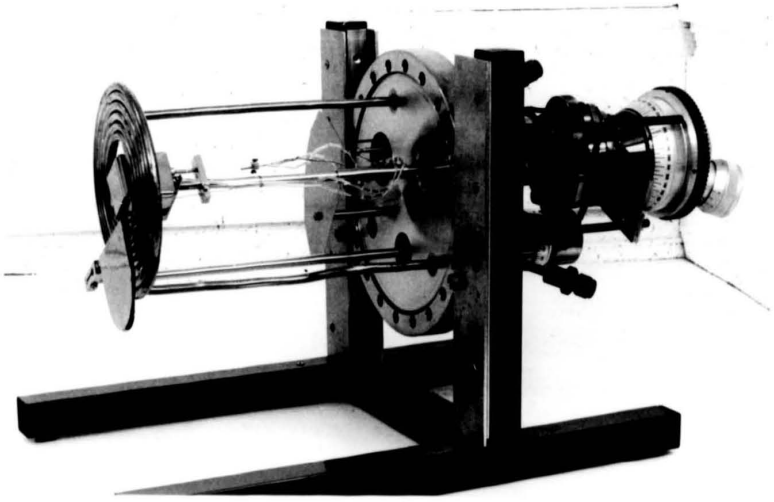

b)

Figure 2.13 Substrate mounting flange in (a) initial and (b) final states. Showing cryocoil, substrate heater and substrate, shield for electrical feedthroughs, substrate shutter and ion gauge flux monitor.

a)

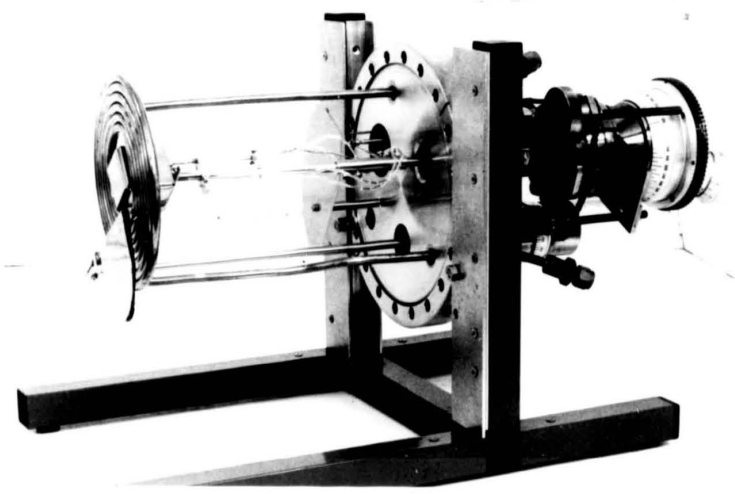

b)

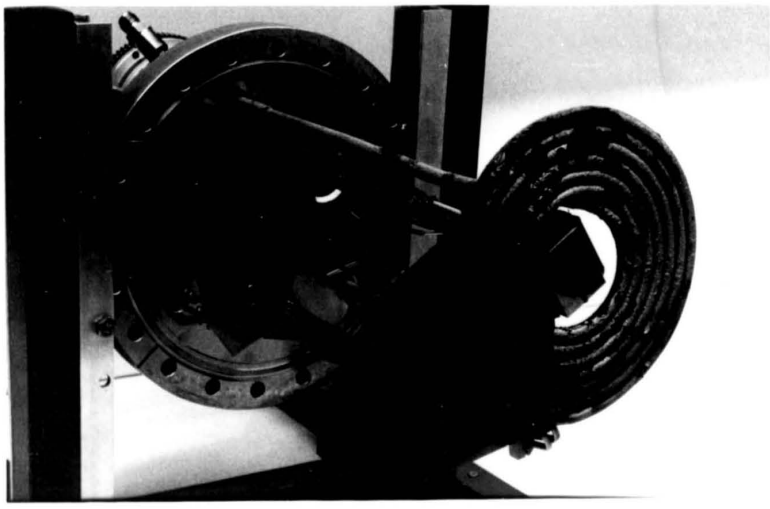

Figure 2.13 Substrate mounting flange in (a) initial and (b) final states. Showing cryocoil, substrate heater and substrate, shield for electrical feedthroughs, substrate shutter and ion gauge flux monitor.

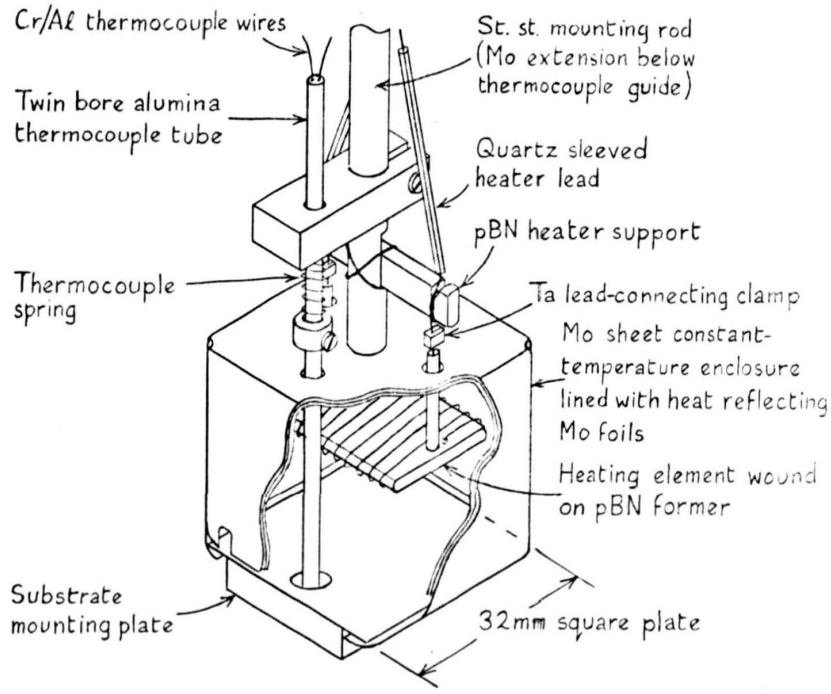

Figure 2.14 Substrate Heater

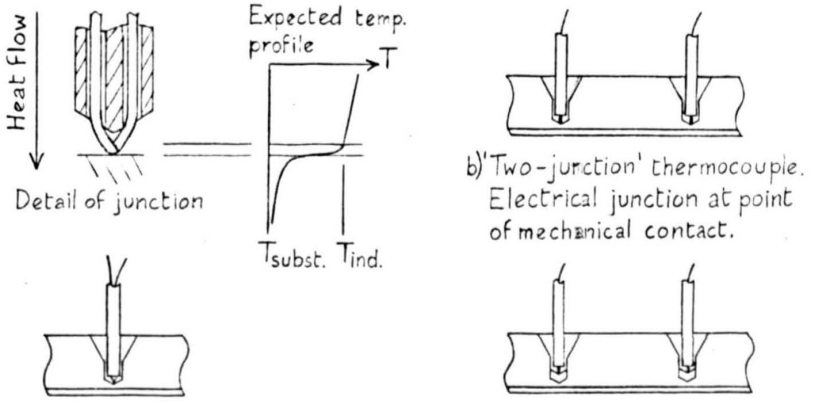

Figure 2.15 Substrate temperature measurement.

substrates were mounted on a plate bent from 0.5 mm thick molybdenum sheet held in place by a molybdenum foil spring within the heating enclosure. However, this did not prove satisfactory and was replaced by the design shown in the figure using 1/4" thick molybdenum plate, which leaves smaller gaps for stray light from the heater, should give better uniformity of temperature across the substrate, and permits more positive location by means of the thermocouple rod locating in the substrate plate. Temperature of the substrate is monitored by means of this chromel/alumel thermocouple which is held in place in the recess by a stainless steel spring, except when withdrawn to permit removal of the substrate. Connecting wires to the heater and thermocouple are insulated with short lengths of quartz tube to permit the necessary translation and rotation of the substrate holder without shorting together, and the electrical vacuum feedthroughs are shielded from the source cells by a stainless steel plate to prevent any build up of conducting material. Small deposits of gallium arsenide on the substrate plate could be scraped off when spreading the indium solder, but larger deposits were removed by etching with hot concentrated hydrochloric acid to remove free indium, followed by sulphuric-peroxide to remove the gallium arsenide. Plates were then washed in deionised water and isopropanol, and degassed before reuse. The substrate heater is powered by a two term (proportional and differential) temperature controller and details of this will be discussed in section 2.2.7.

The major weakness of the substrate heater proved to be the measurement of substrate temperature. Because of the proximity of the thermocouple to the heating element and major heat losses from the substrate there is a heat flow along the thermocouple wires into the substrate. Due to thermal resistence between the thermocouple junction and the substrate (see figure 2.15 (a)) this means that the thermocouple will always indicate a higher temperature than the substrate block under steady state conditions (by $\sim$ 100 °C at normal operating temperatures form calibrations given in Chapter 3). However this temperature difference does not remain constant but changes abruptly by up to 50 °C when the substrate holder is rotated and the thermocouple moves within the recess, and also tends to decrease when the substrate holder is left stationary for a long period producing a better thermal contact. Various ways to reduce these effects were attempted. Shielding the thermocouple with

molybdenum foils inside the heater enclosure had little effect. Placing a small bead of indium (molten at normal operating temperatures) in the thermocouple recess greatly reduced the changes in indicated temperature observed when the holder was rotated but this dissolved the thermocouple tip. Bending the thermocouple wires outwards to give a 'two-junction' thermocouple did not produce reliable electrical contact.

I believe that the most promising modification to this substrate heater in order to improve the accuracy and repeatability of temperature measurement will be to replace the single spring loaded thermocouple with two independently sprung thermocouple wires each locating in their own recess as shown in figure 2.15 (b) to give a 'two junction' thermocouple. A further improvement should be possible by fixing a piece of the relevant thermocouple material at the base of each recess as shown in figure 2.15 (c). If this is soldered in place with aluminium or a high melting point alloy it should give a good thermal contact to the block at the thermocouple junction and hence a good temperature measurement.

2.2.6 Source Cell Cluster

A drawing of the source cell cluster and associated components is provided in figure 2.16 and photographic view in figure 2.17. The flange is designed to accommodate five effusion cells, each of up to 35 mm overall diameter and 110 mm long, within the watercooled tank. Dimensional constraints imposed by the existing main chamber limited the minimum possible source - substrate distance to 160 mm and necessitated tilting the cells on their individual mounting flanges. This meant that it was not possible to remove individual cells without removing the whole cluster from the vacuum system, but the unit was still designed to use source cells mounted on individual flanges to enable quick replacement of broken or damaged cells or vacuum feedthroughs, although the ideal of spare, fully assembled, source cells was not achieved during this project. The necessary cell shutters were designed as a concentric pair operated by a single rotary drive which could be engaged with either shutter, that not engaged being held stationary by sprung carbon brake blocks. The shutters were not entirely satisfactory, there being an occasional tendency for them to bind together and rotate as a pair, and some cross-contamination due to build-up of gallium on the shutters which would flow to the lowest point and could then fall off.

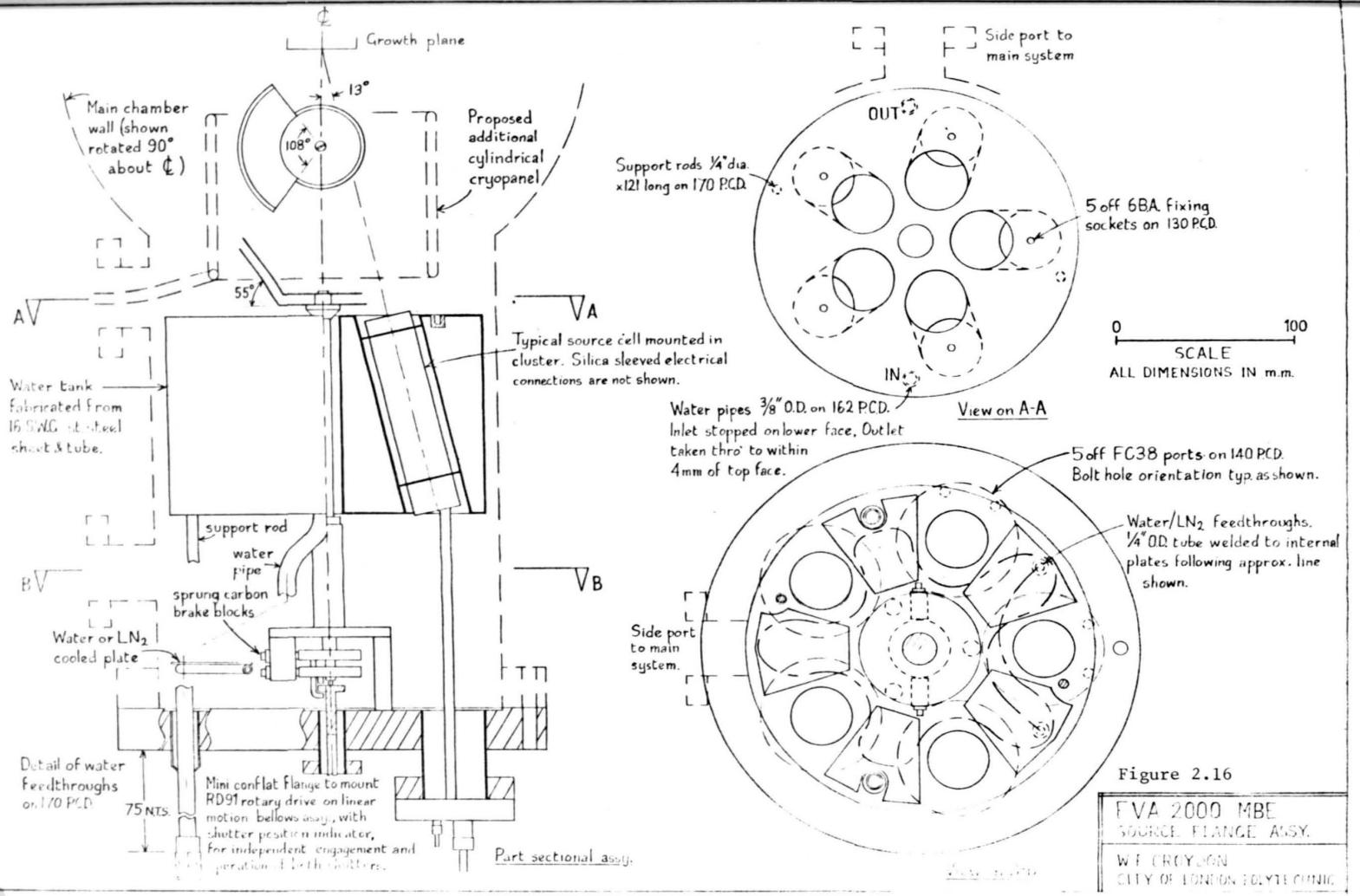

Figure 2.16

FVA 2000 MBE
SOURCE FLANGE ASSY.
W.F. CROY & SON
CITY OF LONDON POLYTECHNIC

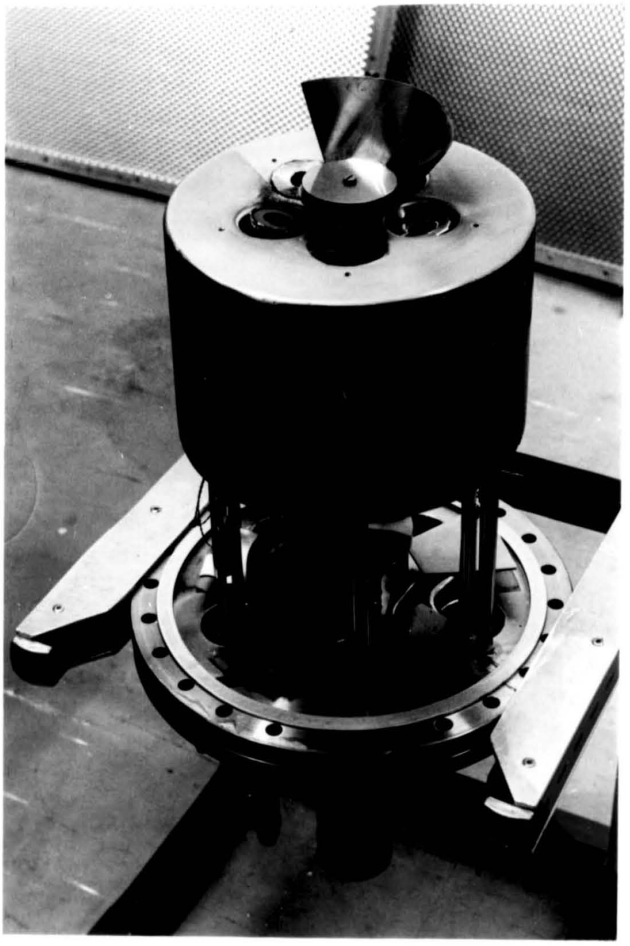

Figure 2.17 Source cell cluster.
The two concentric shutters may be positioned to shutter any one, two, three or four of the five source cells. The four source cells visible are, reading clockwise, the silicon dopant cell, gallium cell, tapered gallium cell with 6mm dia. orifice, and finally the arsenic cell.

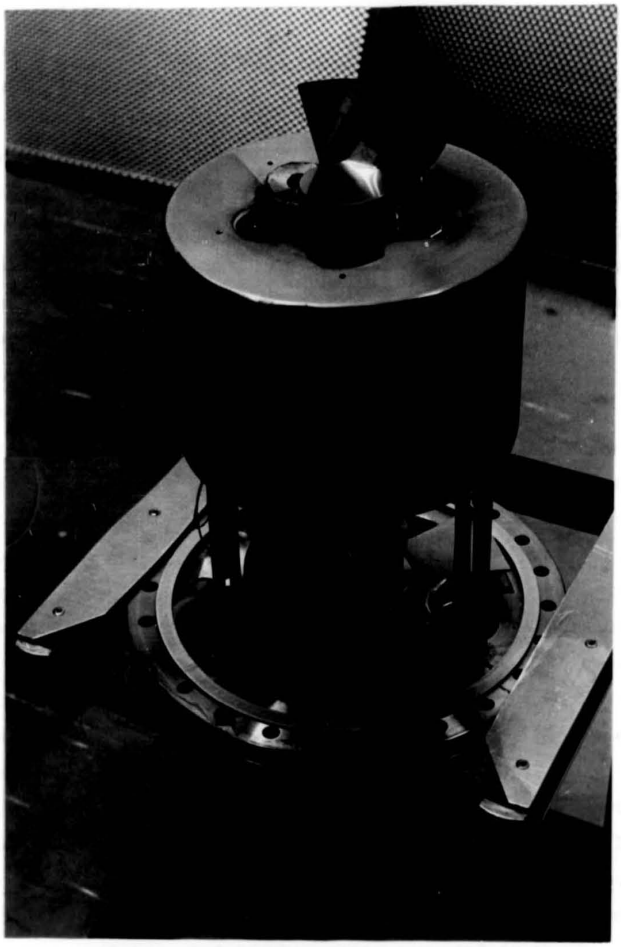

Figure 2.17 Source cell cluster.
The two concentric shutters may be positioned to shutter any one, two, three or four of the five source cells. The four source cells visible are, reading clockwise, the silicon dopant cell, gallium cell, tapered gallium cell with 8mm dia. orifice, and finally the arsenic cell.

However, cross contamination was not critically important in this project and, given the restricted space and money available, any other feasible design would probably have entailed equivalent disadvantages. The position of both shutters could be set on a small indicator dial made for this purpose and visible in figure 2.4 whilst the operating knob showed directly the position of the shutter currently engaged. A series of notches in the knob and a spring locating wire enabled the shutter to be operated whilst observing electron diffraction patterns. A series of stainless steel plates, welded to a stainless steel tube, were positioned in the otherwise unused spaces of the flange to provide cooling of the flange and possibly additional pumping of condensible species produced by the source cell heaters.

The design of the source cells themselves is shown in figure 2.18. The arsenic cell is the largest volume since films are grown under excess arsenic conditions and it is also supplied in large crystalline lumps which do not pack efficiently within the cell. Since this is a low temperature cell fewer precautions were taken in shielding the heating element, although direct line of sight to the substrate was avoided. All other cells are variations on the basic design of Kubiak et al (1982) with the annular heater enclosure an integral part of the source cell, ensuring that all volatile species generated at the heater are directed away from the growing epilayer. The essentially non-inductive winding minimises distortion of electron diffraction patterns due to stray fields from the heaters. All cell temperatures were monitored using chromel/alumel thermocouples. Initially 0.1 mm dia wires were used, spot welded to a tantalum foil heat collector, and inserted in the recess provided in the base of the cell. However this thin wire deteriorated fairly rapidly in the higher temperature cells and subsequently 0.3 mm dia wires were used instead. This is expected to give somewhat low readings for the cell temperatures due to the heat losses down these wires but attainment of a stable, reproducible reading is of greater importance than its absolute accuracy.

Initially the high temperature source cells were outgassed at 1200 °C prior to use and after filling with source material (800 °C and 350 °C respectively were used for the arsenic cell) and this gave few problems with the thermocouples (1000 - 1200 °C is generally considered a working maximum for chromel/alumel thermocouples).

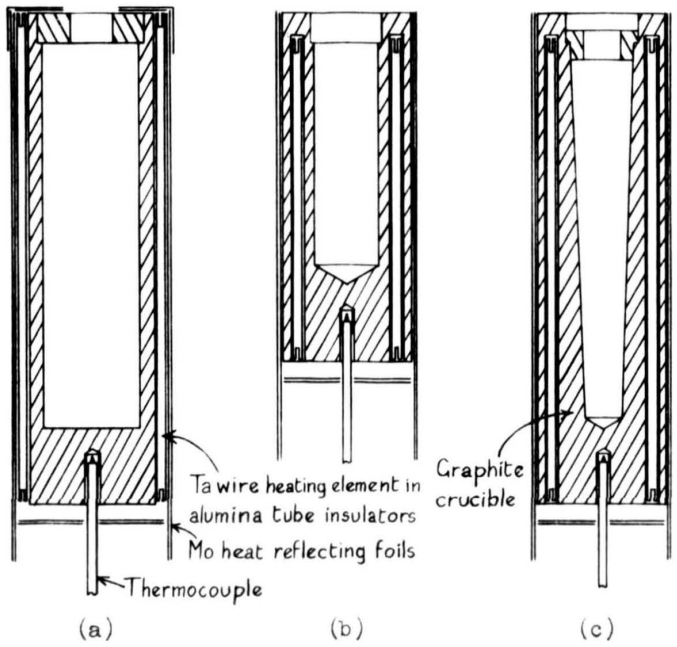

Figure 2.18 Cylindrical source cell designs (approx. full size).

a) Large volume arsenic cell.

b) Standard high-temperature cell.

c) Tapered gallium cell.

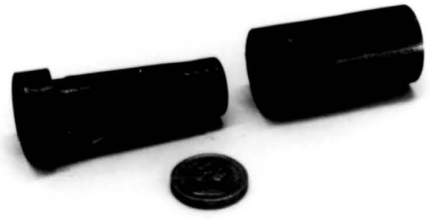

Figure 2.19 Cracked silicon source cell after heating to > 1300°C.

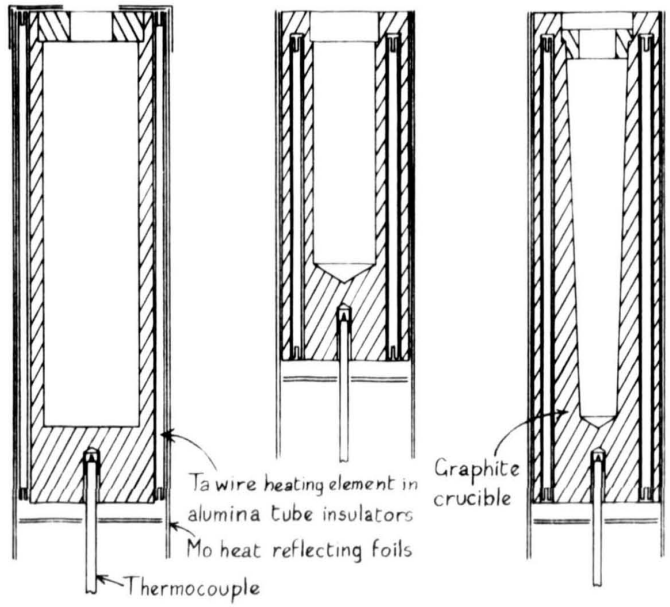

Figure 2.18 Cylindrical source cell designs (approx. full size).
a) Large volume arsenic cell.
b) Standard high-temperature cell.
c) Tapered gallium cell.

Figure 2.19 Cracked silicon source cell after heating to $> 1500^{\circ}C$.

However, reports of improved layer properties after longer, higher temperature outgassing eventually lead to the use of higher outgassing temperatures of 1300 and even 1400 °C. Under these conditions the thermocouples were found to fail rapidly and the silicon source cell cracked badly (figure 2.19) as previously found by Grange (1980) and had to be replaced. Construction of a 5/25% tungsten-rhenium thermocouple was attempted but the junction became brittle after spot welding and always went open circuit before the cell was finally assembled and mounted in the cluster. Additional mechanical support of the thermocouple junction was obviously required and because of this, together with the absence of the correct compensating leads, it was decided to retain chromel/alumel thermocouples throughout, and limit the maximum indicated outgassing temperatures to 1200 °C. Some problems were also experienced with the gallium cell thermocouples due to attack by gallium. The gallium metal was also, in these cases, found on the substrate heater and it is believed that the most likely explanation is that small cracks developed in the graphite cell, possibly due to thermal stresses on heating or to stresses generated by expansion of the gallium source material on solidification and the tapered cell was made to test this latter possibility. However, this cell has been little used and, unlike the broken silicon cell, no cracks or other damage were visible in any of the three failed gallium cells found with gallium around the heater, so that the cause of this particular mode of failure has not been positively identified. One further possibility, particularly in view of the extremely dusty nature of some of the machined graphite, was that we had in error obtained a sample of a porous grade of graphite, but this possibility was strenuously denied by the manufacturer and at this stage of the project we had neither the time nor the money available to purchase and machine additional cells from new material.

The decision to make the cluster to accept source cells of up to 35 mm diameter in all five positions was the major factor in determining the long source-substrate dimension and consequent high operating temperatures required for the source cells. In view of the problems encountered, and the fact that the standard cell was of only 27 mm overall diameter and located within the cluster using spacing rings, it would have been better to have designed for the use of these smaller cells, permitting a shorter source-substrate distance.

A problem then arises with the arsenic cell which was of 33 mm overall diameter and reduces to only half the capacity for a similar design of 27 mm overall diameter, but simultaneous reduction in source-substrate distance should result in a reduction of only ~30% in growth capability. Various design options are possible which all involve trade-off between different aspects of system design and subsequent requirements in use, particularly the quantity of material to be grown between system bake-outs, the number of different dopants required, the size of substrates and uniformity required across a substrate, and the number of matrix species required for growing heterostructures and ternary or quaternary compounds. A few possibilities are:

(a) Accept the reduced growth capability.

(b) Duplicate the arsenic cell.

(c) Position the large arsenic cell at a larger distance from the cluster axis, directing the molecular beam using an inclined hole in the end cap.

(d) More effective use of the arsenic charge by using an end cap with several small diameter long holes to reduce the peripheral flux in the molecular beam whilst retaining the same on-axis flux.

(e) Construct smaller dopant cells and mount these adjacent to the arsenic cell, thus obtaining space for a larger arsenic cell.

(f) If individual cell shutters are used then rotational symmetry is not required and the cells need not be equiangular around a cluster axis, thus permitting a larger cell within the cluster.

For the intended use of this system - surface studies on a limited number of MBE grown layers - option (a) is the most appropriate. However, if a high temperature 'cracker' is to be used to produce As_2 then the cluster need only accommodate the cracking section. The main body of the cell must be adequately thermally isolated from the high temperature cracking section which will probably necessitate it being placed behind the immediate cluster of source cells.

The conflicting requirements briefly outlined above illustrate the necessity for a good overall understanding of the various techniques and equipment available, together with the project requirements, in order to design the optimum apparatus for the projected use. Construction of an arsenic cracker was considered near the end of this project since the use of As_2 in place of As_4 is generally found to produce gallium arsenide of higher quality (Neave et al (1980), (1983); Kunzel et al (1980), (1982); Krusor & Bachrach (1983). A simple high temperature chimney with a central baffle was designed to fit onto the arsenic cell in place of the existing end cap without obstructing the rotating shutters. However, approximate calculations indicated that the heat radiated from the cracker into the source cell would be larger than that required to maintain the cell at its operating temperature, thus a practical design would require a larger distance between the cell and the cracker to reduce the heat transfer. This would be a more complicated modification requiring alteration of the arsenic cell and its mounting, in addition to construction of the cracker, and was not pursued further due to the lack of time available.

2.2.7 Temperature Controllers

The temperature of each source cell and the substrate heater was controlled by a two term (proportional and differential) temperature controller, built in this laboratory to an existing design but fairly extensively modified during the course of the project. The source cells were powered by two dual controllers, which will be described first, whilst the substrate heater used an earlier version differing in several details but of the same basic design. The temperature controllers were connected to the source cells by a cable taken under the system frame to a terminal block mounted beneath a removable plate in the lower panel of the baked volume. From here PTFE insulated bakeable wires were used to connect to the electrical vacuum feedthroughs for each source cell and the substrate heater. Chromel/alumel compensated thermocouple leads were used throughout in order to obtain reliable temperature measurements during system bakeout. A simplified block diagram of the controller is shown in figure 2.20. A linear thermocouple amplifier was used, and it was not until after writing the majority of this thesis that it was realised that the non-linearity of the thermoelectric emf generated over the range of temperatures used was of importance. With the amplifiers set

correctly to 1000 °C then they are reading ~20 °C low at 1200 °C but only 6° high at 800 °C. This explains some discrepancies between measured and calculated variations with temperature and, although all temperatures quoted in this thesis are the indicated temperature assuming a linear relationship, any future work should include correction for this effect. Automatic cold junction compensation was not provided for the thermocouple amplifier, it being thought that room temperature would be a sufficiently stable reference. However, due to inadequacies of the air conditioning system, room temperature was not particularly stable, varying by a few degrees during the course of the day. The associated change of cell temperature was apparent for the low temperature arsenic cell where changes of ~3% per °C in effusion flux are expected but is probably not important in this project. With the gallium cells the expected change of ~1% per °C was not noticable, but with the silicon cell an expected flux change of ~5% per °C may explain some of the apparent flux variation at nominally constant temperature. The common mode rejection of the thermocouple amplifier had to be carefully set to prevent leakage currents into the thermocouple from affecting the indicated temperature - a 27 ohm resistor was necessary in the lower resistivity alumel lead to balance the lead resistances and various circuit modifications were necessary to prevent unwanted feedback and crosstalk between controllers, mainly through common power supplies.

Ideally, for any future work, the thermocouple amplifier in these controllers should be rebuilt to provide better electrical isolation, cold junction compensation and corrections for the non-linear temperature response of the thermocouple. The outputs from the proportional and differential amplifiers were summed in the soft-start circuit, which also provided a gradually increasing output, with a time constant of ~1 minute from initial switch on, to prevent sudden application of maximum output voltage to a cold (low resistance) filament. The power output was from an isolated, unsmoothed, switched DC supply. The maximum power was set by switching to different tappings on the transformer, whilst the minimum current control set the minimum ON period and could be used to provide a constant (average) current supply, useful in the event of thermocouple failure.

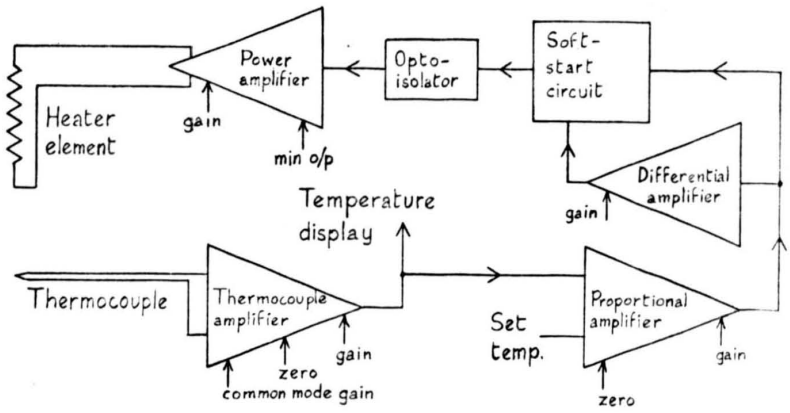

Figure 2.20 Temperature controller block diagram

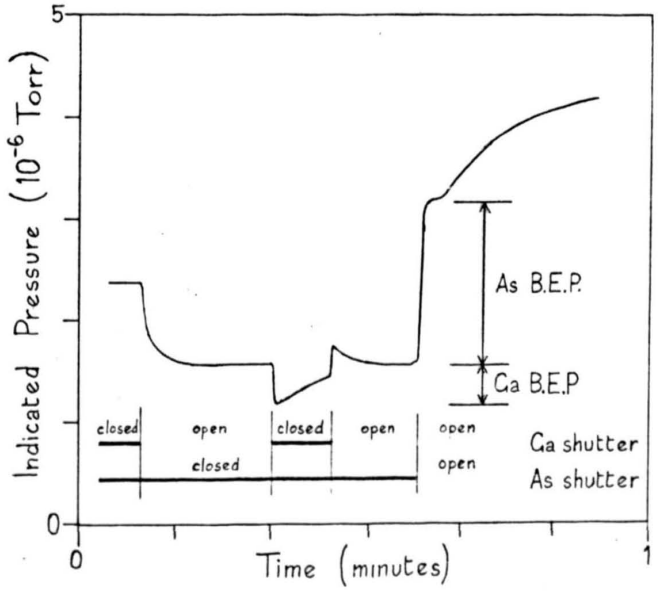

Figure 2.21 Typical flux monitor trace

The most significant difference in the substrate temperature controller was the use of a smoothed DC power output. This meant that, although a slight deflection of the electron beam occurred due to stray magnetic fields, diffraction patterns were still sharp and easily visible. If the switched mode power supply was used the 100 Hz ripple present on the heater caused considerable blurring of any diffraction patterns. In addition a sample and hold circuit was fitted after the thermocouple amplifier which could be 'switched in' before rotating the sample holder so that the output current remained constant over a period of several minutes despite the changes in indicated temperature occurring due to deficiencies in the thermocouple mounting already discussed.

2.2.8 Flux Monitor and Other Ion Gauges

The miniature ion gauge flux monitor used in this system was manufactured by KH Instrumentation (Type IG01) and mounted below the substrate shutter as shown in figures 2.6 and 2.13, all connecting wires being insulated with quartz tube and tied to the shutter operating rod. The initial design (not specifically intended for flux monitoring) suffered from a build-up of semiconducting gallium arsenide on the insulating base, leading to significant leakage currents. However this was etched off and the area around the collector pin shielded by means of a tantalum foil box, spot welded to existing shield pins in the base as visible in figure 2.22. No further problems with leakage currents were encountered.

The substrate shutter was designed so that it could be positioned within the area of the copper cryopanel for removal of the substrate flange assembly from the vacuum chamber, but rotated to screen the flux monitor behind a tantalum foil baffle within the main chamber except when in use to measure molecular beam fluxes. The flux-monitor was powered by a slightly modified Vacuum Generators TCS5 ion gauge power supply also used to power the load lock ion gauge and set for a gauge sensitivity of 25 per Torr. The flux-monitor sensitivity was, however, only 5 per Torr and therefore the overall system sensitivity is low by a factor of 5 and, except where stated otherwise, all quoted 'beam equivalent pressures' should be increased by this factor before comparison with results from any other system. Operation of the flux-monitor is not as straightforward as might at first appear due to the effect of a molecular beam on local residual gas and will therefore be described. The substrate

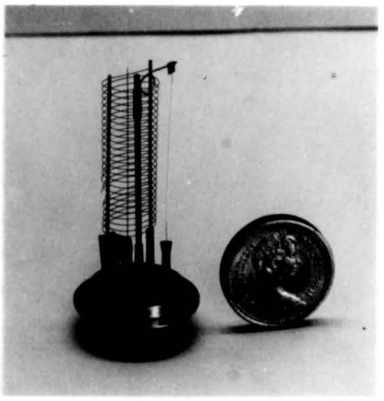

Figure 2.22
Ion gauge flux monitor.

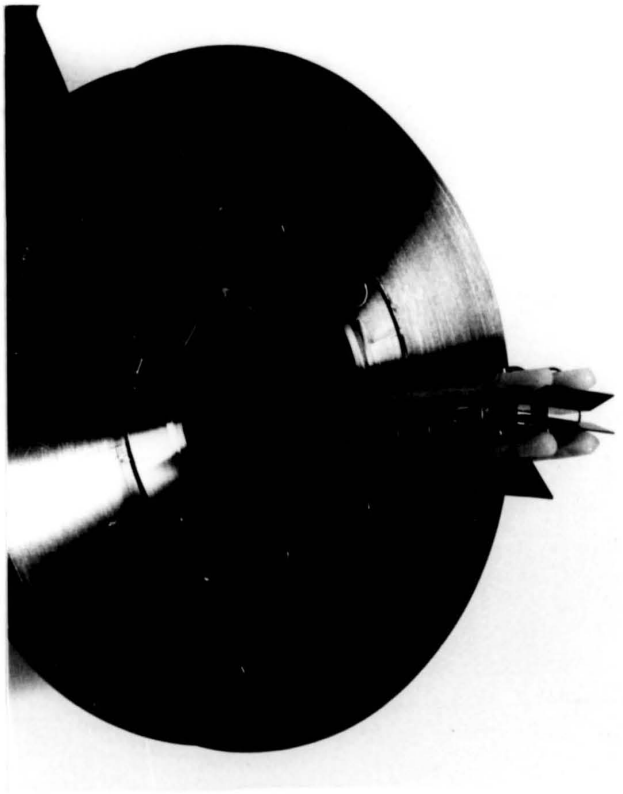

Figure 2.23 Electron gun mounted on double sided FC64 flange to permit operation of the load lock through the $1\frac{1}{2}$" dia. port immediately above the electron gun.

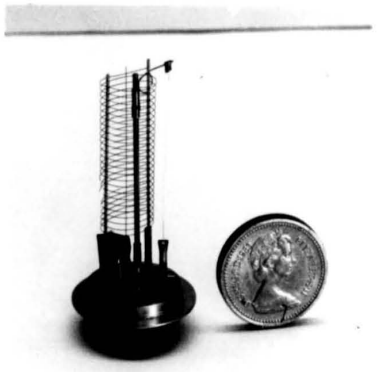

Figure 2.22
Ion gauge flux monitor.

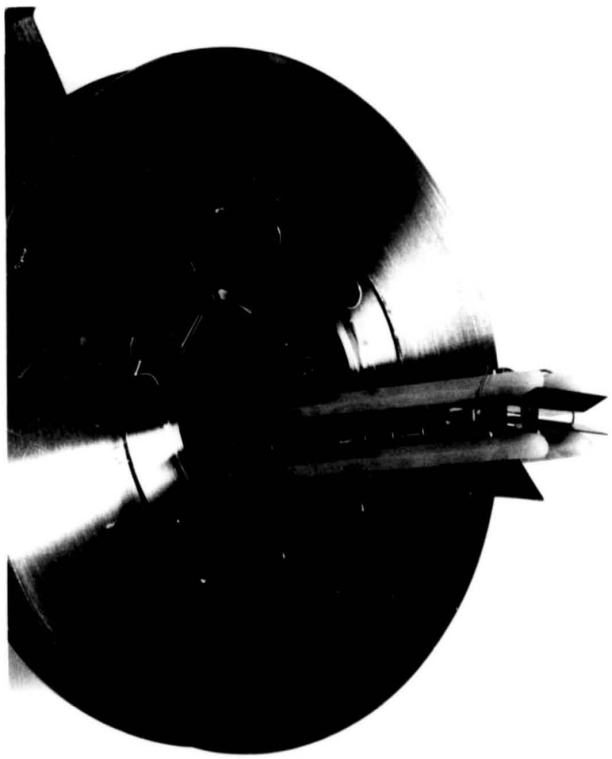

Figure 2.23 Electron gun mounted on double sided CF64 flange to permit operation of the load lock through the 1½" dia. port immediately above the electron gun.

must be shielded from the molecular beams during flux measurement, and it is the variable sticking coefficient of the arsenic species on this shutter that causes most complications. A typical output recorded during measurement of gallium and arsenic molecular beams is shown in figure 2.21 commencing with all beams shuttered and measuring the residual arsenic pressure in the system. On opening the gallium shutter the indicated pressure drops, due to creation of a fresh gallium surface on the substrate shutter with a consequent increased sticking coefficient for residual arsenic. After the output has stabilised the gallium shutter is closed and the sharp drop in signal is a measure of the gallium flux. However the signal immediately starts to increase due to increasing arsenic coverage on the shutter and consequently reduced sticking coefficient. On reopening the gallium shutter there is a sharp increase in signal due to the gallium beam, followed by a decay to the original level. Opening the arsenic shutter gives a rapid rise - the measure of the arsenic flux - followed by a brief period of constant signal, whilst the sticking coefficient on the substrate shutter is still unity, and then a further rise as the arsenic coverage increases and sticking coefficient is reduced. Accurate measurement of the gallium beam flux is obviously limited by the residual arsenic present, and measurement of the arsenic flux is limited by changes in the residual arsenic pressure occurring when the arsenic cell shutter is operated. This latter effect is apparent at the main chamber ion gauge and also on the flux monitor at lower arsenic to gallium ratios when the short constant signal after opening the arsenic shutter actually becomes a decrease due to the reduced background signal. Additional cryopanelling would enable more accurate measurements if this is required. It should be possible to convert from the measured 'beam equivalent pressure' to a flux of particles if the ionisation cross section and velocity distribution of the molecules in the beam is known, but this has not been attempted in the present study.

As mentioned above the ion gauge was powered by a slightly modified Vacuum Generators TCS5 ion gauge controller. Two such controllers were used, one for the main system ion gauge (VIG 17) and the second both for the load lock ion gauge (VIG 22) and the flux-monitor. Both controllers were fitted with additional switches to allow independent selection of alternative ion gauge filaments and to switch in the series resistor necessary for operation of a

thoriated iridium filament. A further modification was the fitting of a switched smoothing capacitor on the filament power supply, to obtain increased output voltage necessary for correct outgassing of the gauges with the long connecting cables used. The collector input socket was changed to a BNC compatible with current equipment and the input amplifiers of the ion gauge controllers were checked with a Keithley high impedence digital meter and found to be correct within ± 10%.

2.2.9 Electron Gun and Power Supply

The electron gun is a commercially available type SE 3K/5u and is mounted on the same FC64 port as is used for the load lock, with connections made by radial feedthroughs in a double sided flange as shown in figure 2.23. The flange was made with eight radial feedthroughs - one between each pair of bolt holes - for the standard four high tension (2 filament, grid and focus) and four low tension (electrostatic deflection) connections required. Feedthroughs rated at 15 kV were used in case it was found necessary to fit a higher energy RHEED system, although a maximum of only 3 kV was used during this project, and they were protected from accidental damage by circular plates tacked to the outside of the flange and flush with its two faces. The internal diameter of the flange was 70 mm - larger than the gasket internal diameter - to give extra space in which to make connections without obstructing the loading arm.

The power supply was constructed utilising a commercially available high tension module, and a circuit diagram is shown in figure 2.24. It was envisaged that this supply would not need adjustment, after initial setting up, and could be conveniently mounted in the 19" rack. However, in practice, many minor adjustments of the electron beam were often required, and it was fortunate that the unit had been made as a removable box, which could be positioned on the main system frame within easy reach when viewing the fluorescent screen. If this had not been the case then it would have been necessary to mount the deflection potentiometers on a remote, hand held, box.

Initially all eight connections to the electron gun were used, with a single positive-going power supply used for both positive and negative deflections. However considerable problems were experienced due to conductive flakes sliding down the port and

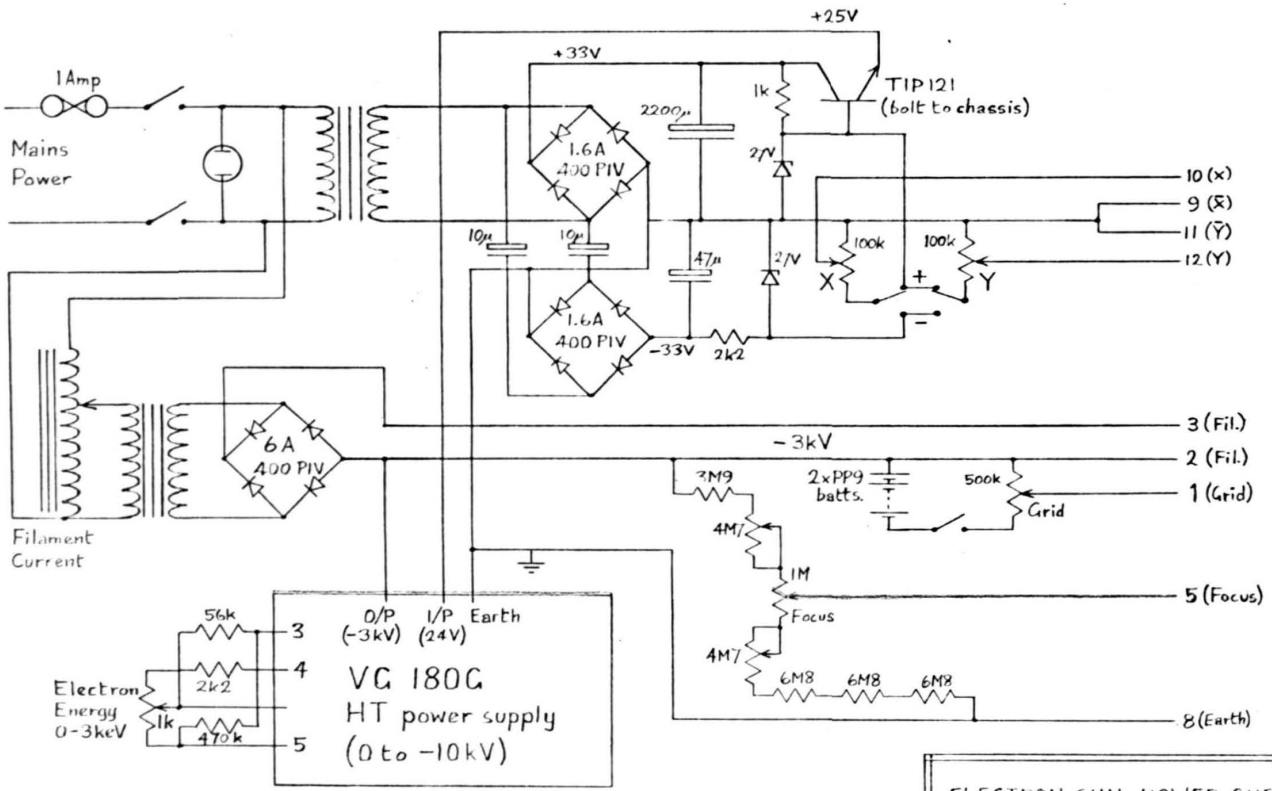

Figure 2.24

ELECTRON-GUN POWER SUPPLY		
	ISSUE	DATE
W.F. CROYDON	1	12·2·82
CITY OF LONDON	2	3·2·82
POLYTECHNIC	3	3·12·82

shorting out the two lowest feedthroughs on the flange, even after fitting some obstructing foils in an attempt to cure the problem. The simple, high impedence, negative supply shown on the circuit diagram was therefore added to enable both positive and negative deflections whilst only requiring connections to one of each pair of deflector plates. When the electron gun was removed from the system it was replaced with two of the deflector plates permanently earthed and only the upper six feedthroughs in the flange utilised, and no further problems have been encountered.

Other initial problems involved distortion and mains frequency deflection of the spot. Distortions were considered as probably due to misalignments within the electron gun and, when available, a different gun was fitted, although in one case spot distortion was cured by machining and fitting a cap with a smaller diameter (0.015") aperture to the electron source, but at the expense of reduced electron current. Deflection of the spot due to mains pick-up was reduced by rectifying the filament current, but no other major reductions were achieved, although it was apparent, by sweeping the beam rapidly, that part of the approximately 1 mm spot size was due to mains frequency beam deflection. Screening relevant parts of the chamber with a soft magnetic sheeting may be effective but was not tried.

The fluorescent screen was a standard 100 mm diameter 'large semi-circle' kindly supplied by Philips Research Laboratories and mounted inside the main FC 150 viewport protected by the viewport shutter, and is just visible in the general views of the system (figures 2.1 and 2.4). A conical shield was constructed from heavy black paper to enable viewing of the diffraction patterns without having to extinguish all the laboratory lights.

2.2.10 Load Lock

The original conception of the combined SIMS-MBE system required movement of samples between the two chambers under vacuum but did not extend to their movement into and out of either chamber. However, in view of the improvement in epilayer quality possible with a load locked system it was considered that this would be a worthwhile addition, and since movement of the sample was already essential, that it would involve few additional complications. The main difficulty

was that the only system port available for the load lock, compatible with requirements for transfer to the SIMS chamber, was that also necessary for the electron gun. The solution of this problem by mounting the electron gun on a double sided flange has already been discussed and an external view of the final arrangement is shown in figure 2.5. Various other, similar, arrangements were used during the development of the system. In particular a 1½" diameter tubular cross was used instead of the final 3" diameter loading chamber. This proved awkward for loading the 32 mm square substrate plates due to the small clearances inside the cross piece, and proximity of the SIMS liquid nitrogen trap further restricted access. The loading chamber was built at the maximum possible diameter (3") compatible with an FC64 flange. The additional space made loading much easier and enabled additional prepared substrates to be stored under vacuum before use. A 35 mm clear bore VAT valve is used to isolate the load lock from the main chamber. The original plastic operating handle was removed and a shorter metal handle fitted to enable operation with the adjacent baking panel in place and also enable baking without removal of the handle. Before the VAT valve became available a 28 mm bore VG gate valve, which had given persistent problems through jamming when partially closed, was modified by replacing overstressed leaf springs in the expanding gate with stainless steel coil springs and guide pins, and a zero length FC64 - FC38 adaptor made with the intention of using this for the load lock. This would have entailed remaking the substrate heater to accept smaller substrates, and fortunately the larger VAT valve became available. The VG valve was subsequently used on the SIMS system with no further problems.

A drawing of the magnetically operated drive mechanism is shown in figure 2.25, with photographs of the two ends in figure 2.26. The magnet used is cylindrical, with an axial magnetic field, and mild steel pole pieces were made to concentrate the field within the $1\frac{1}{8}$" diameter outer tube, with sufficient non-uniformity to enable rotation of the drive. Use of an axial magnetic field gives sufficient axial force to support the weight of the loading drive within the inclined tube. However, the central position of the soft iron slug within the cylindrical magnet is one of unstable equilibrium and it is pulled sideways against the inside of the tube.

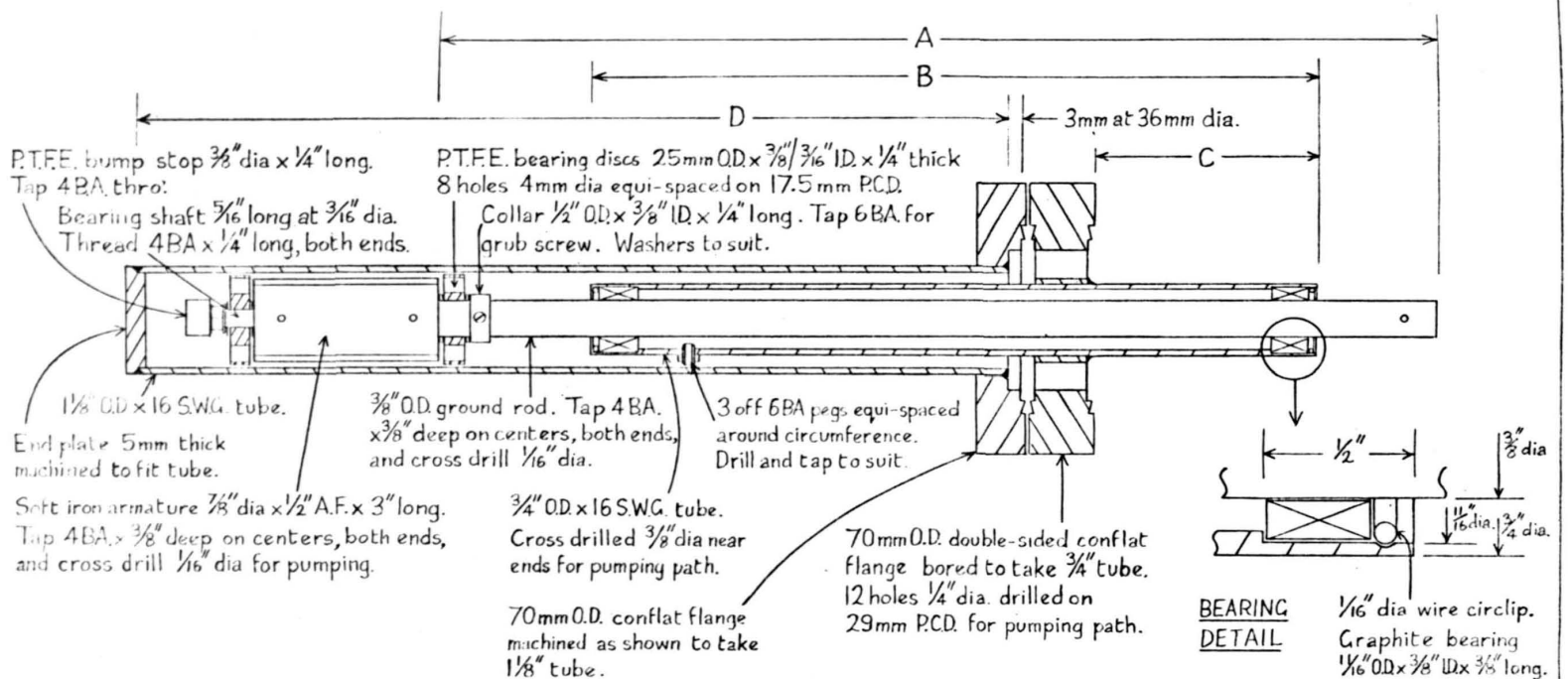

Figure 2.25

Dimension	Transfer	Load Lock
A	1500 mm	1000 mm
B	650 mm	450 mm
C	150 mm	20 mm
D	1400 mm	1040 mm

Material: 316 St. steel except where noted.

Welded assembly as shown.

All bearings to be free running, without excessive play.

MAGNETIC DRIVE LINEAR MOTION

W.F. CROYDON CITY OF LONDON POLYTECHNIC	ISSUE	DATE
	1	1·9·81
	2	13·1·82
	3	3·4·84

SCALE: F.U.L.L.

a)

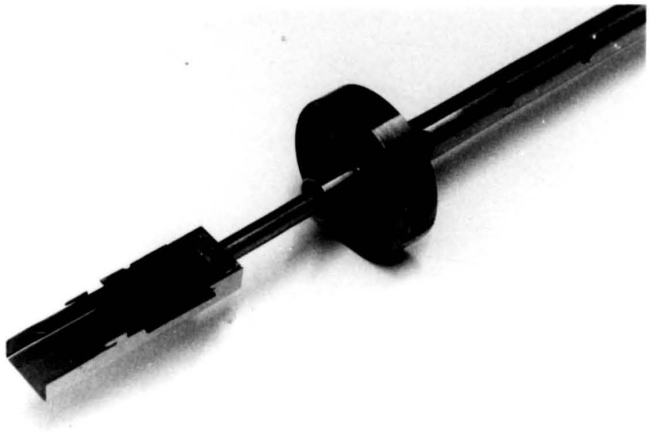

b)

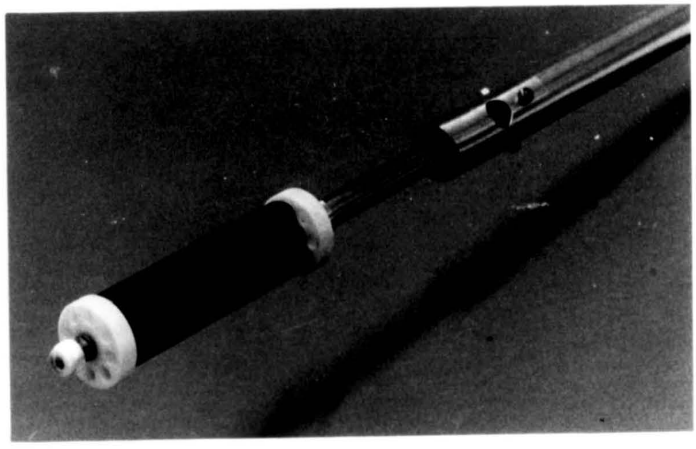

Figure 2.26 Load lock linear drive.
a) Loading tray complete with substrate mounting plate and showing mounting of drive mechanism on double sided flange. Note the thermocouple recess and locating notch on the substrate mounting plate.
b) Soft iron drive slug complete with final design of PTFE bearings and bump stop. Note pumping holes in bearings and centering pins on fixed tube.

a)

b)

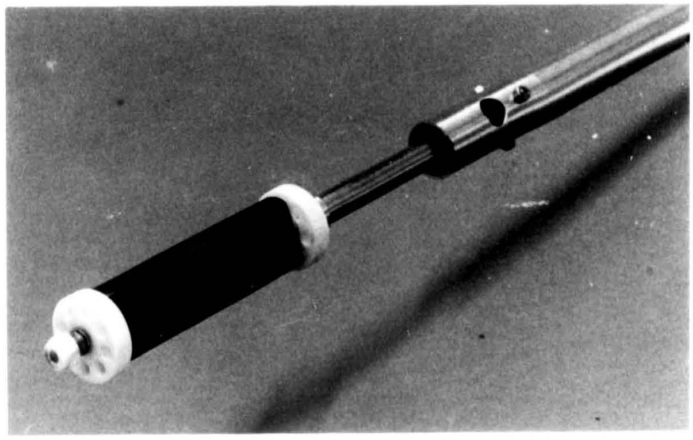

Figure 2.26 Load lock linear drive.
a) Loading tray complete with substrate mounting plate and showing mounting of drive mechanism on double sided flange. Note the thermocouple recess and locating notch on the substrate mounting plate.
b) Soft iron drive slug complete with final design of PTFE bearings and bump stop. Note pumping holes in bearings and centering pins on fixed tube.

Initially a single carbon bearing was used at the end of the rod but this wore on the relatively rough bore of the tube allowing the slug to bind against the tube wall. Finally the two PTFE bearings shown were fitted, giving a much smoother operation of the drive. No noticeable wear in the other carbon bearings running on the ground rod was apparent. A PTFE buffer was also fitted to the end of the rod to give some cushioning on the occasions when the drive was accidentally released and fell to the end of the tube.

Pumping of the load lock is effected by the rotary and diffusion pumps used for the main system as shown in figure 2.8. Use of the main UHV pump for the load lock means that the main chamber must be left unpumped and restricts the pressure obtained in the load lock before opening it to the main chamber. Use of a separate UHV pump to attain better vacuum conditions within the load lock should reduce residual contamination of the main chamber.

In operation the new substrate is positioned in the lower position of the loading tray as shown in figure 2.26 (a) and, after evacuation of the load lock, passed through the gate valve. The previous substrate, currently held on the substrate heater, is located in the upper position of the loading tray and the thermocouple locating pin withdrawn from the locating hole. The loading arm is then moved forward, removing the previous substrate from the heater and at the same time sliding the new substrate into place. The thermocouple locating pin is then lowered into the locating hole and the substrate disengaged from the loading tray. Finally the loading tray, complete with the previous substrate, is withdrawn through the gate valve. Correct positioning of the various items at all times is observed through both the main viewport and the small loading viewport. The field of view from this latter viewport is very restricted and, since there is no direct line of sight to any source cell, it may prove advantageous to replace the existing window with an unshuttered zero-length window to obtain a larger field of view, but this will depend on how badly obscured it becomes in operation. This viewport is essential for observing the loading process whilst actually operating the loading drive so that any misalignment or jamming may be rectified before causing serious damage.

Initial alignment of the loading drive is difficult involving careful compression, due to the large mechanical advantage present, of the various copper gasket sealed flanges to obtain the correct position for the transfer drive, maintaining adequate clearance between it and other parts of the system throughout its travel. The axis of the loading drive is deliberately inclined at 1½° to the main 45° tilt of the system, by means of the FC64 - FC38 adaptor flange, in order to clear the substrate flange mounted cryopanel, and this brings the drive close to the edge of the FC64 port where it enters the main chamber. The lack of clearance between the 32 mm wide substrate and the 35 mm bore valve and connecting tubing means that careful alignment is necessary here also. After correctly aligning and tightening all flanges the drive is held to the main system frame by the small bracket visible in figure 2.5 a few inches above the lower graphite bearing.

2.2.11 Transfer Drive

The transfer drive is of similar design to the load lock drive described above and shown in figures 2.25 and 2.26. The major difference is that the movement is longer, and the transfer tray visible in figure 2.6 is designed both to retain the substrate when rotated through 180° or more and to push on and pull off the substrate from the SIMS manipulator. Initially the substrate was held on the centre line of the drive similar to the load lock but had to be offset since movement of the SIMS manipulator was insufficient to give correct alignment in the original position. This offset also entailed moving the tray forward, away from the drive rod, to give clearance for the substrate heater when removing the substrate, which in turn meant that the tray no longer withdrew into the aperture in the main cryopanel, protruding past the edge of the substrate cryocoil and hindering removal of the substrate flange.

As with the load lock, graphite bearings were initially used at the soft iron slug, but as these wore the slug began to bind on the inside of the tube, producing a jerky movement of the transfer drive. This resulted in the substrate sliding forward on the tray to a position where it could not be safely inverted for mounting on the SIMS manipulator, and the stops visible in figure 2.6 were filed to stop this movement before the jerky motion was cured by fitting PTFE bearings. The transfer drive was aligned similarly to the load lock by careful compression of the copper gaskets and adjustment of

the support positioned near the farthest carbon bearing. The same cylindrical magnet was used as for the load lock, fitted with a long handle, visible in figure 2.4, to enable direct observation of the transfer tray during its movement.

2.2.12 Mass Spectrometer

A Vacuum Generators Q7B quadrupole mass spectrometer was fitted to the system for residual gas analysis. When first used the output was so eratic as to be meaningless and the mass spectrometer was stripped down and reassembled ensuring that all connections were properly made and adequately insulated. The opportunity was also taken to reconnect the vacuum feedthroughs in accordance with the manufacturers original specification. A channel electron multiplier was fitted in place of the original 'venetian blind' type. 'Noisy' potentiometers on the control unit were replaced. However two intermittent faults became apparent during the project and were not rectified. First was a tendency for the tuned mass to change abruptly both whilst sweeping or when tuned to a supposedly fixed mass. The sensitivity did not appear to change at these times and since the spectrometer was only used for residual gas measurements this fault was readily apparent and the measurement repeated. Changes in sensitivity to the residual arsenic pressure of up to a factor of two compared with the ion gauge were, however, observed at times during the project although the quadrupole settings remained unaltered. Secondly, after some hours of use, an offset appeared on the input to the main output amplifier resulting in saturation of the output. This condition cured itself when the HT supply to the electron multiplier was switched off, probably indicating that it was due to leakage currents, but long term monitoring of any particular residual gas species was difficult.

The mass spectrometer was initially used for helium leak testing of the source cell flange. Use of an ion gauge had shown the presence of a leak in the water tank mounted on this flange but precise location of the leak required 'reverse pumping' of the tank through comparatively long, small bore pipes and proved impossible using the ion gauge. The flange was kindly leak tested by SIRA who located a small leak. This leak was rewelded but on retesting it was apparent that a similar sized leak was still present and that we did not have the equipment to locate it. The

mass spectrometer was therefore repaired as indicated above and, after considerable difficulty, the leak was located and cured. A similar problem was encountered with the SIMS system liquid nitrogen trap which developed a leak in the liquid nitrogen reservoir. This assembly was 'reverse pumped' to allow location of the leak by inverting it on the body of the liquid nitrogen trap and sealing the join with RTV silicone rubber. The leak was eventually located, and subsequently cured, but was only apparent under these pumping conditions when the assembly was heated to > 100 °C using electrical heating tape. Throughout the project the mass spectrometer was used for checking leak tightness of the system after replacing flanges or fitting new components.

2.2.13 System Electronics

The various electrical and electronic units required to power and control the MBE system were mounted in a single 19" rack unit visible in figure 2.4. Power was supplied to the rack through a 20 amp mains relay energised via the ion gauge controller trip relay, with suitable switches for by-passing the trip mechanism on start-up and if overranging of the ion gauge controller is anticipated for some reason.

Operation of the trip circuit due to a system pressure in excess of the range set at the ion gauge controller removes mains power from all equipment supplied from the rack, protecting, in particular, hot filaments from accidental operation in high background pressures. The diffusion and rotary pumps, and bakeout heaters, are not powered through this supply but directly from the main combined system supply, and are protected by a mechanical pressure switch in the backing volume in case of a major loss of vacuum. Various, more complicated protection schemes were considered but in the absence of an automatic system isolation valve and more sophisticated fault detection it was considered that the system implemented was quite adequate. Power was distributed to units mounted in the rack by 6 amp IEC mains sockets fitted to the instrument runners, and two independently switched and fused banks of standard 13 amp sockets were used to supply other equipment not permanently mounted in the rack.

2.3 SIMS System Components

Components of the SIMS system will be described in sufficient detail to enable adequate understanding of its operation and limitations to the SIMS data.

2.3.1 Main Chamber and Pumping

A schematic diagram of the SIMS chamber and associated components is shown in figure 2.27. As already discussed the major pump is a liquid nitrogen trapped diffusion pump, but a titanium sublimation pump is also used. Rough pumping of the system is by means of an oil-free carbon vane rotary pump and sorption pumps, both pumping through the load lock. The load lock was designed for use with samples for dynamic SIMS analysis and is not compatible with the mounting of static SIMS samples. A Spectramass 1000 quadrupole mass spectrometer is fitted to the system for residual gas analysis.

2.3.2 Sample Holder

A sketch of the SIMS sample holder is given in figure 2.28. The horizontal portion of the holder was designed to locate MBE grown epilayers, transferred from the MBE system, in the correct position for static SIMS analysis and was mounted onto the existing sample holder designed for dynamic SIMS use. A small fluorescent screen was made by painting saturated potassium bromide solution onto a copper plate mounted as shown, flush with the top surface of the epilayer, for location of the primary ion beam. However, movement of the sample holder was inadequate to bring the screen into the ion beam, which was itself of too low an intensity, at normal static SIMS conditions, to give visible fluorescence on such a screen. The primary ion beam was, therefore, set up using the TEM sample grid, as for dynamic SIMS operation and described in the next section, before moving onto the static SIMS sample.

The MBE grown sample is slid onto the SIMS sample holder in the direction indicated, with the edges of the molybdenum plate locating against the roller bearings, the flanges on these bearings preventing the sample lifting off the holder. The two fixed bearings maintain the alignment of the sample whilst the third, mounted on a sprung arm, locates in a notch on the molybdenum plate, holding it in position and enabling the transfer tray to be removed. Removal of the sample from the SIMS system is effected by locating the

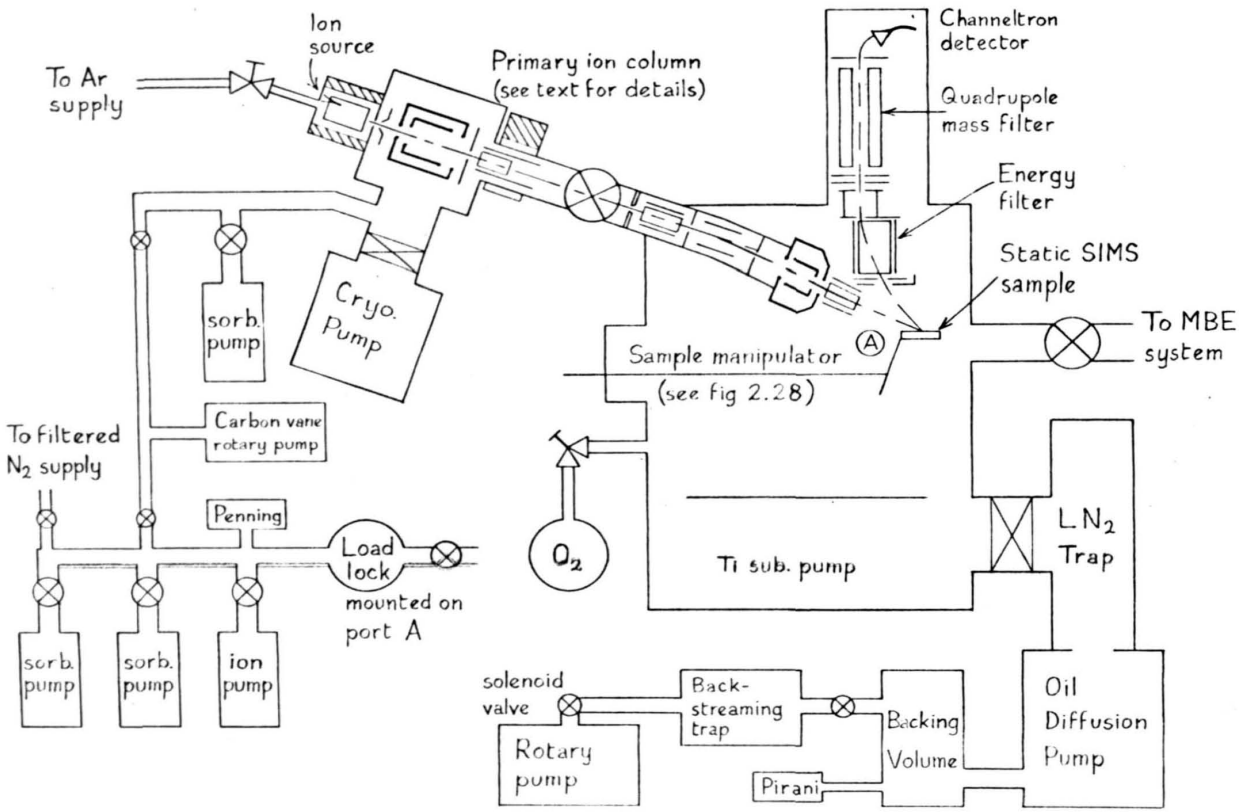

Figure 2.27 SIMS system schematic diagram.

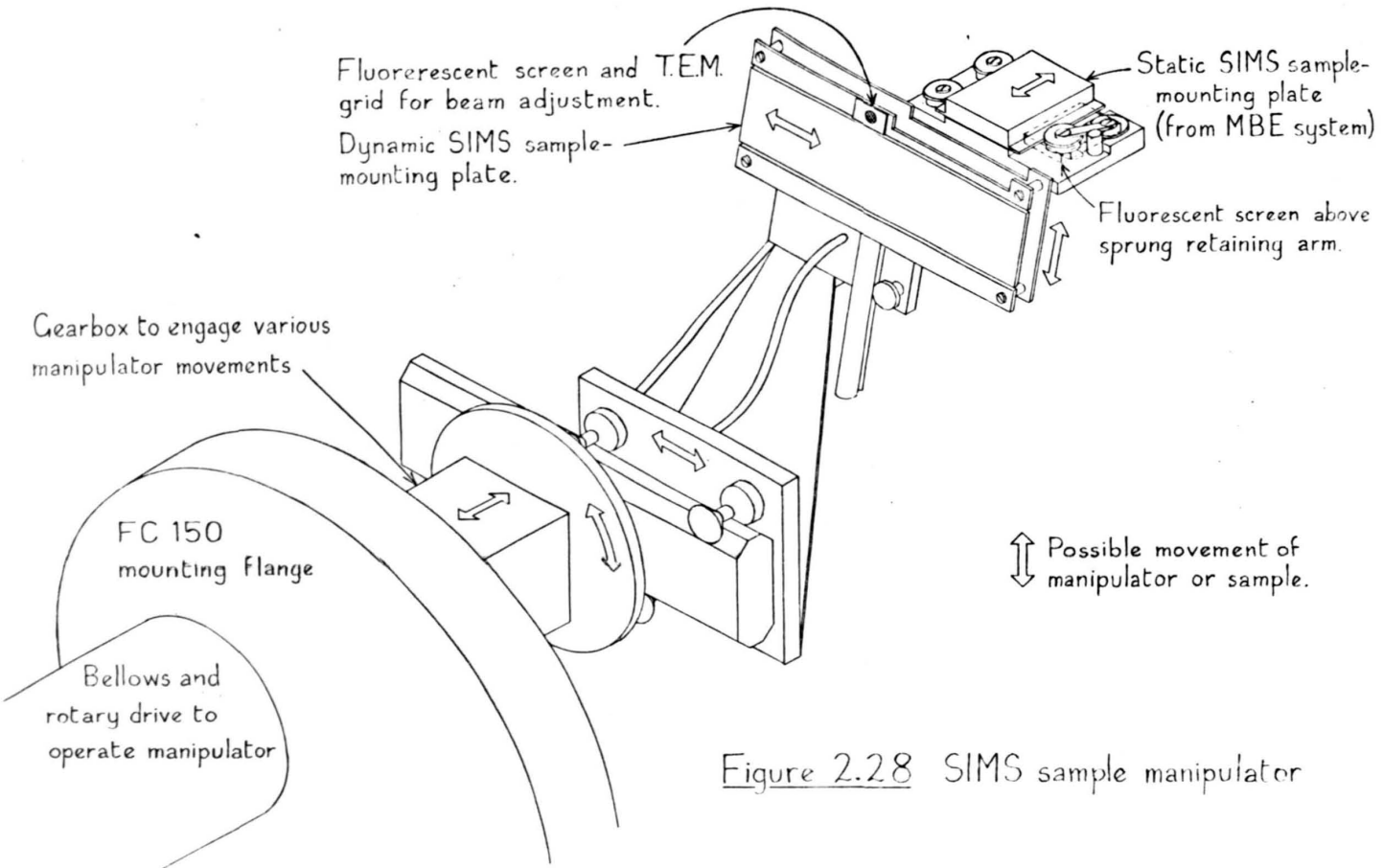

Figure 2.28 SIMS sample manipulator

sample in the front position of the transfer tray and simply pulling it off the SIMS sample holder. A tapped hole, compatible with an adaptor made for the SIMS loading arm, was made in one substrate plate with the intention of being able to remove samples directly from the SIMS chamber. However, movement of the SIMS manipulator was inadequate to give correct alignment with the load lock and all static SIMS samples had to be loaded and removed through the MBE system.

The final series of static SIMS results were obtained after the SIMS manipulator had been stripped down and reassembled with various bearings replaced, due to seizure of some types of bearing. It was only after the SIMS system had been baked out and set up ready for static SIMS measurements that the transfer of the MBE grown epilayer proved very difficult. It was finally realised that this was caused by a rotation of the sample holder, due to a fault in reassembly, such that the molybdenum sample block was jamming inside the transfer tray when located on the sample holder. Fortunately it was possible to load the samples by disengaging them from the transfer tray when only partially located on the sample holder, and only one sample was lost in the process. Loading of samples for dynamic SIMS analysis was not possible until the manipulator was correctly realigned.

2.3.3 Ion Source and Primary Ion Column

The ion source is a Penning-type discharge, fitted with a hot cathode for production of argon ions used for static SIMS analyses. Under the conditions required to generate the fairly low primary ion currents used for static SIMS (0.5 - 3 nA) the hot cathode filament would last for a few days, whereas for the several microamps required for dynamic SIMS profiles its lifetime could be as little as a few hours. Various materials were used for the filaments - Tantalum, Tungsten, Thiorated Tungsten - but with little apparent difference between cleaned filaments of different composition wires of the same diameter. The most important factor in extending filament lifetime appeared to be in adequately outgassing the source by running the filament at increasing powers for an extended period before starting the discharge. Filaments did not fail at the high temperature, coiled tip but along the uncoiled side wires of the filament, suggesting that sputtering of the wire

by the discharge may be the cause of failure of the filament. However the previous use of a twisted pair of wires leading to the coiled filament tip had not apparently given any improvement in filament lifetime. The ion source was pumped, through the aperture in the anticathode by a 1000 l/s cryopump, with the carbon vane pump and sorption pump for roughing. The argon supply for the discharge was 99.995% Ar, BOC research grade, admitted through a Vacuum Generators MD6 leak valve which had been cleaned and fitted with a replacement knife edge and copper sealing pad. Argon pressure in the ion column was maintained at 1×10^{-6} Torr corresponding to $\sim 10^{-3}$ Torr in the discharge.

The major components of the primary ion column, shown in figure 2.27 are, in order, the extraction lens used for beam current control by defocussing on the pressure step aperture, Wien filter incorporating alignment plates, pressure step aperture, alignment plates, 4° bend for elimination of neutral species, final lens for focussing on the sample, and deflection rods for scanning the beam. The beam is set up by optimising the various alignment and focus controls for maximum current on the target, and then reducing the target current by defocussing the extraction lens whilst simultaneously adjusting the various alignments to maximise the target current, thus maintaining the best alignment and least aberration of the ion beam. Previous calibration with a Faraday cup has shown that the primary ion current is equal to the target current measured with the ion beam incident perpendicularly onto the stainless steel target, biassed at +5 V to collect secondary electrons.

Focussing of the beam is achieved by means of a TEM specimen mounting grid. When the focussed beam is swept across the grid a slight modulation of the target current is observed, as the centre of the beam passes over the grid wires, and the focus is adjusted to maximise this modulation. The grid is formed of 30 μm 'wires' at 100 μm pitch and for the usual static SIMS operating conditions of 500 eV ion energy and 0.5 - 3 nA beam current a target current modulation of 10 - 15% was obtained, indicating a spot size of ~100 μm. Beam deflection potentiometers were calibrated by deflecting the beam the known diameter of the grid.

2.3.4 Secondary Ion Column

Secondary ions from the sample are extracted by a 100 Volt extraction potential into the electrostatic energy filter fully

described by Wittmaack et al (1982). Briefly the purpose of the energy filter is to limit the energies of the transmitted ions to the range effectively mass filtered by the mass spectrometer, and provide some focussing of the ions into the geometrical entrance aperture of the quadrupole. Plate potentials on the energy filter were set to maximise the mass spectrometer signal for a selected ion species at the standard target potential ($^{69}Ga^+$, +5 V; $^{35}Cl^-$, -5 V for positive and negative ions respectively). The mass spectrometer is an Extranuclear ELFS quadrupole fitted with 9.6 mm diameter rods and detection of transmitted ions is by an off axis channel electron multiplier. A soft iron pole piece is fitted near the exit aperture of the quadrupole to enable the use of an external magnet to deflect electrons, which may cause a high background signal, away from the multiplier when set for negative ion detection. Mass tuning of the quadrupole is controlled by the 380Z microcomputer. The output from the electron multiplier is taken through a head amplifier floating at the multiplier potential to a 5CI Brookdeal photon counter also controlled by the 380Z microcomputer. The output from the photon counter was stored by the microcomputer for display and subsequent processing.

2.3.5 Gas Inlet System

The gas inlet system was constructed for controlled oxygen exposures of the MBE grown surfaces and is visible in figure 2.1. A two litre glass flask of 99.995% O_2, BOC research grade, is connected to the system by a Vacuum Generators MD6 leak valve. The worn knife edge and deformed copper pad were remachined and the copper pad etched in $H_2SO_4/H_2O_2/H_2O$ mixture to remove obvious surface contamination before reusing the valve. Initially, whilst the glass flask was mounted where it was partly protected by the system frame, no special protective screen was made and on one occasion when reattaching cables after baking the system this was hit and broken by a swinging connector. The leak valve had to be stripped down to remove fragments of glass and the knife edge and copper pad replaced with a second remachined pair. A protective screen was subsequently made for the glass flask from expanded metal sheet. Use of a medium pressure gas supply from a steel cylinder was considered but the additional expense and testing of such a system, necessarily incorporating a high purity gas regulator, was not considered feasible for this project alone.

CHAPTER 3

Growth and Characterisation of Epilayers

3.1 Surface Preparation

Substrate surface preparation can be conveniently divided into two sections. Firstly any chemical and/or light mechanical treatment, outside the vacuum chamber, of the commercially purchased GaAs wafers "polished for epitaxial growth". This is designed to give a reproducible flat surface, free from dust and other contaminants, and generally passivated with a thin, reproducible oxide layer. Secondly there are further treatments within the vacuum system to remove the passivating surface layer, together with residual contaminants, and generate a flat, ordered surface suitable for epitaxial growth.

3.1.1 Ex-Situ Substrate Preparation

Commercially available GaAs wafers "polished for epitaxial growth" have generally been sawn from a bulk ingot with the required crystallographic orientation, possibly lapped with a purely mechanical abrasive and finally subjected to a chemo-mechanical polishing process. The basic principles and procedures are well described by Fynn & Powell (1979), Tuck (1975) and Jensen (1973). Commercial manufacturers are understandably reluctant to divulge their exact processes but the majority of wafers used in this project were supplied by Cambridge Instruments and of these the first batch was finished with a bromine-methanol etch, whilst the second used a combined sodium hypochlorite and syton [Colloidal Silica, Walsh & Herzog (1965)] chemo-mechanical polish. It is generally considered that most manufacturers now use a hypochlorite based chemo-mechanical polish as the final stage of wafer preparation. Briefly, the chemical oxidant in the etch produces a thin oxidised layer on the wafer surface, which is then either directly abraded, or preferentially dissolved, at the high-spots giving a long-range flatness not attained with a free etch, and freedom from localised damage caused by direct mechanical abrasion of the substrate.

A final free etch of the wafers was performed with a sulphuric acid-peroxide etch, composition 7:1:1 H_2SO_4:H_2O_2:H_2O as previously used in this laboratory [Meggitt (1979), Grange (1980), Kubiak (1983)]

to remove residual damage and contaminants from the wafer surface leaving a reproducible, thin oxide layer. Such an etch is commonly used elsewhere for preparation of gallium arsenide wafers [Cho et al (1977), Neave & Joyce (1978), Laurence et al (1979), Chai (1980), Chang et al (1981), Koschel et al (1981), Ballingall & Wood (1982), Akimoto et al (1983), Metze & Calawa (1983)] and has been extensively studied for selective etching of gallium arsenide [Iida & Ito (1971), Shaw (1981), MacFadyen (1983), Adachi & Oe (1983)] although several other etches, and series of etches, have been proposed for optimising the thickness and composition of the surface oxide, and minimising residual contaminants [see eg Aspnes & Studna (1981), Cho et al (1980), Zilko & Williams (1982), Kern & White (1970), Oda & Sugano (1976), Shiota et al (1977)]. It is of interest to note that Aspnes & Studna (1981) observed rapid film growth on prepared surfaces subsequently exposed to air, and suggest that reported differences attributed to different surface treatment may be due to sample handling prior to analysis.

The bromine methanol polished wafers initially used in this project were contaminated with dust particles on removal from the manufacturer's packaging (see figure 3.1) and cleaning proved to be somewhat difficult, partly because of the comparatively rough surface left by the bromine methanol etch. Lightly wiping the wafer surface with a filter paper whilst washing with isopropanol proved to be the most effective way of removing the dust particles but random scratches appeared on the substrate after the sulphuric acid peroxide etch. It was shown that these scratches were due to the wipe with filter paper by wiping in one direction only, when all the scratches appeared in this direction, and their absence from un-wiped surfaces. Since no damage is apparent before etching, this must be due to latent, subsurface damage inflicted during the wiping operation and revealed by the etch in spite of the diffusion limited, polishing properties of the sulphuric acid peroxide etch. Surprisingly, the scratches were still visible even after removal of over 10 μm of material, and using an abrasive free lens tissue for wiping reduced, but did not eliminate, the scratching apparent. Dust particles were much less adherent on smoother wafers, polished by the hypochlorite process and could be removed without resorting to wiping the surface. At this stage it was also realised that the

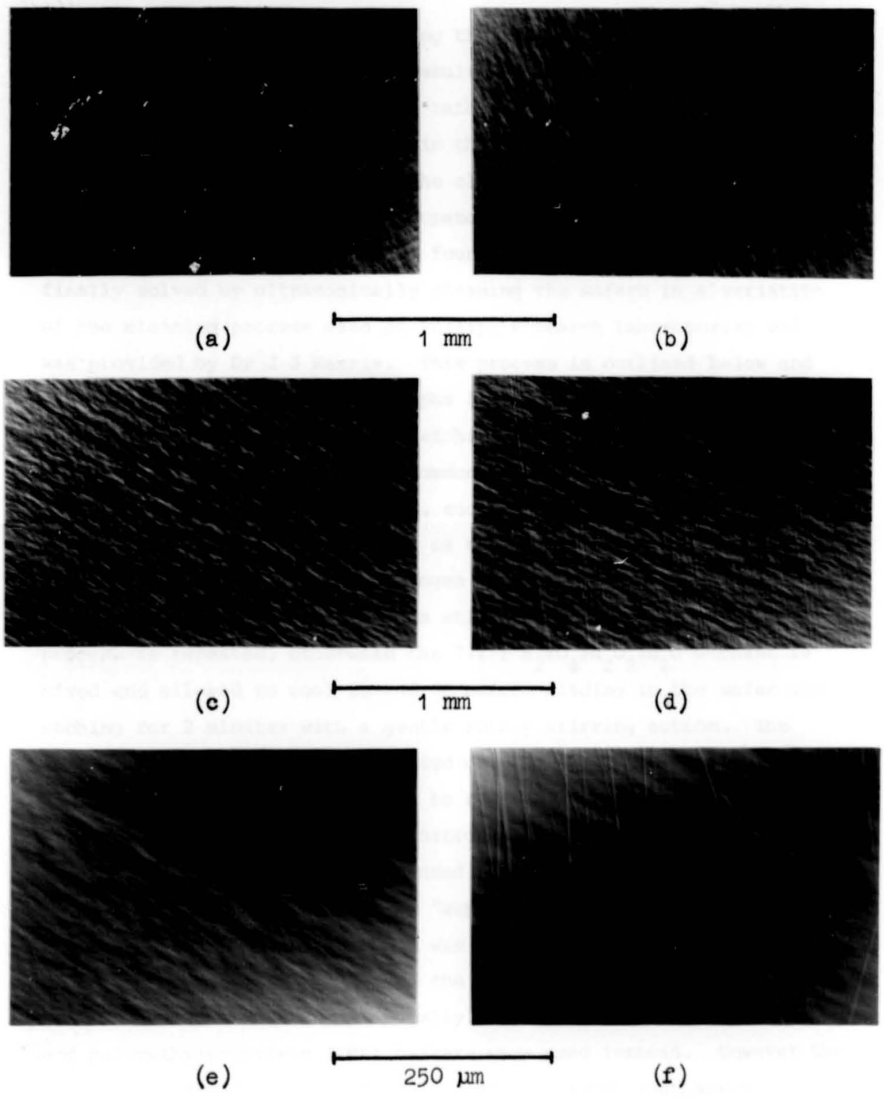

Figure 3.1 Nomarski micrographs showing contamination and scratching of bromine-methanol polished wafers.

a) Particulate contamination on typical wafer, as removed from manufacturer's packageing,

b) Same wafer after wiping with filter paper and isopropanol,

c&d) Typical cleaned wafer before and after sulphuric acid-peroxide etch,

e&f) As (c&d) but higher magnification.

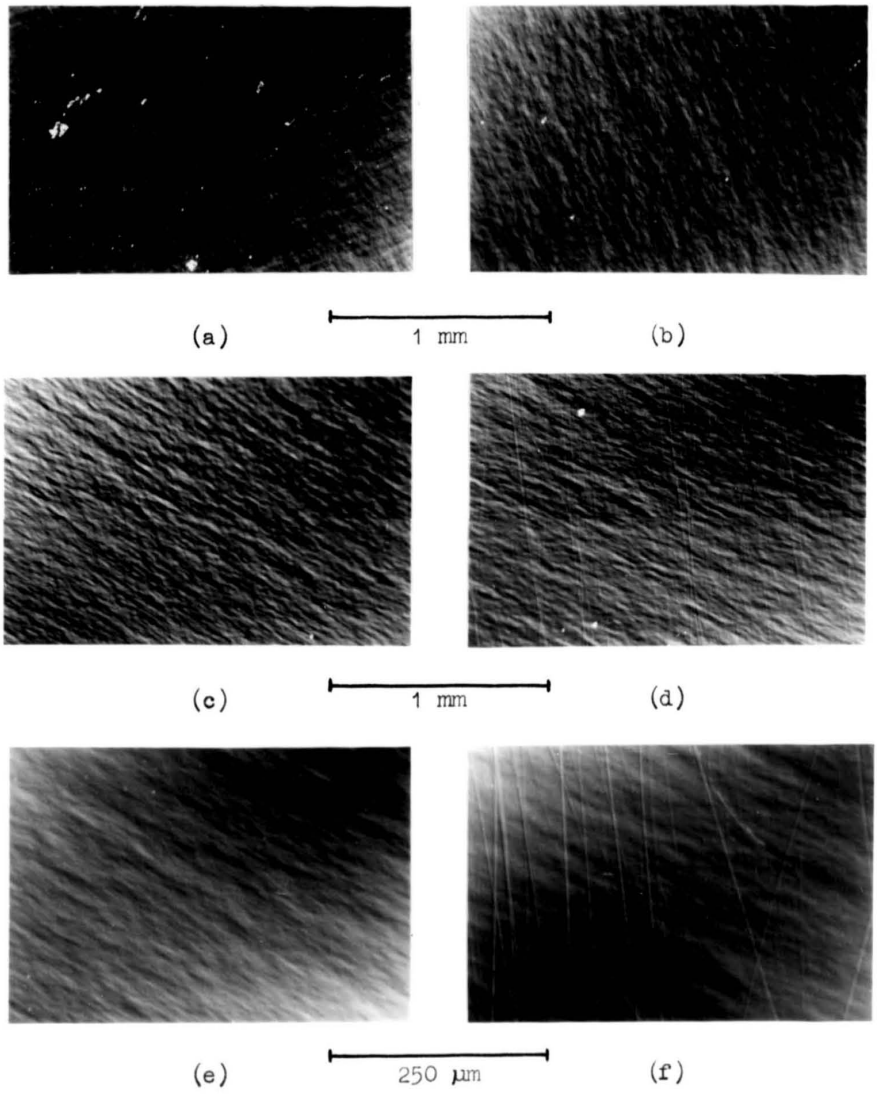

Figure 3.1 Nomarski micrographs showing contamination and scratching of bromine-methanol polished wafers.

a) Particulate contamination on typical wafer, as removed from manufacturer's packageing,

b) Same wafer after wiping with filter paper and isopropanol,

c&d) Typical cleaned wafer before and after sulphuric acid-peroxide etch,

e&f) As (c&d) but higher magnification.

reflux apparatus used for cleaning the wafers provided minimal cooling to the wafer, with the result that there was a minimal flow of solvent across the wafer, but rather a continual cycle of condensation and re-evaporation in the changing convection currents. The initial refluxing stage of the cleaning procedure was therefore changed to a short boil in isopropanol, but no marked improvement in removal of dust particles was found. This cleaning problem was finally solved by ultrasonically cleaning the wafers in a variation of the cleaning process used at Philips Research Laboratories which was provided by Dr J J Harris. This process is outlined below and Nomarski phase contrast micrographs [Nomarski & Weill (1955)] of typical wafers before and after etching are shown in figure 3.2.

The first cleaning stage commences with boiling in isopropanol followed by ultrasonic cleans in, successively, trichloroethane, acetone and methanol. The wafer is then washed with super-Q water, blown dry with filtered dry nitrogen and examined using the Nomarski microscope. If excessive dust is still visible then the cleaning process is repeated, otherwise the 7:1:1 H_2SO_4:H_2O_2:H_2O etchant is mixed and allowed to cool to ~40 °C before sliding in the wafer and etching for 2 minutes with a gentle rotary stirring action. The majority of the etchant is decanted off, the wafer thoroughly rinsed with super-Q water and then left to stand under water for a few minutes before blowing dry with nitrogen. "Aristar" grade sulphuric acid and hydrogen peroxide were used for the etchant, "analar" grade solvents were used elsewhere and "super-Q" deionised distilled water with a resistivity $\geq 10^{18}$ ohm cm was used throughout. Quartz beakers were also made for each stage of the process but the wafers were found to shatter when ultrasonically cleaned in a quartz beaker and polymethylpropylene (PMP) beakers were used instead. However the PMP beaker used for the ultrasonic clean in trichloroethane was slowly attacked by the solvent and a PTFE beaker substituted. All beakers were labelled and used for a single, specific stage of the cleaning process to minimise cross contamination, and all operations except the ultrasonic cleaning and Nomarski examination were carried out in a nominal class 100 fume cupboard.

Some other defects were also observed after the sulphuric acid-peroxide etch despite its supposed diffusion limited polishing action, and are shown in figure 3.3. The formation of shallow pits or mounds

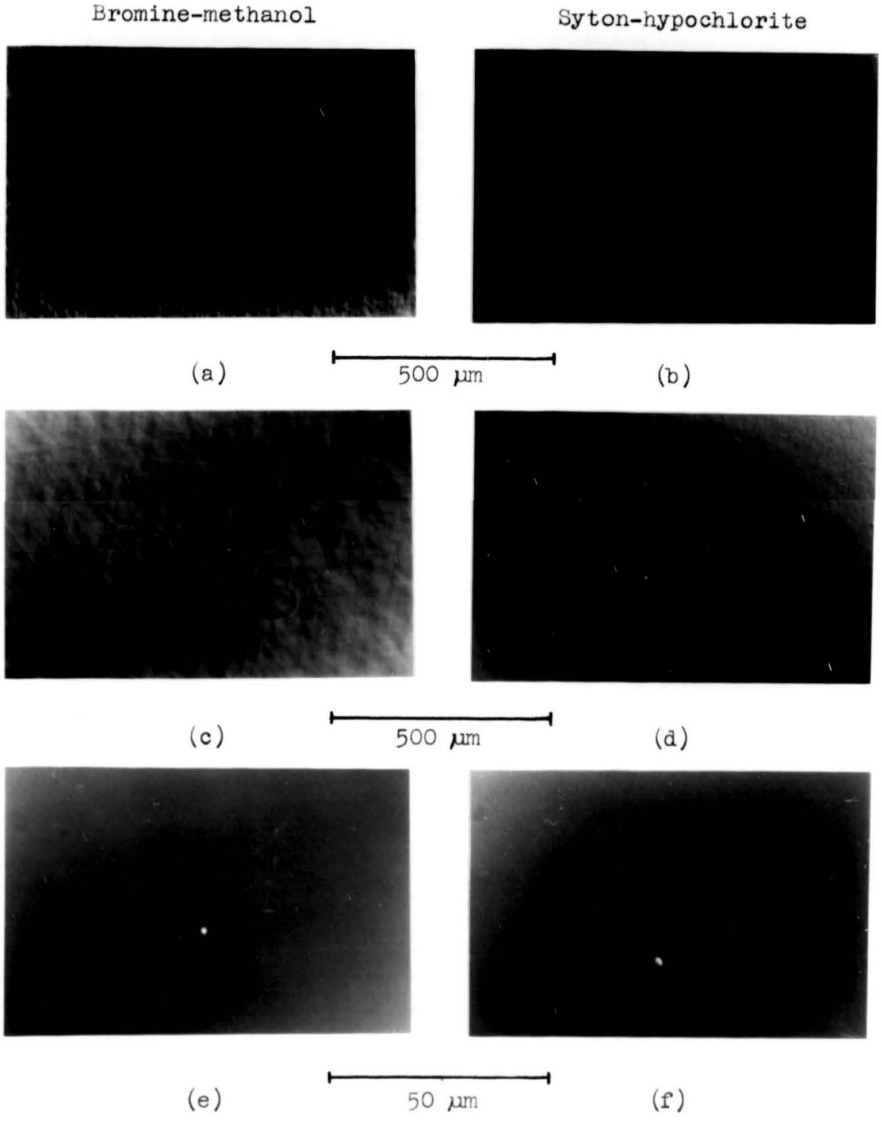

Figure 3.2 Nomarski micrographs showing cleaned and etched surfaces without wiping. Note the difference between bromine-methanol and syton-hypochlorite polished surfaces.

a&b) Cleaned but not etched.

c&d) After sulphuric acid-peroxide etch.

e&f) As (c&d) but higher magnification.

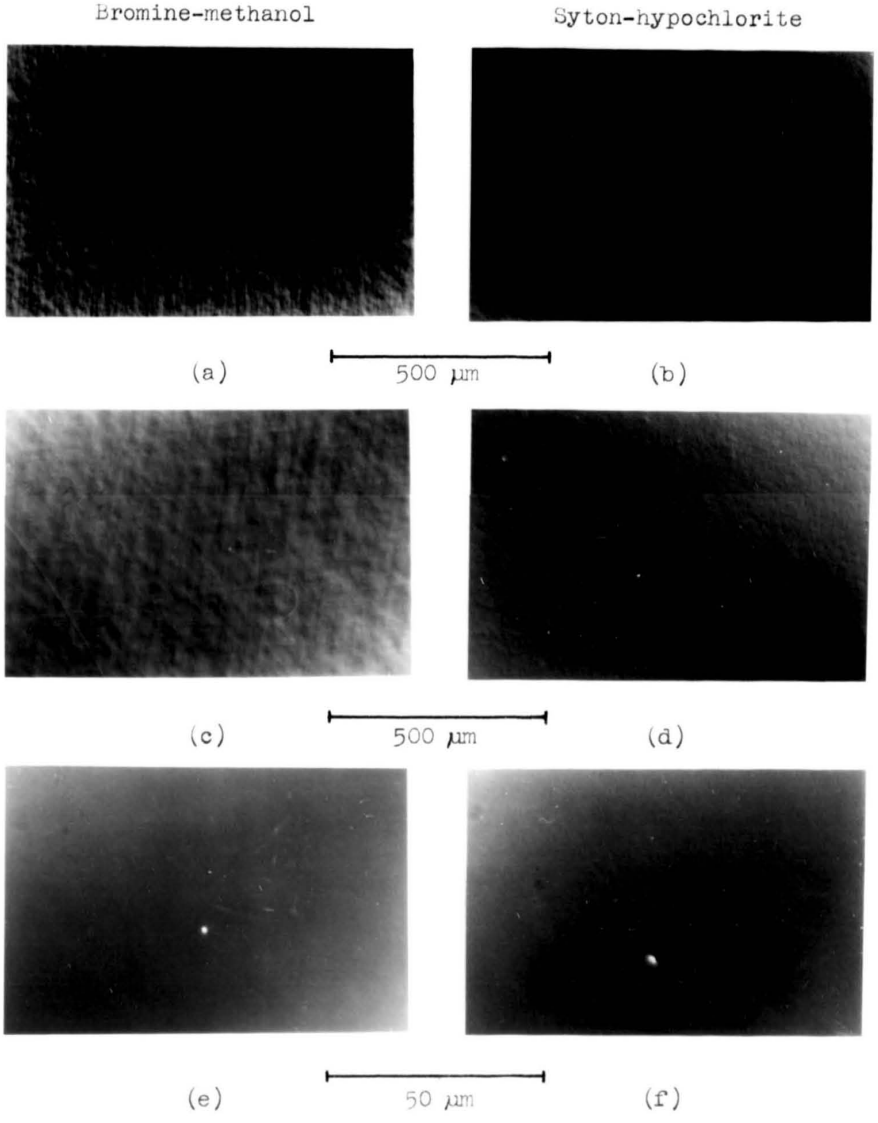

Figure 3.2 Nomarski micrographs showing cleaned and etched surfaces without wiping. Note the difference between bromine-methanol and syton-hypochlorite polished surfaces.

a&b) Cleaned but not etched.

c&d) After sulphuric acid-peroxide etch.

e&f) As (c&d) but higher magnification.

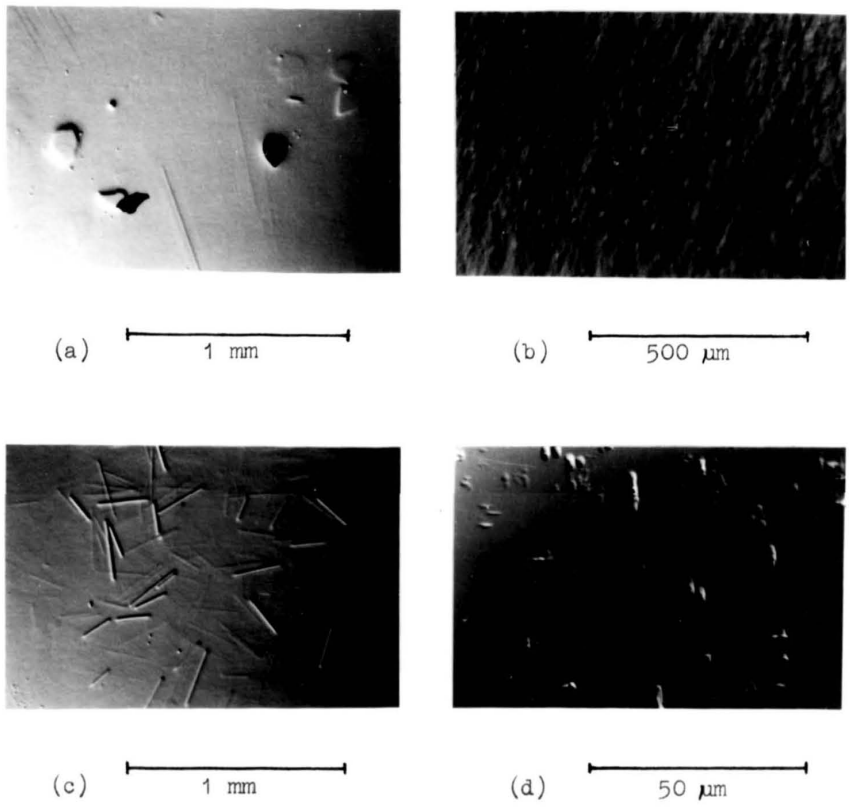

Figure 3.3 Nomarski micrographs of defects observed after sulphuric acid-peroxide etch.

a) Mounds due to collection of debris on wafer surface during etching, with two pieces remaining.

b) Mounds or saucers due to imperfect cleaning prior to etching.

c) Random line defects, probably due to contamination from nylon tweezers.

d) Patch of associated fine defects of unknown origin.

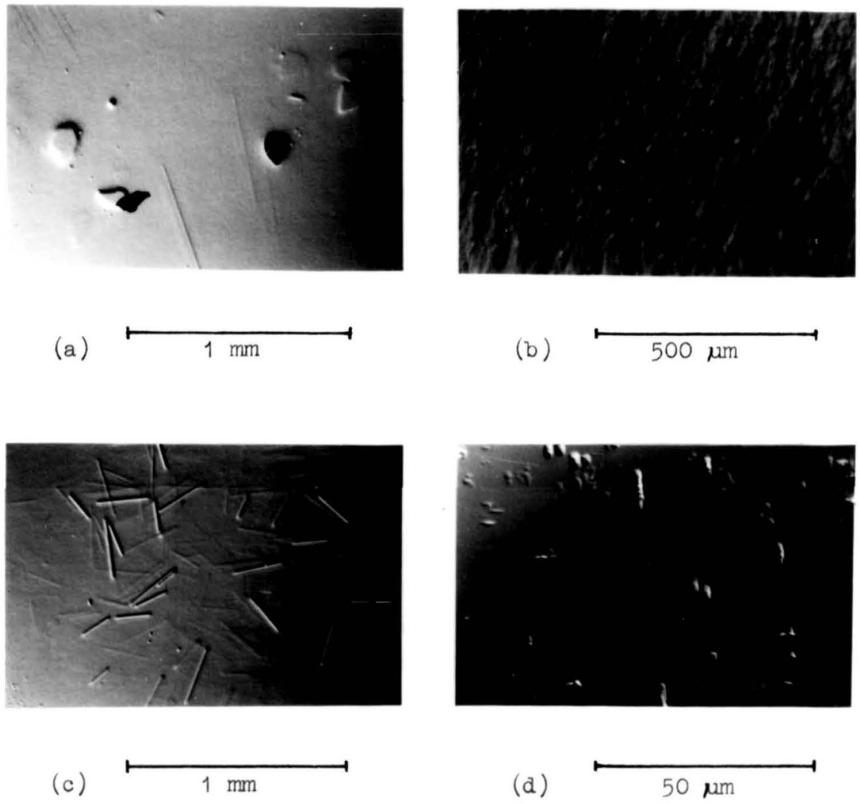

Figure 3.3 Nomarski micrographs of defects observed after sulphuric acid-peroxide etch.

a) Mounds due to collection of debris on wafer surface during etching, with two pieces remaining.

b) Mounds or saucers due to imperfect cleaning prior to etching.

c) Random line defects, probably due to contamination from nylon tweezers.

d) Patch of associated fine defects of unknown origin.

is probably associated with contamination of the surfaces, since it did not occur when wafers had been correctly cleaned by the procedure just described. Irregular mounds occurred on some large substrates due to the collection of small pieces of material (including gallium arsenide chips from the corners of the substrate) at the centre of the beaker on the substrate surface. Groups of short line features were occasionally apparent with similar lengths but random orientation but their origin is not known, although contamination of the surface from nylon tweezers is suspected. The etched wafer was finally soldered to a molybdenum substrate mounting plate with indium and positioned in the MBE system loading chamber, after removal of any airborn dust by blowing over with helium-nitrogen mixture.

3.1.2 In-Situ Substrate Preparation

After loading in the MBE system the residual oxide film left by the ex-situ substrate preparation must be removed to give a clean surface suitable for epitaxial growth. This is achieved by heating the wafer to a temperature of approximately 600 °C in an arsenic overpressure, when the reflection electron diffraction pattern changes from diffuse scattering, characteristic of the amorphous oxide layer, to distinct spots or streaks characteristic of the smooth crystal surface.

This heat cleaning process has been extensively covered by various workers [eg Uebbing (1970), Gonda et al (1975), Cho & Arthur (1975), Covington & Meeks (1979), Laurence et al (1979), Chai (1980), Koschel et al (1981), Munoz-Yague et al (1981), Ballingall & Wood (1982), Metze & Calawa (1983), Heiblum et al (1983), Hwang et al (1983), Akimoto et al (1983), Buonaquisti et al (1983), Vasquez et al (1983)] and surface composition has been monitored with AES and ESCA. The basic results are that the chemically prepared surface is covered by a thin oxide layer with some carbon contamination. Other minor contaminants such as Cl, S, F, K, Na have occasionally been observed also, and Stirland & Straughan (1976) report that sulphur contamination has been shown to originate from the sulphuric acid-peroxide etch. On heating the wafer there is a change in the oxide structure at a temperature of ~350 °C, however it is uncertain whether this is due to loss of volatile arsenic oxides or their

reaction with the substrate to produce additional gallium oxides and free arsenic. Similar results have been obtained by Su et al (1982) with oxidised cleaved surfaces, where oxygen either transferred from arsenic to gallium bonding or desorbed together with arsenic depending on the heating rate. Further heating leads to loss of the remaining oxide at temperatures variously reported in the range 500 - 650 °C. Most results show desorption occurring fairly abruptly at a temperature of between 550 and 600 °C. The larger ranges quoted may be due to different heating rates, measurement of commencement or completion of desorption, effect of oxide layer thickness or composition - thicker layers are reported to require higher desorption temperatures [Laurence et al (1979)] as do oxides grown by different methods [Buonaquisti et al (1983)], simple inaccuracies in temperature measurement, or, more probably, a combination of these effects. In this project some variation in the indicated substrate temperature required to obtain a streaked electron diffraction pattern was observed but, due to deficiencies in the temperature measurement it is not possible to state categorically whether these were real variations between substrates, or simply due to inaccuracy of the temperature measurement. Oxygen and all other contaminants except carbon are reported to be reduced to below the detection limits of AES by this heat cleaning procedure, but the effect on carbon depends on exposure to the electron beam. Chang (1982) has shown that for efficient removal of surface carbon the wafer must not be subjected to AES analysis at temperatures below 350 °C; if this is not ensured then carbon removal becomes progressively less effective with duration of the electron beam exposure. Most previous investigations had simply reported that heat cleaning was ineffective in removing carbon contamination and the ex-situ substrate preparation optimised for minimum initial carbon contimation. The standard method for in-situ removal of carbon contamination is by low energy ion bombardment followed by annealing in an arsenic overpressure to restore surface crystallinity. It is also reported that epilayers grown on ion bombarded and annealed substrates are somewhat smoother in appearance than those on heat cleaned substrates [Cho et al (1977)], although a high resistance interfacial layer on sputter cleaned substrates [Chang et al (1981)] shows that not all residual damage is removed by the annealing process.

SIMS results obtained in this laboratory by Boyle (1984) showed various oxide, sulphate and hydrocarbon related signals, together with Na, K, Al, Cr, Fe, In and Cl contamination on etched surfaces. Sulphate related signals were of variable intensity from different surfaces and remained a major signal after heat cleaning, along with hydrocarbon species. These signals were significantly reduced by low energy argon sputter cleaning, and a cyclic treatment of heat cleaning, sputtering and annealing was recommended for preparation of substrates with minimal surface contamination.

The MBE chamber used in this project was not designed to permit sputter cleaning of substrates, there being no suitable port for mounting a standard ion gun fitted with an external magnet and directed at the substrate. In-situ preparation of all substrates was, therefore, limited to heat cleaning. Substrates were heated to ~600 °C and maintained at this temperature for ~10 minutes. Electron diffraction patterns usually showed some streaking of diffraction spots and inclined relrods consistent with (114) and ($\bar{1}\bar{1}$4) facets reported by Laurence et al (1979) visible in the [$\bar{1}$10] azimuth. Typical diffraction patterns are shown in figure 3.4. If a streaked diffraction pattern did not occur at the initial heat cleaning temperature then increasing the temperature by 20 - 30 °C was usually sufficient to do so. It is not clear whether this is due to additional contamination of the surface, or simply to poor thermal contact with the thermocouple. Occasionally a weak (2 x 4) reconstruction would be apparent with no indications of faceting after simple heat cleaning, probably indicative of lower than usual contamination. Although the occurance of faceting is indicative of surface contamination, epilayer growth of a few hundred Angstroms was usually sufficient to produce an evenly streaked, reconstructed diffraction pattern, as shown in figure 3.4, indicative of a flat surface. Inclined relrods were also apparent after heat cleaning epilayers which had been exposed to air and then replaced in the system, indicating that the relevant contamination may not be from the etching process but could be either airborn, or generated within the vacuum system. This latter possibility is also indicated by two separate substrates which were heat cleaned and then left overnight whilst the system cryopanels warmed up and degassed, in an attempt to minimise the background of residual gas in the system during subsequent growth of epilayers. However both epilayers were highly

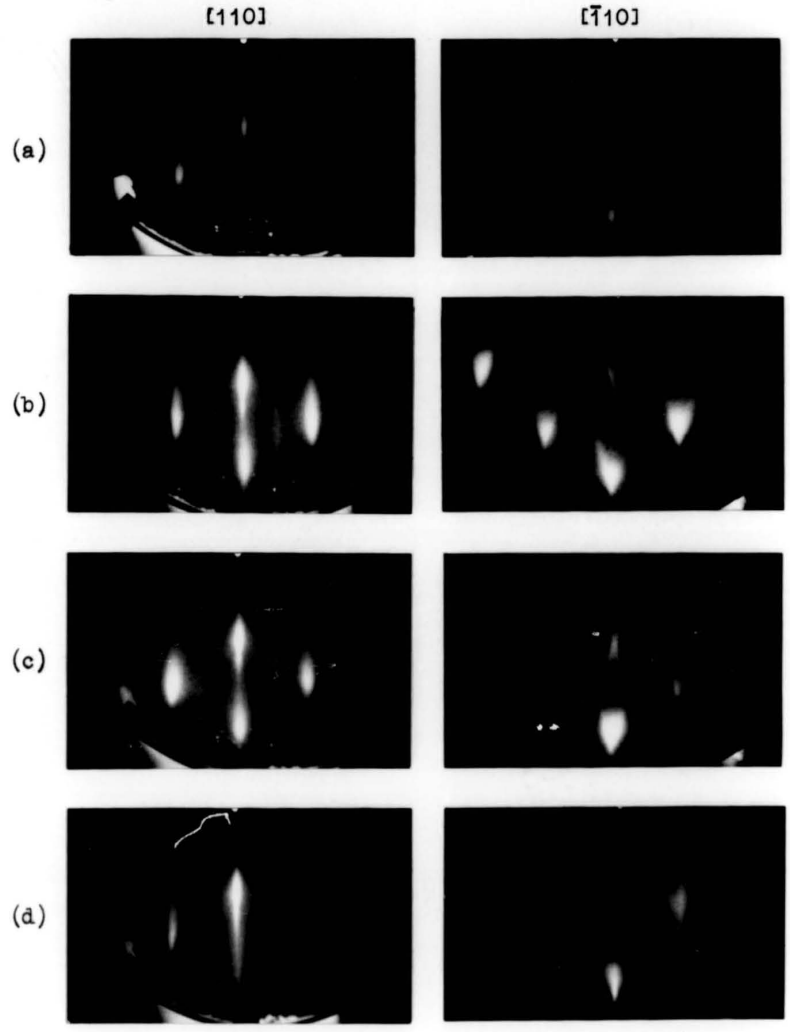

Figure 3.4 3keV RED patterns during initial growth of epilayer 43.

a) After heat cleaning at 600°C. A weak (2x1) reconstruction with slight arrowing of points on [$\bar{1}$10] azimuth. A stronger reconstruction with longer streaks is usually apparent.

b&c) After 30A & 60A growth respectively. Note increased streaking of the diffraction pattern in [110] azimuth and development of 'relrods' in [$\bar{1}$10] azimuth.

d) After 200A growth - $\frac{1}{2}$ order streaks much more uniform, $\frac{1}{4}$ order streaks just apparent beneath 'relrods'.

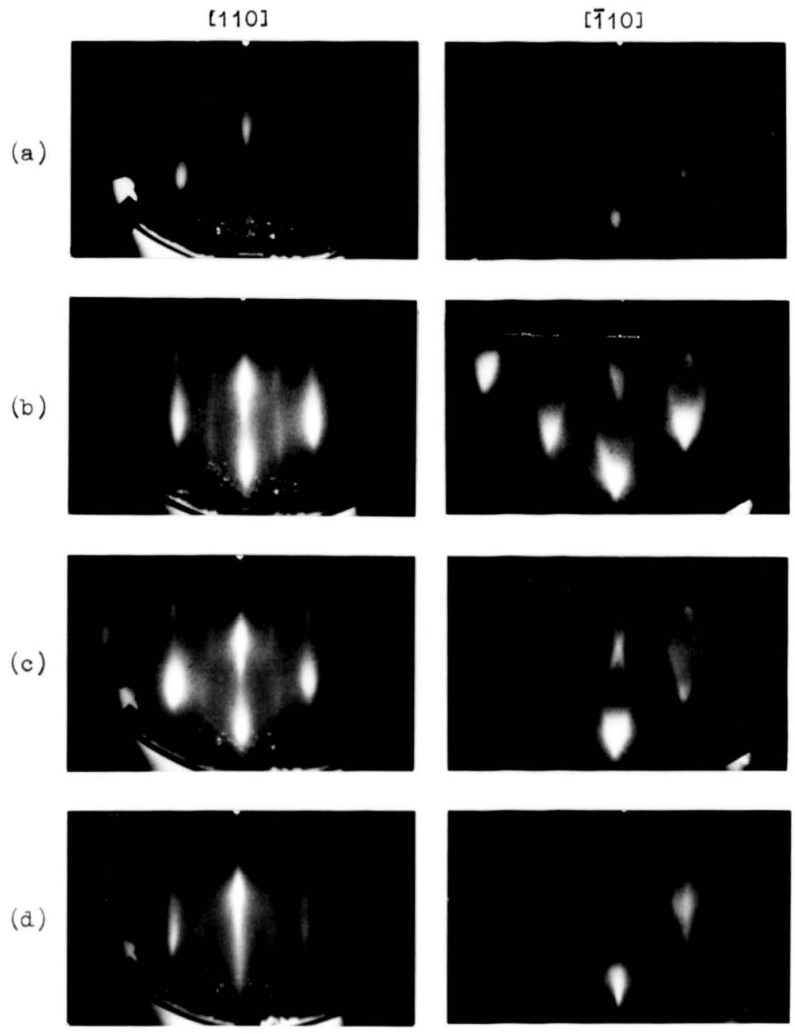

Figure 3.4 3keV RED patterns during initial growth of epilayer 43.

a) After heat cleaning at 600°C. A weak (2x1) reconstruction with slight arrowing of points on [$\bar{1}$10] azimuth. A stronger reconstruction with longer streaks is usually apparent.

b&c) After 30A & 60A growth respectively. Note increased streaking of the diffraction pattern in [110] azimuth and development of 'relrods' in [$\bar{1}$10] azimuth.

d) After 200A growth - $\frac{1}{2}$ order streaks much more uniform, $\frac{1}{4}$ order streaks just apparent beneath 'relrods'.

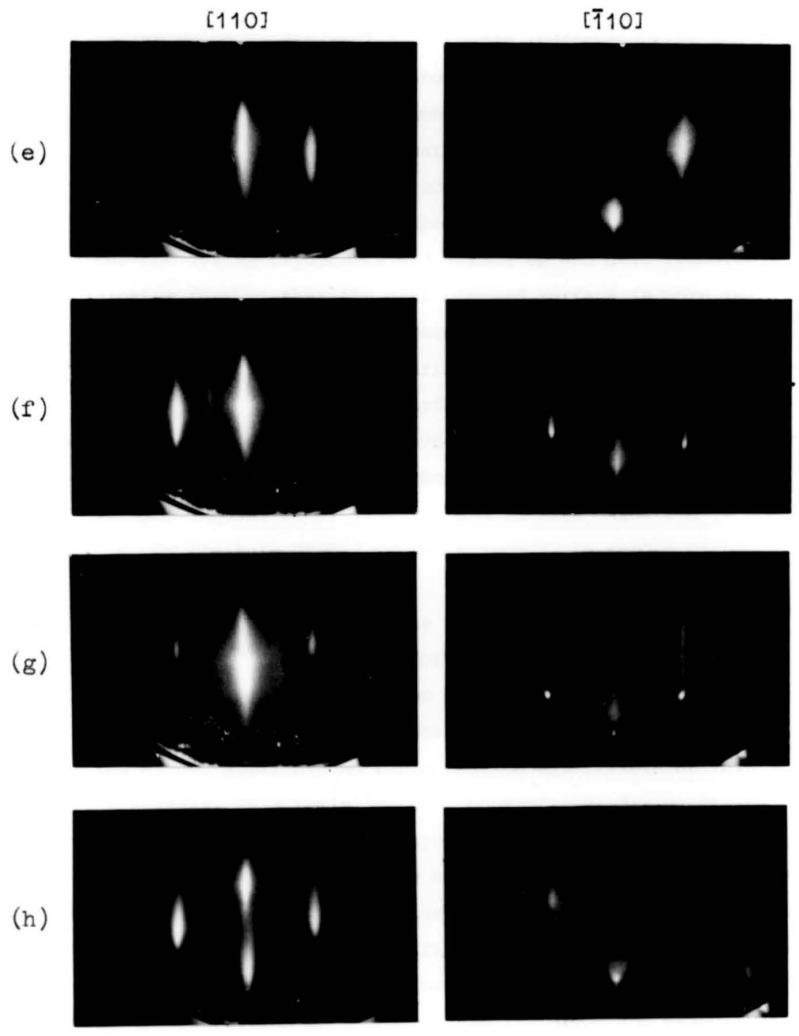

Figure 3.4

e) After 260A growth - uniform $\frac{1}{2}$ and $\frac{1}{4}$ order streaks.

f) Exposed to arsenic flux only. Note increased sharpness of $\frac{1}{4}$ order streaks.

g) During growth at 550°C and 30A/min.

h) Same layer after exposure to atmosphere and heat cleaning. Note the presence of both $\frac{1}{4}$order streaks and 'relrods' - many chemically cleaned substrates show similar diffraction patterns.

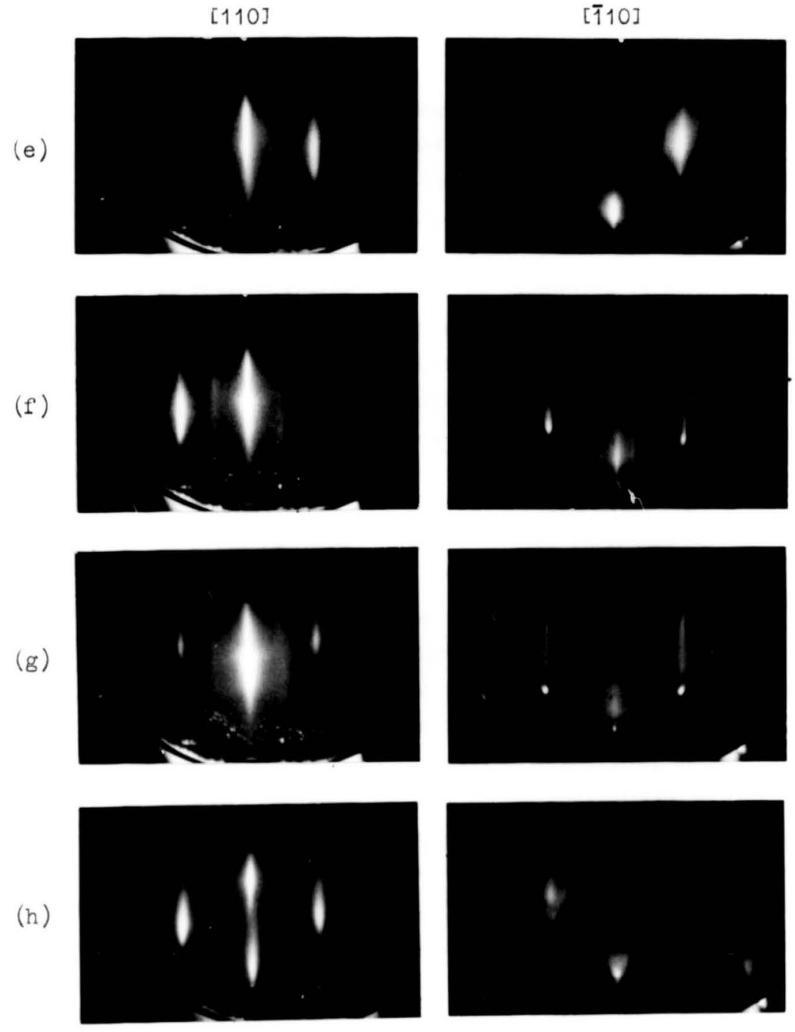

Figure 3.4

e) After 260A growth - uniform $\frac{1}{2}$ and $\frac{1}{4}$ order streaks.

f) Exposed to arsenic flux only. Note increased sharpness of $\frac{1}{4}$ order streaks.

g) During growth at 550°C and 30A/min.

h) Same layer after exposure to atmosphere and heat cleaning. Note the presence of both $\frac{1}{4}$order streaks and 'relrods' - many chemically cleaned substrates show similar diffraction patterns.

defective, as shown in figure 3.5, strongly indicating that additional contamination had occurred and had not been desorbed by an additional heat clean immediately prior to commencement of epilayer growth. The most likely source of such contamination is from species previously adsorbed on the cryopanels, but no comparable effects were found when growth of an epilayer was stopped and recommenced at a later date after the system cryopanels had warmed up and been recooled. This indicates further that the heat cleaned surface is more reactive than the MBE grown surface, presumably due to defects or other active sites created or revealed during desorption of the oxide.

Other suggested methods of surface preparation include UV-ozone cleaning [McClintock et al (1983)] immediately prior to loading in the vacuum chamber to remove carbon contamination from the oxide, laser cleaning [Rodway et al (1980)], and in-situ oxidation [Wood (1976)] in low pressure oxygen or water vapour, to remove carbon contamination.

One problem encountered at the final blowing dry of etched wafers was an occasional tendency for the water film to break up into droplets, or for droplets to be blown-up from the edge onto the surface of the wafer, and for these droplets then to be blown across the etched surface. No contamination was visible at this stage but streaks, very reminiscent of conventional drying stains, would appear on the deposited epilayer. On close examination, see figure 3.5, these marks proved to be highly faceted regions possibly ending in a region of polycrystalline or 'whisker' growth. It seems apparent that this is caused by a trail of contamination left by the evaporating droplets as they are blown across the surface, with additional contamination if a droplet finally stops and evaporates on the surface. It may be possible to reduce this form of contamination by holding the wafers on a vacuum chuck to minimise solvent collecting at the edge, or spinning dry under a reduced dry nitrogen flow.

General faceting of epilayers occurred during initial use of the system whilst correct operating parameters were being established and typical Nomarski micrographs of such layers are shown in figure 3.6 (a) - (c), together with RED patterns obtained from the most highly faceted layer. The included angle of ~50° between the relrods shows that these facets are (113) planes and not the (114)

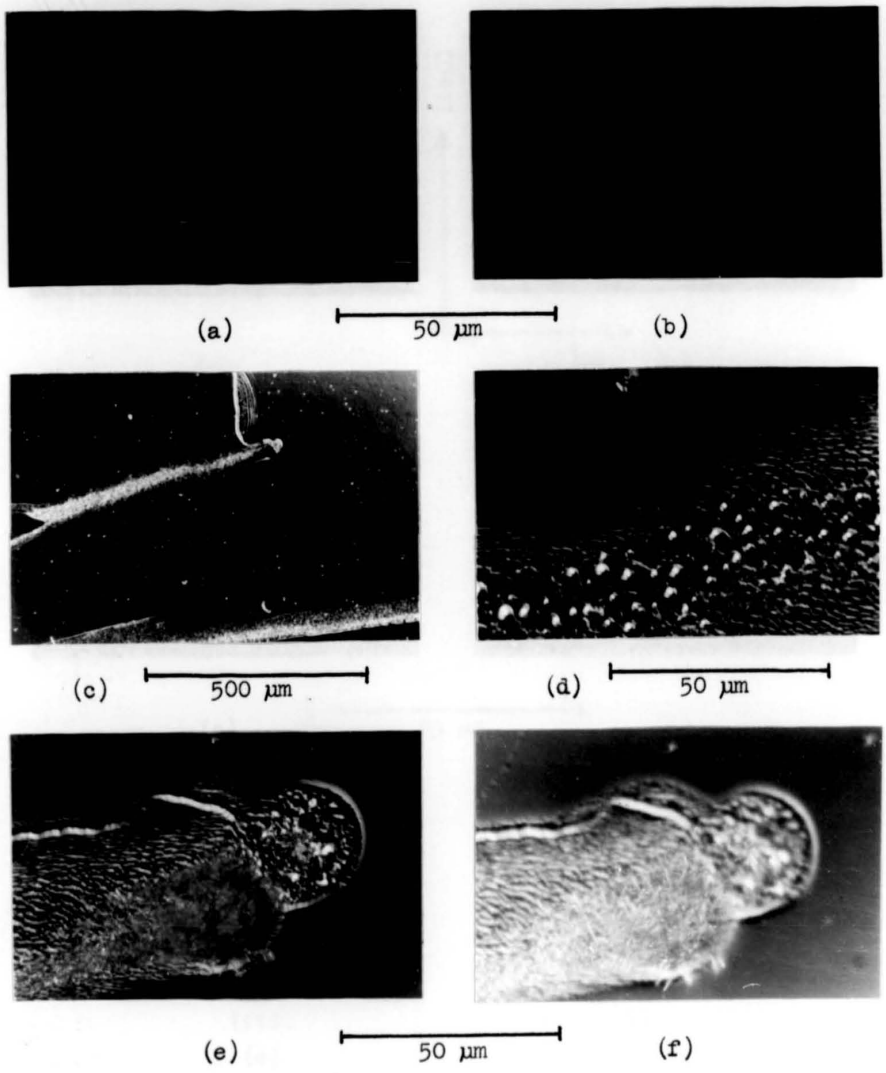

Figure 3.5 Nomarski micrographs showing :-

a&b) Highly defective epilayers produced after heat-cleaned surface was exposed to outgassing products from cryopanels.

c) Defective area of epilayer with 'drying stain'.

d) Enlarged portion of 'drying stain' showing localised faceting and possibly gallium droplets.

e) Head of drying stain showing faceting and area of whisker growth.

f) As (e) but with focal plane raised by ~1um to give better definition of whiskers.

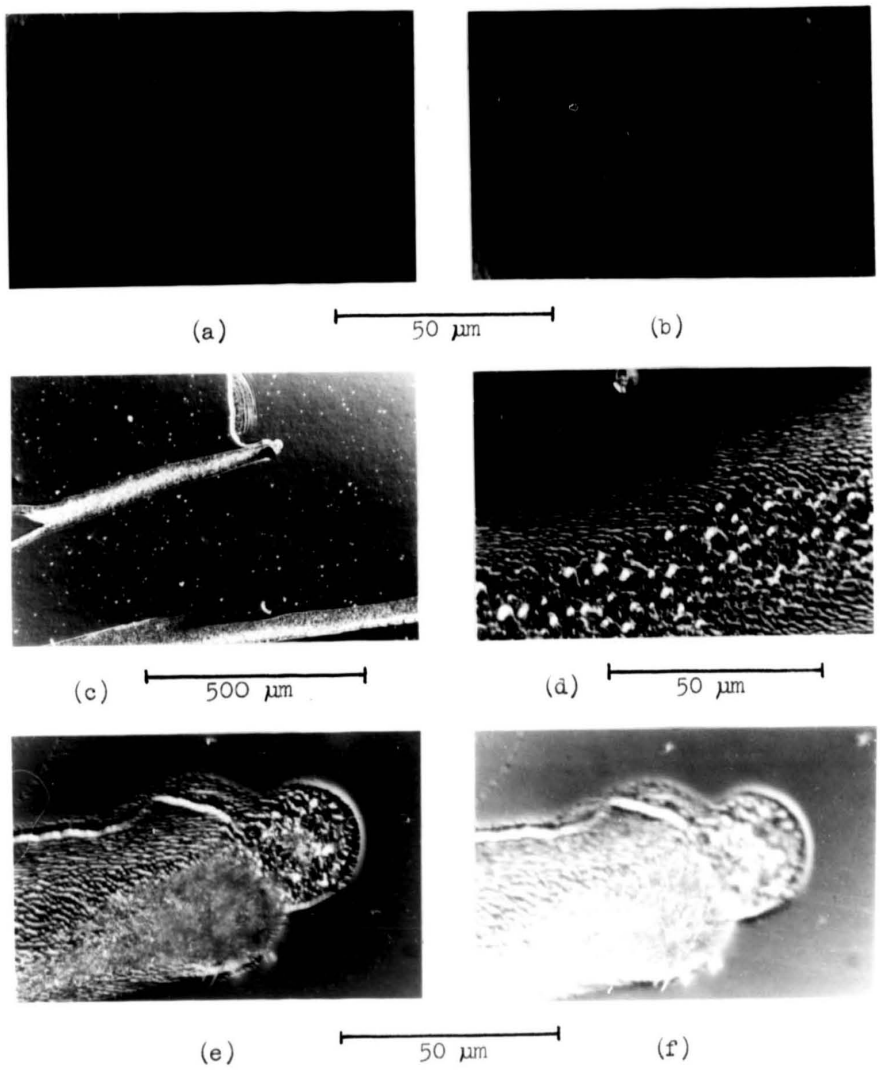

Figure 3.5 Nomarski micrographs showing :-

a&b) Highly defective epilayers produced after heat-cleaned surface was exposed to outgassing products from cryopanels.

c) Defective area of epilayer with 'drying stain'.

d) Enlarged portion of 'drying stain' showing localised faceting and possibly gallium droplets.

e) Head of drying stain showing faceting and area of whisker growth.

f) As (e) but with focal plane raised by ~1um to give better definition of whiskers.

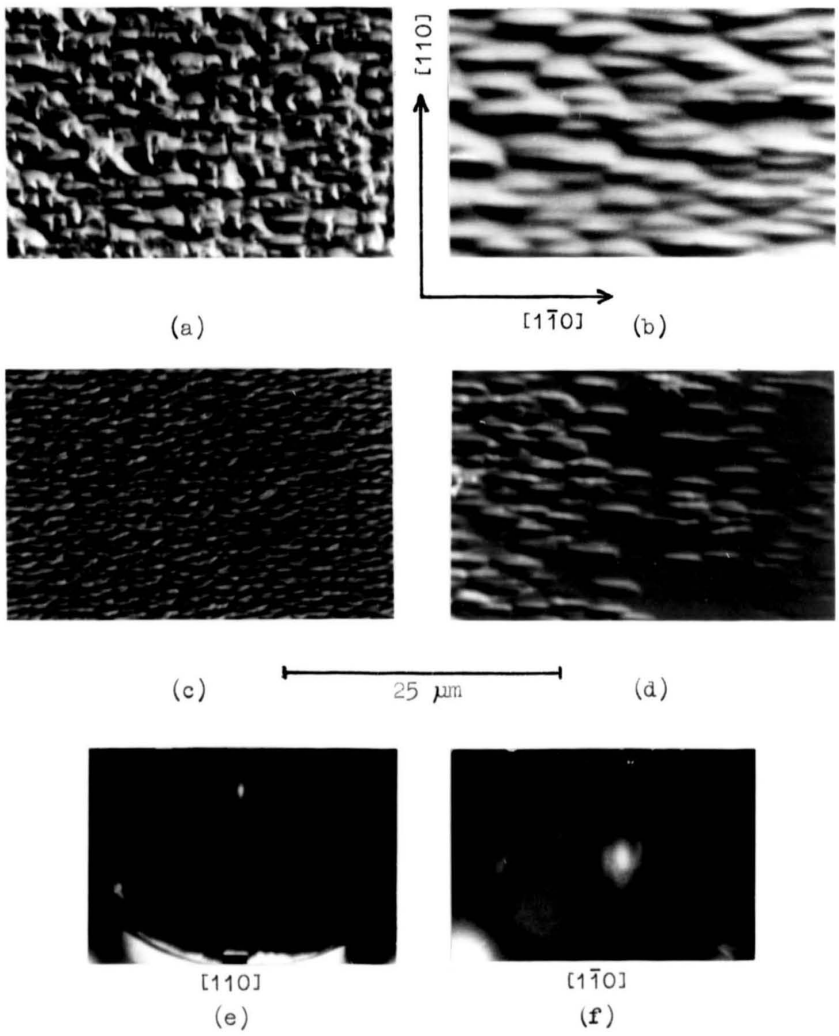

Figure 3.6 Nomarski micrographs of various faceted epilayers as described in the text.
e&f) 3keV RED patterns obtained from the epilayer shown in (a).

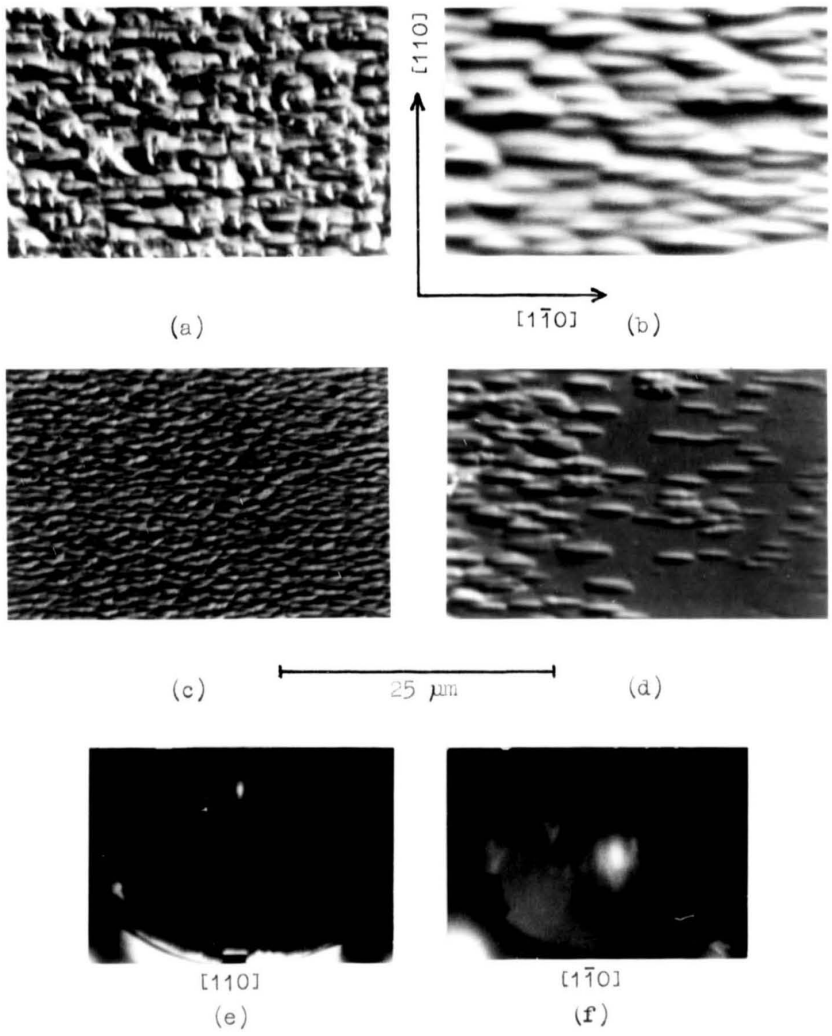

Figure 3.6 Nomarski micrographs of various faceted epilayers as described in the text.
e&f) 3keV RED patterns obtained from the epilayer shown in (a).

facets often observed for a short time after commencement of growth on a fresh substrate. The RED pattern obtained from this epilayer in the [100] direction showed spots moving along lines at 45° to the main streaks, indicative of (011) facets being present also. Faceting of this layer occurred when the system cryopanels warmed up, releasing previously adsorbed material, during the growth, and is believed to be due to adsorption of these contaminant species from the residual gas onto the growing surface.

Overall faceting of epilayers also occurred, as shown in figure 3.6 (d), when an additional ion gauge, placed in the growth region of the chamber with direct line of sight to the substrate, had been used extensively to compare residual pressures in this region with those indicated by the main chamber ion gauge. This is probably due to stray electrons from the ion gauge bombarding the surface and converting the residual carbon contamination into the strongly bound form not desorbed by heating. The pressure measurements showed that, with the cryopanels liquid nitrogen cooled, the arsenic background in the growth region was approximately twice that indicated by the main chamber ion gauge, and the increase observed on shuttering the arsenic cell was only 10% compared with 50% at the main chamber ion gauge, but this may have been due to partial shuttering of a direct line of sight from the arsenic cell to the ion gauge.

3.2 Substrate Temperature Calibration

As already mentioned in Chapter 2 the substrate thermocouple is not in good thermal contact with the substrate mounting plate and requires calibration. This was effected by drilling one plate to fit a second thermocouple in good thermal contact. The thermocouple was formed from 0.1 mm diameter wire spot welded to tantalum foil and positioned at the base of the blind hole, with a small quantity of indium solder to ensure good thermal contact. The deep hole and fine thermocouple wires minimise heat losses along the wires. Simple heat flow calculations indicate that any temperature difference across the plate should be less than 5 °C, so this second thermocouple should be within a few degrees of the actual substrate temperature. The indicated substrate temperatures were measured at various settings of the heater current and are shown in figure 3.7 (a). Note the increase in temperature when the substrate shutter is closed due to reduced radiant heat loss. The results are replotted in figure 3.7 (b) to compare the two temperature indications, and bars show the range of readings obtained from the first thermocouple when the substrate holder was rotated. This is caused by changes in thermal contact between the thermocouple and substrate plate. The plot shows that a convenient calibration over the temperature range relevant for epitaxial growth (400 - 600 °C) is that actual temperature = nominal temperature - 100 °C ± 20 °C. Figure 3.8 shows the response of the thermocouples when the substrate is heated to a controlled temperature. In normal operation only the first thermocouple signal is available, whilst the actual temperature will more nearly follow that indicated by the second thermocouple. It is apparent that temperature measurements made other than under reasonably stable conditions will be highly inaccurate and that it is difficult to measure durations of short heat treatments at a specified temperature. Furthermore the use of a PD controller to minimise the time for TC1 to reach the set temperature is not the optimum control, and experiments showed that quickest stabilisation of the actual substrate temperature occurred without use of the differential stage of the controller, the nominal substrate temperature, TC1, overshooting and then reducing whilst the actual temperature, TC2, continued to increase to a steady value. The precise form of the temperature rise varied both with the

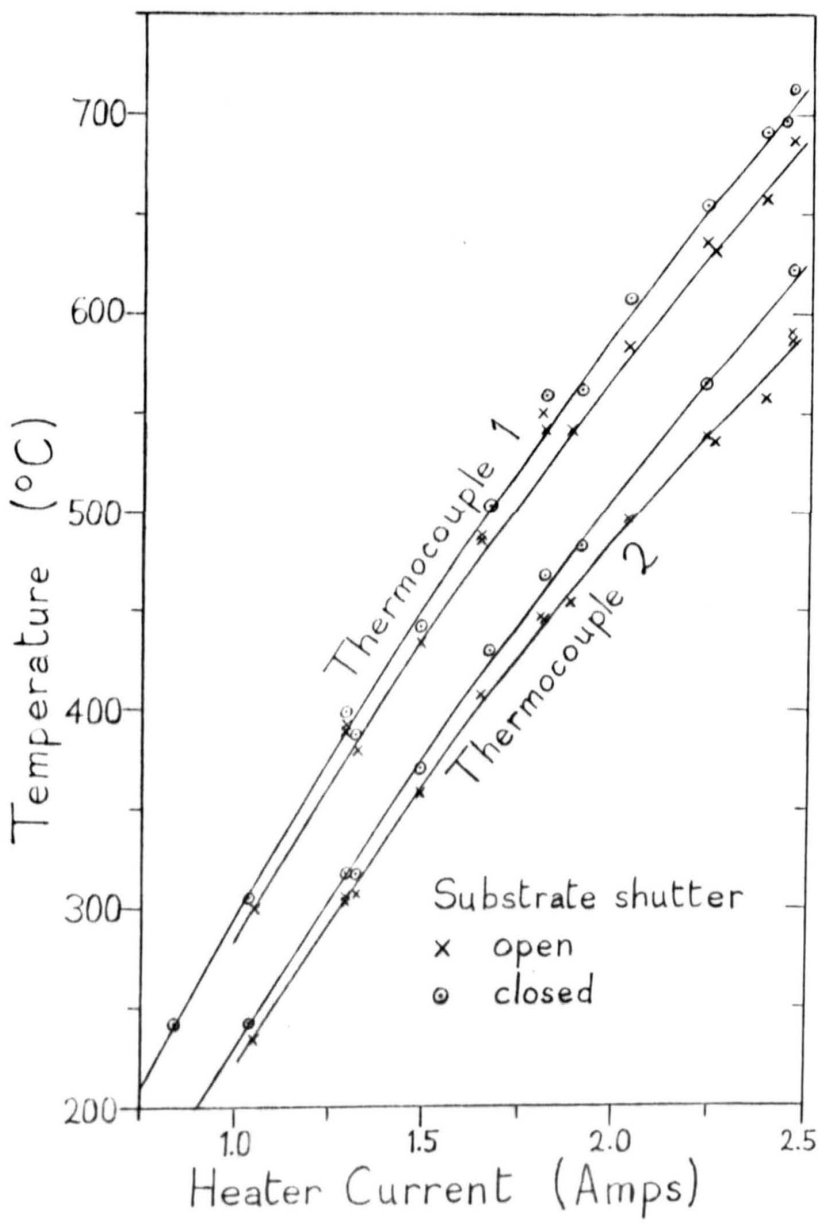

Figure 3.7(a) Substrate temperature dependence on heater current.

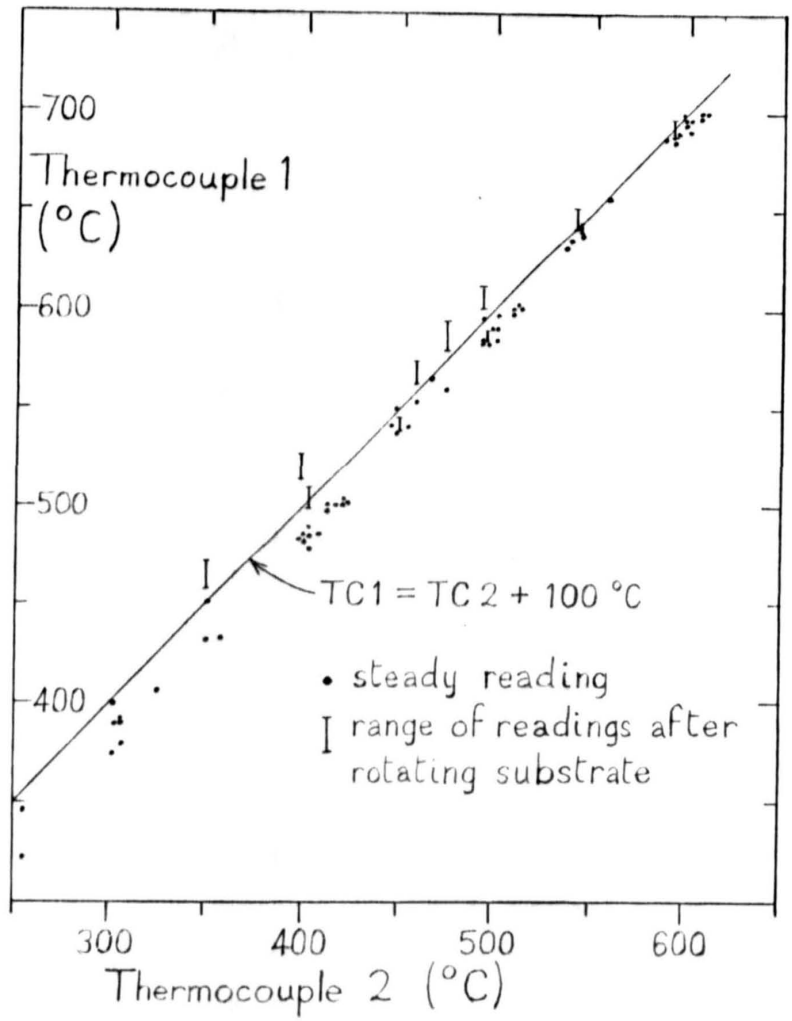

Figure 3.7(b) Comparative plot of indicated substrate temperatures.

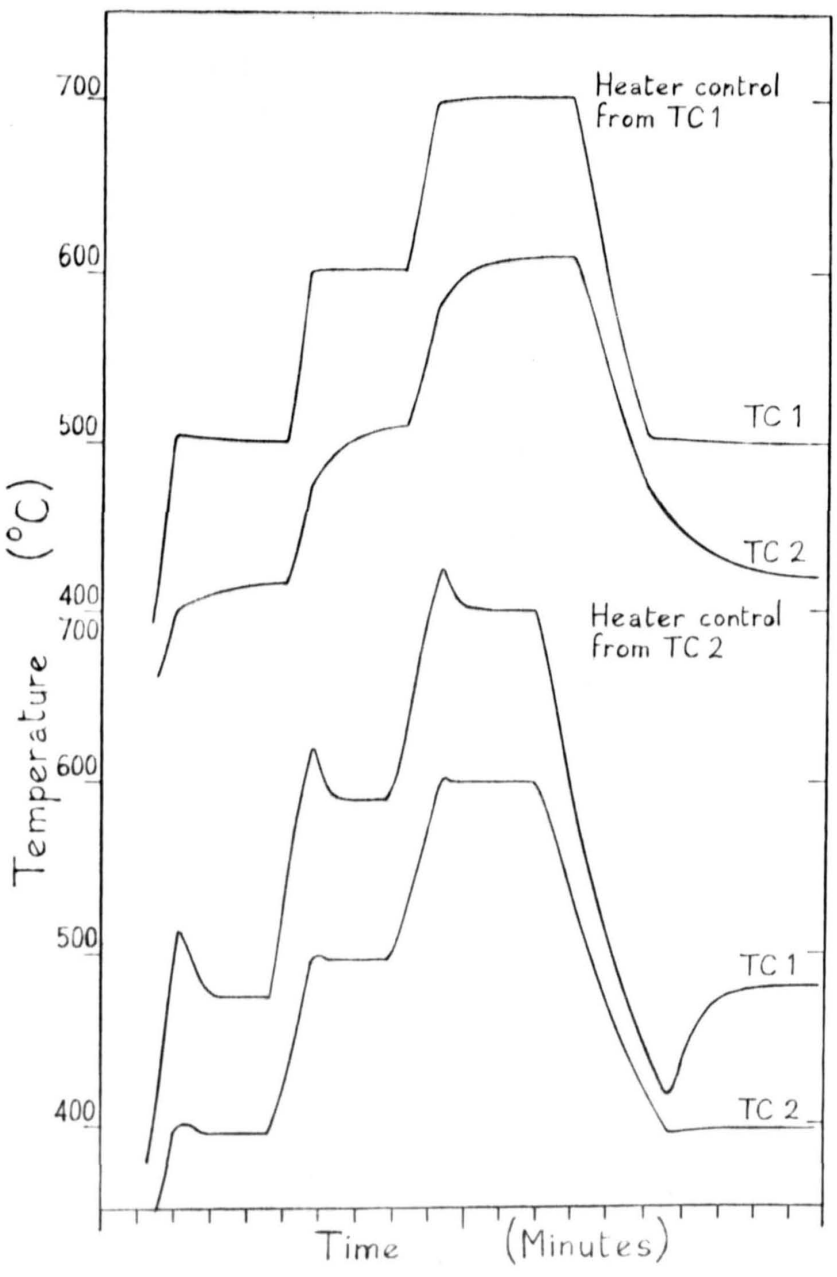

Figure 3.8 Response of substrate heater to changes in set temperature.

temperature set and maximum output power setting in use. The usual procedure when growing an epilayer was to heat clean in an arsenic flux at a nominal temperature of 700 °C (actual temperature 600 ± 20 °C) for ~15 minutes, increasing the temperature to a nominal 720 or possibly 750 °C if the electron diffraction pattern had not become streaked, and then to reduce the substrate temperature to a nominal 650 °C (actual temperature 550 ± 20 °C) before commencing growth of the epilayer. The calibration of substrate temperature against heater current was useful on occasions when the thermocouple was open circuit, enabling continued use of the system. Similar calibrations of source cell temperature against heater current were made and are shown in figure 3.9. These calibrations are less convenient both to use and obtain due to the long time constants of the source cells, and when the ion gauge flux monitor was later fitted this could, of course, be used to monitor the matrix species and set a suitable cell current in the event of thermocouple failure. As graphically indicated for the substrate heater in figure 3.8, the available thermocouple temperature measurement may not track the actual temperature of importance. This is most apparent for the arsenic source cell where the arsenic flux and residual background pressure in the chamber lags behind the indicated source cell temperature due to poor thermal contact between the source cell and its granular arsenic contents. A similar, but much reduced, effect is expected for the silicon dopant cell with a much smaller charge of silicon granules. The gallium cell, on the other hand, with its liquid gallium charge shows much better uniformity of temperature, and when the temperature controller was adjusted so that it gave a large oscillating power output, synchronous variation in the gallium flux was observed, consistent with the indicated one degree temperature variation, and shown in figure 3.10. The gain of the proportional and differential stages of the source cell controllers were set to give reasonably steady outputs at normal operating conditions and rapid stabilisation of the cell temperature.

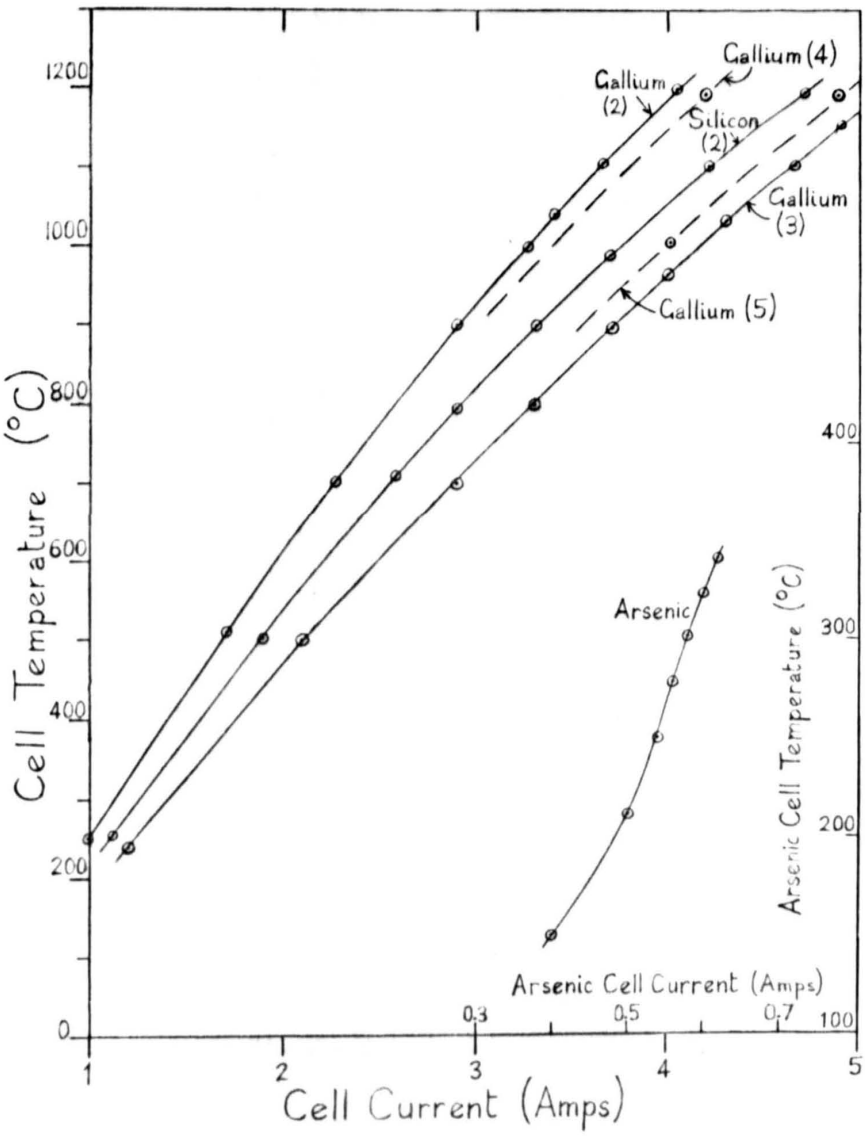

Figure 3.9 Source cell temperature dependence on heater currents.

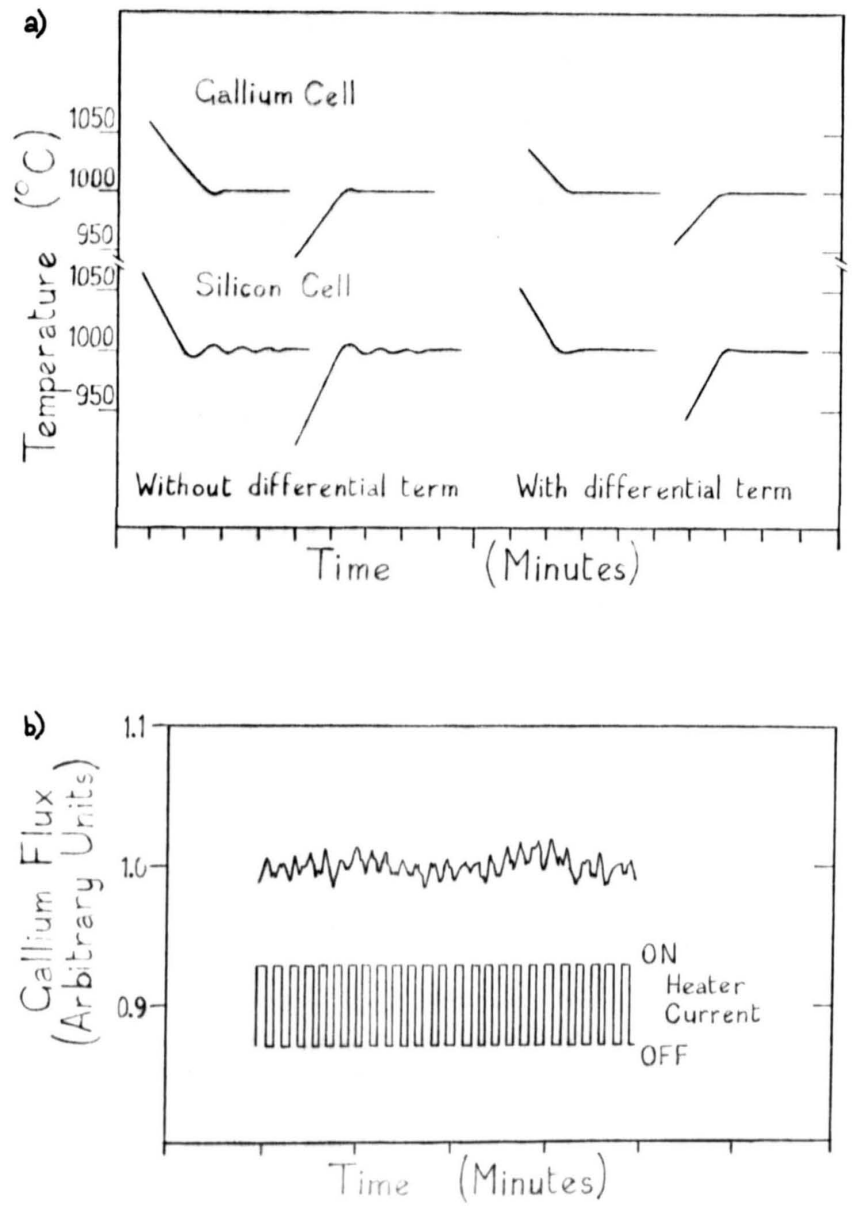

Figure 3.10 a) Stabilization of source cell temperatures.
b) Oscillation of gallium flux with unstable heater current.

3.3 Surface Reconstructions

A variety of surface reconstructions have been observed on growing (001) GaAs epitaxial films since the initial development of the MBE technique [see eg Cho & Arthur (1975), Ploog (1980), Neave & Joyce (1978)] dependent on growth conditions, and more recent results have confirmed different surface compositions of the various reconstructions [Drathen et al (1978), Bachrach et al (1981), Larsen et al (1982), (1983)] as shown in Table 3.1. The growth of surfaces with different reconstructions and compositions was an essential part of the project and was monitored using reflection electron diffraction. As already mentioned the diffraction pattern became evenly streaked after growth of a few hundred Angstroms of material on the heat cleaned substrate, generally considered to be indicative of a substrate flat on an atomic scale.

Several different reconstructions could be established for various incident fluxes and substrate temperatures. Some, which gave distinct diffraction patterns are shown in figure 3.11, but several other less distinct patterns were also observed. The majority of reconstructions were not particularly stable or reproducible and were not easily retained when the substrate was cooled to room temperature. The commonly reported C(4 x 4) As rich, (2 x 4) As stabilised and (4 x 2) Ga stabilised reconstructions were all attained with little difficulty and close examination of the (4 x 2) Ga stabilised diffraction pattern, see figure 3.11 (a) & (b), showed that it was in fact a C(8 x 2) reconstruction since the second order reconstruction fringe was visible not with the electron beam incident along the $[\bar{1}10]$ azimuth but at 14° to this along $[\bar{5}30]$ and $[\bar{3}50]$. This is contrary to the generally held view stated by Neave & Joyce (1978) that it is impossible to distinguish these reconstructions using RHEED, since the necessary fractional order fringes are not separable. Such a distinction was not, however, possible with (2 x 4) or C(2 x 8) reconstruction due to the much longer and stronger half order fringes in the [110] direction as is apparent in figure 3.4 (e) - (g).

Maintaining the surface reconstructions whilst the substrate cooled to room temperature was not straightforward. The (4 x 2) Ga stabilised reconstruction consistently changed to a (4 x 6) reconstruction on cooling below ~500 °C and back again on heating to ~550 °C. It has been suggested by Dobson (1984) that this is probably due to a high background CO level in the chamber. The

Table 3.1 Composition of different GaAs(001) surface reconstructions

Reconstruction	Approximate surface composition (%As)				
	Ref 1	Ref 2	Ref 3	Ref 4	Ref 5
c(4x4) As rich	-	86	100	120-175	87
(2x4) As stab.	50-60	61	89	100	62
(4x6) Ga stab.	-	27	31	-	18
(4x2) Ga stab.	<10	22	52	-	-

References:

1. Arthur (1974)
2. Drathen et al. (1978)
3. Bachrach et al. (1981)
4. Larsen et al. (1983)
5. Ludeke et al. (1983b)

Other investigations (Neave & Joyce (1978), Chiang (1983), Massies et al. (1980)), whilst not giving absolute coverages, generally agree with the ordering of Drathen et al (1978) finding the (4x2) reconstruction to be the most gallium rich surface. They also find overlapping ranges of surface composition for the different reconstructions.

Table 3.1 Composition of different GaAs(001) surface reconstructions

Reconstruction	Approximate surface composition (%As)				
	Ref 1	Ref 2	Ref 3	Ref 4	Ref 5
c(4x4) As rich	-	86	100	120-175	87
(2x4) As stab.	50-60	61	89	100	62
(4x6) Ga stab.	-	27	31	-	18
(4x2) Ga stab.	<10	22	52	-	-

References:

1. Arthur (1974)
2. Drathen et al.(1978)
3. Bachrach et al.(1981)
4. Larsen et al.(1983)
5. Ludeke et al.(1983b)

Other investigations (Neave & Joyce (1978), Chiang (1983), Massies et al.(1980)), whilst not giving absolute coverages, generally agree with the ordering of Drathen et al (1978) finding the (4x2) reconstruction to be the most gallium rich surface. They also find overlapping ranges of surface composition for the different reconstructions.

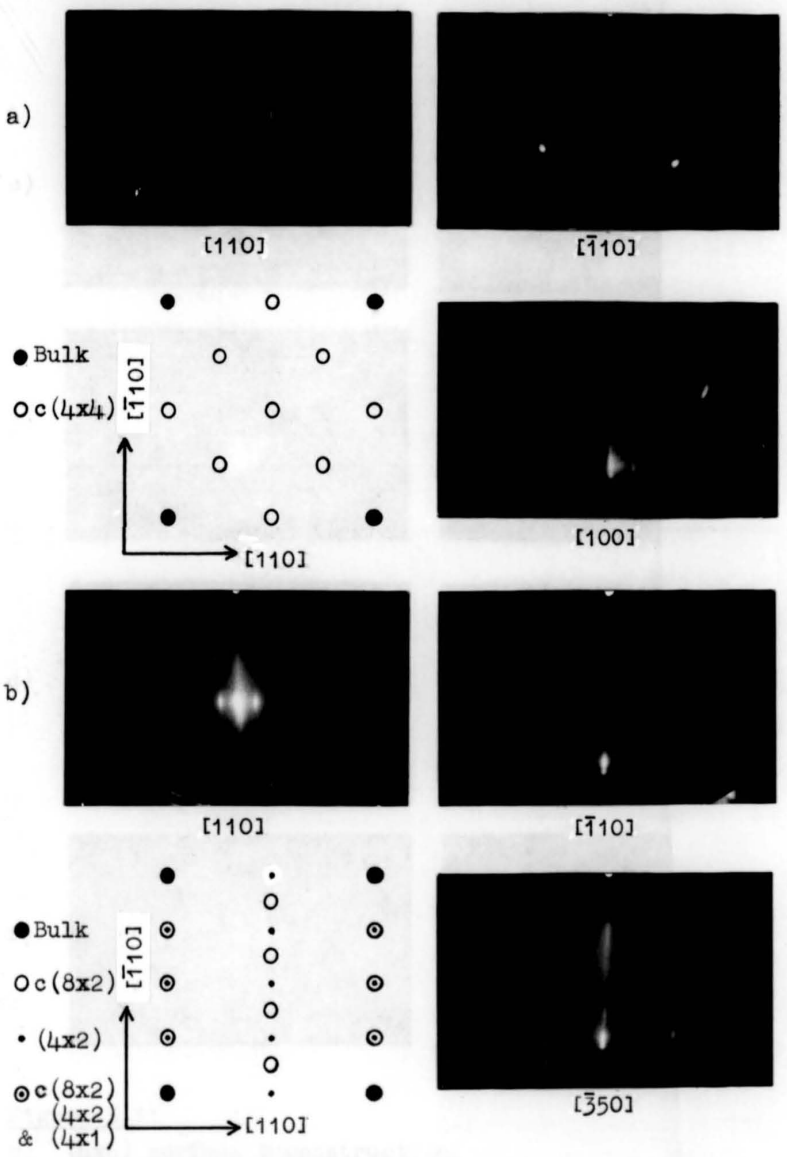

Figure 3.11 RED patterns and reciprocal lattice cell of various surface reconstructions on (001)GaAs.

a) c(4x4)As rich surface.

b) c(8x2)/(4x2)/(4x1)Ga stabilised surface. The 1/2 order reconstruction is weak and only just visible.

Diffraction patterns characteristic of the (2x4)As stabilised surface are shown in Figure 3.4, and the reciprocal lattice cell is identical to the (4x2)Ga stabilised, but rotated by 90°.

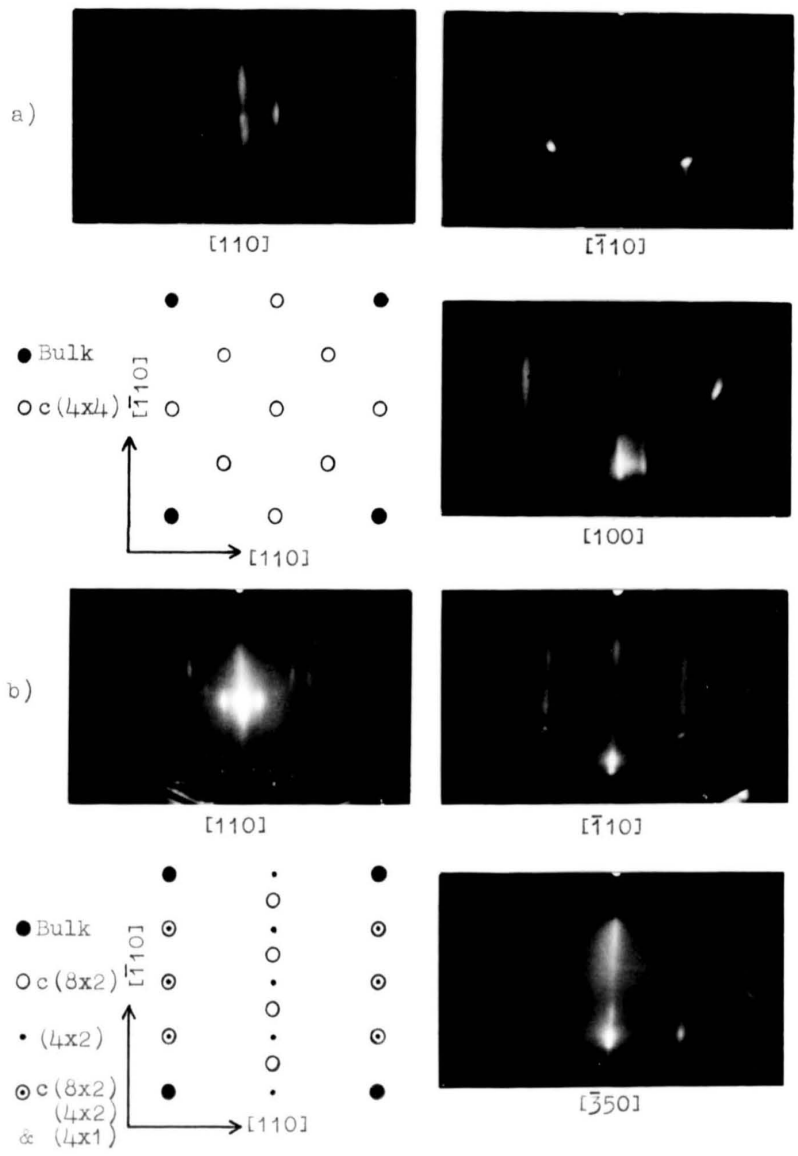

Figure 3.11 RED patterns and reciprocal lattice cell of various surface reconstructions on (001)GaAs.

a) c(4x4)As rich surface.

b) c(8x2)/(4x2)/(4x1)Ga stabilised surface. The 1/2 order reconstruction is weak and only just visible.

Diffraction patterns characteristic of the (2x4)As stabilised surface are shown in Figure 3.4, and the reciprocal lattice cell is identical to the (4x2)Ga stabilised, but rotated by 90°.

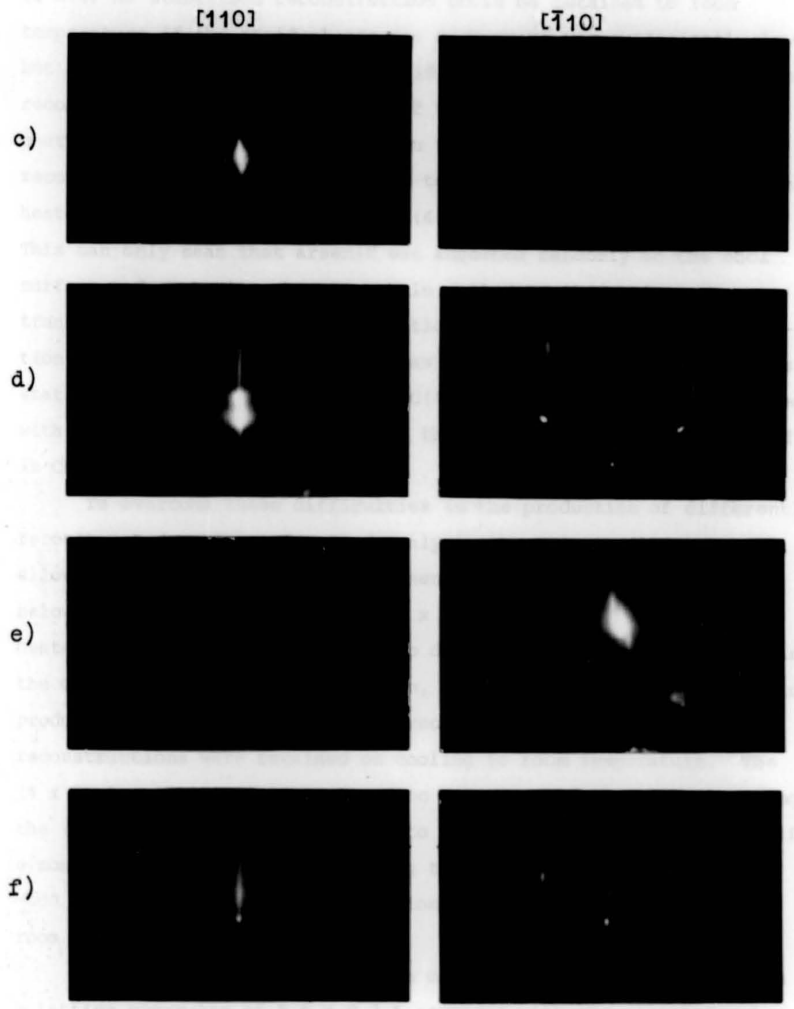

Figure 3.11

c) (4x6) surface reconstruction.
d) Mixed (2x6) & (3x6) surface reconstruction.
e) (4x8) surface reconstruction.
f) (3x6) surface reconstruction.

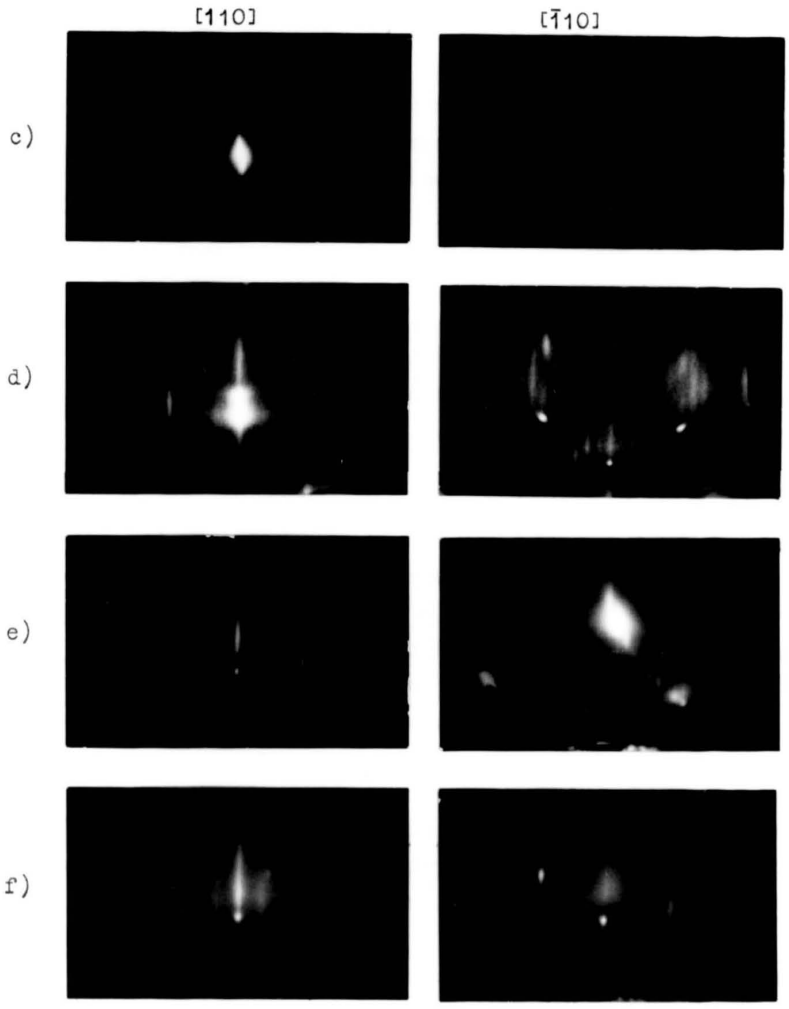

Figure 3.11

c) (4x6) surface reconstruction.
d) Mixed (2x6) & (3x6) surface reconstruction.
e) (4x8) surface reconstruction.
f) (3x6) surface reconstruction.

(2 x 4) As stabilised reconstruction could be retained to room temperature if the residual arsenic background was sufficiently low, but at pressures $\gtrsim 10^{-7}$Torr it would change to the C(4 x 4) As rich reconstruction due to adsorption of the residual arsenic, although shuttered from the direct beam. On some occasions when the (2 x 4) reconstruction had been maintained to room temperature and was then heated it would transform to the C(4 x 4) As rich reconstruction. This can only mean that arsenic was adsorbed randomly on the cool surface and on heating became mobile, allowing the surface to transform to the stable reconstruction with higher arsenic composition. The adsorption of arsenic was also tentatively inferred from static SIMS results obtained from C(4 x 4) As rich surfaces prepared with and without heating to desorb the arsenic, and fully described in Chapter 4.

To overcome these difficulties in the production of differently reconstructed surfaces for SIMS analysis the grown epilayer was allowed to cool in the residual arsenic background until this was below 10^{-8}Torr. The resulting C(4 x 4) As rich surface was then heated to 400 °C for ~10 minutes to desorb excess arsenic but retain the C(4 x 4) As rich reconstruction, or to 500 °C for ~10 minutes to produce the (2 x 4) As stabilised reconstruction. Both of these reconstructions were retained on cooling to room temperature. The (4 x 2) Ga stabilised reconstruction was prepared by further heating the (2 x 4) As stabilised surface to 550 °C and then depositing half a monolayer of gallium. On cooling this surface it transformed at ~500 °C to the (4 x 6) reconstruction which was then retained to room temperature.

Measurement of the separation of the diffraction streaks gave a lattice parameter of 5.6 ± 0.3 A compared with the accepted value of 5.65 A.

Other interesting effects observed in the electron diffraction patterns included splitting of the primary spot by vicinally oriented surfaces and fluctuations in intensity on commencement of epilayer growth. Splitting by vicinally oriented surfaces has been investigated by Pukite et al (1984) and attributed to destructive interference between diffracted beams from adjacent terraces on the vicinal surface. Calculation of the angle of misorientation requires knowledge of the precise angle of incidence of the electron beam,

which is not easily measured in this simple diffraction system and the effect was not investigated further. Fluctuations in intensity of diffracted beams have been investigated by van Hove et al (1983) and Neave et al (1983) and shown to be caused by essentially monolayer growth on an atomically flat surface; the period of the fluctuations corresponds to one monolayer growth and the amplitude reduces with growth due to random nucleation of additional monolayers on only partially completed layers. During this project such fluctuations were only observed at recommencement of growth onto epilayers which had been used for SIMS analysis. These are presumably the least contaminated surfaces available, since they have not been exposed to outgassing products from the MBE system cryopanels, and the epilayers are being grown with minimum impurities in the residual gas due to the extended pumping period without exposure of the main chamber to the load lock or to outgassing of a freshly loaded substrate. This is a further indication of the desirability of reducing system impurities to lower levels.

3.4 Growth Rate Calibration

The ion gauge flux monitor was not obtained until a relatively late stage in the project, and before this the only indication of epilayer growth rate was the temperature of the gallium cell. A calibration of growth rate against gallium cell temperature was, therefore, essential, and remained useful, even with the flux monitor fitted, since cell temperature is the parameter used to maintain the growth rate and is more precise than the flux monitor signal in this system.

The first few epilayers were grown with a 5 mm diameter orifice to the gallium cell but this was soon removed to obtain the maximum flux from the cell. The first attempt at growth rate calibration was to measure the gallium flux by depositing onto weighed pieces of aluminium foil mounted on the substrate holder. However, the mass of deposited gallium was too small to provide sufficiently accurate measurements and subsequently a small piece of tantalum foil was bent to clip onto the substrate plate and cover a small portion of the substrate. The resulting step, after growth of the epilayer, was then measured using a Tallystep stylus-based surface profiler. This procedure was most convenient in use, the tantalum clip interfering much less than anticipated with electron diffraction patterns, and was used routinely for measurement of final epilayer thickness rather than relying totally on previous calibration of the growth rate.

Standard kinetic theory of gases [see eg Tabor (1969), Ramsey (1963), Holland (1956)] shows that the flux of molecules, effusing from a small, sharp edged aperture (an ideal Knudsen source) is given by

$$\delta Q = \frac{n}{4\pi} \bar{c} \cos\theta \, A_s \, \delta\omega = \frac{N_o P \, A_s}{\sqrt{2\pi \, MRT}} \frac{\cos\theta}{\pi} \, \delta\omega \qquad (3.1)$$

using standard symbols as indicated in figure 3.12. Integrating over the 'half-space' above the aperture gives the total flux as

$$Q_T = \frac{1}{4} n \bar{c} A_s = \frac{N_o P \, A_s}{\sqrt{2\pi \, MRT}} \qquad (3.2)$$

If the aperture is not sharp edged but is a cylindrical tube then, although the on-axis flux is unchanged, the total flux is reduced by a factor $1/\kappa$ due to diffuse scattering of molecules from the tube walls, where in the limit of a long tube $1/\kappa = 8r/3\ell$. In the

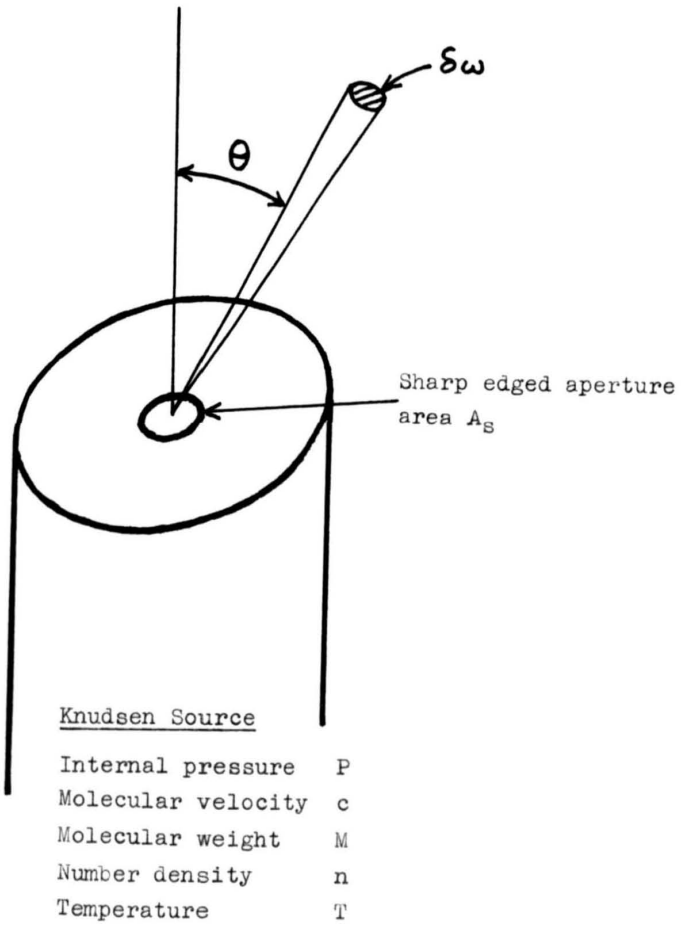

Figure 3.12 Effusion from Knudsen source cell.

case of Langmuir evaporation from a flat surface it is found that

$$Q_T = \frac{a N_o P A_s}{\sqrt{2\pi MRT}} \qquad (3.3)$$

where P is now the saturated vapour pressure of the material and a is the so-called accommodation coefficient. The source cells used in this investigation, and generally in other MBE systems, are intermediate between the ideal Knudsen source with a small, sharp-edged aperture and vapour in equilibrium with the source material, and the freely evaporating Langmuir source. However the functional relationship between on-axis effusion flux per unit area at distance ℓ and source temperature is in all cases given by

$$Q = K \frac{P(T)}{\sqrt{MT}} \frac{A_s}{\ell^2} \qquad (3.4)$$

where for a Knudsen source

$$K = \frac{N_o}{\pi\sqrt{2\pi R}}$$

and P(T) is the saturated vapour pressure of the source material at temperature T. Vapour pressure may be obtained from published tables eg Honig & Kramer (1969), Kaye & Laby (1975) but an analytical expression is obtained by standard approximation and integration of the Clausius-Clapeyron equation as

$$P = P_o \exp(-L/RT) \qquad (3.5)$$

where L is the latent heat of evaporation (assumed constant). Combining this with equation 3.4 we find

$$Q = \frac{K P_o A_s}{\ell^2 \sqrt{MT}} \exp(-L/RT) \qquad (3.6)$$

The exponential variation with temperature is much stronger than that due to the square root, as is apparent from figure 3.13 (a) where experimental growth rates are plotted logarithmically as a function of reciprocal temperature, together with that calculated assuming ideal Knudsen effusion from the source cell. Two major effects are believed responsible for the differences between predicted and measured growth rates, in addition to the departure

from ideal Knudsen effusion conditions. Firstly there is the problem of accurate source temperature measurement which, since the measured temperature is likely to be low, will produce higher growth rates than would otherwise be expected, and poorer thermal contact is believed to be responsible for the higher growth rates observed for epilayers 58 - 74. In addition, non-linearities in the chromel-alumel thermocouple over the full range 0 - 1200 °C will reduce the discrepancy in slope of the two lines, since the linear amplifier, when correctly set at 1000 °C will be reading 20 °C low at 1200 °C. Secondly, a skin of gallium arsenide builds up on the surface of the gallium charge due to reaction with the residual arsenic background and this reduces the flux below that for a clean surface [Bachrach & Krusor (1981)]. This effect is shown directly in the measurements with the ion gauge flux monitor described below. A light grey surface was generally visible on the gallium charge, when open to atmosphere at room temperature, rather than a bright metallic mirror surface, but after growth of epilayers 44 - 51, with progressively lower growth rates, a dark grey skin was present suggesting some additional contaminant. Dark grey to black deposits had also been observed on system components after outgassing the source cell prior to loading the gallium charge, suggesting that this contamination may be carbon from the source cell. The skin was therefore carefully removed, along with a small but unavoidable amount of gallium, and chemically analysed for carbon contamination. The resulting 0.11% carbon found in the 25 mg sample would produce a 0.3 μm thick carbon skin if evenly distributed across the gallium surface. Such a layer would undoubtedly have a large effect on the gallium flux and shows that carbon contamination from the source cell is the most likely reason for the reduced flux, although the use of true surface analysis techniques and microscopic examination of the surface are probably necessary to confirm this beyond doubt.

The reduction in growth rate apparent in epilayers 15 - 24 is, on the other hand, believed to be due to increased leakage current into the gallium cell thermocouple, together with incorrect setting of the common mode rejection circuit in the temperature controller.

Correct alignment of the source cell is necessary to ensure uniformity of flux, and hence growth rate, across the whole substrate.

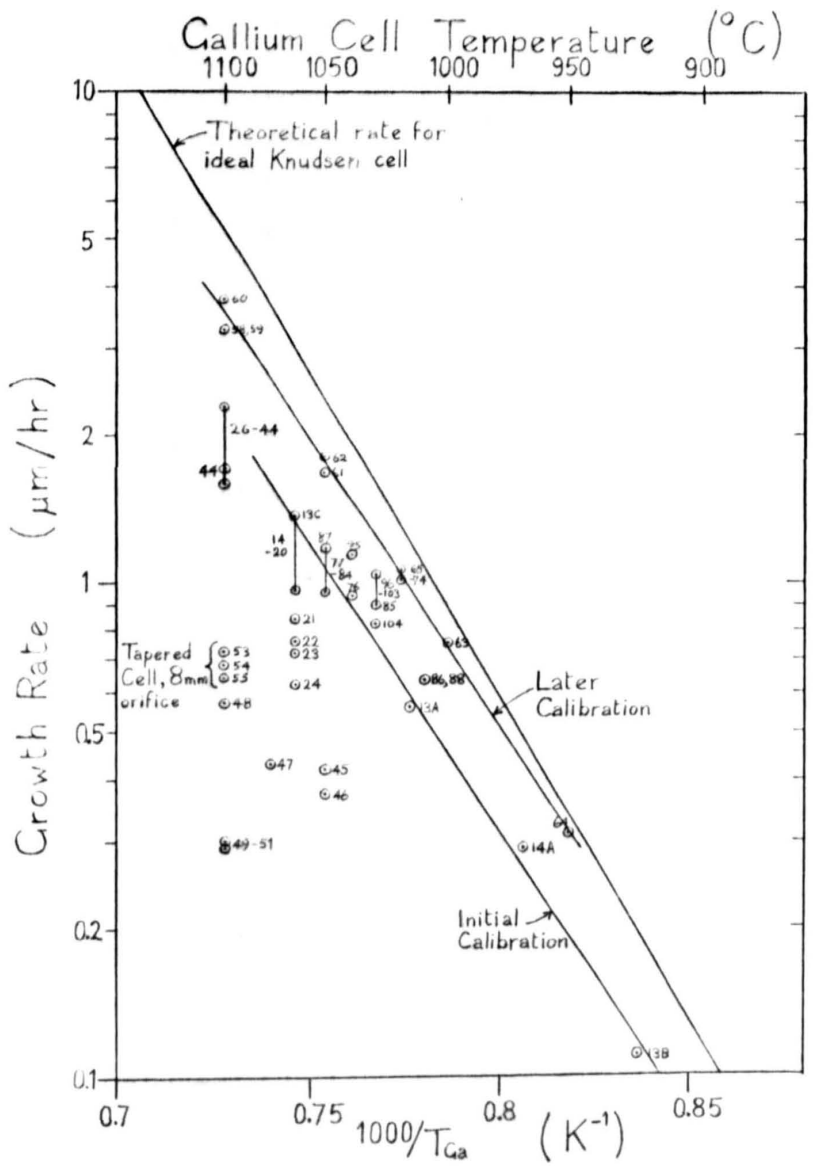

Figure 3.13(a) Calibration of epilayer growth rate with gallium source cell temperature.

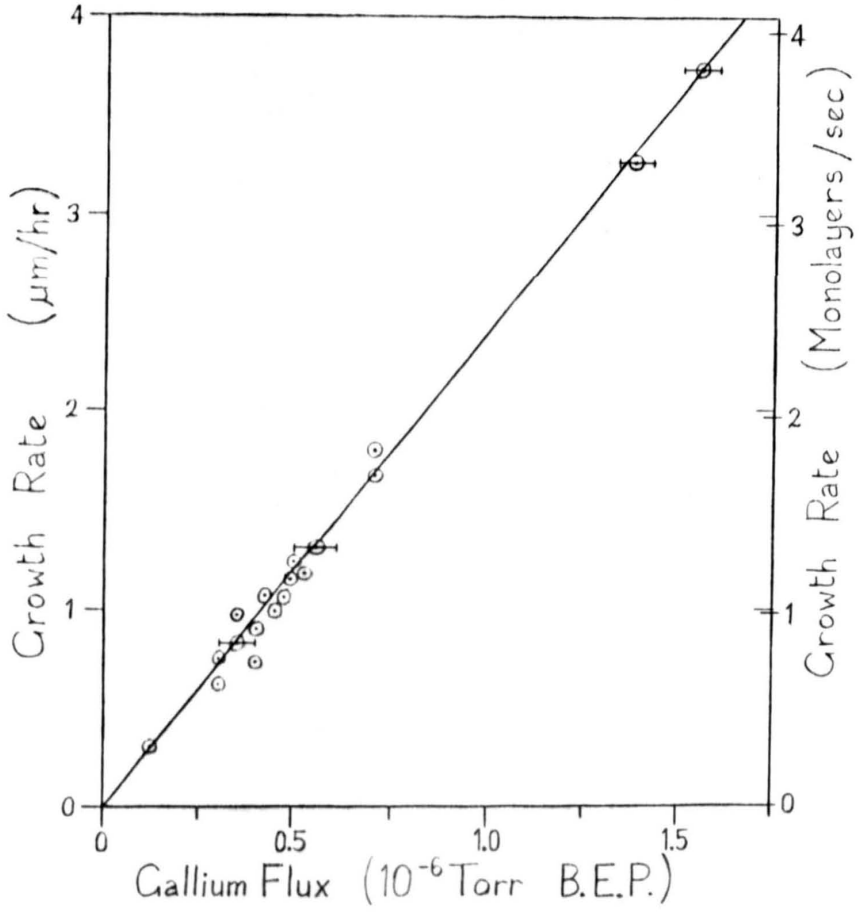

Figure 3.13(b) Calibration of epilayer growth rate with gallium flux-monitor reading.

When checked, by measuring epilayer thickness at several positions on a large substrate, a monotonic variation across the substrate of ~25% was found, but this was reduced to ~10% after realigning the gallium source cell. However, at this early stage in development of the system the source cells were not held well-aligned with the cluster; subsequently locating rings were made as outlined in Chapter 2 and are expected to have improved the uniformity of later epilayers. When fitted, the ion gauge flux monitor was used to measure the gallium beam flux as described in Chapter 2. Since the ion gauge measures the number density in the molecular beam the actual flux, is given by

$$Q = S \bar{c} B/a_M \qquad (3.7)$$

where B is the indicated beam equivalent pressure,

$\bar{c}$ is the average molecular velocity in the beam,

a_M is the ionisation cross-section of the molecule of molecular weight M,

and S is a geometrical factor.

Including the standard expression for $\bar{c}$, we obtain

$$Q \propto \frac{B}{a_M}\sqrt{\frac{T}{M}} \qquad (3.8)$$

where T is the source temperature. However, as already discussed, the $\sqrt{T}$ factor is small over the range of temperatures used for any one cell, and a plot of growth rate against beam equivalent pressure is a straight line to within experimental error as shown in figure 3.13 (b).

Combining equations 3.6 and 3.8 gives

$$B \propto \frac{1}{T} \exp(-L/RT) \qquad (3.9)$$

Again the exponential term dominates the expression, so that the logarithmic plots of beam equivalent pressure against reciprocal temperature in figure 3.14 are essentially straight lines. The results obtained for the gallium cell show a reduced flux after the arsenic cell is heated, which may be due to the formation of a GaAs skin on the gallium charge, or alternatively may be due to

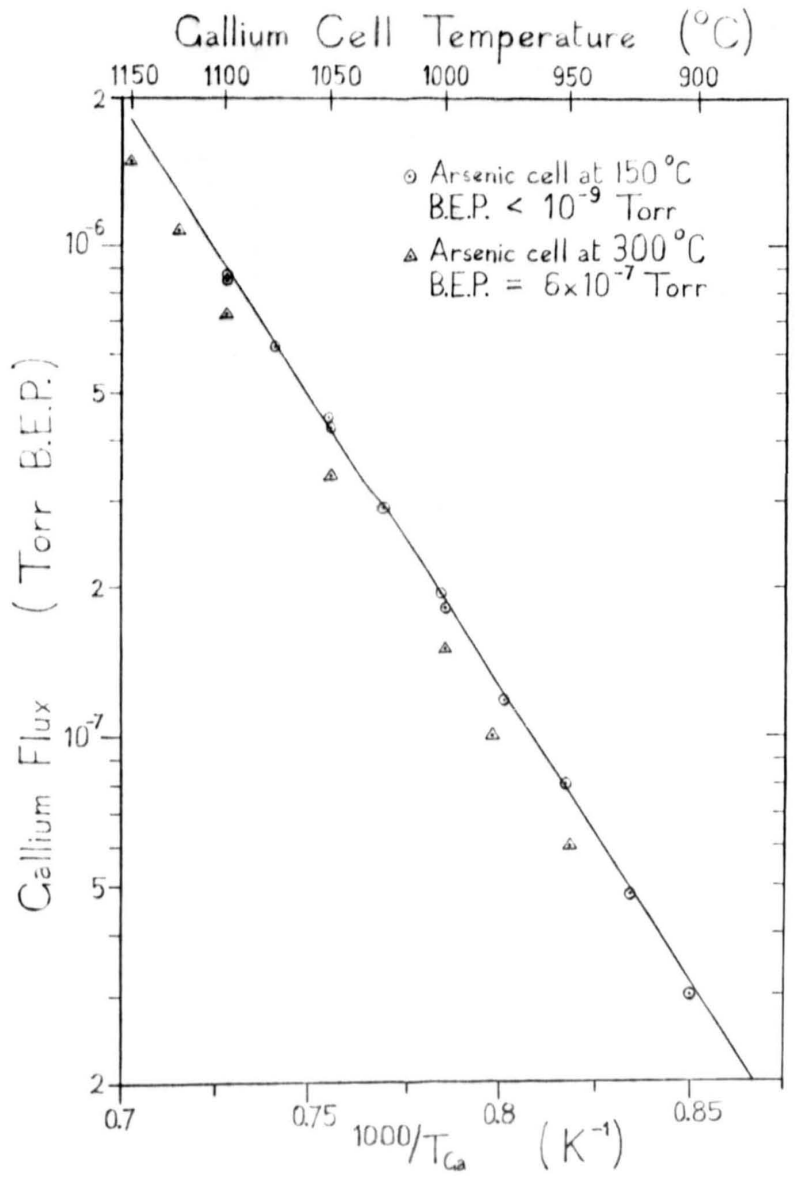

Figure 3.14(a) Variation of gallium flux with cell temperature. Note the reduction in flux apparent when the arsenic cell is heated.

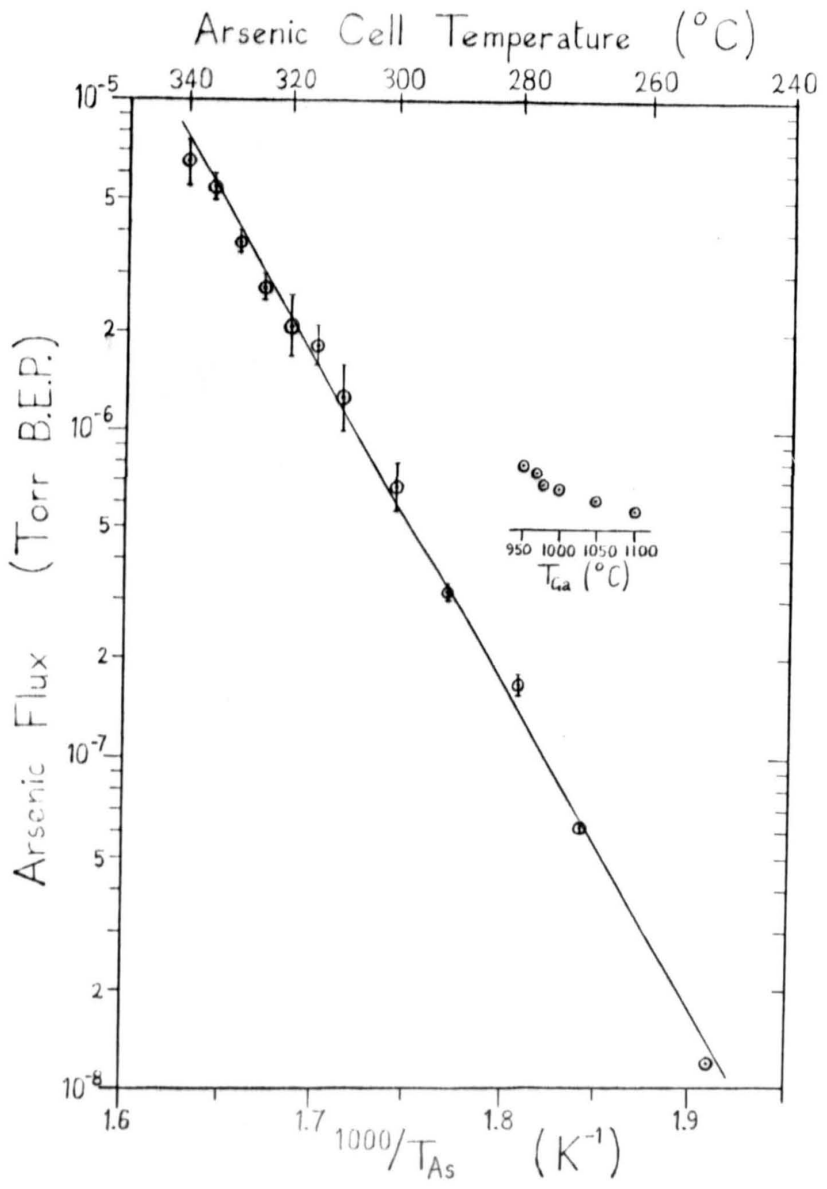

Figure 3.14(b) Variation of arsenic flux with cell temperature. Inset is the variation in flux apparent (at constant T_{As} = 300°C) with changing gallium cell temperature.

the influence of varying residual gas pressure on the flux monitor. The results for the arsenic cell were obtained over an extended period of use of the cell for epilayer growth due to the large time constant, and bars show the variation in flux observed at the various temperatures. Low fluxes were observed when the cell was almost full or empty, the latter is due to reduced As surface area for evaporation and equilibriation of the cell, and the former presumably to obstruction of the cell aperture by the charge itself, again leading to loss of equilibrium conditions near the aperture. The apparent arsenic flux also changes with gallium flux, as shown in the inset to figure 3.14 (b), presumably caused, again, by the varying effect of residual gas pressure on the flux monitor.

Although epilayer thickness was generally measured using a step generated by screening the substrate with a tantalum clip as already described, some effort was expended in using an alkaline potassium ferricyanide etch to reveal epilayer thickness on a cleaved edge of the wafer. The dissolution rate obtained with this etch is dependent on local electrical properties of the gallium arsenide [Menezes & Miller (1983)] and should therefore reveal changes in doping level and conductivity on the edge of a cleaved epilayer. Nomarski micrographs of such a cleaved epilayer are shown in figure 3.15 with the step formed by the tantalum clip clearly visible. Various defects in the substrate, epilayer and interfacial region are apparent in 3.15 (a) and (b) immediately after cleaving. A micrograph of the surface is shown in (e) for comparison. During etching various loose debris have been removed as shown by figure 3.15 (c), which is of the same area as (a), but the only etch induced feature on a well-cleaved section of the layer (d) is manifestly not at the interface. No explanation of this feature, or the similar lines visible in (b), is apparent since the epilayer was grown continuously with uniform doping, apart from a thin, nominally undoped, interfacial buffer layer. The layer thickness cannot be measured directly with the microscope, but comparison with photographs of an etched scale at the same magnification gives the scales shown. Using this scale the epilayer thickness is calculated as 3.0 ± 0.2 μm from the visible step or 1.2 ± 0.2 μm from the etch induced line, although a systematic error of several tenths of a micron due to diffraction effects cannot be ruled out. However the step height was measured as 4.7 ± 0.05 μm

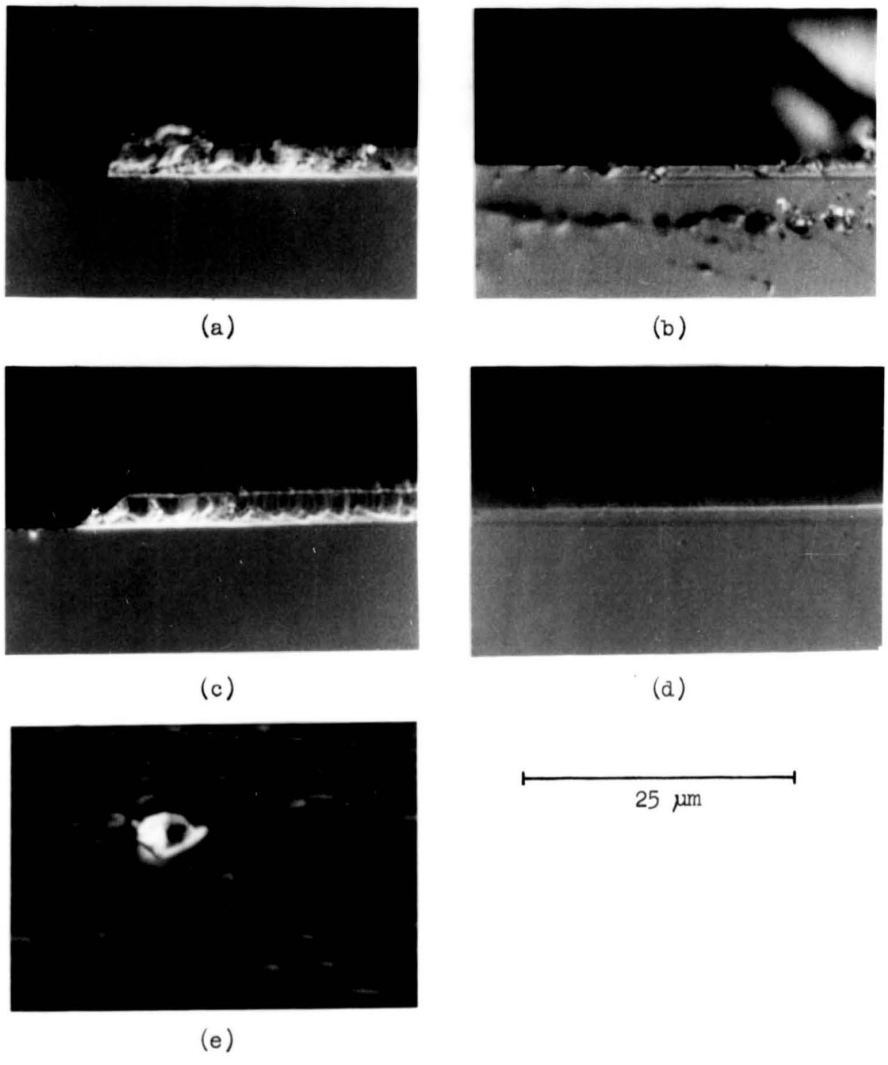

Figure 3.15 Nomarski micrographs of epilayer subjected to alkaline ferricyanide etch.
a&b) Edge of wafer as cleaved.
c&d) Cleaved edge after alkaline ferricyanide etch.
e) Epilayer surface.

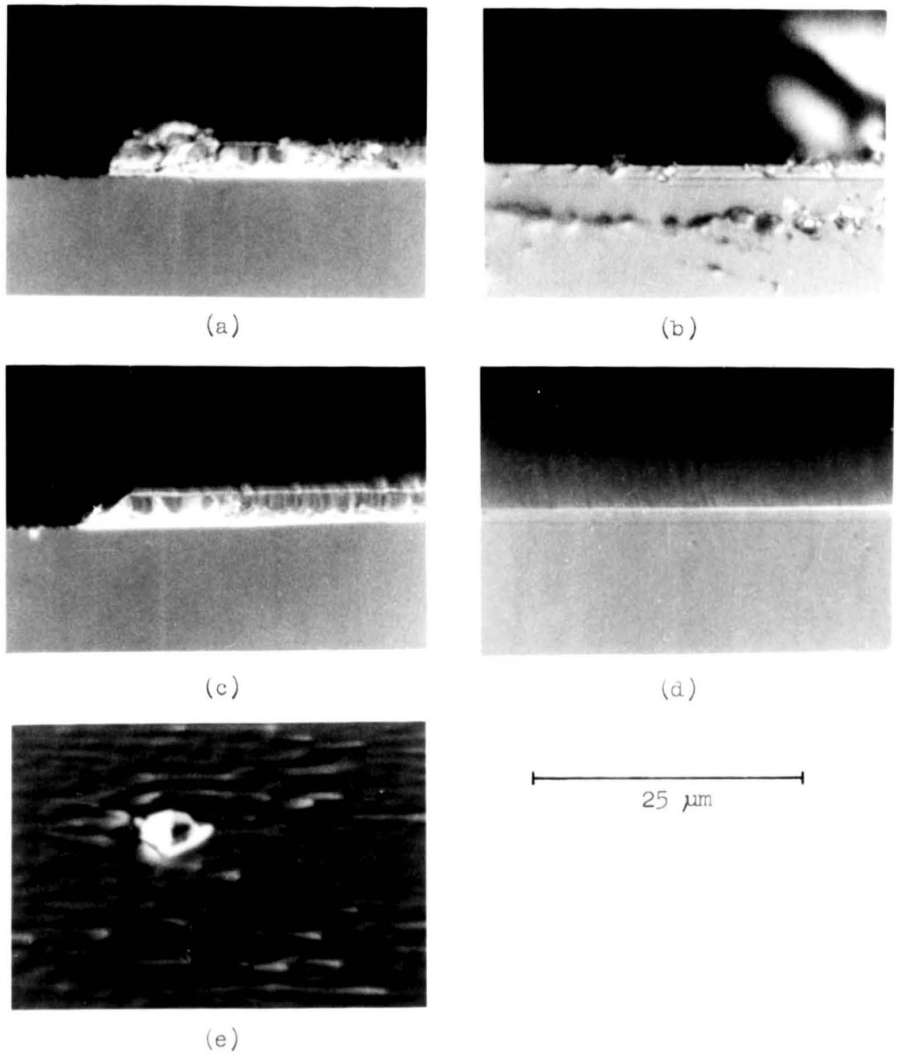

Figure 3.15 Nomarski micrographs of epilayer subjected to alkaline ferricyanide etch.
a&b) Edge of wafer as cleaved.
c&d) Cleaved edge after alkaline ferricyanide etch.
e) Epilayer surface.

with the Tallystep. In view of the problems outlined above it was decided that the technique did not warrant further investigation for use on the relatively thin, uniformly doped epilayers being grown, although it has potential advantages for measuring thick, multilayer structures using a vernier eyepiece in the microscope.

3.5 Electrical Characterisation of n-Type Epilayers

Epilayers were doped n-type with silicon to enable evaluation of layer quality from electrical properties. Silicon was chosen as the dopant because it has been previously used in this laboratory [Grange (1980), Kubiak (1983)] and, for a wide range of growth conditions, exhibits unity sticking coefficient and direct incorporation in the lattice as an n-type dopant [Cho & Arthur (1975), Ploog (1980)]. There are reports in the literature of variable incorporation of silicon due to changes in arsenic flux, growth rate, or substrate temperature, [Parker, Kubiak et al (1981), Chai et al (1981b), Hwang et al (1983b), Akimoto et al (1983)] but there are also complementary reports attributing the same effects to incorporation of other impurities present in the arsenic flux or background residual species [Kubiak (1983), Chai (1980), Heiblum et al (1983a), Nottenberg et al (1984)]. Other n-type dopants in gallium arsenide are Ge, Sn, Pb, S, Se, and Te. Of these Ge and Sn are most frequently used in MBE, but Ge is amphoteric leading to variable compensation ratios dependent on precise growth conditions, and Sn exhibits surface accumulation effects due to limited incorporation in the growing epilayer, and again dependent on substrate temperature. The remaining species have high vapour pressures leading to poor control within the vacuum system and requiring some form of 'captive' source such as PbSe, SnTe, PbTe or T&Te, or the electrochemical cell of Davies et al (1981). Possible p-type dopants are Be, Zn, Cd, Mg, Mn, Ge and C. Be appears to be the simplest to use, with unity sticking coefficient and no problems with surface accumulation, but is highly toxic. Zinc and cadmium both have high vapour pressures and very low sticking coefficients which effectively prevent their use in MBE, although low energy Zn+ ions have been used. Both Mg and Mn have been used in the past but both suffer from limited incorporation in the growing film with Mn producing a relatively deep level and Mg having a low doping efficiency, although unity doping coefficient has recently been achieved by Kirchner et al (1981a, 1981b) following the reduction of oxide contaminants also present. Germanium has also been fairly extensively used but, as already mentioned, it is amphoteric and only incorporates predominantly as an acceptor under a very limited range of growth conditions. Carbon, whilst widely found as a residual impurity, has not proved susceptible to control for use as an intentional acceptor impurity. Ploog (1980) provides a use-

ful, brief review of the various dopants used in gallium arsenide MBE.

Electrical resistivity and Hall coefficient of the grown epilayers were measured at 300 and 77 K using the van der Pauw (1958) technique. Cross shaped samples were used to minimise errors caused by departure from the ideal of point contacts on the periphery. Samples were prepared by cleaving a 5 - 10 mm square from the wafer, masking with two ~2 mm wide strips of Scotch brand adhesive tape to delineate the cross, and then etched in sulphuric acid-peroxide. Electrical contacts were formed by placing freshly cut discs of 1 mm diameter indium wire at each of the four corners, and heating to 250 °C for 30 minutes in air. Alloying of the indium with the gallium arsenide generally served to produce a good ohmic contact, as verified by linear I - V characteristics between pairs of contacts at both 300 and 77 K. On occasion it was necessary to anneal for longer times or remake the contacts to obtain suitably ohmic conduction.

Hall mobility of all measured n-type layers is shown plotted as a function of measured carrier concentration at 300 and 77 K in figure 3.16 (a) and (b) respectively, together with the theoretical curves of Rode (1975) for various levels of compensation, and Poth's (1978) empirical curve for best quality material at 77 K. Recent calculations of electron mobility by Walukiewicz et al (1982) agree to within about ±5% with the more widely quoted results of Rode (1975). Hall measurements were made at a field of 0.5 T (5 KGauss) and errors are estimated to be less than 10%. No corrections have been made for depletion occurring in surface or interface layers [Chandra et al (1979)] or for the non-unity Hall factor [Rode et al (1982)]. It is apparent that most measured values over the carrier concentration range 10^{15} - 10^{19} are clustered around Poth's curve showing that electrical properties of the material are comparable with that grown elsewhere. The highly doped layers show a maximum carrier concentration of 7.6×10^{18} cm^{-3} comparable with that found by other workers for Si doped GaAs and will be discussed fully in section 3.9. Other deviation of points from Poth's curve are generally indicative of specific system problems and will be discussed later in this section.

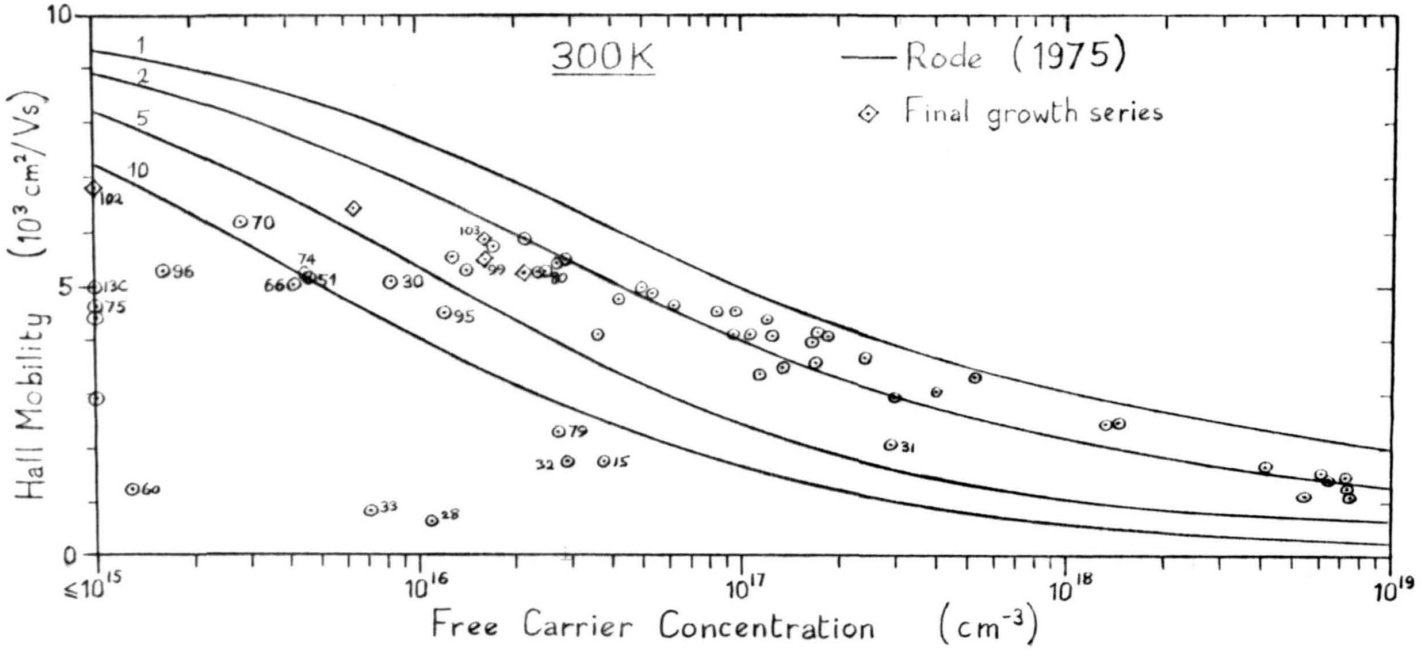

Figure 3.16(a) 300K Hall mobility as a function of free electron concentration for all measured epilayers.

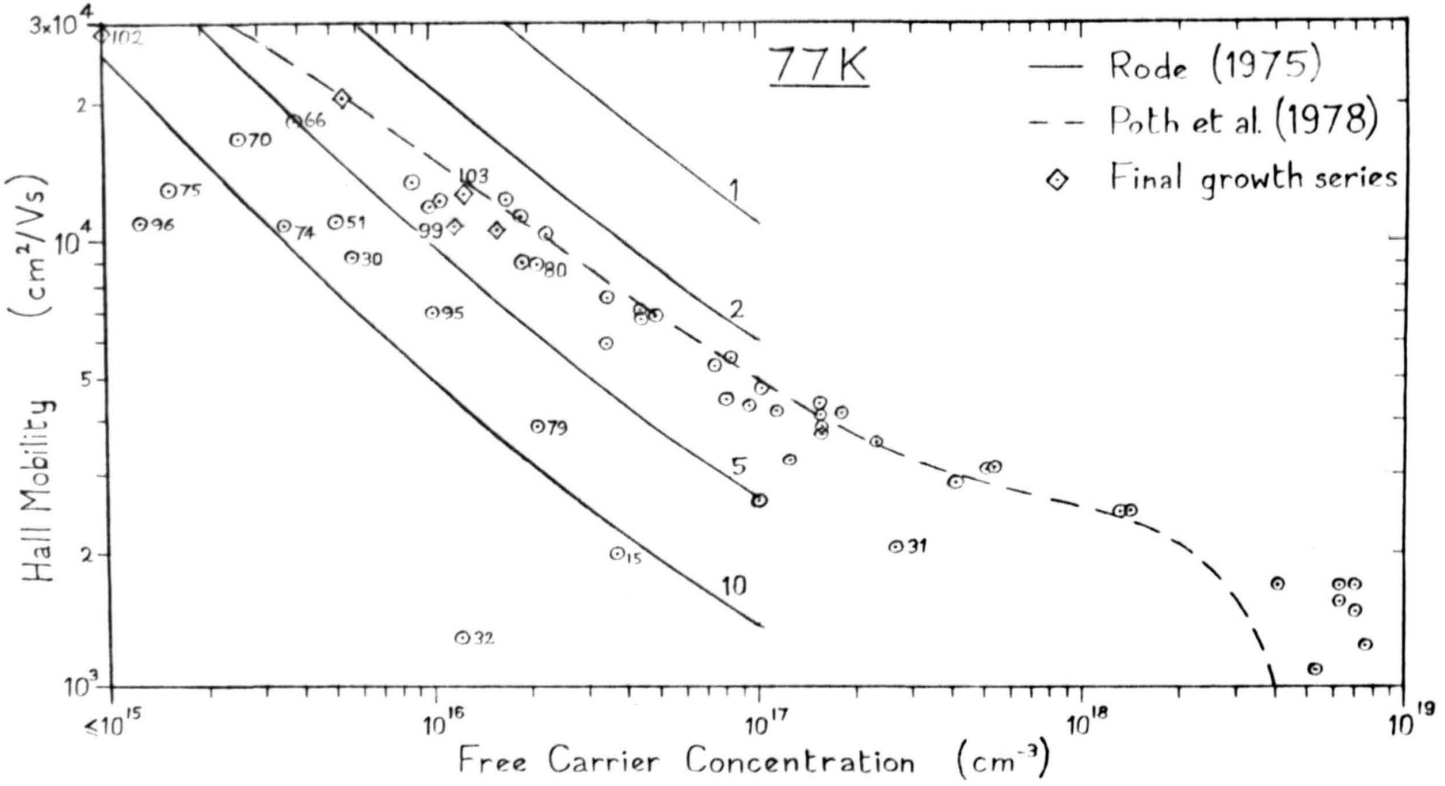

Figure 3.16(b) 77K Hall mobility as a function of free electron concentration for all measured epilayers.

Uniformity of doping across the epilayers was checked by preparing several Hall samples from one epilayer. Results showed a monotonic change ~15% in carrier concentration going across the wafer with a random variation of ~5% between adjacent samples. Repeating measurements on Hall samples after 12 months or more also showed changes of only ~2% in all samples tested, except one on a comparitively thin, low doped sample (0.7 μm, $3.5 \times 10^{16} cm^{-3}$) with a visibly defective surface and these changes can probably be attributed to changes in the surface potential and carrier depletion within the layer. The small variation in electrical properties supports the estimated accuracy of the Hall measurements, whilst the monotonic change in carrier concentration across the wafer indicates that uniformity could be improved by careful alignment of the source cells if this were found to be necessary.

Electrochemical CV profiles of the epilayers usually showed doping to be uniform to within 10% when the source cell temperature controllers were working correctly but larger variations near the commencement of growth were sometimes observed and will be discussed in section 3.7.

As already mentioned departure of measured mobility from the Poth curve was generally indicative of system problems and will be briefly considered in chronological order together with the remedial action taken.

Epilayer 15 was the first silicon doped epilayer grown in the system and low mobility is probably due to contaminants still present in the sources. Subsequent epilayers show much improved properties although no deliberate changes were made in growth parameters.

Epilayers 31 - 34 were all very low mobility or semi-insulating due to cracking of the silicon dopant cell after attempting to outgas at 1300 °C. Replacing the cell was necessary to cure the problem. However, electrical properties of epilayers with intended doping levels of $\sim 10^{16} cm^{-3}$ remained eratic and several layers at $\sim 10^{17} cm^{-3}$ were grown whilst investigating various other aspects of the system.

With continued use of the system it became apparent that the pressurised liquid nitrogen supply for the cropanels was not being adequately controlled, allowing the temperature of the cryopanels, and the main chamber near the nitrogen vent, to alter slightly

with nitrogen flow. Changes in the temperature of the cryopanels should be avoided since they will give rise to pressure bursts as previously adsorbed species are liberated by a slight rise in temperature. This is most apparent with the CO residual pressure since the equilibrium vapour pressure is large ($\frac{1}{2}$ atm) at liquid nitrogen temperature and changes rapidly with temperature. Use of a larger flow of liquid nitrogen through the cryopanels with the surplus directed to a suitable container enabled reliable growth of epilayers with mobilities close to the Poth curve at carrier concentrations of $10^{16}cm^{-3}$ and below. The effect of accidental warming of the cryopanels during epilayer growth was most dramatically demonstrated by epilayers 79 and 80. These layers were grown under similar conditions except that the rubber bung blew out of the pressurised liquid nitrogen container during growth of epilayer 79, allowing the cryopanels to warm for several minutes and background pressure of CO and other residual species to rise by a factor of ten or more as shown in figure 3.17 before liquid nitrogen flow was re-established. As can be seen the mobility of epilayer 79 is slightly less than half that obtained when the cryopanels were maintained at liquid nitrogen temperature throughout the growth.

Another cause of increased partial pressures of residual impurities arose from the need to switch off the rotary backing pump to prevent sample vibration in the SIMS chamber during dynamic SIMS analyses. This produced increased pressures in the backing volume and could lead to some backstreaming past the diffusion pump, although the indicated backing pressure was kept below 10^{-1}Torr. Such backstreaming was not immediately apparent due to the high background of arsenic usually present in the chamber, but was discovered as an unstable residual pressure 3×10^{-9}Torr when the arsenic pressure was low. The major component of this background was hydrogen, which has been reported to improve epilayer properties by Calawa (1978); however it is possible that another, relatively minor, component may have the most significant effects on the epilayer properties.

Background pressure of CO and other contaminants was monitored during growth of all the later epilayers in this project but insufficient results were obtained to be able to correlate electrical

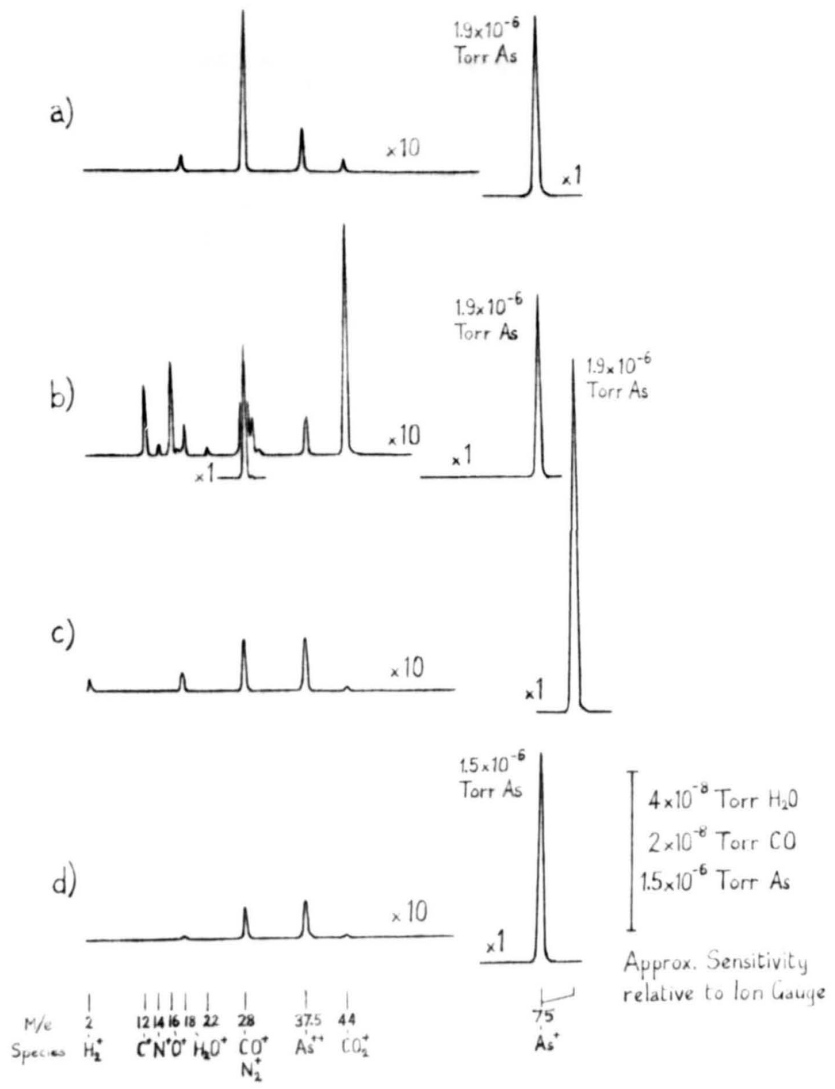

Figure 3.17 Residual gas spectra during epilayer growth.

a) Epilayer 79, also typical of epilayer 80 and other epilayers grown at this time.

b) Epilayer 79, immediately after reconnection of LN_2 supply to cryopanels.

c) Epilayer 103, typical of epilayers grown after overnight pumping of the system.

d) Epilayer 91, grown after extended pumping during SIMS analyses.

Note the change in As^+ sensitivity apparent in (c), which is not fully reflected in the As^{++} signal.

properties of the epilayers with small changes in measured partial pressures of background species possibly affected by varying sensitivity of the residual gas analyser. The final three epilayers were grown with additional cryopanelling and show lower p-type backgrounds than other epilayers but with no definite change in residual gas species monitored during growth. However, larger effects would be expected in the growth region than occur at the mass spectrometer, due to the position of cryopanels and other baffles within the chamber.

Epilayers 74 and 75 were grown with the arsenic cell almost exhausted and operating at higher than usual temperatures to maintain the necessary arsenic flux. It is likely that this has resulted in additional impurities in the arsenic beam, leading to higher compensation ratios and lower mobilities than normally obtained.

Epilayers 95 and 96 were grown on substrates which had been heat cleaned and then left in the vacuum system whilst the cryopanels warmed up and the desorbing species pumped away by the diffusion pump, in the attempt to minimise residual system impurity pressures during growth. However both layers were highly defective, probably due to adsorption of contaminants on the substrate surface after the initial heat cleaning, and show lower free carrier concentrations and mobilities than would be expected. This result, together with the photoluminescence results presented later is indicative of compensating electrical defects being associated with the visible crystallographic defects, and that they also scatter the free carriers.

Unintentional impurity incorporation in the final series of epilayers grown in this study was minimised by loading a substrate on one evening, and leaving the vacuum system overnight to pump out species both introduced during the loading operation and previously adsorbed on the cryopanels. 5 μm thick epilayers were then grown at a rate of 1 μm/hr, and 77 K mobilities of 20,000 cm^2/Vs at 6 x $10^{15} cm^{-3}$ and 29,000 cm^2/Vs at 8 x $10^{14} cm^{-3}$ were obtained in n-type, silicon doped, layers. This is the best material grown to date in this laboratory.

The silicon dopant flux from the source cell can be calculated from equation 3.4 and the vapour pressure data of Honig & Kramer (1969)

assuming an ideal Knudsen source, and is plotted logarithmically in figure 3.18 as a function of reciprocal cell temperature, together with that calculated from measured carrier concentration of epilayers assuming unity sticking coefficient and no compensation. The points plotted are for the better epilayers with low compensation ratios, highly compensated layers give lower apparent fluxes. The measurement of higher silicon fluxes than theoretically predicted is probably due to poor thermal contact between the silicon source cell and its thermocouple, producing higher source temperatures than indicated. However, other tabulations of silicon vapour pressure [Kaye & Laby (1975), Perry (1963)] give pressures higher than Honig and Kramer (1969) by ~30 times at pressures of several Torr, but do not extend to the much lower pressures and temperatures used in this source cell. Extrapolation from these higher temperature results is not straightforward and has not been attempted due to lack of data on latent heat of vapourisation and inclusion of the melting point within the necessary extrapolation range. The discrepancy in slope of the theoretical and experimental lines is partially due to non-linearity of the chromel-alumel thermocouple over the full range 0 - 1200 °C. The linear amplifier, when set correctly at 1000 °C, will be reading 20 °C low at 1200 °C. The progressive increase in flux, at a specific temperature, observed during the project is probably due to progressive deterioration of the thermocouple at the high outgassing temperatures, just below those found to cause rapid failure.

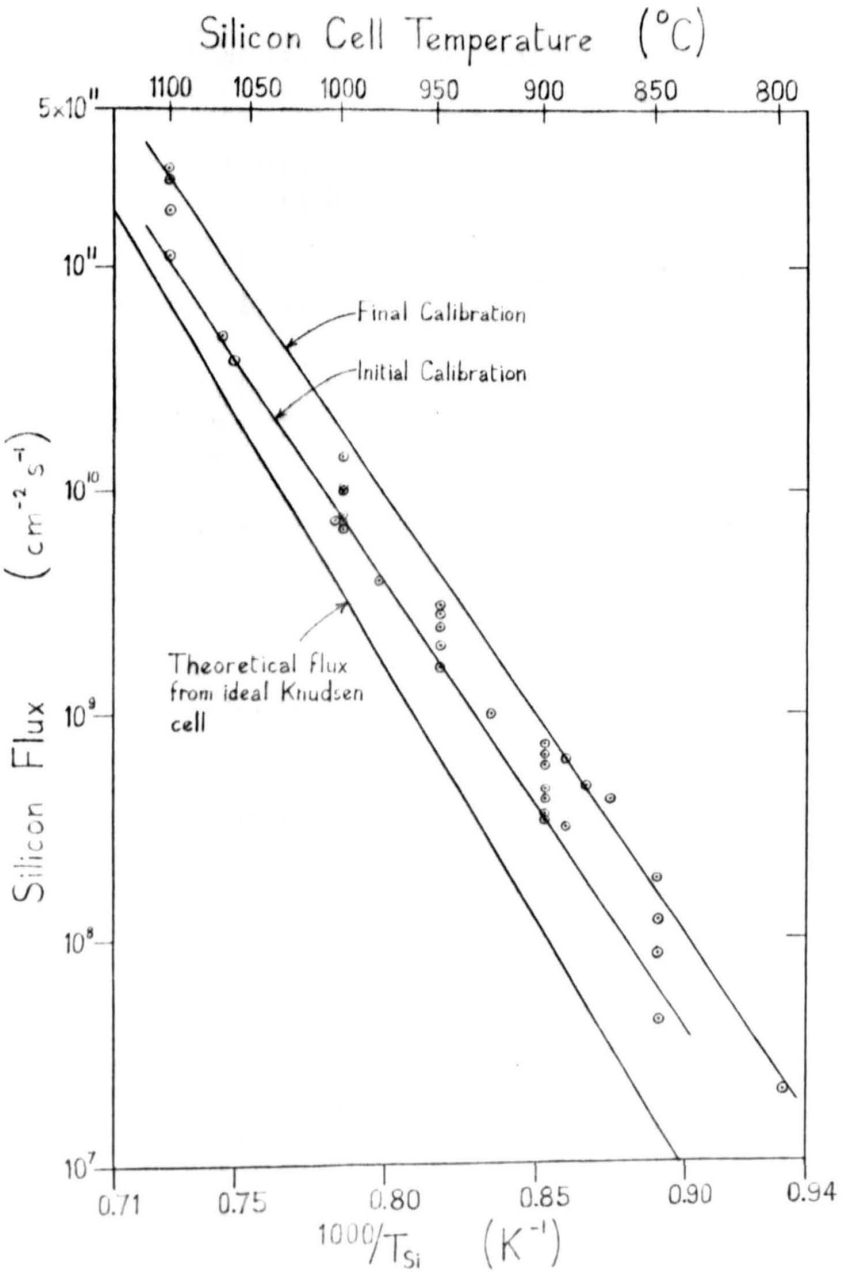

Figure 3.18 Calibration of silicon flux with source cell temperature.

3.6 P-Type and Semi-Insulating Epilayers

As already mentioned the unintentionally doped epilayers finally grown in this system were p-type with carbon as the major impurity. However, at earlier stages in the development of the system, nominally undoped and low silicon doped epilayers showed variable electrical properties, different epilayers being either n-type, p-type or semi-insulating with a resistance > 10^7 ohms/square. Properties of these epilayers are tabulated in Table 3.2 together with the expected Si concentration in low doped layers, and Hall mobility of p-type epilayers is plotted as a function of carrier concentration in figure 3.19. Theoretical calculation of hole mobilities in gallium arsenide is much less advanced than that for electrons, due to the additional complications presented by non-parabolic bands and the existence of both light and heavy holes. The semi-empirical calculation of Wiley (1975), incorporating Brooks-Herring screening, and the empirical fit of Hilsum (1974) are shown for comparison with room temperature data, and the recent empirical fit of Ilegems (1984) using Hilsum's formula shown with the 77 K results.

The variable net doping levels and high compensation ratios apparent in the early epilayers show that there were uncontrolled impurity levels $\sim 10^{16}$ cm^{-3} or greater present in these early epilayers. Before considering particular epilayers it is worth noting that silicon and other common donor impurities in gallium arsenide produce donor states with ionisation energies ~6 meV, which is comparable with the thermal energy kT = 6.6 meV at 77 K, thus giving essentially full ionisation in an uncompensated material. Common acceptors, however, have larger ionisation energies eg carbon ~20 meV and manganese ~100 eV [see references in section 3.9] which will not be fully ionised at 77 K, leading to partial 'freeze-out' of the carriers; deeper trap levels will have a greater influence on the net carrier concentration as the sample is cooled.

The nominally undoped epilayer 23 has the highest 300 K hole concentration of 2 x 10^{17} cm^{-3} attained in this project, and mobility of 250 cm^2/Vs is consistent with a low degree of compensation. However the complete freeze-out of carriers on cooling to 77 K indicates that these carriers are associated with relatively deep acceptor levels. Manganese is such an impurity commonly found in MBE systems

Table 3.2 Electrical properties of p-type and semi-insulating epilayers.

Epilayer Number	Si conc. (cm^{-3})	Carrier type	n_{300} (cm^{-3})	μ_{300} (cm^2/Vs)	n_{77} (cm^{-3})	μ_{77} (cm^2/Vs)
13C	undoped	n	$4x10^{11}$	5000	SI	
23	undoped	p	$1.2x10^{17}$	250	SI	
28	10^{16}	n	$\sim 10^{16}$	$\sim$600	SI	
29	$2x10^{15}$	p	$1x10^{15}$	365	$6x10^{14}$	1060
33	10^{16}	n	$7x10^{15}$	800	SI	
34	10^{16}	SI				
36	10^{16}	n	$6x10^{14}$	3000	SI	
37	10^{16}	SI				
38	10^{16}	n	$\sim 10^{14}$	$\sim$1000	SI	
39	10^{16}	SI				
59	$5x10^{15}$	p	$1.5x10^{14}$	300	SI	
60	$5x10^{15}$	n	$1.3x10^{16}$	1200	SI	
81	$5x10^{14}$	n	$3x10^{14}$	4600	SI	
82	$5x10^{12}$	SI				
83	$5x10^{13}$	p	$7x10^{14}$	445	$7x10^{13}$	3400
100	undoped	p	$1x10^{15}$	430	$6x10^{14}$	8000
101	10^{15}	p	$1.1x10^{15}$	407	$1.7x10^{15}$	3500
102	10^{15}	n	$7.2x10^{14}$	7000	$7.7x10^{14}$	29000
104	undoped	p	$6.0x10^{14}$	430	$2.7x10^{14}$	6700

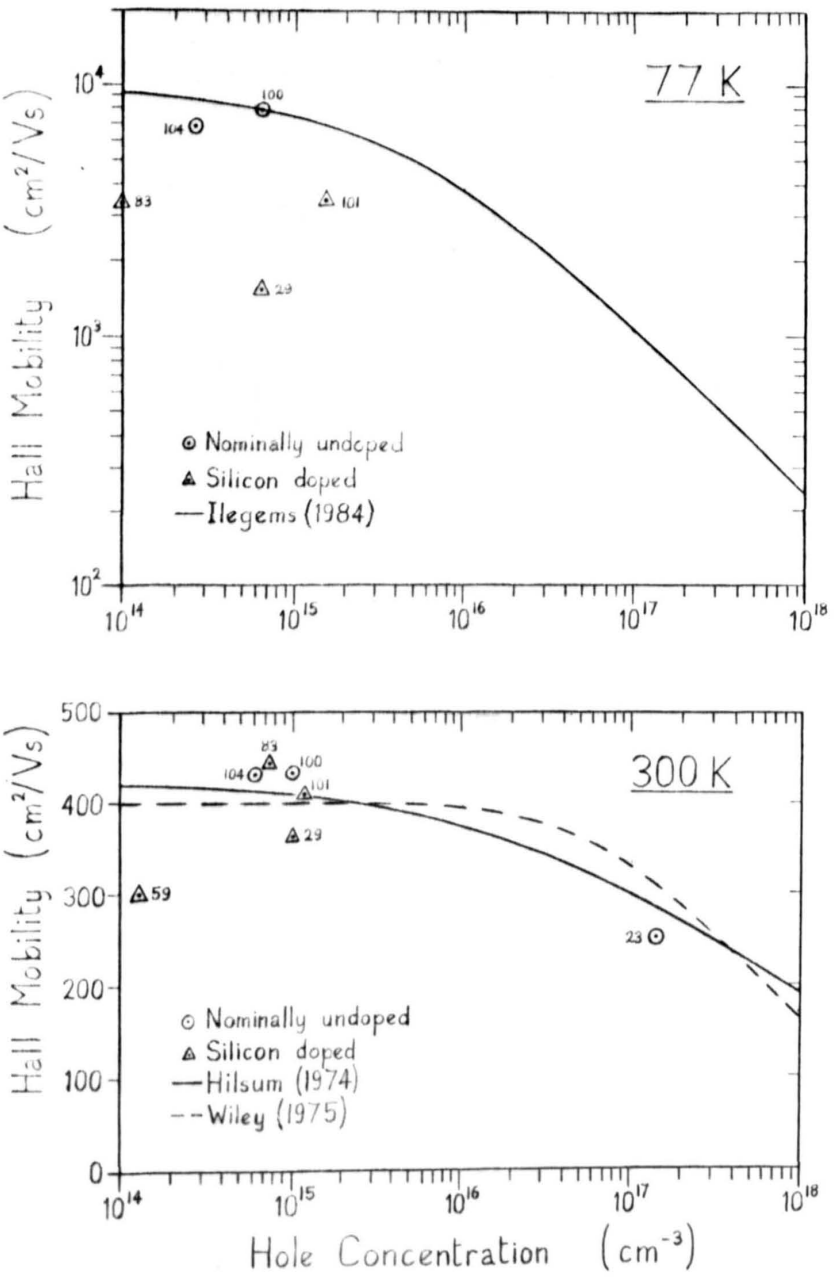

Figure 3.19 Hall mobility as a function of free hole concentration for all measured epilayers at 300 and 77K.

[Grange (1980), Koschel (1981), Covington & Meeks (1979), Cho & Arthur (1975)] and caused by unintentional hot stainless steel components. Surface conversion of heated gallium arsenide substrates has also been attributed to out-diffusion of manganese [Klein et al (1980), Palmateer et al (1983), Heiblum et al (1983a)]. However, the high doping level apparent on this layer only seems to rule out surface conversion as the sole dopant source, whilst the absence of similar doping in other epilayers and simultaneous growth of an $10^{16}cm^{-3}$ n-type epilayer on an n+ substrate (see section 3.7) appears to rule out system generated impurities. Unintentional surface contamination seems to be the most likely explanation.

Epilayers 28 - 60 show variable residual impurities $\sim 10^{16}cm^{-3}$ and it is not until growth of epilayers 81 - 83, when more attention was paid to ensuring efficacy of the cryopanelling, that a residual acceptor level $\sim 10^{15}cm^{-3}$ is achieved, although the large freeze-out still apparent indicates a high proportion of deep traps. Only in the final epilayers, when residual species in the MBE system had been minimised by allowing the system to pump out overnight after loading each substrate through the load lock, are acceptor concentrations $\sim 10^{15}cm^{-3}$ achieved, together with lower concentrations of trapping levels as indicated by the small degree of freeze-out and high 77 K hole mobilities. The increased p-type doping evidenced by layer 101, grown with a low level of intentional silicon doping, suggests that additional unintentional impurities are generated by the hot silicon source cell. But these impurities can be reduced by additional cryopanelling, as shown by epilayer 102, (parameters included in Table 3.2) which is n-type although grown with the same intentional level of silicon doping. Results from epilayer 104 are ambiguous since it exhibits a lower carrier concentration, but also a lower mobility indicating a larger total ionised impurity concentration. However this will also be influenced by the arsenic cell being nearly exhausted and operating at a higher temperature than usual to maintain the necessary arsenic flux, which could lead to additional impurities in the beam.

It is interesting to note that layer 13C is the only nominally undoped layer to show net n-type conduction, and is also the only layer with measurable conductivity grown prior to fitting the silicon dopant source and ion gauge flux monitor, suggesting that the later

p-type background may be associated with these components.

A further point, which may be of relevance, is that the reduction in background impurity levels noted above occurred after the batch of bromine methanol etched wafers had been completely used, suggesting that the high level of residual impurities in the epilayer may have been associated with out-diffusion of impurities from these wafers. However, not all epilayers grown on these wafers suffered from high levels of background impurities.

In addition to acceptor impurities already mentioned several deep trapping levels have been observed in gallium arsenide but there is not an agreed assignment of these levels to specific defects or impurities. See eg Martin et al (1977); Mitonneau et al (1977); Hasegawa & Majerfeld (1975), (1976); Lum et al (1977), (1978); Lang et al (1976), (1977); Ploog (1980); Masterov & Samorukov (1978); Stall et al (1980); Spicer et al (1980); Beyer et al (1982). Even the effect of simple vacancies is not clear, although theoretical work of Daw & Smith (1980) suggests that both electron and hole traps are associated with simple gallium and arsenic vacancies. Oxygen is, however, known to produce deep traps which has been exploited to grow semi-insulating material [Casey et al (1979)], and also blamed as the major impurity responsible for carrier freeze-out on cooling to 77 K [Morkoç & Cho (1979)]. The oxygen is incorporated from residual water vapour in the vacuum system which must be reduced by extensive cryopanelling [Morkoç & Cho (1979)] to obtain high purity epilayers. Prior et al (1984) have studied the thermodynamics of oxygen incorporation in gallium arsenide from residual gas species present during MBE growth and conclude that oxygen incorporation from H_2O and CO_2 is likely but that CO - generally present at higher partial pressures - is not a significant source.

The exact source and method of incorporation of the carbon acceptor impurity is also problematical, partly because of the many carbon containing species present in the residual gas of a typical MBE system. Deliberately increasing the residual gas pressure is well known as a cause of increased residual impurities in the grown epilayer and Stringfellow et al (1981) have specifically shown this to lead to increased carbon acceptor concentration. It has been generally considered that any carbon containing residual species may give rise to carbon acceptors in the epilayer, with specific

reference to CO since this is generally by far the highest pressure residual species, although it is possible that a relatively minor component may be more significant due to, eg a higher sticking coefficient on the growing surface. Deliberate introduction of CO and CH_4 into an MBE system during epilayer growth has not, however, produced significantly increased carbon acceptor concentration [Ilegems & Dingle (1975)]. The theoretical work of Prior et al (1984) also indicates that carbon incorporation from CO and CO_2 is unlikely. On the other hand Ploog (1980) has reported that a high temperature reaction, between a carbon source cell and alumina heater supports, produces highly reactive carbon containing species, which can incorporate in the growing gallium arsenide film giving carbon acceptor concentrations of up to $8 \times 10^{17} cm^{-3}$. Finally, the results of Nottenburg et al (1984), and Heiblum et al (1983a) both show that changing the As_4 flux during growth changes the incorporation of carbon acceptors in the layer, but the two investigations show differing effects, and Künzel et al (1980b) found that incorporation of carbon acceptor impurities increased rapidly as substrate temperature fell below 550 °C.

In summary, the properties of these unintentionally doped p-type and semi-insulating layers show significant reduction in unintentional impurity incorporation with improvement in vacuum conditions, consistent with a reduction in oxygen incorporation from the residual gas. Other impurities are undoubtedly present in the layers (in addition to the major carbon and minor manganese and copper acceptors found by photoluminescence measurements described in section 3.9) but extensive further investigation would be necessary to positively identify all sources of such impurities. However, there are indications that the p-type carbon contamination is associated with the high temperature source cells, and their replacement with pyrolitic boron nitride should be considered for future improvement of the MBE system.

3.7 Electrochemical CV Profiles

Various epilayers were profiled using a Polaron plotter to check uniformity of doping throughout the thickness of the epilayers. The later epilayers showed even doping profiles with a decrease of approximately 20% from surface to interface as shown in figure 3.20 (a). It is difficult, from this measurement alone, to know whether this decrease is real or an artefact due to increased series resistance in the measuring circuit as the epilayer thickness is reduced. Since the temperature coefficient of the silicon flux is ~5% per °C such a change could be due to a rise in room temperature of 5 °C during the 5 hour growth period, assuming no effects other than the absence of cold junction compensation on the temperature controllers. Epilayers 45 and 47 showed increases of similar magnitude in carrier concentration across thinner layers, grown at approximately half the rate. But this could also be explained by the decreasing growth rate observed at this stage of the project. Epilayer 43, whilst still showing a small increase towards the surface, has a much larger increase in carrier concentration near the start of the doped region, although a 2 μm thick nominally undoped layer had already been grown, and the reason for this is not known. Similar, and perhaps even better, uniformity of doping is observed in appropriate sections of epilayers 72 and 71A shown in figure 3.21 and epilayer 88 shown in figure 3.23.

Epilayers 71 and 72 were grown with the sandwich structure shown in figure 3.21 in an attempt to measure the abruptness of doping changes possible with the system. Epilayer 71 was grown without interruption, merely resetting the silicon cell and monitoring the indicated temperature, which took ~2½ minutes to stabilise at the new value, whilst growth of epilayer 72 was interrupted for 15 minutes at each change in doping level to ensure that the silicon cell temperature was fully stabilised before recommencing growth. However, little difference is apparent between the near surface regions of the two epilayers in the CV profiles, partly because the Debye length in the low doped material (800 A at $3 \times 10^{15} cm^{-3}$) is larger than the thickness grown during stabilisation of the silicon cell temperature (400 A), but this does show that there is no great lag between the silicon flux and the indicated cell temperature. Less sharp changes in carrier concentration in

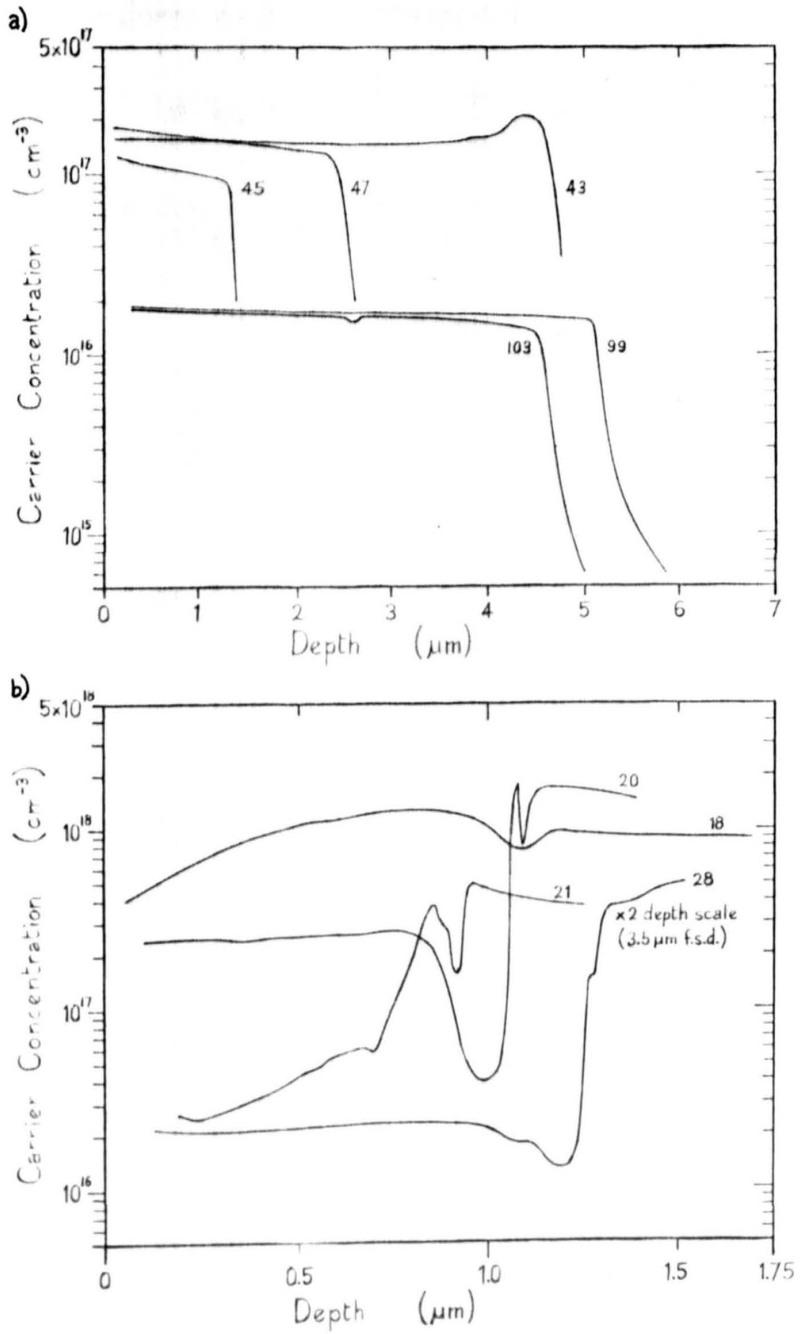

Figure 3.20 Electrochemical C-V profiles of epilayers.
a) Later epilayers on semi-insulating substrates.
b) Early epilayers on n^+ substrates.

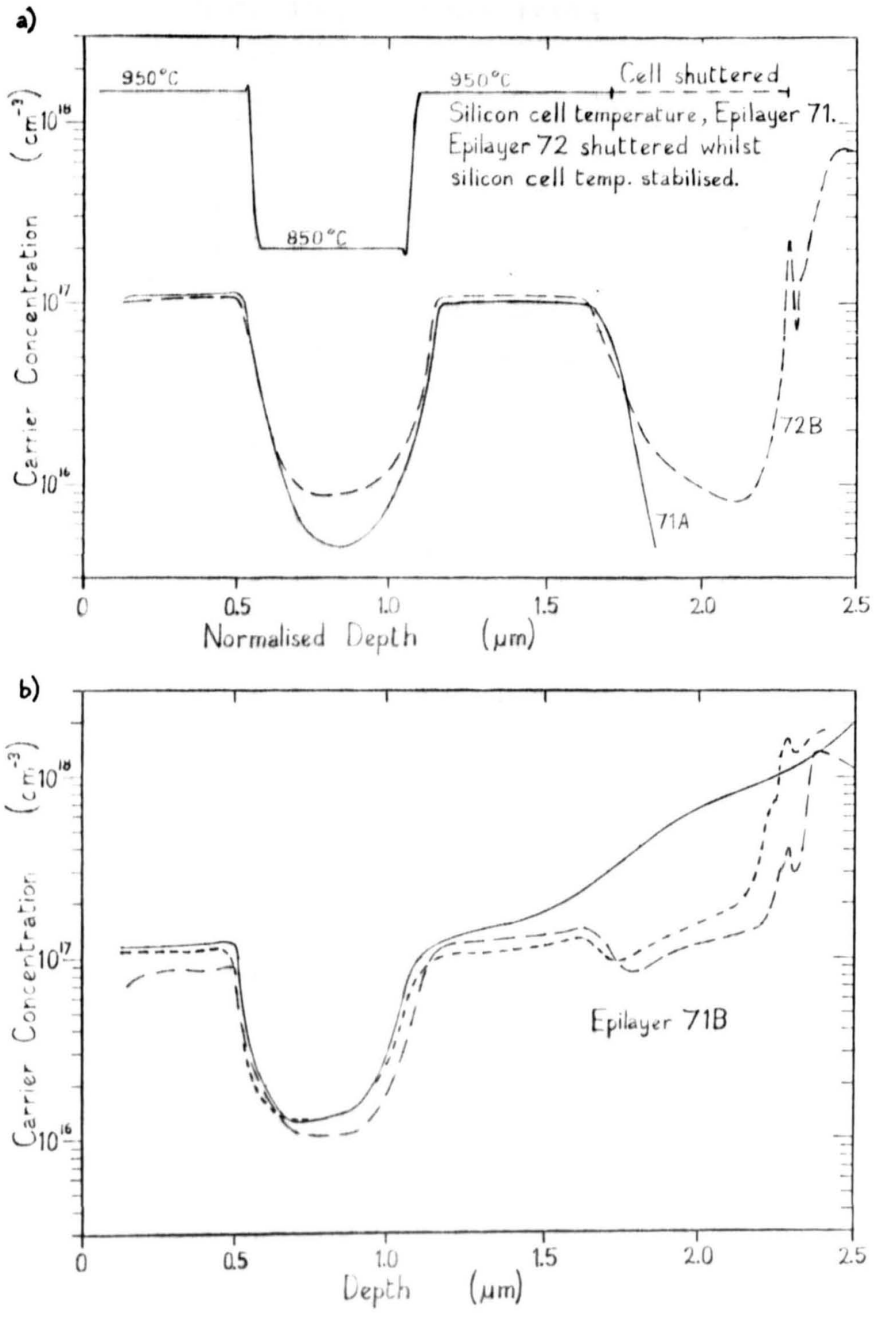

Figure 3.21 Electrochemical C-V profiles of 'sandwich-doped' epilayers.

a) Different epilayers together with temperature profile of dopant cell during epilayer growth.

b) Epilayer 71B with variable highly-doped region near the substrate.

the deeper regions are probably due to roughening of the crater base and the influence of the crater edges on the CV measurements. SIMS profiles of the epilayers have been requested, since direct measurement of the silicon profile is obviously required in order to obtain further information on the abruptness of the doping change, but are not available at the time of writing.

CV measurements on epilayer 71B, grown simultaneously with 71A, show marked differences between profiles in the second half of the epilayer. A partial explanation for this could be that the silicon dopant cell was incompletely shuttered during growth of the nominally undoped layer, but this does not explain the differences apparent in the inner, high-doped layer. A second explanation could be diffusion of impurities originally present on the substrate into the first micron of the epilayer. The 'spike' at the substrate interface indicates the presence of localised contamination. A similar effect was found with the nominally undoped epilayer 23. Hall measurements obtained from the portion grown on an insulating substrate showed the layer to be p-type at $2 \times 10^{17} cm^{-3}$, whilst the CV profile of the portion grown on an n+ substrate shows the layer to be n-type with carrier concentration varying over the range $2 \times 10^{15} - 2 \times 10^{16} cm^{-3}$. The simplest explanation is that mobile impurities were originally present on one of the substrates and have been incorporated into the growing epilayer in addition to the system-generated impurities. Surface conversion of the substrate is possible [Klein et al (1980), Palmateer et al (1983), Heiblum et al (1983a)] but subsequent incorporation in the epilayer at the doping level and thickness observed seem unlikely, especially in view of the absence of any other comparable effects with other epilayers grown in this system. Use of an alternative profiling method on both samples would be useful in elucidating the cause of these effects.

Epilayers grown early in the project, without temperature feedback used to control the silicon cell, could show much greater variations in doping level as is apparent in figure 3.20 (b). These epilayers were all intended to be uniformly doped, with a thin buffer layer, and grown on different portions of the same n+ substrate, enabling profiling to be continued through the interface into the substrate. Many plots show a 'spike' or other discontinuity at the interface, presumably indicative of residual contamination, and the

poor quality of the nominally undoped buffer layers can be partially explained by variable background ionised impurity levels $\sim 10^{16}\ cm^{-3}$ found in low doped layers at this stage. However, it is also difficult to know how reliable the CV profiles were at this early stage in the use of the Polaron plotter. Three profiles obtained from adjacent spots on each of two epilayers, grown with temperature feedback applied to the dopant cell, are shown in figure 3.22. It is extremely unlikely that these are all real differences between different parts of the epilayer. Furthermore, since all n+ substrates were different portions cleaved from the same original wafer, the polaron plots should give the same doping level for all n+ substrates but this is manifestly not the case. Some of the differences could, however, be caused by small regions with variable concentrations of electrically active contaminants remaining after substrate cleaning.

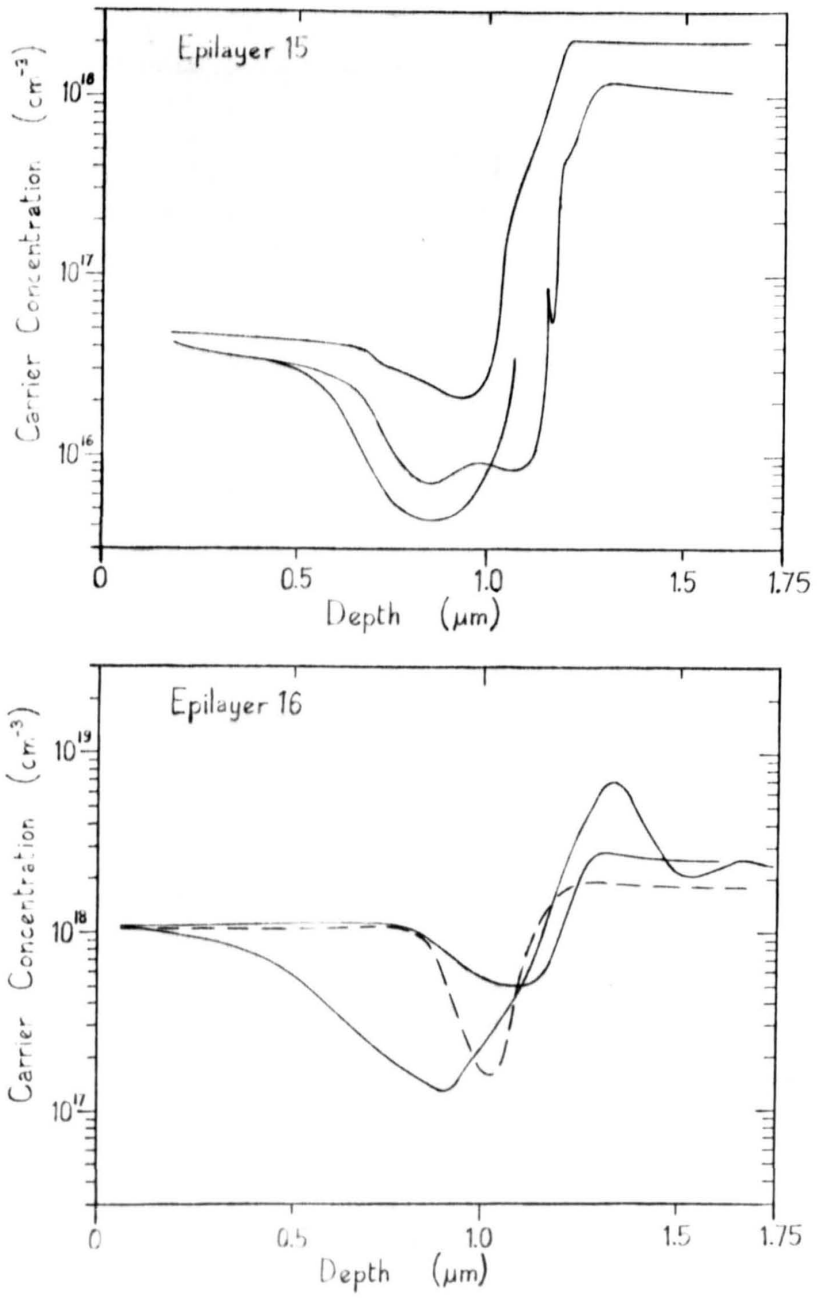

Figure 3.22 Electrochemical C-V profiles from adjacent points on single epilayers, grown with temperature feedback control to dopant cell.

3.8 Heavily Si Doped Epilayers

The Hall mobilities of heavily Si doped epilayers already shown in figure 3.16 are replotted in figure 3.23 (a) as a function of the Si impurity concentration, calculated from the incident Si flux. Figure 3.23 (b) shows the dependence of carrier concentration, measured using the Hall effect, on the silicon impurity concentration at a growth rate of ~1 μm/hr and substrate temperature ~550 °C. Data for epilayer 76 is omitted from these plots since it was the first epilayer grown after baking the system, and its low mobility shows the presence of significant additional impurities. These results are similar to those of Neave et al (1983b), Chai et al (1981b) and Akimoto et al (1983) showing a maximum carrier concentration ~7 x 10^{18} cm^{-3} with increasing compensation at higher impurity levels, although Heiblum et al (1983b) report that higher carrier concentrations are obtained at lower growth rates. The effect is confirmed in the profile of a step doped layer also shown in figure 3.23 (b) and (c) and grown at 0.7 μm/hr, but the carrier concentrations indicated during CV profiling are believed to be low because of the poor Schottky barrier formed with the highly doped material. It may be noted that the CV profile of epilayer 18 (figure 3.20) shows a carrier concentration ~1 x 10^{18} cm^{-3} compared with the Hall measurement of 4.1 x 10^{18} cm^{-3}.

The precise form of silicon incorporation in gallium arsenide at these high concentrations is not known. Chai et al (1981b) rule out autocompensating Si pairs because of the abrupt change in carrier concentration at higher doping levels, concluding that there is precipitation of a second phase, which is supported by their observed degradation of surface morphology at silicon concentrations above ~10^{19} cm^{-3}. Heiblum et al (1983b) - who did achieve a more gradual change in layer properties at higher silicon concentrations - produce photoluminescence evidence for Si pairs together with Si precipitates at these high concentrations. However Neave et al (1983b) have used TEM to examine highly doped films and have not found evidence of significant precipitation. They suggest that simple autocompensation occurs, with silicon incorporated as independent donors and acceptors, on Ga and As sites respectively, in the lattice.

No degradation of surface morphology was found in this investigation for silicon concentrations of up to 1.5 x 10^{19} cm^{-3}, as shown in figure 3.24 but the most highly doped portion of the step-doped

3.8 Heavily Si Doped Epilayers

The Hall mobilities of heavily Si doped epilayers already shown in figure 3.16 are replotted in figure 3.23 (a) as a function of the Si impurity concentration, calculated from the incident Si flux. Figure 3.23 (b) shows the dependence of carrier concentration, measured using the Hall effect, on the silicon impurity concentration at a growth rate of ~1 μm/hr and substrate temperature ~550 °C. Data for epilayer 76 is omitted from these plots since it was the first epilayer grown after baking the system, and its low mobility shows the presence of significant additional impurities. These results are similar to those of Neave et al (1983b), Chai et al (1981b) and Akimoto et al (1983) showing a maximum carrier concentration ~7 x 10^{18} cm^{-3} with increasing compensation at higher impurity levels, although Heiblum et al (1983b) report that higher carrier concentrations are obtained at lower growth rates. The effect is confirmed in the profile of a step doped layer also shown in figure 3.23 (b) and (c) and grown at 0.7 μm/hr, but the carrier concentrations indicated during CV profiling are believed to be low because of the poor Schottky barrier formed with the highly doped material. It may be noted that the CV profile of epilayer 18 (figure 3.20) shows a carrier concentration ~1 x 10^{18} cm^{-3} compared with the Hall measurement of 4.1 x 10^{18} cm^{-3}.

The precise form of silicon incorporation in gallium arsenide at these high concentrations is not known. Chai et al (1981b) rule out autocompensating Si pairs because of the abrupt change in carrier concentration at higher doping levels, concluding that there is precipitation of a second phase, which is supported by their observed degradation of surface morphology at silicon concentrations above ~10^{19} cm^{-3}. Heiblum et al (1983b) - who did achieve a more gradual change in layer properties at higher silicon concentrations - produce photoluminescence evidence for Si pairs together with Si precipitates at these high concentrations. However Neave et al (1983b) have used TEM to examine highly doped films and have not found evidence of significant precipitation. They suggest that simple autocompensation occurs, with silicon incorporated as independent donors and acceptors, on Ga and As sites respectively, in the lattice.

No degradation of surface morphology was found in this investigation for silicon concentrations of up to 1.5 x 10^{19} cm^{-3}, as shown in figure 3.24 but the most highly doped portion of the step-doped

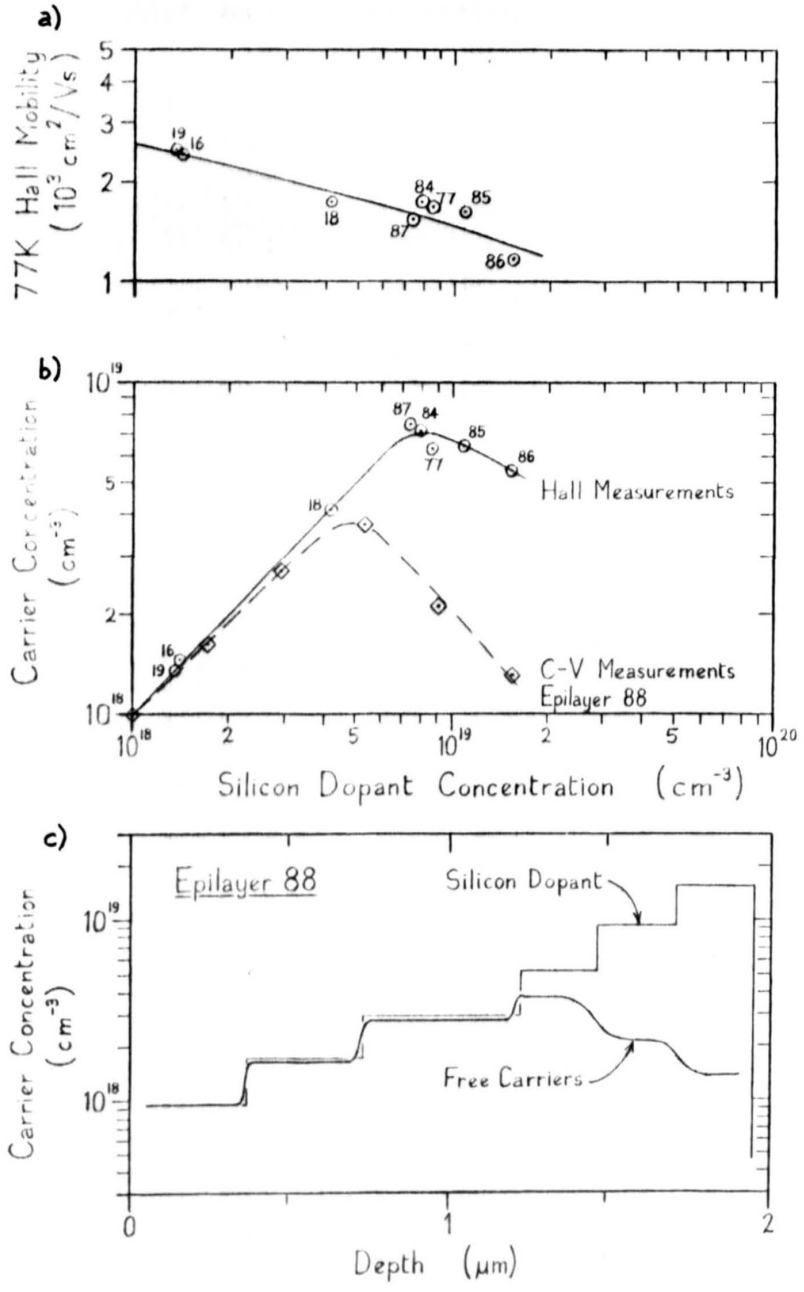

Figure 3.23 Results from highly doped epilayers.

a) Hall mobility as a function of dopant concentration.

b) Free carrier concentration as a function of dopant concentration.

c) Electrochemical C-V profile of free carrier concentration in a highly doped epilayer, together with calculated silicon dopant profile.

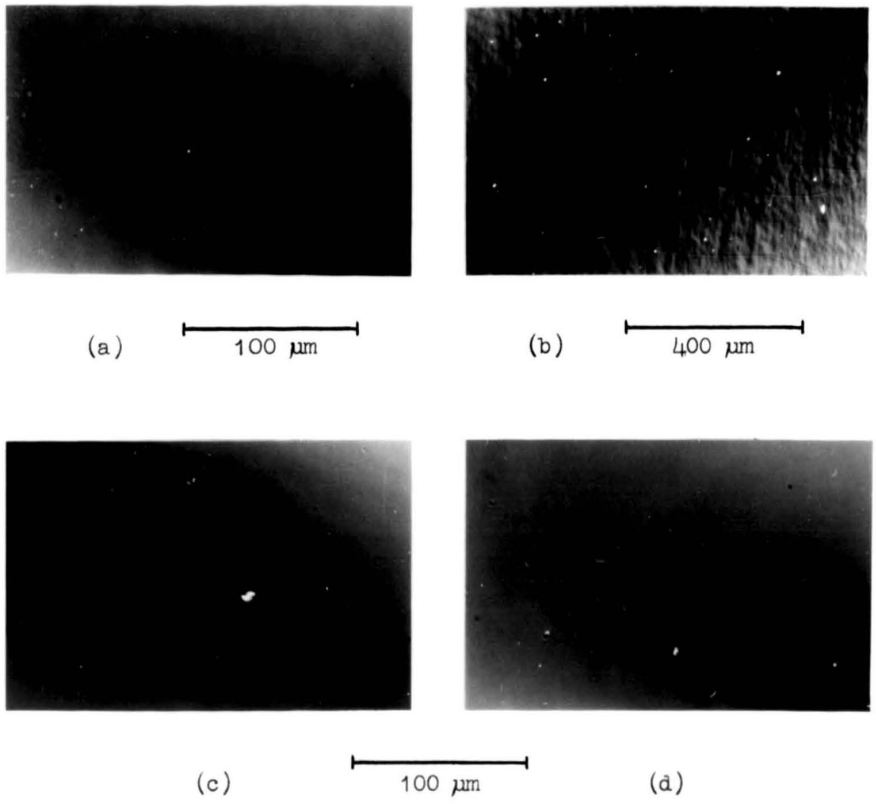

Figure 3.24 Nomarski micrographs of highly doped epilayers.
a&b) Epilayer 87 - 7 x 10^{18} Si/cm^3
c) Epilayer 85 - 1.1 x 10^{19} Si/cm^3
d) Epilayer 86 - 1.5 x 10^{19} Si/cm^3
These micrographs may be compared with those of lower doped layers shown in figures 3.32 - 39 , and do not show any additional features indicative of precipitation of the silicon dopant.

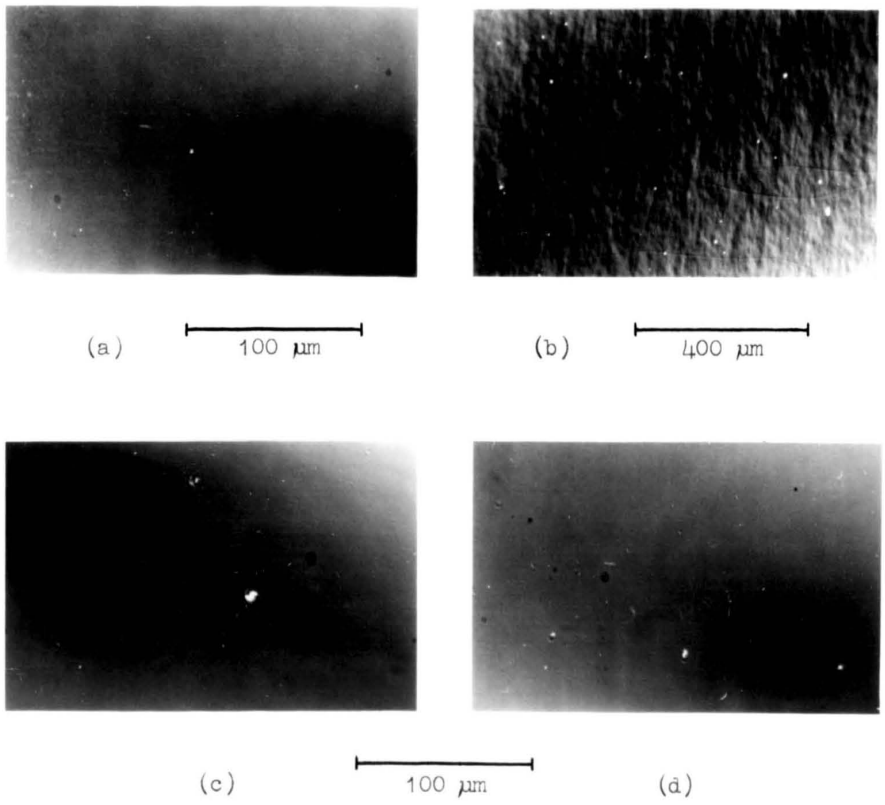

Figure 3.24 Nomarski micrographs of highly doped epilayers.
a&b) Epilayer 87 - 7 x 10^{18} Si/cm^3
c) Epilayer 85 - 1.1 x 10^{19} Si/cm^3
d) Epilayer 86 - 1.5 x 10^{19} Si/cm^3
These micrographs may be compared with those of lower doped layers shown in figures 3.32 - 39 , and do not show any additional features indicative of precipitation of the silicon dopant.

epilayer (again 1.5 x 10^{19} cm^{-3}) etched at a much slower rate than the remainder of the layer, there being more electronic conduction rather than dissolution at the semiconductor-electrolyte interface. This suggests a major change in the electronic properties at this high doping level, and a SIMS profile of the epilayer would be useful, both to confirm that all the incident silicon flux was incorporated and to see whether diatomic silicon secondary ions, or any other species, could provide any information on its incorporation at these high doping levels. It was also thought that SIMS profiles might show changes in other impurities incorporated due to changes in the partial pressures of residual background species within the MBE chamber, which were monitored during growth of this epilayer.

3.9 Photoluminescence and Other Residual Impurity Measurements

Low temperature photoluminescence measurements identify energy levels within the semiconductor band gap by optically exciting carriers and measuring the wavelength of emitted light, characteristic of the specific recombination processes occurring. Quantitative measurements are hampered by the existence of competing non-radiative recombination processes. The basic transitions are shown in figure 3.25 but these are complicated by the existence of excitons. The exciton is a bound state of a positive and negative charge carrier forming a hydrogen-atom-like series of energy levels, slightly below the bandgap energy. The energy levels of the free exciton are influenced by nearby point defects in the lattice (eg impurities), and if the total energy of the system is reduced then it is favourable for the exciton to remain near the defect. Thus a series of bound excitons, with energy less than that of the free exciton, exists associated with the various lattice defects present. The precise energy levels are dependent both on the nature of the exciton and on other defects present within the orbit of the free charges, leading to broadening of the lines and loss of spectral resolution at high impurity levels. Notation commonly used for identifying the various transitions is listed in Table 3.3. A brief review of the technique is given by Smith (1981), more extensive coverage by Dean (1977) and Bebb & Williams (1972). Heim & Hiesinger (1974) is a standard reference for the energies of specific exciton transitions in gallium arsenide, whilst impurity transitions are covered by Williams & Bebb (1972) and Ashen et al (1975).

One transition which requires specific mention is a broad peak between 1.47 and 1.48 eV. This corresponds in energy to the transition of a free electron to a Ge acceptor, but is often found in MBE grown material, and recent evidence tends to associate the peak with lattice defects such as carbon-vacancy complexes [Briones & Collins (1982)] or antisite defects [Neave et al (1983b)]. Most recently Akimoto et al (1984) have presented evidence associating this peak with incorporation of CO from the residual gas background.

Low temperature photoluminescence measurements on epilayers grown in this project were obtained on two separate occasions. The first results, obtained whilst growing the final films, were from fairly early epilayers and confirmed suspicions of relatively high

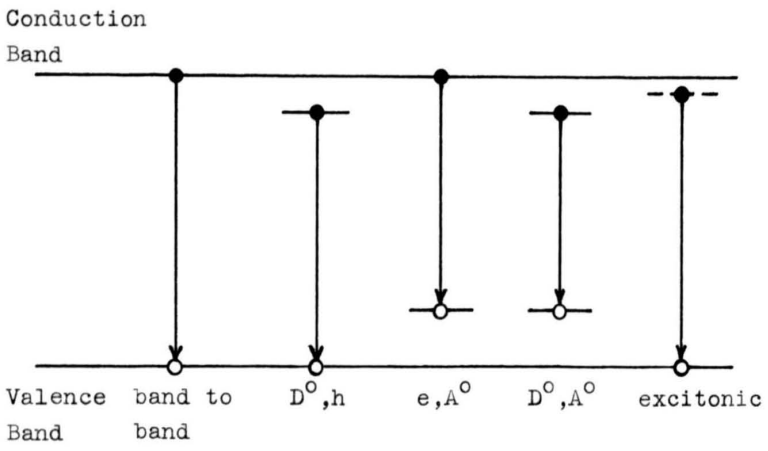

Figure 3.25 Basic recombinations observed with photoluminescence.

Table 3.3 Notation for photoluminescence spectra.

FX	recombination of free exciton
D^o,X	recombination of exciton bound to neutral donor
D^+,X	recombination of exciton bound to ionised donor
A^o,X	recombination of exciton bound to neutral acceptor j-j coupling of the electron and holes causes splitting of the energy levels of the three states with J=½,3/2,5/2
d,X	recombination of exciton associated with lattice defect
D^o,h	electron transition from neutral donor to free hole in valence band
e,A^o	electron transition from free electron in conduction band to neutral acceptor
D^o,A^o	electron transition from neutral donor to neutral acceptor
d	transition associated with lattice defect
LO_Y	longitudinal optical phonon replica of peak associated with element Y

compensation levels but did not identify any serious contamination, apart from carbon acceptors.

The lowest doped of these epilayers was p-type and showed a partially resolved exciton spectrum, consistent with the estimated ionised impurity concentration $\sim 1 \times 10^{16} cm^{-3}$ with some evidence for defect related excitons as shown in figure 3.26. At lower energies only the donor to carbon acceptor transition and other defect related transitions were observed. The other three epilayers investigated at this stage were silicon doped with estimated ionised impurity concentrations $\sim 2 \times 10^{16} cm^{-3}$. These epilayers gave similar results with unresolved exciton spectra indicative of the higher impurity density, and both carbon and defect related donor to acceptor transitions are apparent, although with varying intensities. The exception was epilayer 69 which also showed a peak corresponding to the presence of a silicon acceptor. This sample contained a small defective region, as shown in figure 3.27, which implies that silicon may be incorporated as an acceptor at such defects. However, at higher temperatures the peak did not decrease as rapidly as that due to carbon acceptors, but remained comparable to the lower energy defect related band, which may indicate that silicon is not involved but that the transition is due entirely to an additional type of defect being present.

Due to limitations of the detector it was not possible to look for deeper impurity levels corresponding to manganese or copper which might be expected to be present as system generated impurities.

Results from the final nominally undoped films showed well resolved exciton spectra consistent with much reduced impurity levels, and reproduced in figure 3.28 where the various transitions are identified. There is a surprisingly large difference in the spectra from the two nominally undoped layers but there are several factors which could influence this. The carrier density of epilayer 104 is lower than that of 100 (this is still correct after allowing for possible surface and interface depletion effects in the different thickness epilayers) but the carrier mobility is also lower, implying a larger total ionised impurity concentration which does correlate with the generally increased strength of donor related transitions found in epilayer 104. However Briones & Collins (1982) have found large changes in photoluminescence spectra obtained

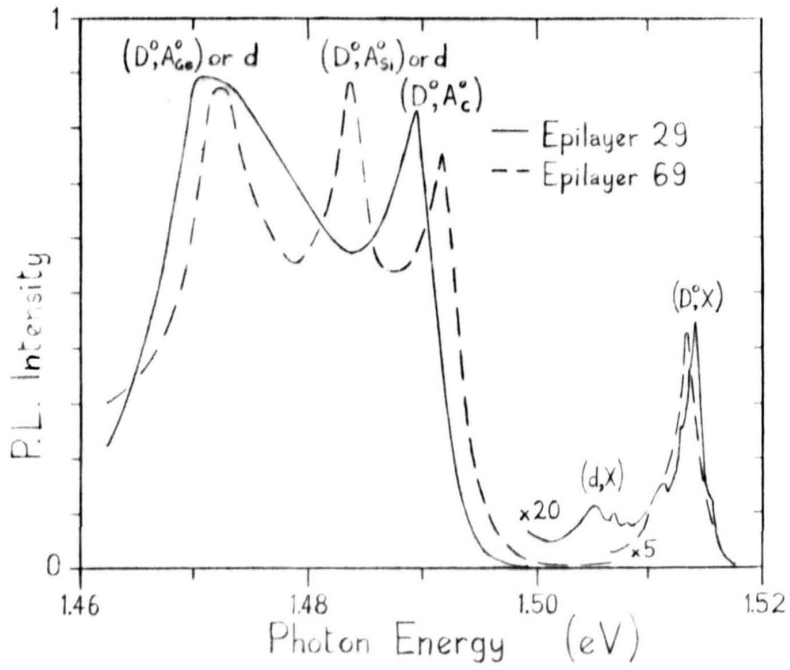

Figure 3.26 Low temperature photoluminescence spectra from early epilayers. Epilayer 69 was unique in showing the 1.484eV peak.

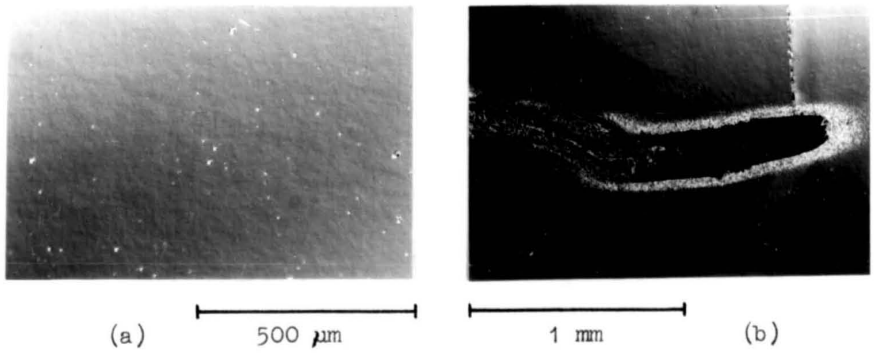

Figure 3.27 Nomarski micrographs of epilayer 69.
a) Typical region of epilayer.
b) Large defective region present on PL sample. Note also cracks present on cleavage planes around this defect.

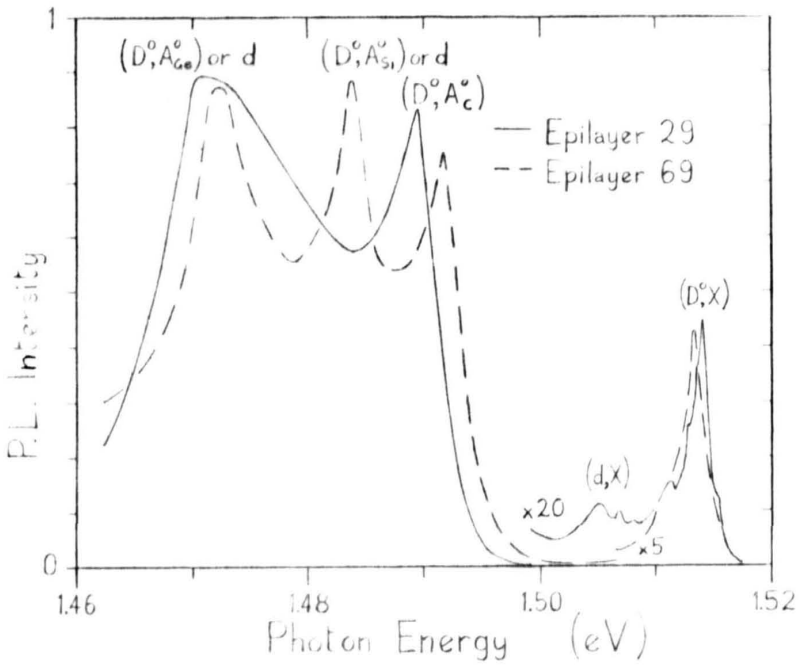

Figure 3.26 Low temperature photoluminescence spectra from early epilayers. Epilayer 69 was unique in showing the 1.484eV peak.

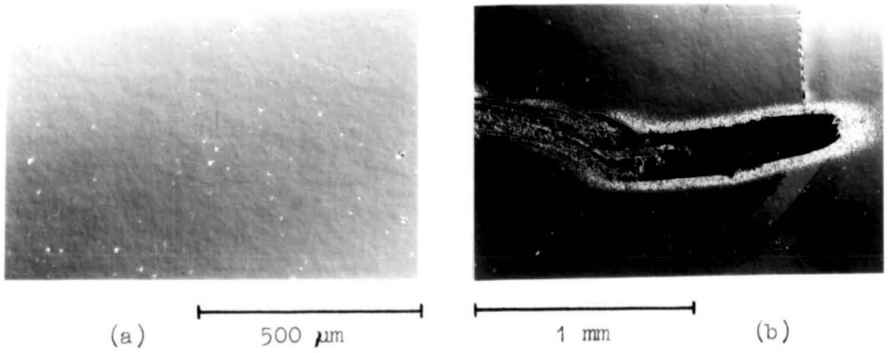

Figure 3.27 Nomarski micrographs of epilayer 69.
a) Typical region of epilayer.
b) Large defective region present on PL sample. Note also cracks present on cleavage planes around this defect.

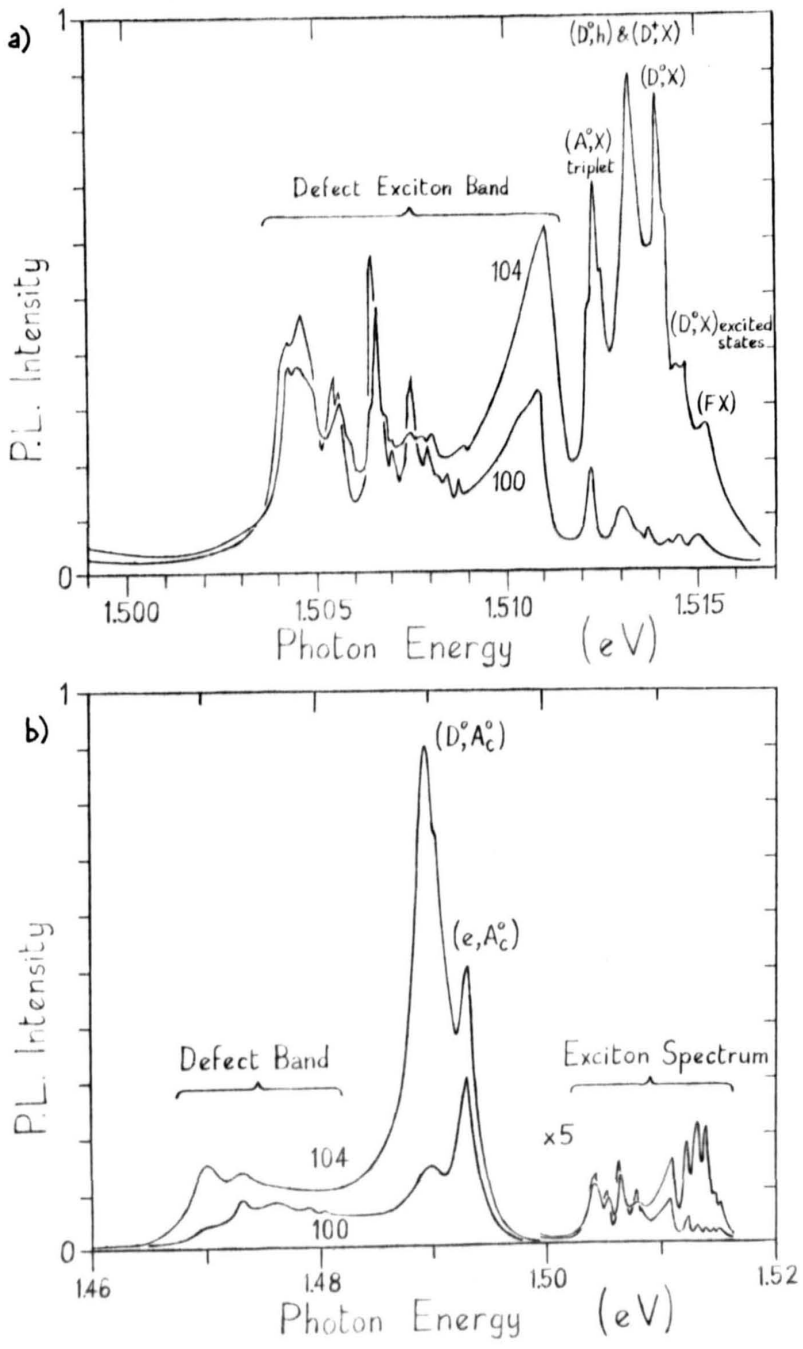

Figure 3.28 Low temperature photoluminescence spectra from final, nominally undoped epilayers.

a) Exciton spectrum.

b) Full range PL spectrum.

when epilayer growth temperature was varied within the range 545 - 625 °C, and substrate temperature is not well controlled in this system. Koschel et al (1981) have also found changes dependent on Ga/As_4 flux ratio, which altered during growth of epilayer 104 due to partial exhaustion of the arsenic cell. It is apparent that growth of additional films is necessary, probably with improved substrate temperature control, to separate these effects. Lower energy portions of the spectra (figure 3.28 (b)) show predominantly carbon acceptor related transitions with the defect band relatively much smaller than was found for the earlier epilayers. The spectra from these nominally undoped layers may be compared with those obtained from high-purity MBE grown epilayers by Kunzel & Ploog (1980), Dingle et al (1982), Briones & Collins (1982), Davis & Andrews (1983), Temkin & Hwang (1983), Heiblum et al (1983a) and Akimoto et al (1984). Although not quite as well resolved as the best spectra presented by these various authors, those obtained in this project show all the major features and, apart from the high background carbon acceptor level and poorly understood defect related bands, appear to be of comparable quality.

As expected, epilayers doped to electron concentrations $\sim 10^{16} cm^{-3}$ showed unresolved exciton peaks and both carbon acceptor and defect related transitions at lower energies (figure 3.29). The carbon acceptor peaks were, compared with the early epilayers, relatively much smaller than the defect related peak, which indicates reduced carbon incorporation but the third peak, corresponding in energy to a silicon acceptor, was present in both layers examined, though at a much lower intensity than found in layer 69.

The much larger intensity of the germanium or defect related bands, compared to the nominally undoped layers, suggests that impurities emanating from the silicon cell are the source of these defects. This could arise either from a contaminated silicon charge or from the graphite cell itself, and both these items should be changed to investigate the problem. It may be worthwhile analysing the silicon charge for germanium impurities. The slightly narrower exciton peak from epilayer 103 is consistent with a lower ionised impurity density also indicated by the higher electron mobility of this layer.

Low temperature photoluminescence measurements on these two layers werealso obtained at UMIST as part of a GaAs MBE Consortium

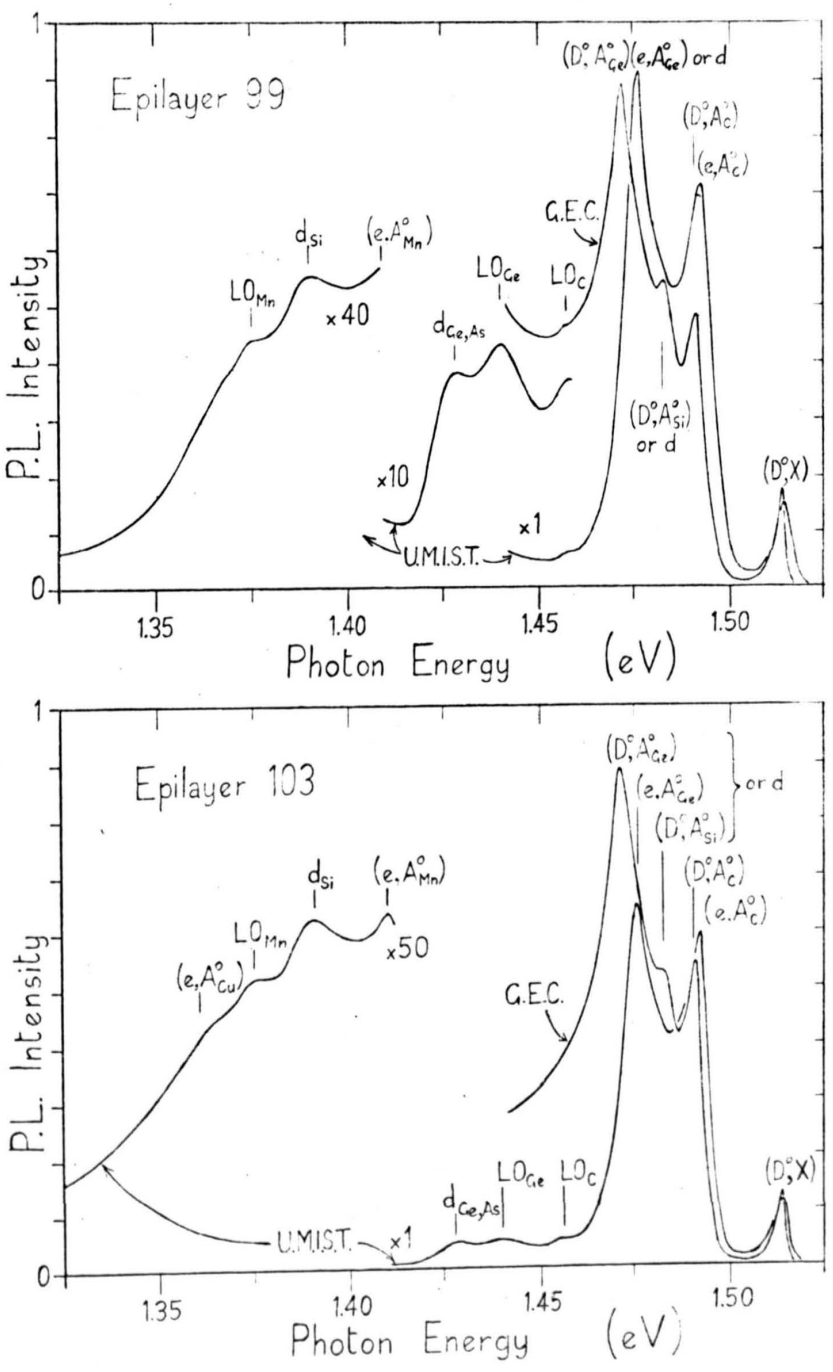

Figure 3.29 Low temperature photoluminescence spectra from $\sim 10^{16}$ cm^{-3} Si doped epilayers.

Round-Robin exercise [Singer & Nicholas (1984)] and the spectra are also plotted in figure 3.29 along with those obtained at GEC. Differences apparent between the two sets of spectra are the broader exciton peaks apparent in the spectra from UMIST together with the relatively larger carbon acceptor peak and absence of any peak intermediate between the carbon acceptor and defect related bands. These effects may be associated with experimental differences between the two laboratories, particularly the higher incident laser power density used by UMIST, as is the change from bound donor-acceptor transitions to the slightly higher energy free electron-acceptor transitions. The UMIST results extend to longer wavelengths showing longitudinal optical phonon replicas of the major peaks and additional impurity related peaks not previously observed. Manganese and copper are identified as impurities, presumably generated from hot stainless steel and the large area of copper cryopanelling respectively, but the results do not permit quantitative estimation of the impurity concentrations present. The very small differences in ionisation energy of the different shallow donor impurities in gallium arsenide has already been mentioned and, because of this, photoluminescence spectroscopy cannot be used to identify these defects. Photothermal ionisation spectroscopy [Stillman & Wolfe (1977)] has been presented as a suitable technique, and used by Low et al (1982) to identify residual shallow donor impurities in MBE grown gallium arsenide from two different systems. In both cases Pb, Si, Sn and S were identified together with the absence of an unidentified but characteristic residual donor in VPE and MOCVD gallium arsenide commonly associated with carbon or germanium donors. However, no measurements capable of identifying the residual donors present have been obtained during the current project.

Deep level traps in epilayer 103 were measured by UMIST as part of the GaAs round robin exercise [Singer & Nicholas (1984)]. Deep level transient spectroscopy (DLTS) and minority carrier transient spectroscopy (MCTS) were used respectively to measure the electron and hole trap densities, which are shown in Table 3.4. With the exception of trap X these traps have all been previously observed in MBE grown GaAs at similar densities, [Blood & Harris (1984) , Martin et al (1977), Lang et al (1976), Stall et al (1980),

Table 3.4 Trap densities in Epilayer 103

Trap type	Activation Energy (eV)	Concentration (cm^{-3})
Electron trap M1	0.18	4.6×10^{13}
" M3	0.30	7.4×10^{13}
" M4	0.48	4.7×10^{13}
" X	0.52	4.0×10^{14}
Hole trap HL3(Fe)	0.59	1.2×10^{15}
" HL4(Cu)	0.42	$< 2 \times 10^{15}$
" HL7	0.35	3.1×10^{15}

Mitonneau et al (1977)], and trap X was observed in all epilayers included in this comparative study. The trap densities were similar to those measured in the other samples, with the exception of HL7 which was larger by two orders of magnitude, but cannot yet be even tentatively associated with any particular atomic defect. As already mentioned the identification of the various trapping levels is not agreed and further work is necessary to reduce their concentration in grown material.

The photoluminescence measurements are characteristic of the surface 0.3 μm due to absorption of the incident light. Profiles through the epilayers would have been useful to obtain the distribution of impurities throughout the epilayer, and perhaps identify other impurities not directly apparent in the photoluminescence spectra. SIMS profiles of various impurities were requested for selected epilayers, but the only results obtained were secondary ion mass spectra, obtained under dynamic SIMS conditions with argon primary ions, from one epilayer at an unspecified depth. These spectra are shown in figure 3.30. Whilst the major species are fairly easily identified from the known composition and common contaminants observed in the SIMS system (see Chapter 4 for a full discussion), the assignment of other peaks is often ambiguous as

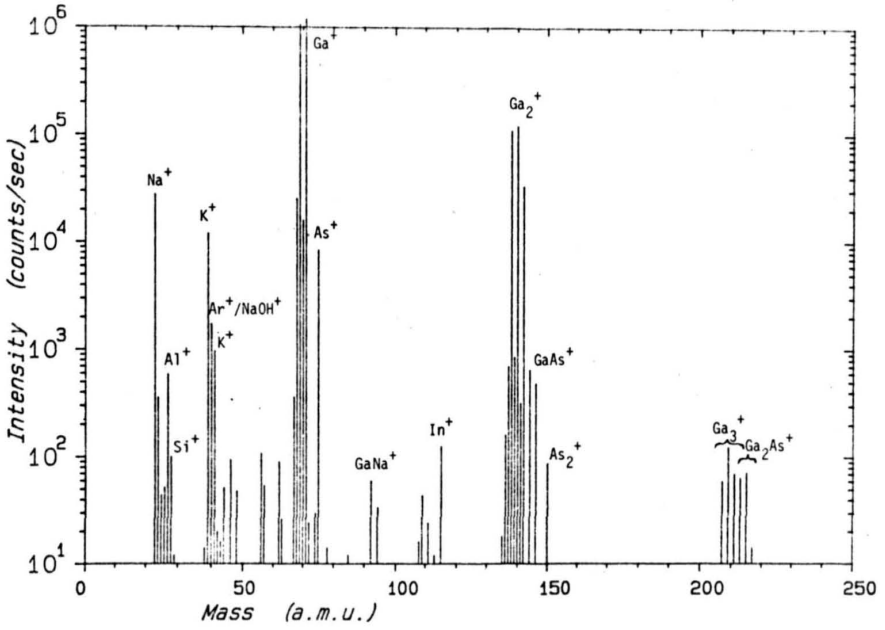

Figure 3.30 (a) Positive ion SIMS spectrum of MBE grown epilayer.

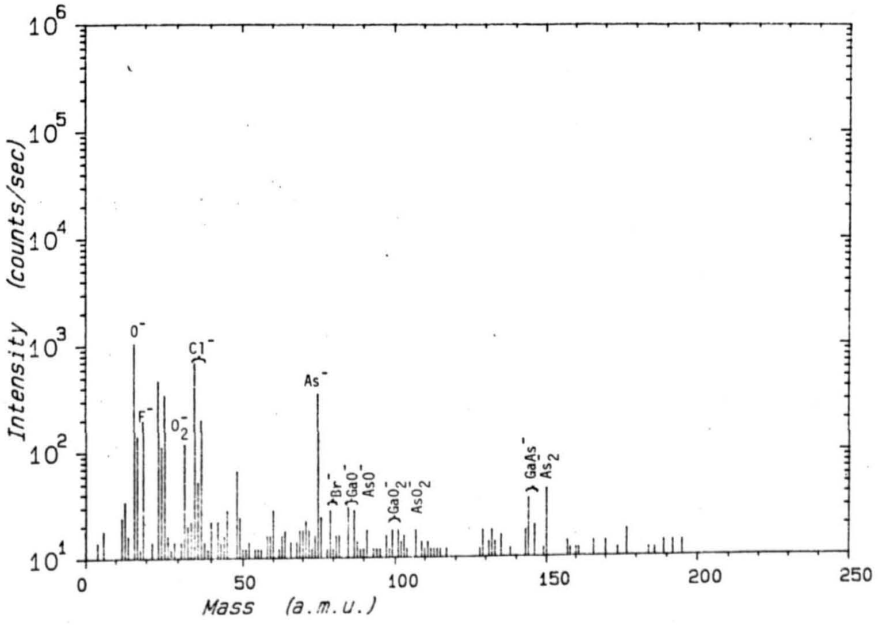

Figure 3.30 (b) Negative ion SIMS spectrum of MBE grown epilayer.

Table 3.5 Possible SIMS mass peaks.

Positive Ions		Negative Ions	
Mass No.	Possible Species	Mass No.	Possible Species
23	Na^+	12	C^-
24	C_2^+	13	CH^-
27	$Al^+, C_2H_3^+$	16	O^-
28	$Si^+, C_2H_4^+, CO^+, N_2^+$	17	OH^-
39,41	K^+	19	F^-
40	$Ar^+, NaOH^+, Ca^+$	24	C_2^-
44	$AlOH^+, CO_2^+, C_2H_4O^+$	25	C_2H^-
46	$Na_2^+, C_2H_6O^+$	26	$C_2H_2^-$
48	Ti^+, C_4^+	32	O_2^-, S^-
55	Mn^+	35,37	Cl^-
56	$Fe^+, Si_2^+, C_3H_4O^+$	40	$C_3H_4^-, C_2O^-$
57	$KOH^+, C_3H_5O^+$	42	$C_3H_6^-, C_2H_2O^-$
59	$KOH^+, C_3H_7O^+$	45	$C_2H_5O^-$
62	$C_5H_2^+, C_2H_6O_2^+$	48	O_3^-, SO^-, C_4^-
63	$Cu^+, C_5H_3^+, C_2H_7O_2^+$	60	$C_5^-, C_3H_8O^-$
65	Cu^+	75	As^-
69,71	Ga^+	79,81	Br^-
75	As^+	85,87	GaO^-
85,87	GaO^+	91	AsO^-
92,94	$GaNa^+$	97 } 99 }	GaN_2^- $GaON^-$
109,111	$GaNaOH^+, GaAr^+$	101 } 103 }	GaO_2^-
115	In^+	107	AsO_2^-
138,40,42	Ga_2^+	144,146	$GaAs^-$
144,146	$GaAs^+$	150	As_2^-
150	As_2^+		
207,9,11,13	Ga_3^+		
213,5,7	Ga_2As^+		

indicated in Table 3.5 for some mass peaks of interest. In the absence of comparative data it is impossible to assign the peaks conclusively to a particular secondary ion or to say whether these are bulk contaminants or species generated by reaction of the instantaneous sputtered surface with the residual gas in the SIMS system.

Sodium and potassium at mass 23 and 39 and 41 amu are almost always observed as contaminants in positive ion SIMS due to their common occurrence and low ionisation energies giving a high positive ion yield, and the 40 amu peak has on previous occasions [Dowsett (1979)] been identified as due to NaOH. Manganese (55 amu) is not found at a significant level and neither is Copper (63 and 65 amu) since although the count at 63 amu could be significant there is no corresponding peak for the 65 amu isotope. Indium can be identified presumably arising from the use of indium solder to mount the wafer, but whilst aluminium and silicon are probably present the relevant peaks may be due to hydrocarbon contaminants $C_2H_3^+$, $C_2H_4^+$ or even CO^+ or N_2^+.

The negative secondary ion spectrum shows a higher level of background noise but various peaks can be identified as shown. The lower mass peaks are all commonly observed in negative ion SIMS and are probably entirely due to interaction of the surface with the residual gas, and the same may be true of the matrix oxide species observed at higher masses. The only way to determine the origin of the various secondary ions is to obtain comparative spectra, with the same SIMS conditions, from samples with different impurity levels. The simplest way of achieving this is to profile through an epilayer grown under various conditions, into the substrate material, when changes in the SIMS signals may indicate their source.

3.10 Surface Morphology

The initial roughness of bromine-methanol etched substrates and the generation of "scratches" on the surface by lightly rubbing to remove adherent contamination has already been mentioned. Both types of large-scale imperfection are reproduced on the surface of MBE grown epilayers as shown in figure 3.31.

Growing with a gallium stabilised surface reconstruction can lead to the formation of gallium droplets, which partially dissolve the growing gallium arsenide leading to an array of saucer like depressions, as shown in figure 3.33 (a). On other occasions crystallographically oriented pits were observed as shown in figure 3.33 (b) which may be indicative of localised nucleation and initial three dimensional growth [Ploog (1980)] but this was only observed after a gallium stabilised surface had been generated. Micrographs from one interesting surface are shown in figure 3.33 (c) - (f). This epilayer was grown with a reduced arsenic flux due to the arsenic cell nearing exhaustion. Since the electron gun was inoperative, maintenance of an arsenic stabilised surface during growth could not be ensured, and surface features are believed to be caused by growth under gallium rich conditions. At the edge of the matt region usually characteristic of gallium rich growth, distinct droplets in circular depressions are observed, but away from the edge the depressions become crystallographically oriented, the droplets become smaller and eventually disappear to leave a surface covered with approximately parallel line-type defects. It is possible that this might be associated with substrate preparation or temperature variations across the wafer but this seems unlikely in view of the gallium droplets present.

Faceting of the epilayer surface has already been mentioned and associated with contamination of the substrate. It may also be due to growth under gallium rich conditions, as suggested by the linear defects present in figure 3.33 (f), or other deviations from ideal conditions which led to the highly textured surfaces of figure 3.32. Electron diffraction patterns near the end of growth of these epilayers were rather indistinct and showed some evidence of inclined streaks indicative of faceting.

A few types of gross defects, visible to the naked eye, were sometimes observed on the films. The most apparent was the type of defect shown in figure 3.34 and generally formed around a central

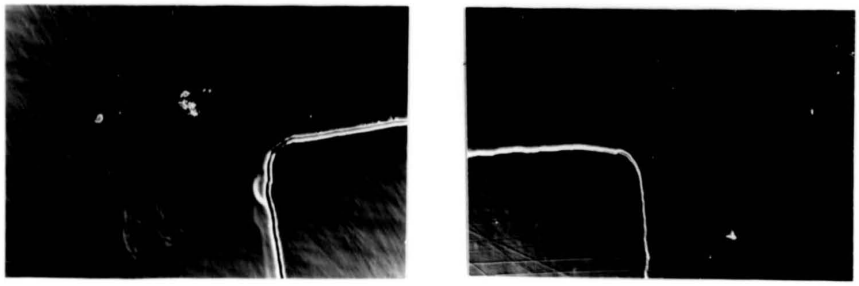

500 μm

Figure 3.31 Nomarski micrographs of typical epilayers grown on rough and scratched substrates. Note the continuity of topography between epilayer and region of substrate shielded from growth flux.

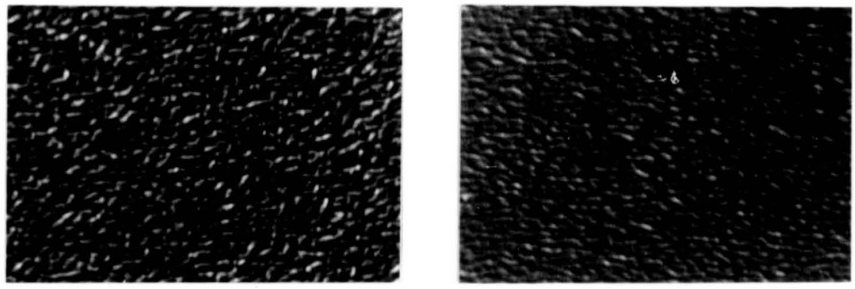

20 μm

Figure 3.32 Nomarski micrographs of highly textured surfaces. RED patterns were indistinct and showed indications of faceting in both cases.

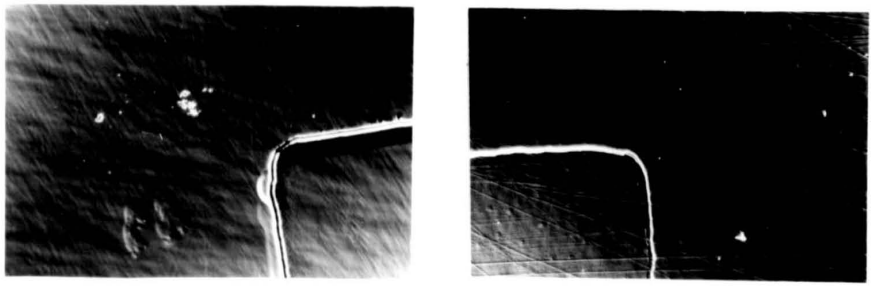

Figure 3.31 Nomarski micrographs of typical epilayers grown on rough and scratched substrates. Note the continuity of topography between epilayer and region of substrate shielded from growth flux.

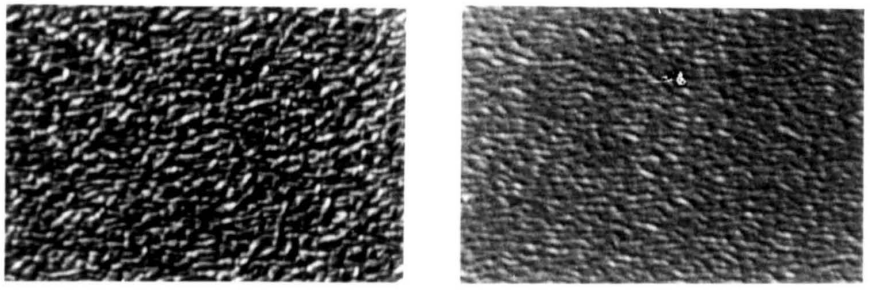

Figure 3.32 Nomarski micrographs of highly textured surfaces. RED patterns were indistinct and showed indications of faceting in both cases.

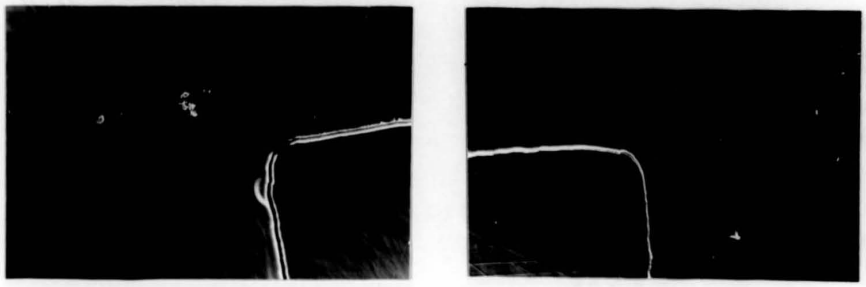

Figure 3.31 Nomarski micrographs of typical epilayers grown on rough and scratched substrates. Note the continuity of topography between epilayer and region of substrate shielded from growth flux.

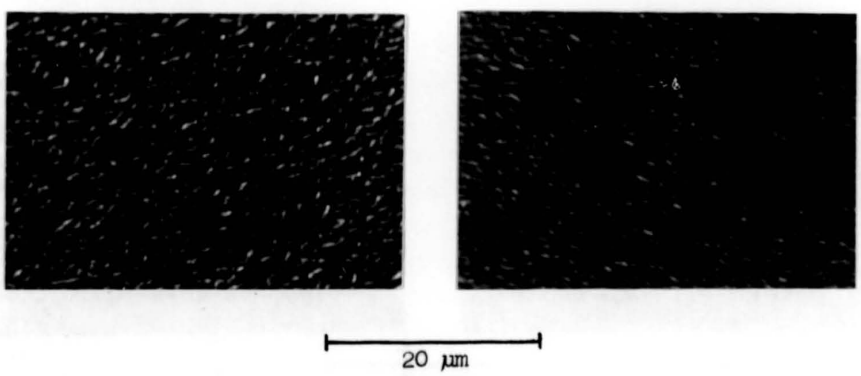

Figure 3.32 Nomarski micrographs of highly textured surfaces. RED patterns were indistinct and showed indications of faceting in both cases.

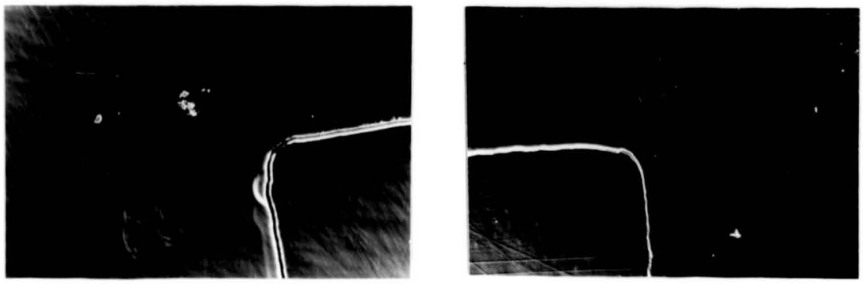

Figure 3.31 Nomarski micrographs of typical epilayers grown on rough and scratched substrates. Note the continuity of topography between epilayer and region of substrate shielded from growth flux.

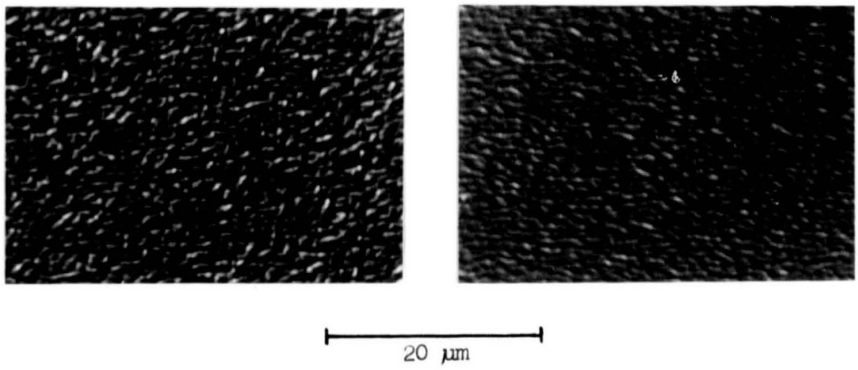

Figure 3.32 Nomarski micrographs of highly textured surfaces. RED patterns were indistinct and showed indications of faceting in both cases.

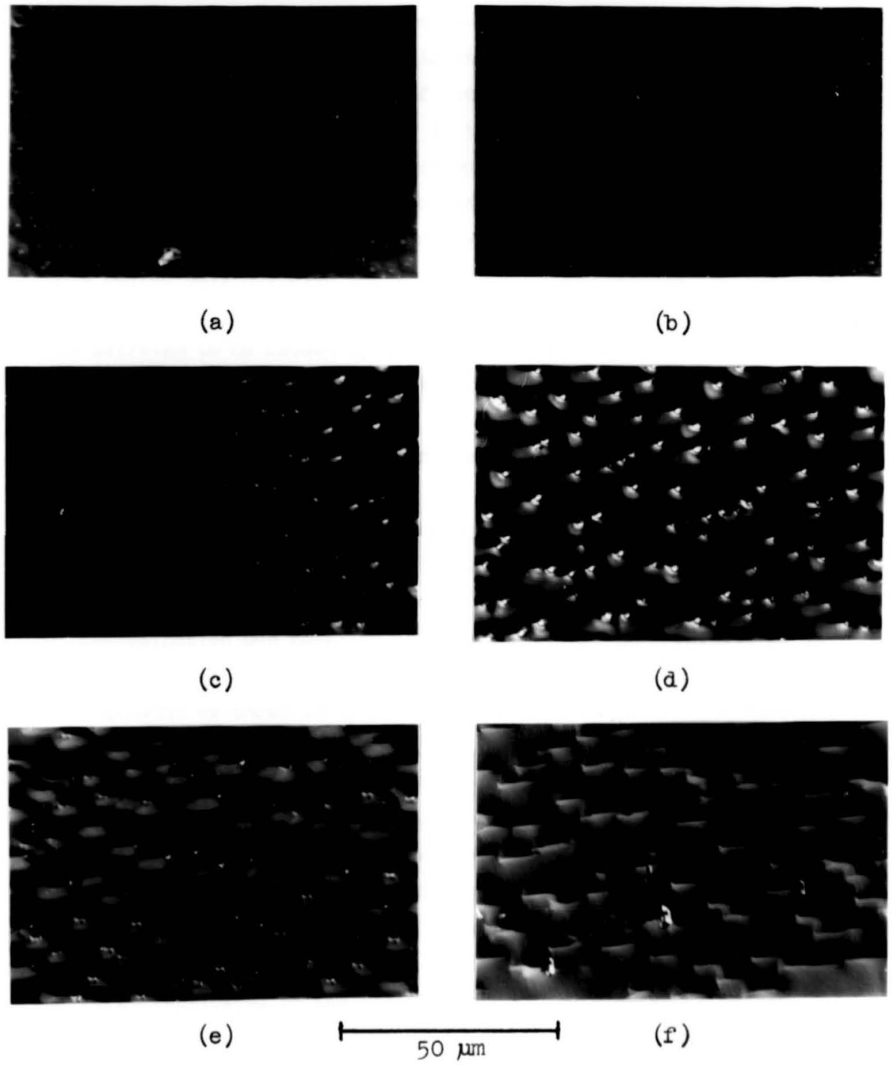

Figure 3.33 Nomarski micrographs of gallium rich surfaces.
a) Gallium droplets randomly positioned on surface in saucer depressions.
b) Gallium droplets in crystallographically oriented pits.
c-f) Transition from isolated droplets to linear defects at the edge of a gallium rich region of growth.

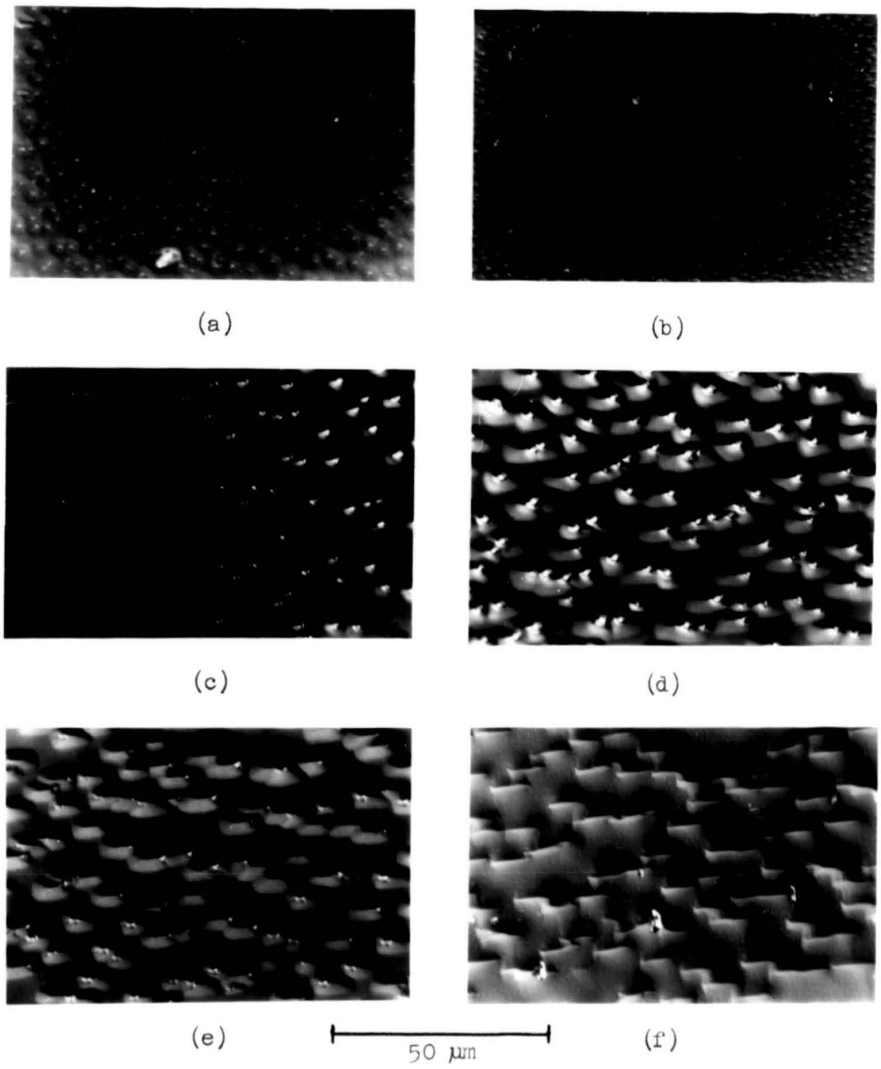

Figure 3.33 Nomarski micrographs of gallium rich surfaces.
a) Gallium droplets randomly positioned on surface in saucer depressions.
b) Gallium droplets in crystallographically oriented pits.
c-f) Transition from isolated droplets to linear defects at the edge of a gallium rich region of growth.

dust particle or other large contaminant. Not infrequently a central hole was observed where the initiating contaminant has presumably been dislodged during handling of the sample. The oval shape of the defect, which is always oriented in the same crystallographic direction, is presumably a reflection of different surface diffusion rates along the two orthogonal surface lattice vectors, but the cause and nature of the oval boundary and the facets visible within this region have not been determined.

Faceted streaks on the epilayer surface as shown in figure 3.5 are believed to be caused by contamination left behind by evaporating droplets of the final Super-Q water rinse before mounting the substrate on its molybdenum plate. It may be relevant that these defects were most apparent near the end of the project when the resistivity of the Super-Q water had fallen to $\sim 10^{18}$ ohm cm, at which stage replacement of the ion-exchange resins is usually considered to be necessary. More highly defective regions were often present at one end of these streaks, presumably where there was a higher level of contamination due to final evaporation of the droplet, either of polycrystalline material or what appeared to be a mass of needle-like growths as shown in figure 3.5 but it was difficult to identify this with certainty due to the small depth of focus available.

One further defect apparent on epilayers grown on substrates cleaved from a particularly fragile wafer were series of lines parallel to the cleavage directions, and shown in figure 3.35. These are identified as slip lines caused by thermally induced slip occurring on {111} slip planes [Stirland & Straughan (1976)] during the initial heating of a highly strained substrate and, like other substrate defects, replicated in the epilayer. The highly strained nature of the substrate is also illustrated by the breakage of the Hall sample also shown, where the fracture edge is only approximately along a cleavage plane, and is noticeably curved.

Defects generally apparent on the epilayers included the common oval defect as shown in figure 3.36. An irregular central portion is apparent in many of the larger defects and large oval defects have been shown by Bafleur et al (1982) using TEM to contain a central region of twinned or polycrystalline material although this was not evident in smaller defects, whilst Suzuki et al (1984) identified stacking faults in all defects. Various investigations into generation of the defects, and hence methods to reduce or eliminate them from

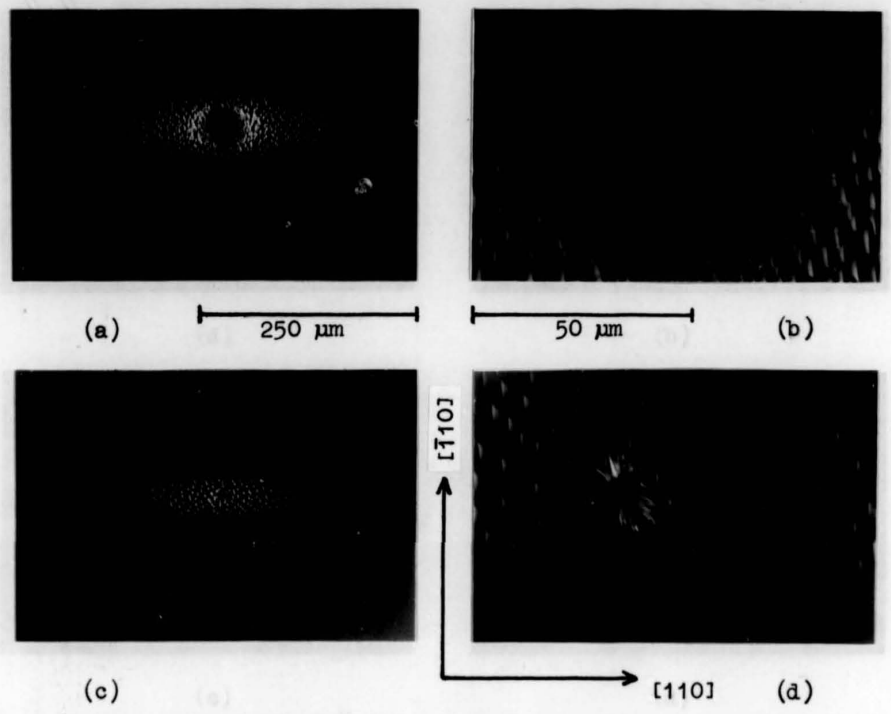

Figure 3.34 Nomarski micrographs of large oval defects.
a&b) Typical defect with central hole. Careful adjustment of microscope focus shows that the hole extends through the epilayer to the original substrate surface.
c&d) Smaller defect with signs of particulate contamination and irregular growth.

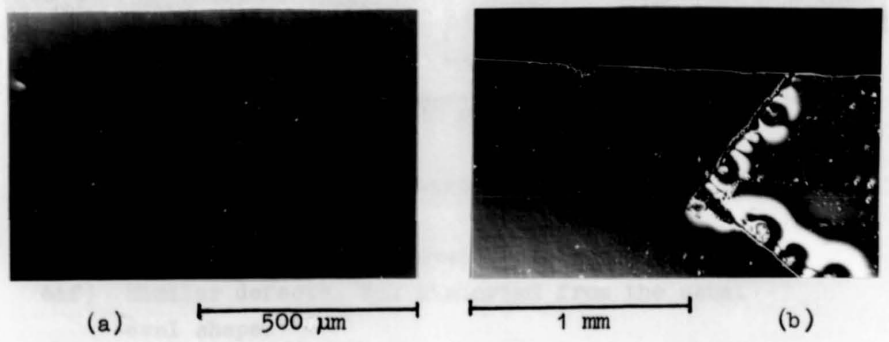

Figure 3.35 Nomarski micrographs of slip lines visible on epilayer surfaces after growth.
a) Epilayer 94
b) Broken Hall sample from epilayer 101. Note the slight curve of the broken edge.

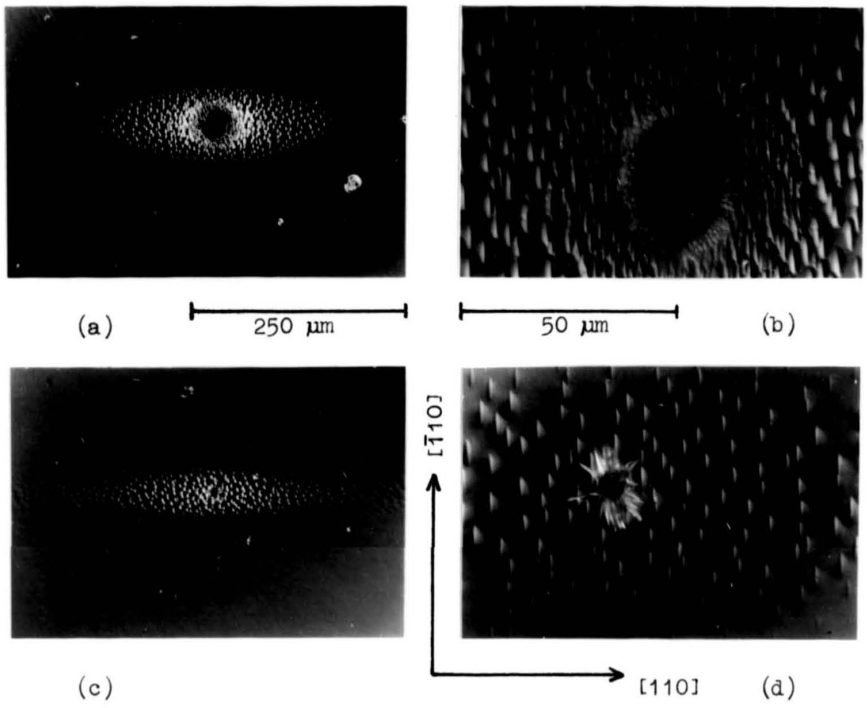

Figure 3.34 Nomarski micrographs of large oval defects.
a&b) Typical defect with central hole. Careful adjustment of microscope focus shows that the hole extends through the epilayer to the original substrate surface.
c&d) Smaller defect with signs of particulate contamination and irregular growth.

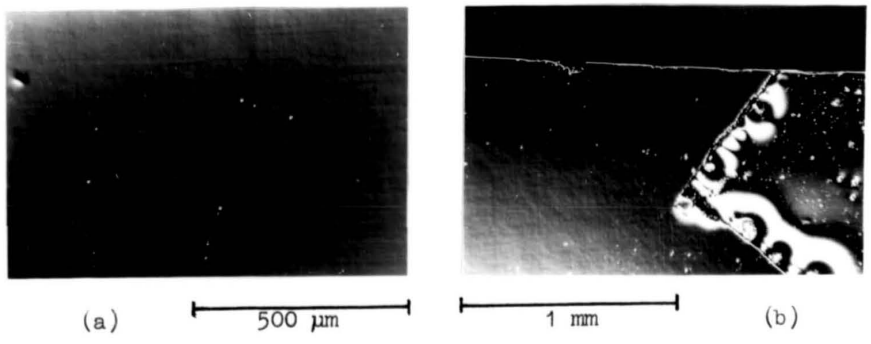

Figure 3.35 Nomarski micrographs of slip lines visible on epilayer surfaces after growth.
a) Epilayer 94
b) Broken Hall sample from epilayer 101. Note the slight curve of the broken edge.

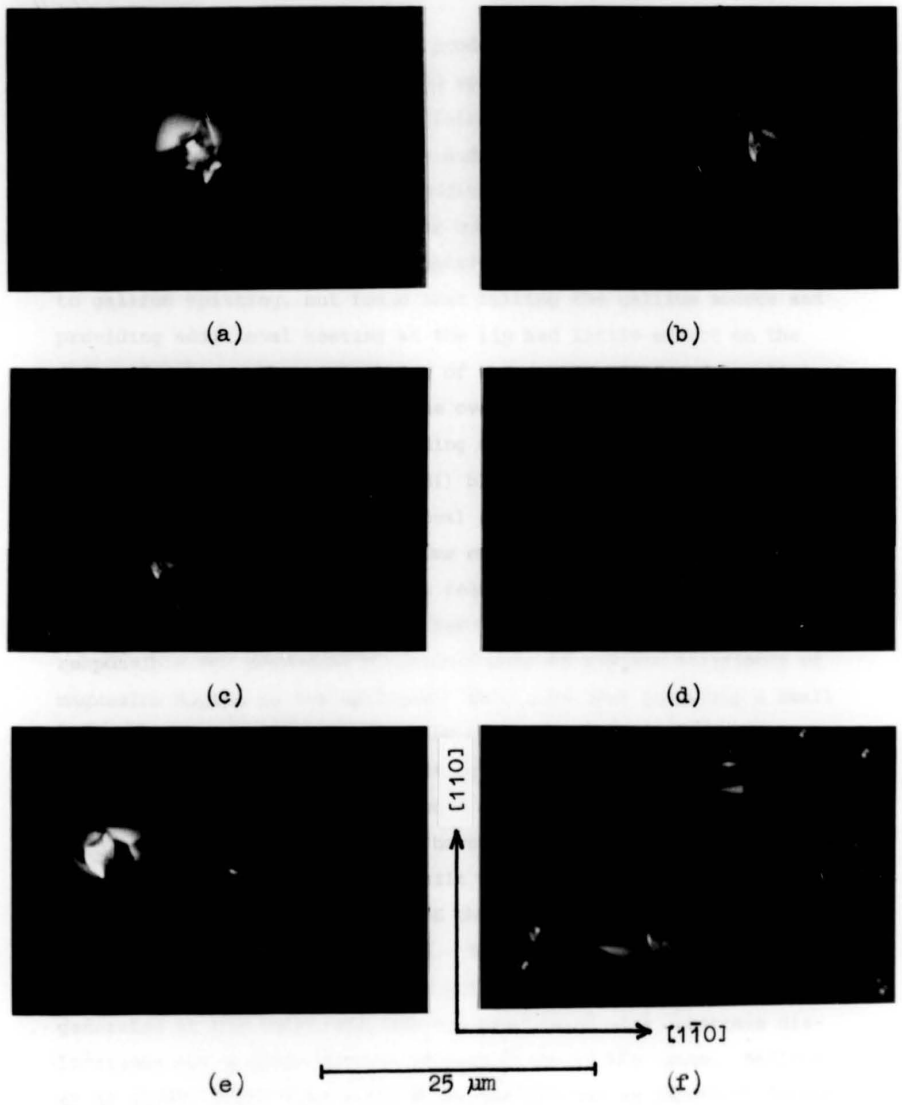

Figure 3.36 Nomarski micrographs of 'oval defects' on MBE grown epilayers.

a-d) Typical selection of oval defects.

e&f) Similar defects, but distorted from the usual oval shape.

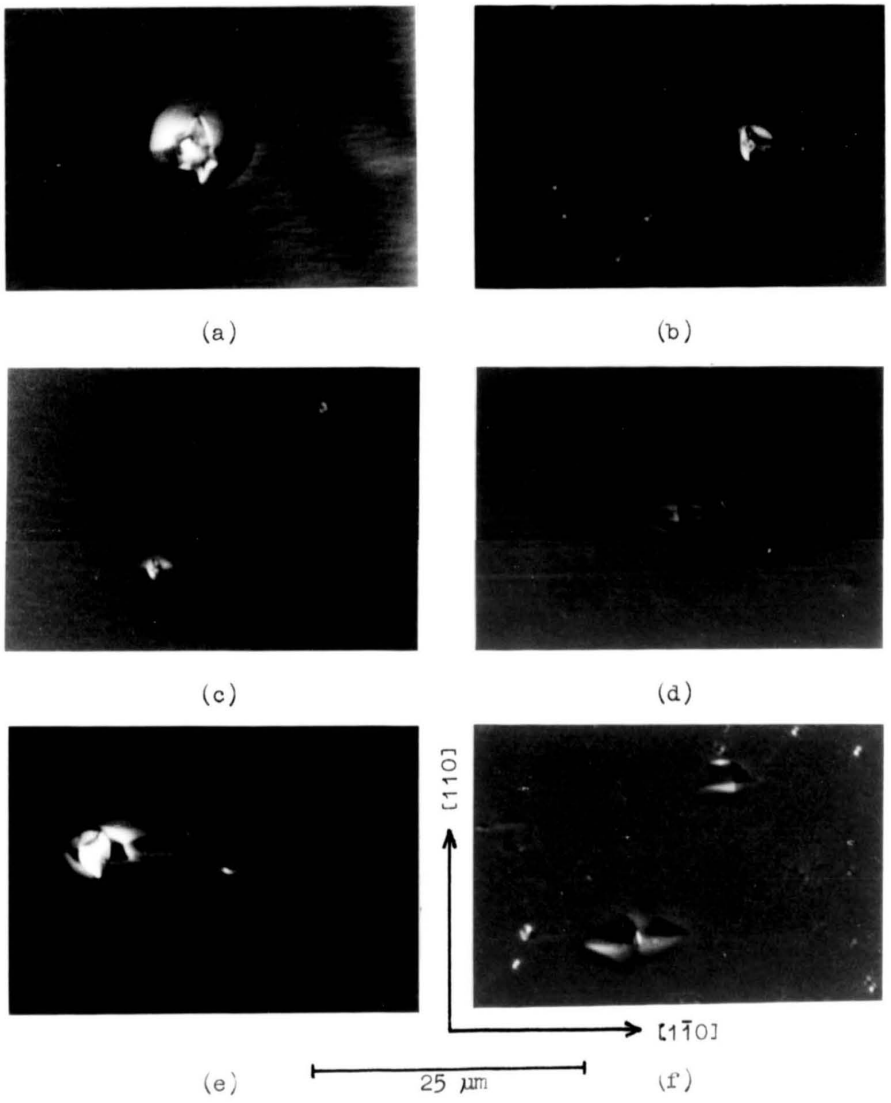

Figure 3.36 Nomarski micrographs of 'oval defects' on MBE grown epilayers.

a-d) Typical selection of oval defects.

e&f) Similar defects, but distorted from the usual oval shape.

epilayers, have, it seems, each produced different prime causes. Wood et al (1981) have identified spitting from the gallium source cell, caused by droplets falling from the front of the source cell into the main charge and breaking the gallium arsenide skin, and report that additional heating at the front of the cell considerably reduced the oval defect density. Hwang et al (1983a) have attributed irregularly shaped gallium rich defects to gallium spitting, but found that filling the gallium source and providing additional heating at the lip had little effect on the defect density. Thorough baking of the system was found to eliminate the irregular defects but not the oval defects, and there is some evidence relating them to threading dislocations originating from the substrate. Chai & Chow (1981) blame Ga_2O contamination in the gallium flux for generation of oval defects and find that use of a freshly cleaned and filled gallium cell, together with thorough outgassing of cells and shutters is required. Kirchner et al (1981a, 1981b) also identify Ga_2O as an impurity in the gallium flux, responsible for producing electronic defects and low efficiency of magnesium doping in the epilayer. They show that including a small amount of aluminium in the gallium cell, as a getter for oxygen, eliminates the Ga_2O flux, permitting efficient magnesium doping, but do not comment on any other effects of this change.

Suzuki et al (1984) have, however, identified the direct spitting of arsenic particles built up on the arsenic cell orifice as the cause of oval defects, and that the cure is additional heating at the front of the arsenic cell. They also show that most such defects are generated within the epilayer and that the remainder, generated at the substrate, are not associated with substrate dislocations but suggest surface contamination as the cause. Bafleur et al (1982) found that surface preparation was an important factor in reducing the density of oval defects and concluded that carbon contamination, which could also occur during epitaxy, was the major cause of oval defects. Both Stringfellow et al (1981) and Heiblum et al (1983a) report that high background pressures, of mainly CO, lead to increased carbon incorporation and p-type doping or reduced electron mobility in n-type epitaxial layers, but do not consider effects on morphological defect density. Heiblum et al (1983a) state that local, mainly oval, defects appear to be correlated with dislocations in the substrates used.

During this investigation oval defect densities of between 5×10^2 and 10^5 cm $^{-2}$ were obtained, although usually $\sim 10^4 cm^{-2}$, but no consistent variation with growth rate, gallium cell contamination or level of source material in the cell was found. Films grown prior to fitting the silicon cell did show generally lower levels of these defects than the majority of later films, but again there was no consistent relationship between silicon cell temperatures and defect density.

It is apparent that there are many possible causes for the oval defects although most seem to involve contamination of some form, either left on the substrate or arriving in the residual gas or directly from a molecular beam. Further work is obviously required to minimise the density of such defects appearing in this system, and is probably best directed initially at reducing still further unintentional contamination of the substrate and growing epilayer. However, considerable modification to the system would be required to enable checking of molecular beam composition or of impurities left on substrates before growth of an epilayer, so that there can be little feedback on the separate aspects influencing final epilayer quality.

On some occasions paired defects were apparent, as shown in figure 3.37, which could be joined by square or triangular deformations of the surface. Such pairs were observed on various layers of 2 - 10 μm in thickness and their separation measured as 1.4 t where t is the layer thickness, although some showed additional, more closely spaced pairs. This strongly suggests that the majority of defect pairs have nucleated at the same point on the substrate surface and travelled outwards on (111) and $(\bar{1}\bar{1}1)$ planes during growth of the epilayer. The nature of the defects must remain speculative. The idea of a twinned region between the defects is initially attractive but does not have the required symmetry for the square surface deformation. Separate twinned regions for the triangular deformations appears feasible and small twinned regions or stacking faults may be responsible for the other defects, but it is difficult to see why they should lengthen as the film grows in thickness. Examination of suitably thinned films with TEM may provide some answers. The surface density of these paired defects varied from zero to $2 \times 10^5 cm^{-2}$ and, although there are contradictory results, seems to be associated with high growth rates and a long

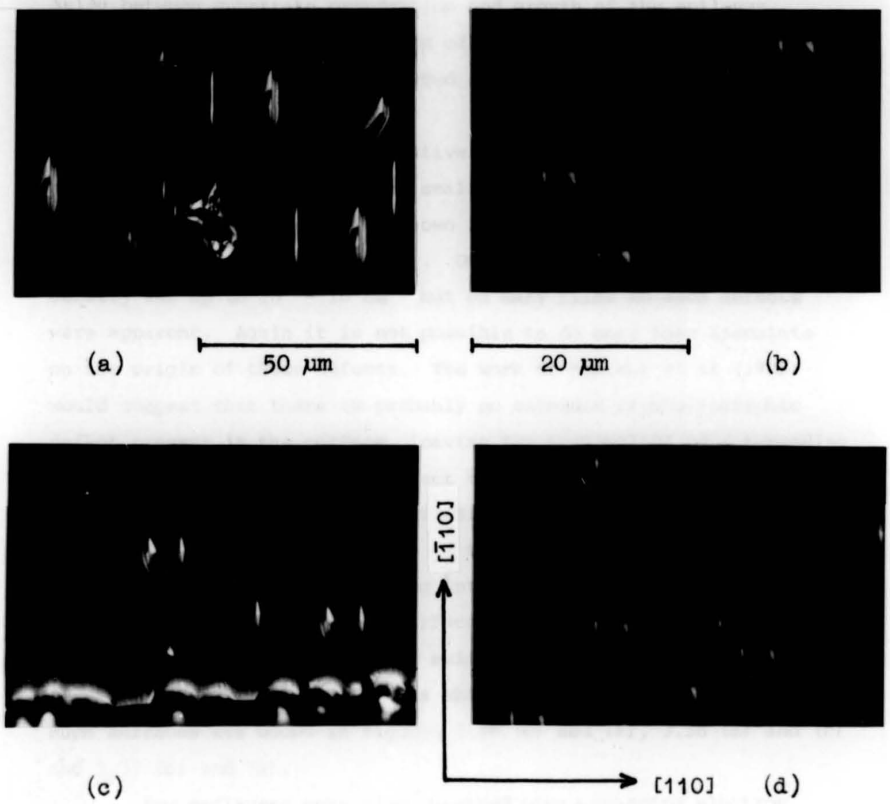

Figure 3.37 Nomarski micrographs of paired defects on MBE grown epilayers.
Seperation of defect pairs = 1.4 x epilayer thickness, indicating that the defects have nucleated at the same point and propogated along (111) & ($\bar{1}\bar{1}1$) planes during growth of the epilayers.

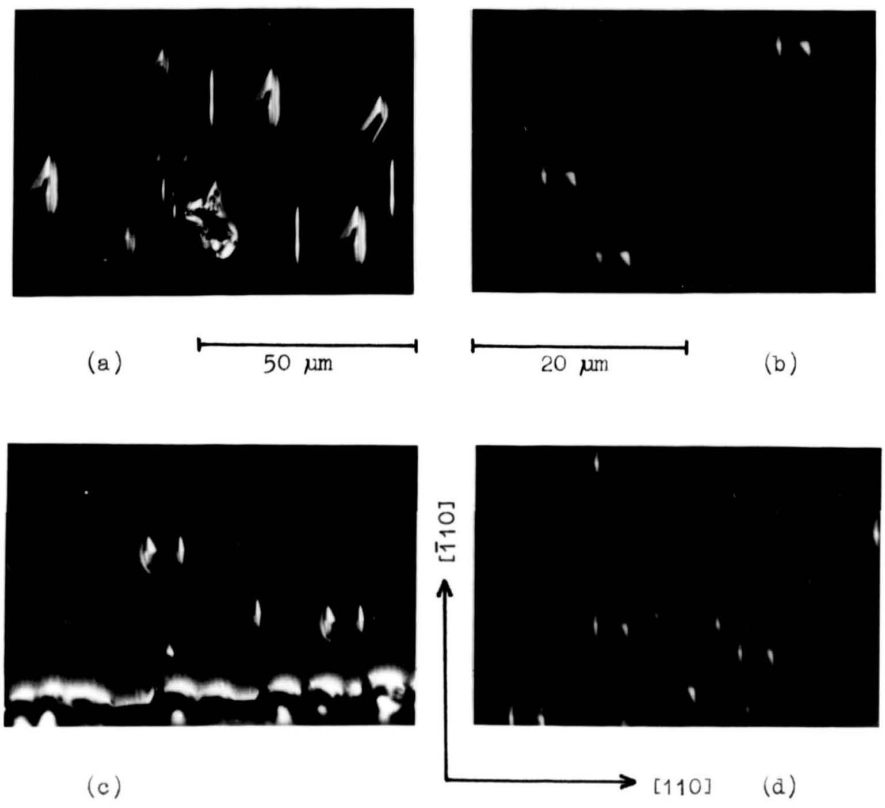

Figure 3.37 Nomarski micrographs of paired defects on MBE grown epilayers.
Seperation of defect pairs = 1.4 x epilayer thickness, indicating that the defects have nucleated at the same point and propogated along (111) & ($\bar{1}\bar{1}$1) planes during growth of the epilayers.

delay between substrate preparation and growth of the epilayer, suggesting that a particular form of contamination may initiate the defect which is then propagated at a high growth rate, rather than being grown over.

In addition to the comparatively large defects discussed above, a fine background of much smaller crystallographically oriented defects was often observed as shown in figure 3.38 and also apparent in figures 3.36 (d) and 3.15 (e). On such occasions the defect density was up to 10^7 - $10^8 cm^{-2}$ but on many films no such defects were apparent. Again it is not possible to do more than speculate on the origin of these defects. The work of Bafleur et al (1982) would suggest that there is probably no extended crystallographic defect present in the surface, leaving the possibility of a threading dislocation which could well affect the surface topography. Another possibility is that they are a transient feature, caused by, for example, localised contamination of the surface, which is rapidly grown over rather than developing into a larger defect. Finally there were occasions when the surface appeared to be textured on a very fine scale, but without any evidence of faceting as had occurred with the highly textured surfaces shown in figure 3.32. Examples of such surfaces are shown in figures 3.38 (e) and (f), 3.36 (a) and (c) and 3.37 (b) and (c).

A few epilayers were also observed using a scanning electron microscope and some typical micrographs are shown in figure 3.39. No additional detail was observed which was not already apparent in the Nomarski micrographs - at higher magnifications the picture became blurred and vibration of the specimen was very apparent. The additional depth of focus available made the identification of surface dust particles much easier and would have been useful to obtain better identification of the needle-like growths already mentioned and shown in figures 3.5 and 3.34, but no such defect was present on the epilayers examined. X-ray spectra generated by the electron beam on the sample showed the presence only of gallium and arsenic even on the most highly silicon doped layers and did not show any compositional variations at any of the observed defects.

So far only those defects directly apparent after epilayer growth have been considered, but it is well known that many defects can only be revealed by specific techniques such as preferential

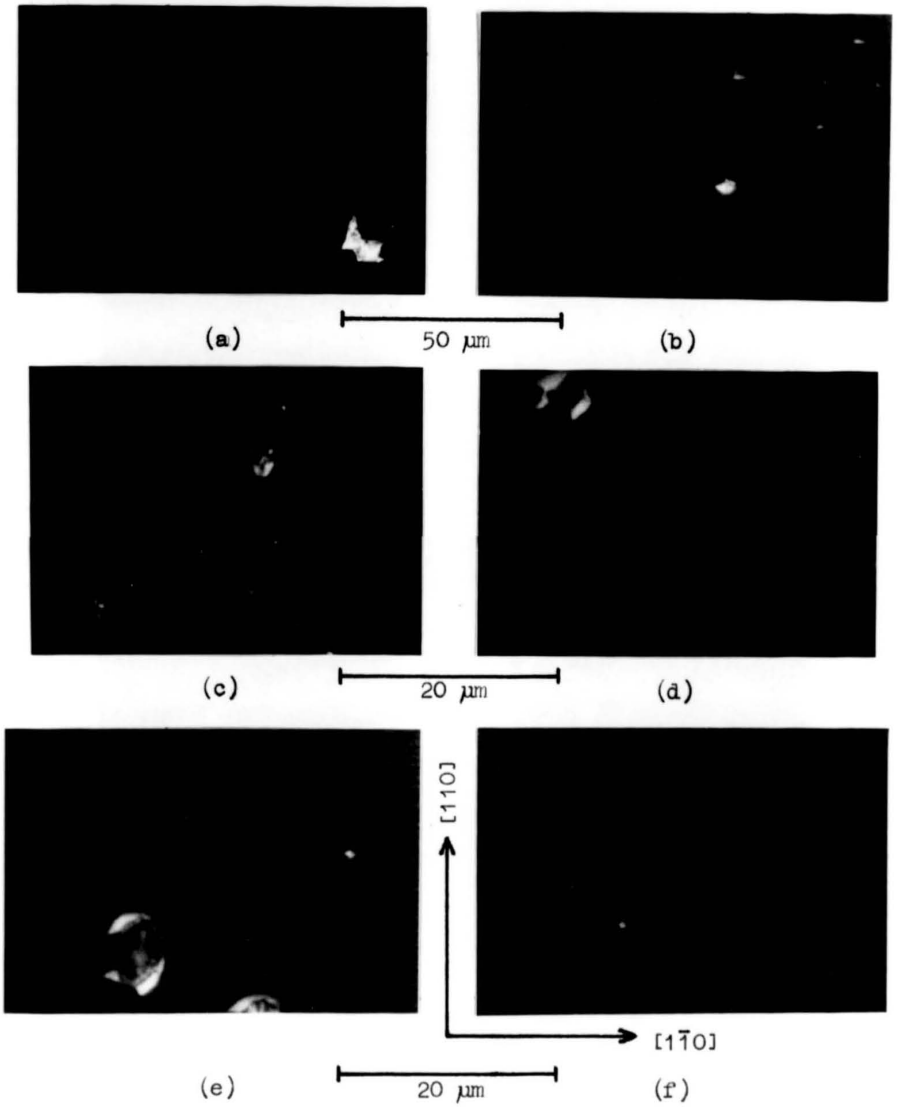

Figure 3.38 Nomarski micrographs of small background defects on MBE grown epilayers.
a-d) Various types of distinct, independent defects.
e&f) Fine background texture.

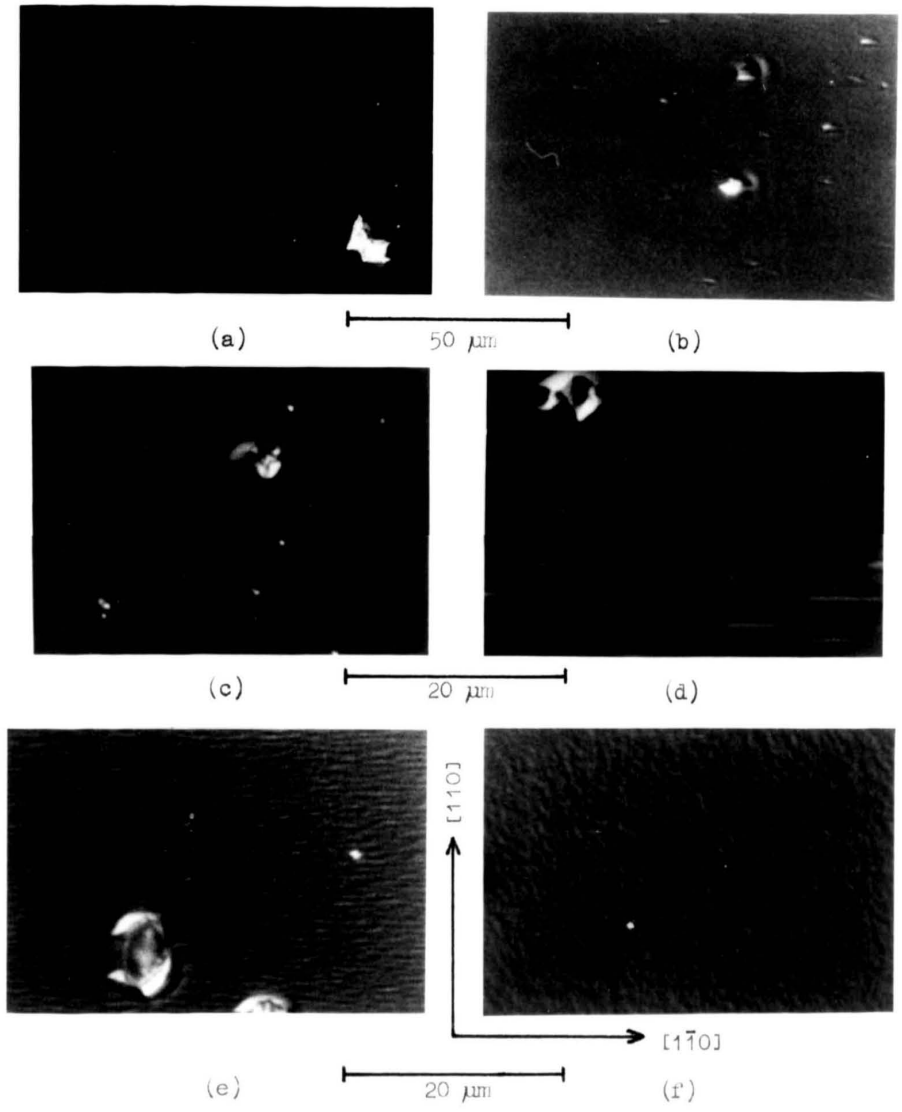

Figure 3.38 Nomarski micrographs of small background defects on MBE grown epilayers.
a-d) Various types of distinct, independent defects.
e&f) Fine background texture.

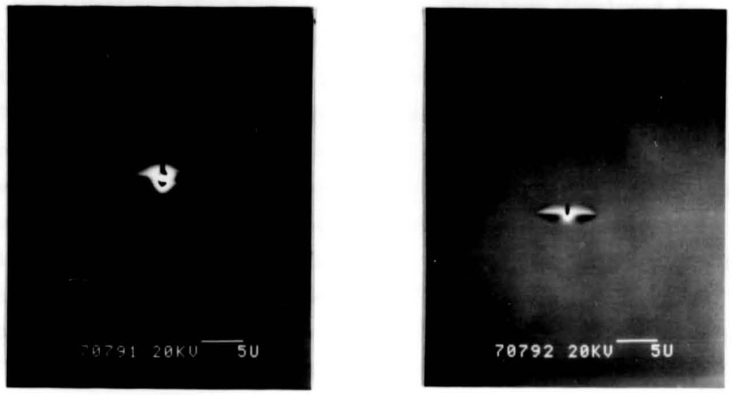

(a) (b)

(c) (d)

Figure 3.39 Scanning electron micrographs of typical epilayers.
a&b) Oval defects with no fine background apparent. Compare with Nomarski micrograph of same epilayer in figure 3.36(c).
c&d) Epilayer after HCl etch, without and with sputter deposited Au film to ensure a conductive surface in the SEM. Compare with Nomarski micrograph of the same epilayer in figure 3.38(c).

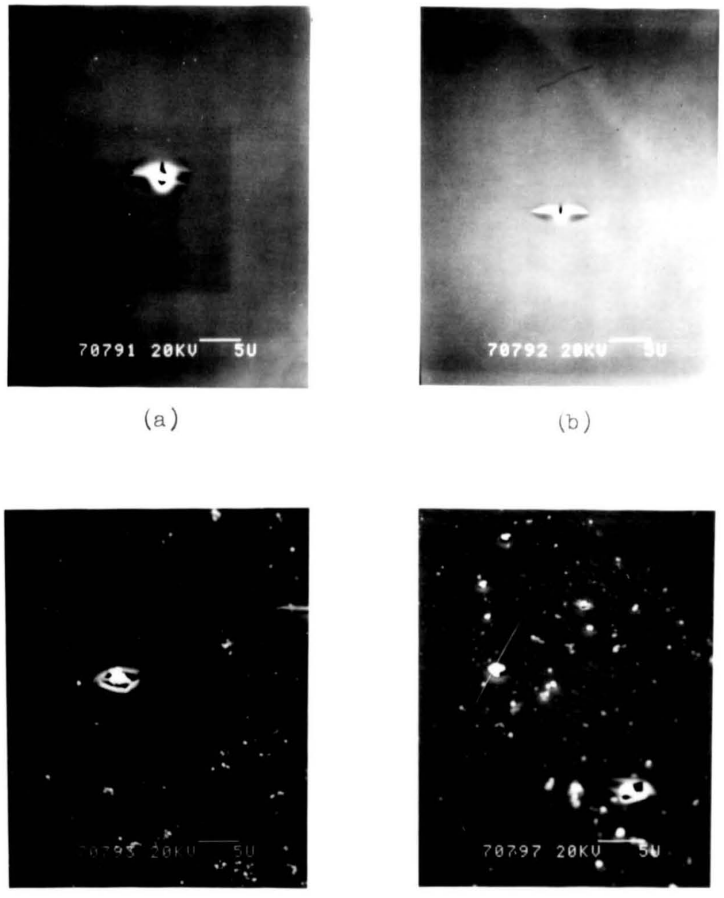

(a) (b)

(c) (d)

Figure 3.39 Scanning electron micrographs of typical epilayers.
a&b) Oval defects with no fine background apparent. Compare with Nomarski micrograph of same epilayer in figure 3.36(c).
c&d) Epilayer after HCl etch, without and with sputter deposited Au film to ensure a conductive surface in the SEM. Compare with Nomarski micrograph of the same epilayer in figure 3.38(c).

etching. Various defect revealing etches have been developed for use on gallium arsenide eg the 'ABetch' [Abrahams & Buiocchi (1965)], molten KOH, 'AHA' [Greene (1977)] and 'Tiron' [Faktor & Stevenson (1978)], as discussed by Stirland & Straughan (1976) and Miller & Rozgonyi (1980), which could be used to help identify defects. Other techniques such as transmission electron microscopy and X-ray topography could also prove useful. However, this seems to be a neglected aspect of MBE investigations, perhaps because there is no obvious, direct relation between visible defects and electrical properties, as exemplified by epilayers 79 and 80 with their widely different electron mobilities but defect densities of $1 \times 10^{4} cm^{-2}$ in both cases, although the ability to maintain a flat surface is essential in many device manufacturing processes.

If the defects are initiated by contamination rather than substrate imperfections or statistical fluctuations in the growth process then I expect that routine use of additional surface analysis equipment will be necessary to identify and eliminate the causes.

3.11 Conclusions

The results presented in this chapter have shown that, after overcoming various problems, the MBE system was capable of producing high mobility n-type films intentionally doped with silicon in the range 10^{15} - 7 x 10^{18} cm^{-3}, and with abrupt changes in doping level. Unintentionally doped material was high mobility p-type $\sim 10^{15}$ cm^{-3} with carbon as the major acceptor impurity. Whilst not conclusively proven it is believed that the major source of this carbon is the high temperature carbon source cells, which should therefore be replaced with pyrolitic boron nitride cells to reduce the carbon incorporation. Additional liquid nitrogen cryopanelling should also be fitted to reduce the flux of background species onto the growing epilayer, both of unintentional contaminants, many of which appear to be generated by the source cell heaters, and also of residual arsenic which hinders the generation of the various surface reconstructions for subsequent analyses. Separate UHV pumping of the load lock would reduce turnaround time and contamination introduced when exchanging substrates.

Further epilayers should also be grown at different (increased) substrate temperatures and with a range of Ga:As flux ratios to see how this affects the incorporation of impurities and other defects in the epilayers. The use of As_2 in place of As_4 is also expected to prove beneficial in reducing the defect density in the epilayers.

Substrate cleaning has been identified as a cause of localised defective regions in the epilayer and should be improved since it may also be the cause of additional defects throughout the epilayer. The routine use of additional surface analysis equipment is considered highly desirable for this purpose.

Several forms of visible surface defect have been observed. Some have been associated with surface contamination, but the source and nature of many remains unidentified. If the system is to be used to generate surfaces for subsequent surface analysis then the reduction and eventual elimination of these defects must be a high priority.

However the epilayers are the best yet grown in this laboratory and, although not of the best quality obtained elsewhere, they are, apart from the carbon contamination, believed to be comparable with those routinely grown in several other laboratories in the UK and elsewhere.

CHAPTER 4

Clean Surface Investigations with SIMS

All SIMS investigations carried out during this project have used argon primary ions with energies of 500 or 1000 eV. The range of these ions in the gallium arsenide sample may be calculated using the approximate rules of Schiøtt (1970) for low energy ions, assuming average values for the mass and atomic numbers of an equivalent 'gallium arsenide' atom. The calculated ranges, which should be accurate to $\sim$ 10% in non-channelling directions, are listed in Table 4.1 and it is apparent that the majority of ions are stopped within a few monolayers of the surface, and that sputtered particles will generally originate within about ten atomic diameters of the initial impact point. However it is not possible to reliably estimate the extent of, or average sputter yield from, a single collision cascade with the atomic data available.

Table 4.1 Range (in Angstrom units) of argon primary ions in gallium arsenide.

Argon ion energy	E_p	500eV	1000eV
Average range	R	24	38
standard deviation	ΔR	11	17
Projected range	R_p	12	19
standard deviation	ΔR_p	9	14
Perpendicular range	$R_\perp$	11	17

4.1 Preliminary Investigation

Initial SIMS investigations were carried out using surfaces with the C(4 x 4) As rich reconstruction grown in the MBE chamber and transferred to the SIMS chamber for analysis. Mass spectra were recorded using both the digital counter and the analogue ratemeter, the spectrum being scanned with approximately 20 points/amu.

These spectra were dominated by a large noise signal at masses above $\sim$ 150 amu, which was thought to be due to ageing of the channeltron electron multiplier and pick-up of the stray fields from the quadrupole mass filter (proportional to tuned mass) at the high mass numbers. However, subsequent replacement of the channeltron did not improve matters and the fault is believed to have been caused instead by malfunctioning of the preamplifier between the channeltron and counter. This large noise signal did not occur on later positive ion spectra, and noise present on some negative ion spectra is believed to have been caused by stray electrons which were subsequently deflected away from the electron multiplier using an external magnet and soft iron pole piece within the vacuum system. Spectra obtained using the digital counter also showed noise at the level of two counts per data point throughout the spectrum due to random resetting of the counter to either zero or two counts before each counting period. The influence of this noise on the plotted spectrum was greatly reduced by forming a running average over three sequential counts and resetting any resulting count of two to zero.

The spectra showed both matrix and contaminant species similar to those found in later spectra, but most apparent was a large increase in the Ga_2^+ secondary ion signal when the primary ion beam was unrastered. The change of this particular signal with ion dose was therefore studied by setting the mass spectrometer to this species, and observing the response when the primary ion beam was switched onto a fresh area of the surface. The resulting curve is plotted in figure 4.1 and shows an increase of more than a factor of four with primary ion dose. This observed increase was most disconcerting since the 200 amu mass spectra were obtained with a primary ion dose of 2.1×10^{13} ions/cm^2, which is sufficient to give a factor of two increase in this signal, and furthermore there is no indication of any initial 'static' region where the primary ion beam has little effect on the secondary ion signal intensity.

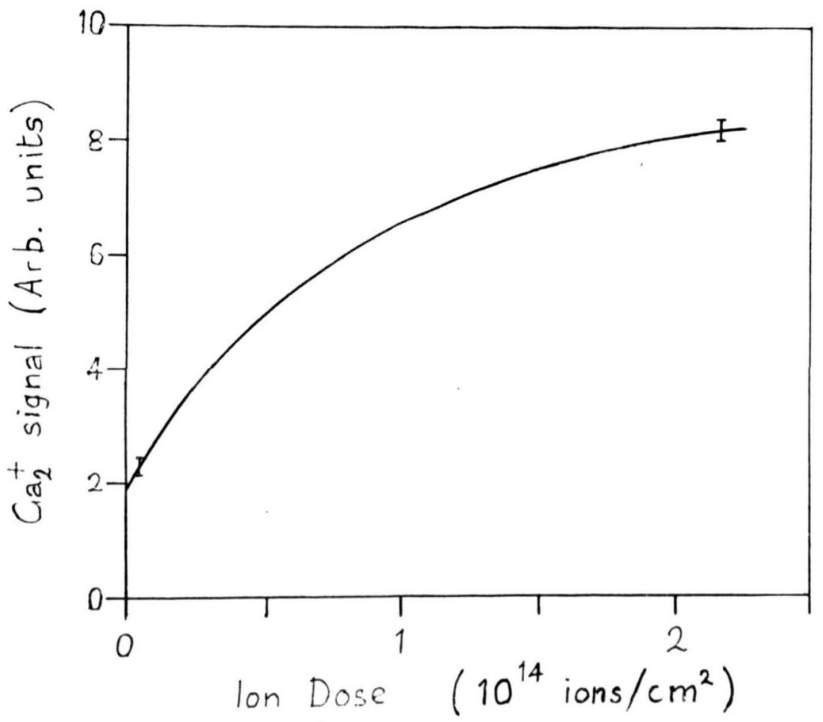

Figure 4.1 Increase in Ga_2^+ secondary ion signal with primary ion dose, for initial c(4x4) As rich surface.

The saturation effect observed at an ion dose $\sim 10^{14}$ cm^{-2} is also quite comparable with that found to produce complete amorphisation of the surface region of gallium arsenide during ion implantation at room temperature [Mazey & Nelson (1969), Townsend et al (1976), Williams & Austin (1980), Grimaldi et al (1981), Bhattacharya et al (1982)], strongly suggesting that this ion dose effect is due directly to surface damage caused by the ion beam. Previously SIMS results had been obtained from GaAs by Boyle (1984) with a primary ion dose of $\sim 10^{15}$ ions/cm^2 on each sample area, but it was reported that no primary ion dose related effects were observed. However, this could have been due to saturation of any such effects before they could be observed, or to their being dominated by residual effects from the ion bombardment and annealing procedure used to prepare the gallium arsenide surfaces, which is known to leave some residual damage [Chang et al (1981), Ranke (1983)], or, anticipating results yet to be discussed, to the primary ion beam being incident in a 'random' direction.

The results shown in figure 4.1 may be fitted, to within the experimental noise level, by an exponential curve of the form

$$I = I_o(1 - \alpha\, e^{-\sigma q})$$

where q is the total ion dose

$\sigma = 1.2 \times 10^{-14}$ cm^2 is the disordering cross section

and $\alpha = 0.77$ is a measure of the initial order

assuming that the signal is due to increasing disorder in the surface. It should be noted that the C(4 x 4) As rich surface used is expected to be totally arsenic covered (see Table 3.1) with no Ga atoms in the surface layer, let alone Ga_2 pairs, so that the detection of any Ga_2^+ secondary ion signal indicates either departure from this structure in the sputtering region or failure of the direct emission models, with sputtering of intact clusters, to adequately describe the sputtering process. Hence, unless the Ga_2^+ signal can be attributed entirely to sputtering from surface defects, there appears to be no direct relationship between this sputtered species and surface molecular groupings. The disordering cross section above is also quite comparable with the damage cross section of 2×10^{-14} cm^2 found by Harrison et al (1978) for 600 eV Ar^+ bombardment of copper.

These results showed that a much lower primary ion dose would be necessary to achieve analysis under conditions approaching the requirements of static SIMS. This was accomplished by modifying the computer control programme (MASTEP) to enable the mass spectrometer to be stepped directly between mass peaks, thus avoiding ion bombardment whilst monitoring non-integer masses where no relevant information is obtained. When using the programme, calibration must first be provided across the mass range of interest - usually common contaminants $^{7}Li^{+}$, $^{23}Na^{+}$, $^{39}K^{+}$ from the stainless steel manipulator and $^{69}Ga^{+}$, $^{115}In^{+}$, $^{140}Ga_{2}^{+}$, $^{184}GaIn^{+}$ and $^{230}In_{2}^{+}$ from the sample mounting block were used. The programme calculates intermediate mass numbers by linear interpolation between the calibration points, enabling the mass spectrometer to be stepped along integral mass numbers in the spectrum. It should be noted that although mass discrepancies, ie the difference between mass number and actual atomic weight, can be in excess of 0.2 amu over the mass range of interest, the difference in these discrepancies between different compounds with similar mass numbers is only a few hundredths of an amu, which is negligible in comparison with the resolution of the mass spectrometer and may be safely ignored.

This programme was used to obtain the mass spectra for the initial clean-surface studies presented in the next section, and oxidation studies presented in Chapter 5. Changes occurring in the various secondary ion signals with ion dose were monitored using the programme DEPRO, developed for depth profiling. Unfortunately it was not realised until these experiments were nearing completion that the use of DEPRO was causing the photon counter to start counting before the mass spectrometer was tuned to the correct mass. This error had not been apparent in the depth profiling mode due to additional gating of the secondary ion signals, but invalidated many of the ion dose dependence curves. Those presented in this thesis are expected to have fairly minor errors which will be pointed out as necessary. The final results were obtained using a re-written MASTEP2 programme, combining the mass tuning abilities of MASTEP with the cyclic measurements and individual peak selection of DEPRO, and also allowing for various changes in system hardware which had been implemented.

A computer programme for data analysis (SSPROC) was also written, compatible with the various data files produced by the different versions of MASTEP and using some parts of the plotting procedures already available, both to enable simple analysis of the spectral data and its presentation in various forms. This is required to enable comparison of the various spectra and identification of data which may provide information about the surface atomic structure present.

4.2 Initial Clean Surface Comparisons

Typical positive and negative secondary ion mass spectra obtained from the three different UHV exposed surface reconstructions with a total primary ion dose of 1×10^{13} cm^{-2} are shown in figures 4.2 - 4.4. It is significant that, even at this low total ion dose, faint square patches corresponding to the SIMS sample areas were just visible to the naked eye, under correct oblique lighting conditions, after the sample had been removed from the vacuum system. This shows that there are differences in the dielectric properties of the oxides formed on the ion bombarded and damaged regions of the sample when it is exposed to air, due either to changes in structure, or possibly changes in composition caused by preferential sputtering. However, no visible damage was apparent with Nomarski or scanning electron microscopy of the epilayer surface.

Considering firstly the positive ion spectra, the most striking difference is the variation in impurity species present, on the different surfaces. This is most apparent for the C(4 x 4) arsenic rich surface (figure 4.2(a)) where the grouping of mass peaks suggests hydrocarbon species $C_mH_n^+$ and $GaC_mH_n^+$. These species are obviously not present to the same extent on the other two surfaces which show a more similar pattern of contaminants with some hydrocarbons (CH^+, $C_2H_3^+$), common metallic contaminants (Na^+, K^+, $NaOH^+$, $GaNaOH^+$, In^+) although the In^+ signal is larger than usual on the (2 x 4) As stabilised surface, and gallium hydroxides $GaOH^+$, Ga_2OH^+. What appears to be the most significant difference between these two surfaces is the pair of peaks appearing at 99 and 101 amu on the (2 x 4) As stabilised surface. The relative heights of the pair and their persistence on other spectra indicate that this is a gallium containing species but its exact formula is uncertain; $GaON^+$, $GaCOH_2^+$ and $GaC_2H_6^+$ are all possibilities but none of these is a particularly convincing identification. Similarly the triplet appearing at 125, 127 and 129 amu also occurs elsewhere but is unidentified - $GaKOH^+$ has the correct mass numbers but the wrong isotropic ratios, and the possibility of related hydrocarbon species such as $GaC_4H_8^+$ and $GaC_3H_6O^+$ cannot be ignored.

Differences in the negative ion spectra are less marked although only contaminant species were detected as summarised in

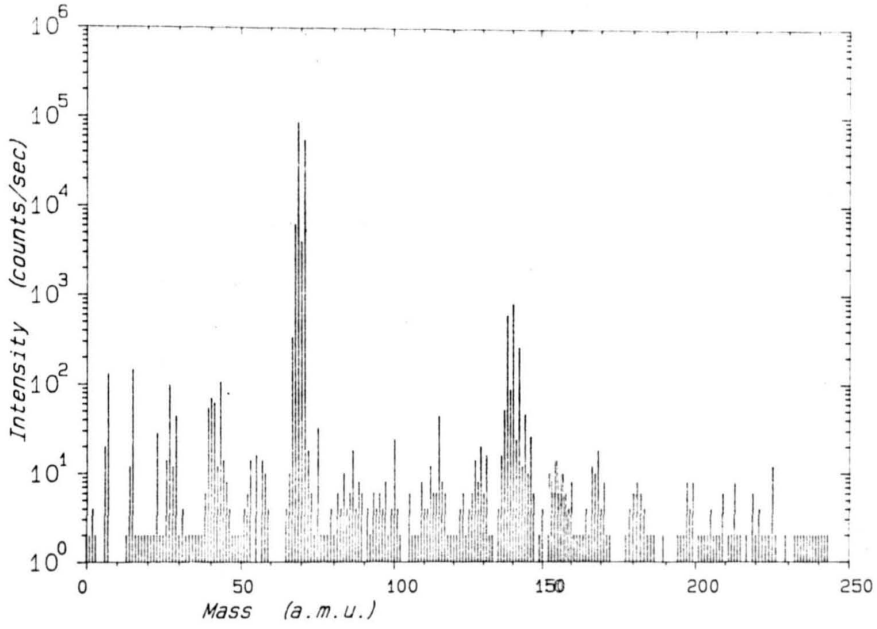

Figure 4.2(a) Positive ion SIMS of c(4x4) As rich surface

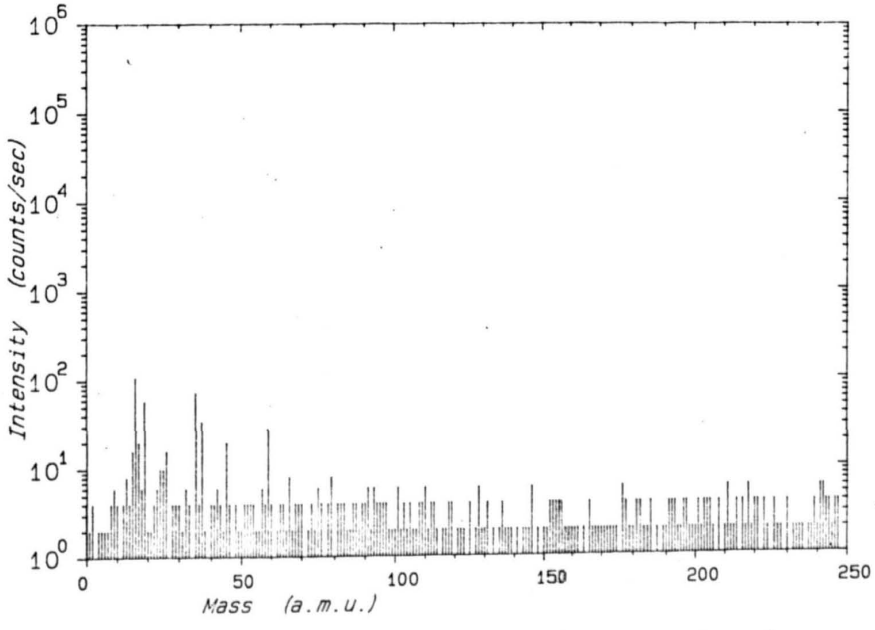

Figure 4.2(b) Negative ion SIMS of c(4x4) As rich surface

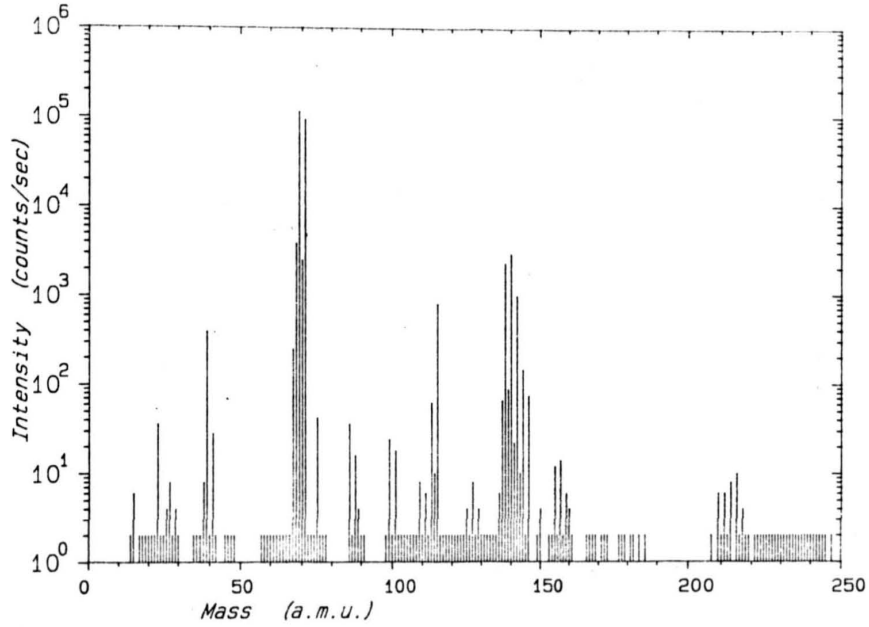

Figure 4.3(a) Positive ion SIMS of (2x4) As stabilised surface

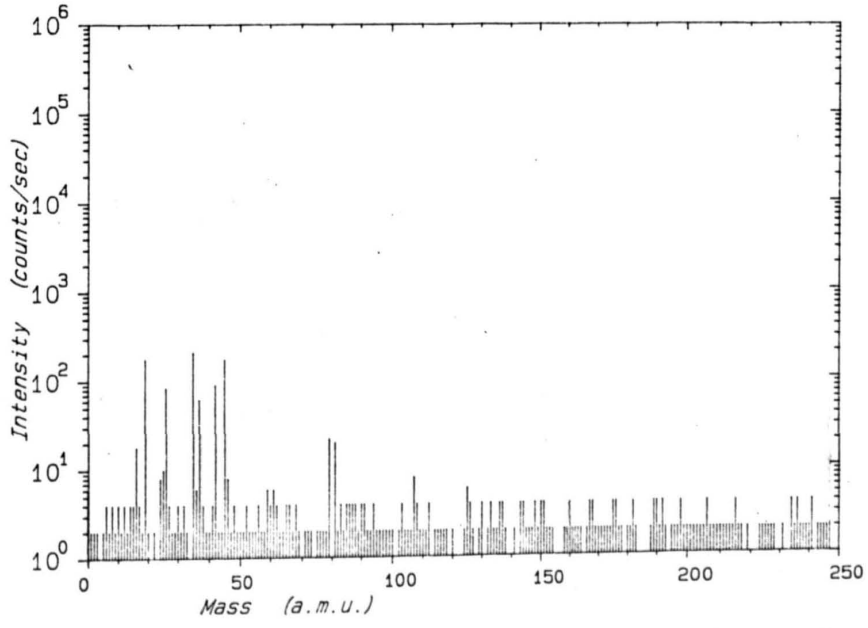

Figure 4.3(b) Negative ion SIMS of (2x4) As stabilised surface

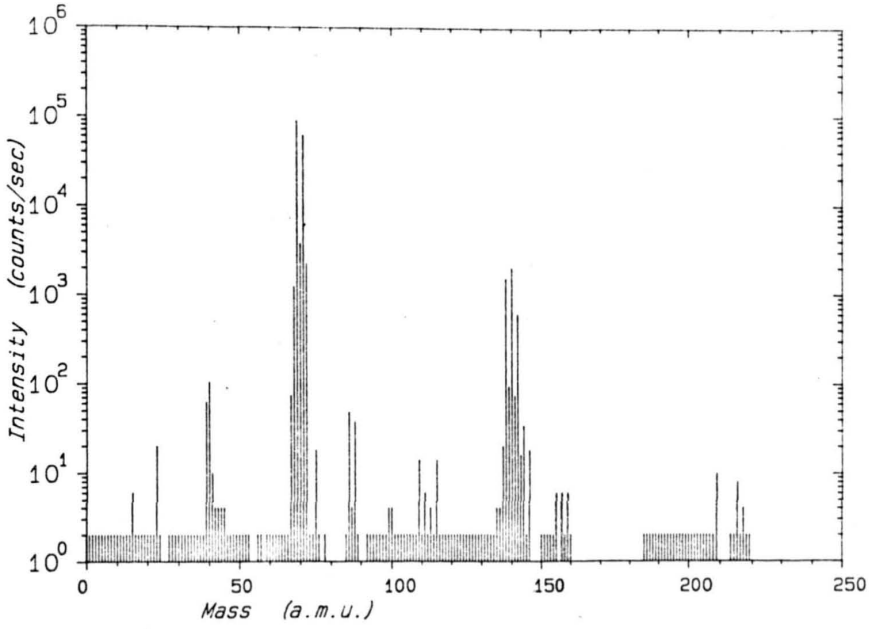

Figure 4.4(a) Positive ion SIMS of (4x6) Ga stabilised surface

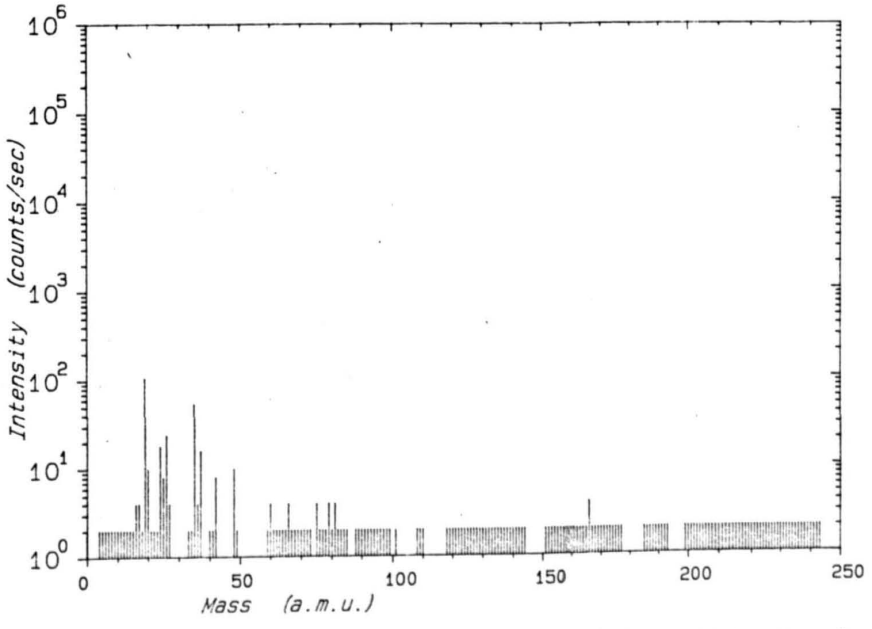

Figure 4.4(b) Negative ion SIMS of (4x6) Ga stabilised surface

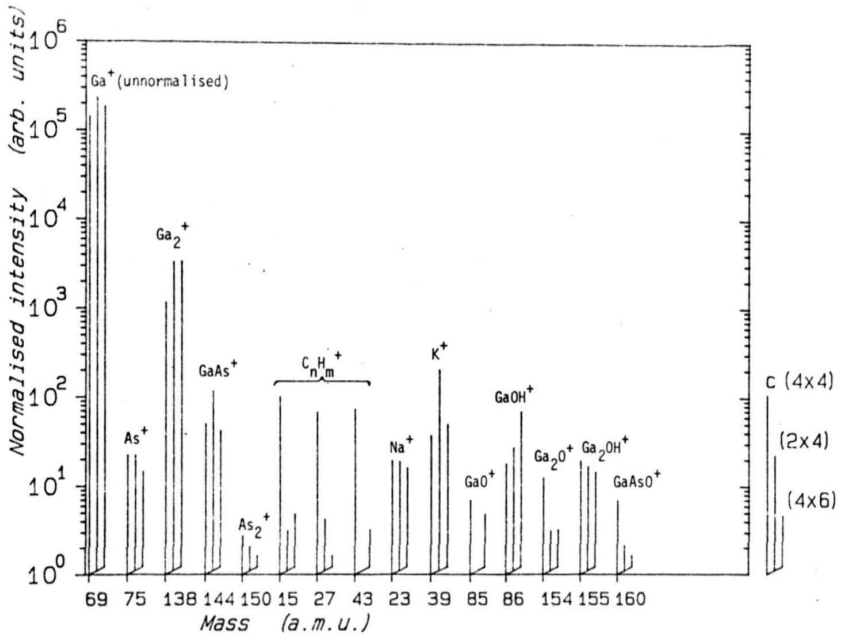

Figure 4.5(a) Comparison of positive ion SIMS spectra from differently reconstructed GaAs surfaces

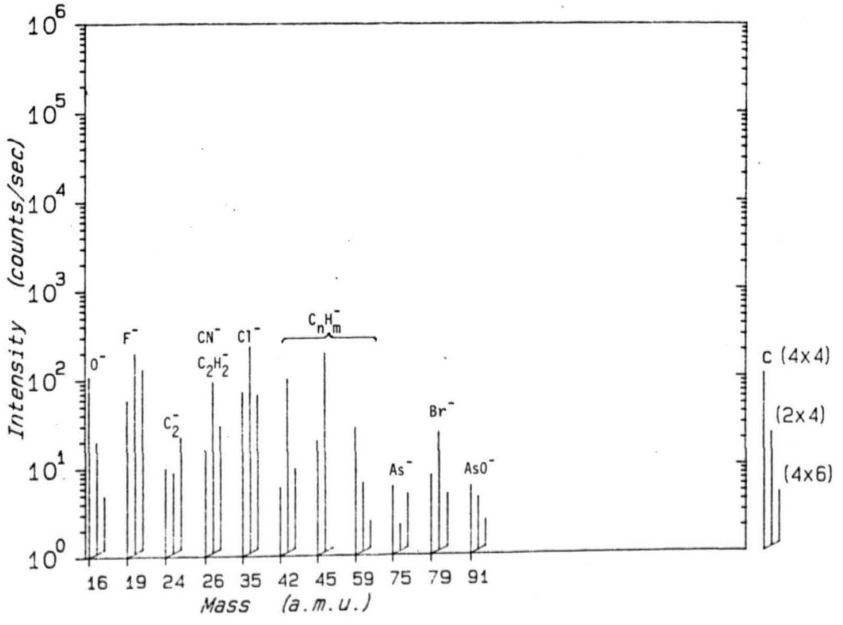

Figure 4.5(b) Comparison of negative ion SIMS spectra from differently reconstructed GaAs surfaces

figure 4.5(b). Bromine contamination is believed to originate from the potassium bromide fluorescent screens present on the sample holder and $C_3H_7O^-$ at 59 amu is characteristic of isopropanol contamination whilst 45 amu ($C_2H_5O^-$ or $COOH^-$) is generally indicative of hydrocarbons. Chlorine, fluorine and oxygen are all commonly observed contaminants within the SIMS system.

Of the three surfaces studied it was only from the (2 x 4) As stabilised surface that SIMS spectra were obtained within a few hours of the preparation of the surface. The spectra presented in figures 4.3 and 4.4, from the (2 x 4) As stabilised and (4 x 6) Ga stabilised surfaces respectively were obtained after approximately 20 hours exposure to the UHV background, and that from the C(4 x 4) As rich surface in figure 4.2 only after some 2 days. The first spectra obtained from the (2 x 4) As stabilised surface showed lower levels of contaminants, but with no major differences in the species visible. It would have been interesting to compare these spectra with a residual gas spectrum, particularly since the SIMS system had been opened to atmosphere between examining the C(4 x 4) As rich and the other 2 surface reconstructions, but unfortunately the SIMS system residual gas analyser was not working at this time.

A further complication, which also affects comparison of the matrix species present in the SIMS spectra is variation in the mass spectrometer response between the different surfaces. The mass spectrometer controls were set to the same values for the (2 x 4) As stabilised and (4 x 6) Ga stabilised surfaces but different values had previously been used with the C(4 x 4)As rich surface. The intention at the time was to achieve the same resolution in all cases and it was thought that the variation from the previous settings could be due to changes in the high frequency power connections to the mass spectrometer. However, it is apparent from the mass spectra obtained from the three surfaces that the relative height of peaks tuned 1 or 2 amu away from a major mass peak (eg Ga, Ga_2) which are indicative of the peak shape rather than ions of the tuned mass, are not constant. This can only be explained as a variation in the mass resolution and/or tuning of the mass spectrometer, and hence in the overall transmission and sensitivity to the different surfaces. It should be noted that when the mass tuning was checked on later occasions drifts of up to 0.2 amu were sometimes

observed, which would have a noticeable effect on the transmitted signal with the high resolution and sharp mass peaks used. However in the absence of any correction terms for the above effects the spectra must be compared directly to obtain any information on the different surface types.

Figure 4.5(a) shows the relative intensities of the various matrix signals, normalised to Ga^+, obtained from the three surface types. It is apparent that for each surface type only one matrix secondary ion signal is significantly different in intensity from that generated by the other two surfaces. These are:

reduced As^+ from the (4 x 6) Ga stabilised surface,
increased $GaAs^+$ from the (2 x 4) As stabilised surface,
reduced Ga_2^+ from the C(4 x 4) As rich surface.

The As_2^+ signal also appears to decrease with decreasing arsenic coverage, but here the total counts are too low to be statistically significant.

The relative intensities of these secondary ion signals are in marked contrast to the measurements of sputtered neutral species by Comas & Cooper (1967) and Oechsner (1984 and private communication) where Ga° and As° were found to be of similar intensity. However, the two investigations found different molecular intensities. Oechsner detected As_2° and GaAs° at ~1% and 0.02% respectively of the atomic signal strengths, whilst Comas & Cooper found only GaAs° at ~2% of the atomic signals. Atom probe measurements by Cerezo et al (1985) show various molecular arsenic species - the precise spectrum depending on whether a voltage or laser pulse is used to stimulate field desorption of the positively charged ions - but only atomic gallium, and no GaAs containing species. Taken together, these results suggest that the method of generating molecular secondary particles may be as important as the atomic surface structure in determining which species are actually formed.

One further point is that the highest absolute Ga^+ intensity was obtained from the (2 x 4) As stabilised surface. This may correlate with the results of Massies et al (1979) showing this reconstruction to have the largest work function of the three surfaces

and the correlations of SIMS intensity with work function discussed in Section 4.4.

Variation of the secondary ion signals with primary ion dose is shown in figure 4.6, and the preliminary results shown in figure 4.1 are replotted on this logarithmic scale for comparison with the later results. For all reconstructions the Ga^+ signal decreases slowly with ion dose whilst the Ga_2^+ signal increases, consistent with this latter signal being due to ion induced disorder in the sample. However the smaller increases apparent from the surfaces with lower arsenic coverage suggest that surface composition, and its variation due to preferential sputtering of arsenic (see eg Singer et al (1981), Barcz et al (1980) and references therein), may also be significant in the generation of this Ga_2^+ signal. Fitting the curves with a function of the form $I = I_o(1 - \alpha e^{-\sigma q})$ as before gives the parameters listed in Table 4.2, with the preliminary results obtained using 1 keV primary ions included for comparison. Similar results were obtained from C(4 x 4) As rich surfaces at current densities of 200 and 10 nA/cm^2 so the differing current densities are not expected to be significant. The wide range of α found for the different surfaces indicates that this signal is unlikely to be due entirely to disorder in the surface, but an interpretation involving the sputter removal of a surface arsenic layer seems more feasible, with Ga_2^+ being characteristic of the underlying matrix. However, the absence of any comparable increase in the Ga^+ signal or decrease of the As^+ signal shows that this cannot be the complete answer, and a combination of the two effects may be more appropriate. Tentative theories for the structure of the (4 x 2) Ga stabilised surface invoke Ga-Ga surface dimers but such bonding is not expected on the (2 x 4) As stabilised surface [Cho (1976), Larsen et al (1982), Harrison (1979)] or in the bulk lattice. A possible explanation is to combine first order sputtering artefacts with surface composition such that Ga_2^+ is generated as a first order artefact (by recombination processes) from any gallium arsenide surface, and that the probability of this species occuring by recombination or direct sputtering increases with initial disorder and reduced arsenic content in the surface layers. The reduced cross section apparent for the C(4 x 4) As rich reconstruction could then be explained as due to a thick arsenic

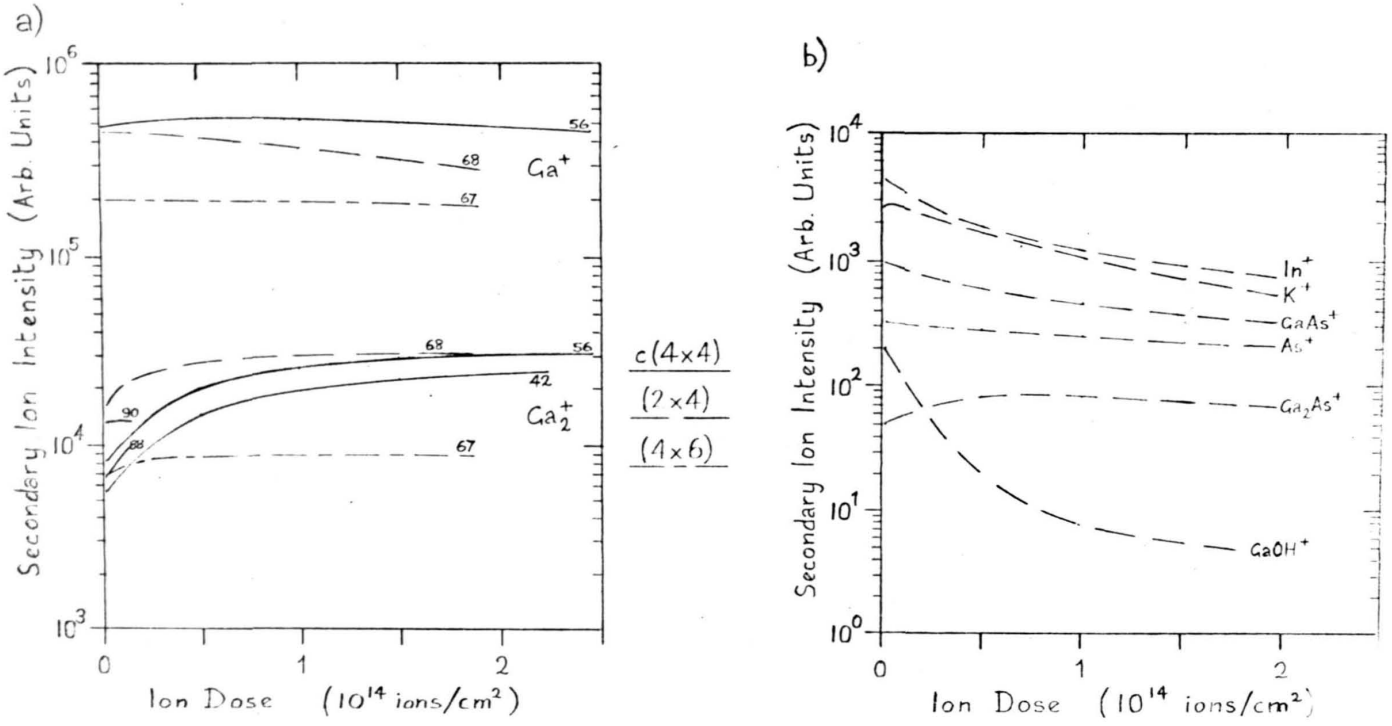

Figure 4.6 a) Ion dose dependence of Ga^+ and Ga_2^+ secondary ion species.
b) Ion dose dependence of other positive secondary ion species.
Note: Results from epilayers 88 and 90 are referenced to a Ga^+ signal of 5×10^5, similar to that of epilayer 56.

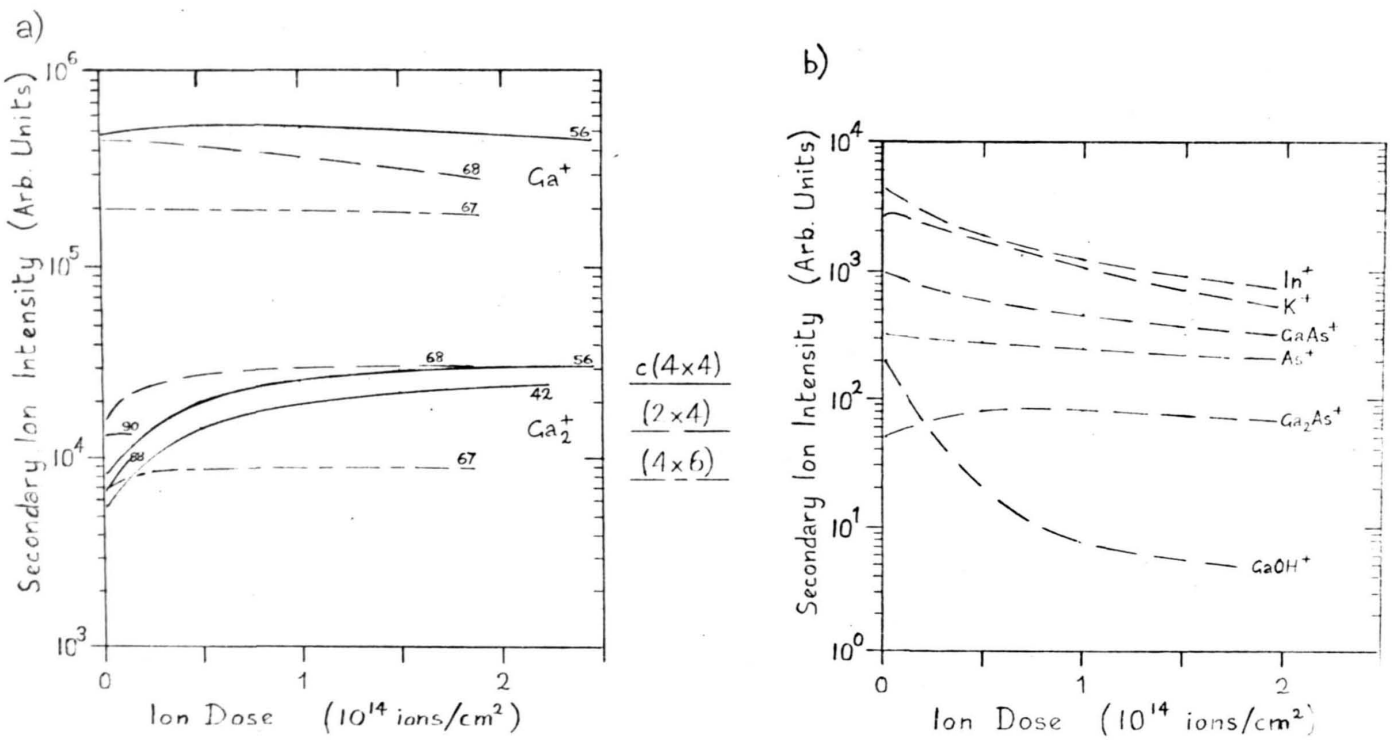

Figure 4.6 a) Ion dose dependence of Ga^+ and Ga_2^+ secondary ion species.
b) Ion dose dependence of other positive secondary ion species.
Note: Results from epilayers 88 and 90 are referenced to a Ga^+ signal of 5×10^5, similar to that of epilayer 56.

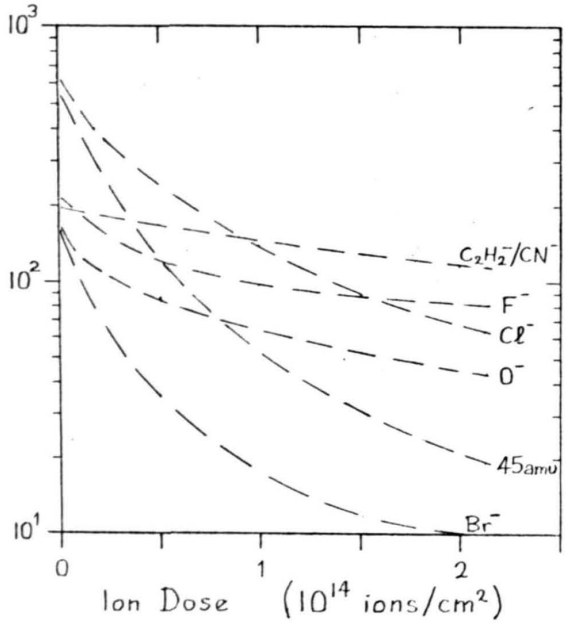

Figure 4.7 Ion dose dependence of negative secondary ion species.

Table 4.2 Variation of Ga_2^+ secondary ion signal with primary ion dose

Surface type	Primary ion energy and current density (eV , nA/cm^2)	I_o (s^{-1})	α	σ ($10^{-14} cm^2$)
c(4x4) As rich	1000 , 50	20000	0.773	1.2
c(4x4) As rich	500 , 100	31500	0.715	1.4
(2x4) As stab.	500 , 30	28500	0.386	4.5
(4x6) Ga stab.	500 , 30	8800	0.250	5.0

The secondary ion response is fitted with a curve of the form $I = I_o (1 - \alpha e^{-\sigma q})$

where q is the total ion dose

and, assuming the change is due to disorder,

σ is a disordering cross section

and α a measure of initial order; or alternatively,

if the change is due to desorption of a shielding layer,

σ is the desorption cross section

and α a measure of the initial coverage.

coverage, partially incorporated in the disordered surface region during sputtering. Careful measurements with different techniques would be essential to separate out the various aspects of surface erosion, recoil implantation, preferential sputtering, bombardment induced disorder and secondary ion formation inherent in this suggestion.

Other secondary ion species emitted from the (4 x 2) As stabilised reconstruction are also shown. The rapidly decreasing $GaOH^+$ signal shows that this is either formed from a weakly bound adsorbate, with a desorption cross section of 5×10^{-14} cm^2, or that the parent hydroxide is rapidly destroyed by the ion beam [Chuang et al (1979)]. Potassium and indium are also apparent as surface contaminants with desorption cross sections of 1.2×10^{-14} cm^2 and 2×10^{-14} cm^2 respectively, but the departure from linearity of the logarithmic plots indicates that they are also present as bulk contaminants. In contrast, the constant value of the 109 amu signal indicates that this is probably a bulk contaminant and, if the identification of $^{69}GaNaOH^+$ is correct, shows that sodium is present in oxidised form in the MBE grown epilayer; however, the possibility of it being $^{69}GaAr^+$ cannot be eliminated at present, and the use of other primary ion species would be useful to obtain an indication of the reactivity of excited noble gas atoms and ions with the matrix species present. Matrix species As^+ and $GaAs^+$ both decrease slowly whilst Ga_2As^+ increases initially - similar to Ga_2^+ - before decreasing slowly.

The ion dose dependence of typical negative secondary ion signals is shown in figure 4.7. The rapid decrease of the Cl^-, Br^-, and $C_2H_5O^-$ signals confirms that these are surface contaminants with desorption cross sections of $\sim 4 \times 10^{-14}$ cm^2. The slower decrease of $C_2H_2^-/CN^-$, O^- and F^- signals indicates either more strongly bound species, influence of residual gas reaction with the sputtered surface, or the presence of a bulk contaminant.

4.3 Further Clean Surface Comparisons

Further results were obtained from additional UHV grown surfaces in the attempt to elucidate the results presented above. Preliminary results (see figure 4.8) obtained whilst gaining familiarity with the system and correcting errors in the new software showed different impurity species, notably CH_3^+ and $GaCH_3^+$, in the SIMS spectra, not previously observed, but this is probably due to transferring the substrate whilst the SIMS system was still warm following bakeout and consequently with higher partial pressures of residual contaminants, as indicated in the residual gas spectrum of figure 4.9(a) obtained some hours before transferring the sample. However, variation of secondary ion signals with ion dose was found to be similar to that previously observed with C(4 x 4) As rich surfaces. It also became apparent that resetting the mass spectrometer resolution and ΔM controls to the same values did not always provide the same mass resolution as is evident from the two spectra in figure 4.8 obtained with the same mass spectrometer settings at different times. Changes in signal amplitude of up to a factor of two were also observed at high masses due to inaccuracies in the resetting of the mass spectrometer controls and it was decided that the quadrupole resolution and ΔM controls should be set and then left unchanged throughout any series of comparative investigations. The resolution selected was similar to that used in the initial study, giving good resolution of adjacent mass numbers as required for oxidation studies (see Chapter 5) and identification of the different secondary ion species. It is apparent from the spectra shown in figures 4.10 - 4.12 that there is less variation in mass resolution than occured during the initial study. However, there was insufficient time to investigate oxidation of these surfaces and, for the matrix species actually studied, it would have been better to have used a lower mass resolution to obtain higher secondary ion count rates and minimise the effect of any drifts in tuning of the mass spectrometer, whilst still maintaining adequate resolution between gallium and arsenic containing species.

Deliberate changes in sample position produced changes of only $\sim$ 10% in secondary ion currents as did tuning the energy filter to Ga^+ or Ga_2^+. Rotation of the sample through $\sim 10°$, which has been reported by Bedrich et al (1982) to have a large effect on

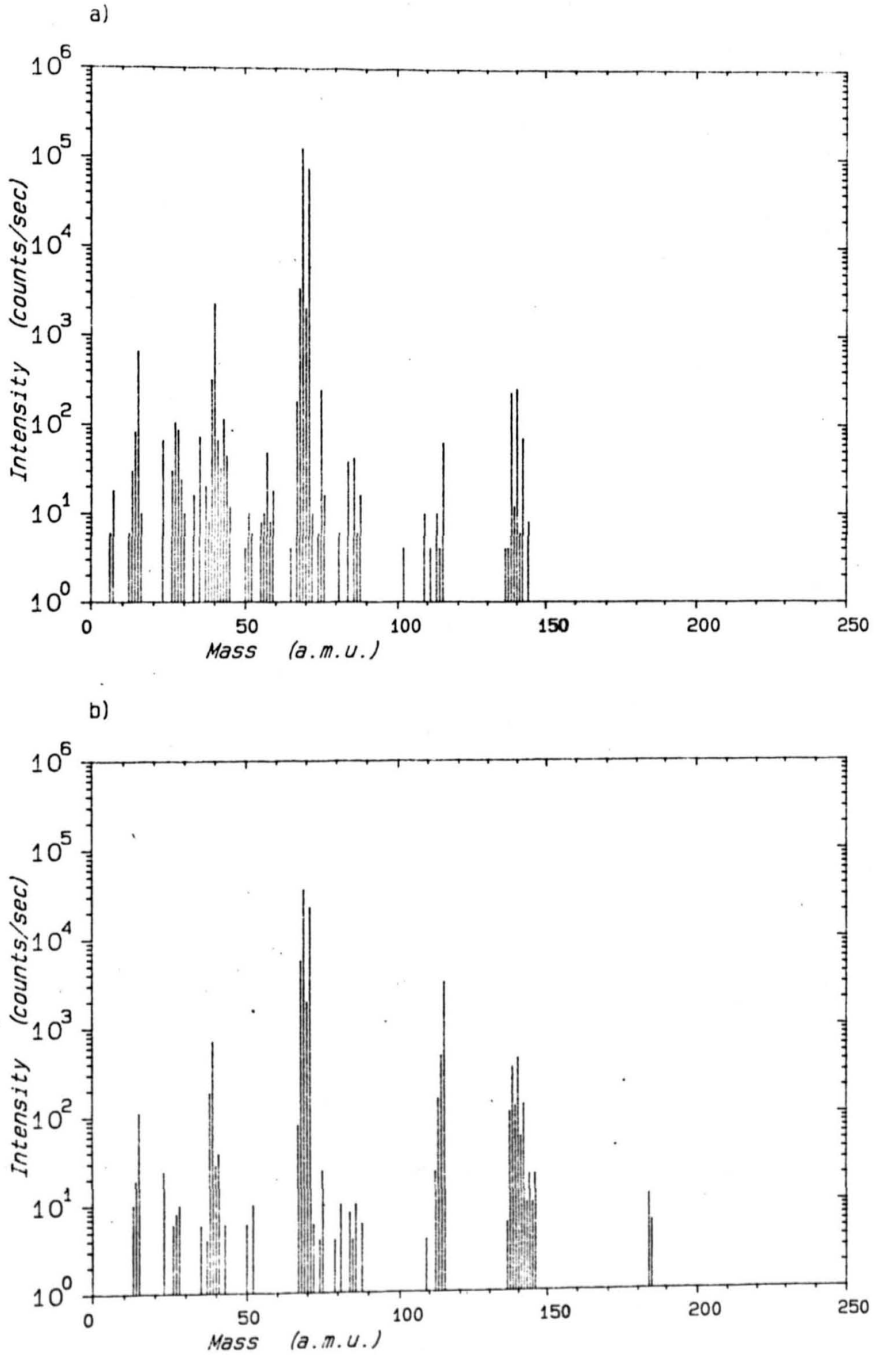

Figure 4.8 Positive ion SIMS spectra from c(4x4) As rich surface obtained at different times with same instrument settings.

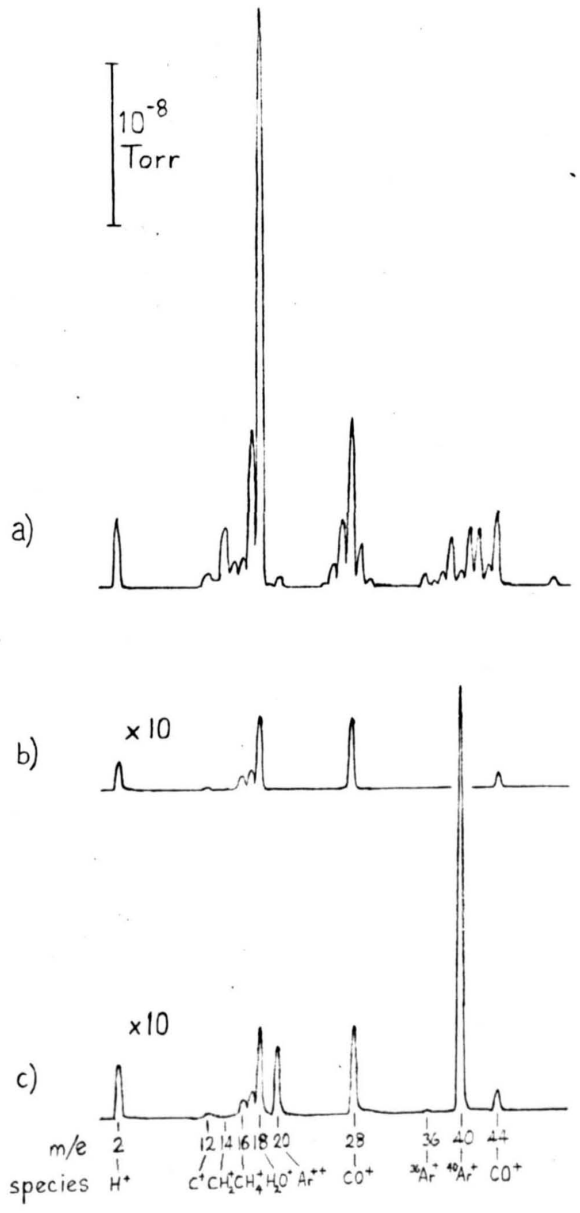

Figure 4.9 SIMS system residual gas spectra.

a) System warm from bakeout

b) Typical cold system.

c) Typical during SIMS analysis.

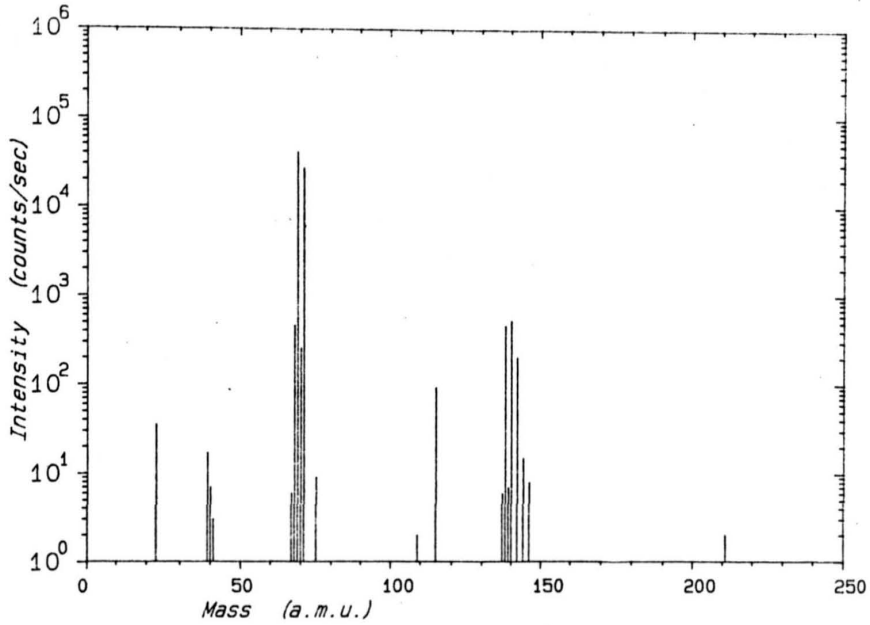

Figure 4.10 Positive ion SIMS of c(4x4) As rich surface.

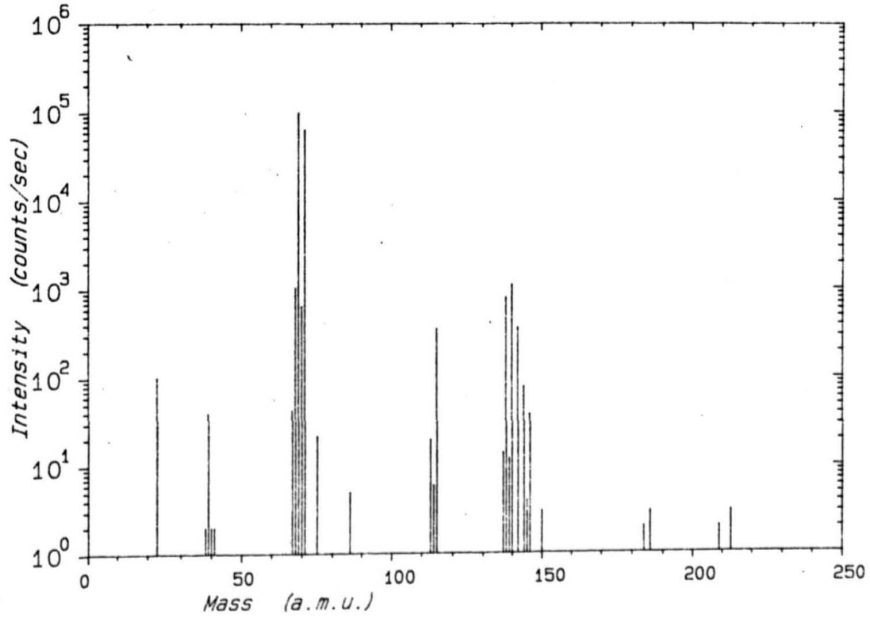

Figure 4.11 Positive ion SIMS of (2x4) As stabilised surface.

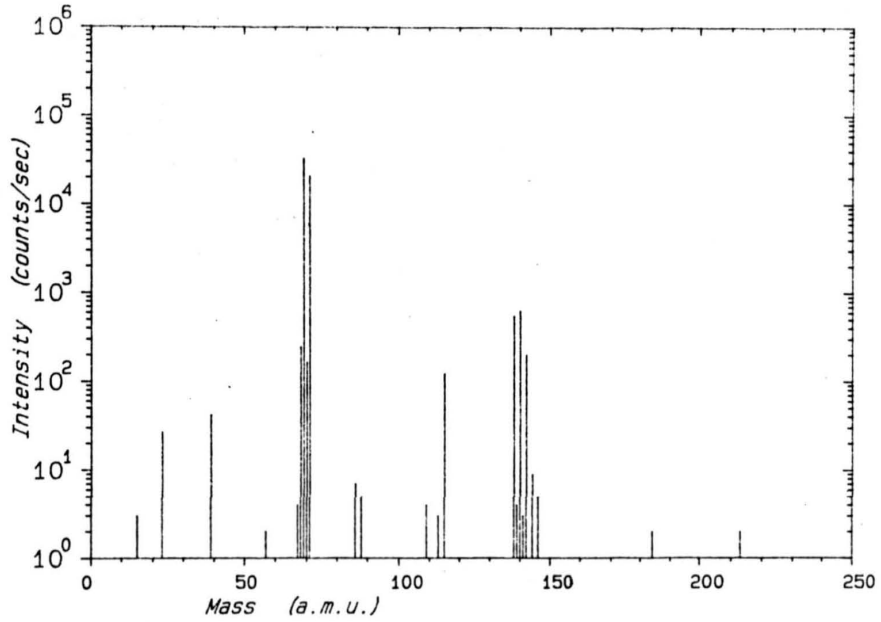

Figure 4.12 Positive ion SIMS of (4x6) Ga stabilised surface.

secondary ion currents, produced only a 20% change in intensity with relative changes between species < 10%. On other occasions, when no deliberate attempts were made to alter the SIMS conditions, changes of up to 30% were found in spectra from adjacent sample areas, but this is much less than the factor of two found during the initial measurements on clean and oxidised surfaces.

Problems were also encountered with stability of the primary ion current. In extreme cases this was visible as synchronous variations in secondary ion signals, and the mass spectrum was repeated after readjusting the primary ion column. However, there was in addition an unexplained, variable offset on the two most sensitive ranges of the current meter, which was simply subtracted away from the indicated reading when setting the primary ion current. It was later found, during the comparative studies to be described, that this offset only occured when the sample holder was connected to the meter and its potential set by a D to A converter in the microcomputer, and that the error in indicated current was less than this offset. Corrections have been made for this effect but errors of ~20% seem likely. The original cause of the offset would appear to be rectification of alternating current generated by digital noise on the sample potential, and this requires further investigation for accurate measurement of low ion currents, using computer control of the sample potential.

One major problem which became apparent during the series of measurements was the sensitivity of the photon counter to electrical interference, with spurious signals causing it to stop or start before receiving the relevant signal from the computer. This was most frequent during the middle of the day and did not occur when the building was otherwise unoccupied. Whilst this fault on its own would be an annoyance causing loss of individual data points, it is compounded by the computer control, which will wait indefinitely, after sending a stop command, for data which may already have been sent. The result is that the system will "freeze-up" indefinitely, waiting for this data until the photon counter is manually restarted, and this can occur at any stage during the recording of secondary ion data, thus invalidating measurements of ion dose and allowing possible residual gas reactions with the sputtered surface. I consider it essential that this fault is rectified before attempting further static SIMS investigations.

4.3.1 Adsorption of Impurity Species

The positive ion SIMS spectra shown in figures 4.10 - 4.12 exhibit lower levels of impurity species than the earlier spectra of figures 4.2 - 4.4 and 4.8. Only alkali metals, indium and GaOH are identifiable in these spectra in contrast to the various hydrocarbon and oxide species previously observed. This may be due both to the low level of residual impurities present in the SIMS system, as evident from the residual gas spectra of figure 4.9, and the more rapid examination, generally within 2 hours of preparation, of the gallium arsenide surfaces. Only a small increase in impurity species was observed on those surfaces which were re-examined after 24 hours' exposure to the UHV background, with no additional species appearing in the spectra. The negative ion spectra are also very similar from the different surface reconstructions, showing only impurity species and with a slight increase apparent after 24 hours' exposure to the UHV background.

Measuring the dependence of these secondary ion signals on primary ion dose gave desorption cross sections $\sim 10^{-14}$ cm^2 for Na, K and In, and $\sim 2 \times 10^{-14}$ cm^2 for GaOH positive ion species, and $\sim 2 \times 10^{-15}$ cm^2 for O, Cl, F and C_2H_2 negative ion species, with little variation between different surfaces examined under the same conditions of ion bombardment. The reduced cross sections compared with previous measurements may indicate reduced levels of weakly bound contaminants with a correspondingly greater influence of bulk contaminants and residual gas reactions with the ion bombarded surface.

4.3.2 Matrix Secondary Ion Comparison

The 250 amu range SIMS spectra considered so far were obtained with a total primary ion dose of 1×10^{13} cm^{-2}. By observing only $^{69}Ga^+$, $^{75}As^+$, $^{140}Ga_2^+$, $^{144}GaAs^+$, and $^{150}As_2^+$ (the latter for 10 seconds to increase the total count) a spectrum was obtained with an ion dose of only 5×10^{11} cm^{-2}. Cycling the measurement sequence showed little change of secondary ion signals with ion dose on any of the surfaces over several cycles (ion dose effects will be discussed in Section 4.3.3) and averaging these readings improves the reliability at low counts. $^{225}As_3^+$ was also monitored for a 10 second period, increasing the ion dose

per cycle to 1 x 10^{12} cm^{-2}, but the count for this species was usually not more than two for all surfaces, and showed no variation with surface type even when the primary ion current was increased from 0.5 to 3 nA, although the count did then increase but remained less than 10. Relative count rates for the different surfaces are shown in figure 4.13.

It will be seen that the three surface reconstructions of epilayers 91, 92 and 93, grown sequentially on the same substrate, exhibit variations in relative signal strengths similar to those found in the initial study (figure 4.5). However, the (4 x 6) Ga stabilised surface shows relatively higher levels of As^+ and As_2^+ contrary to the previous tentative finding of decreases of these species with decreasing surface arsenic composition, and the (2 x 4) As stabilised surface shows a Ga_2^+ signal similar to that obtained from the C(4 x 4) As rich surface rather than that from the (4 x 6) Ga stabilised surface. Two conclusions which are confirmed by these results are the higher absolute Ga^+ and relative $GaAs^+$ signals from the (2 x 4) As stabilised surface.

Variation in the relative secondary ion signals from the different C(4 x 4) As rich surfaces is of similar magnitude to the variation observed between spectra obtained from different sample areas on a single epilayer and further work is necessary to determine the cause of this variation. Whether it is caused, for example, by changes in surface composition due to randomly adsorbed arsenic, or by minor changes in SIMS parameters. It is notable that the array of crystallographically oriented defects present on epilayer 93 (figure 4.14), but not on the other surfaces studied, did not appear to have any major effect on the SIMS spectra obtained from this surface. The similarity of the results obtained from the different surface reconstructions may also be interpreted as an indication that there is little difference in the composition of these surfaces, although an alternative explanation could be the influence of microscopic defects as discussed in Section 4.4.

Increasing the primary ion current from 0.5 to 3 nA had little effect on relative secondary ion currents except for the (4 x 6) Ga stabilised surface where the As^+ and As_2^+ signals rose by a factor of 3 compared to the other species monitored, and the

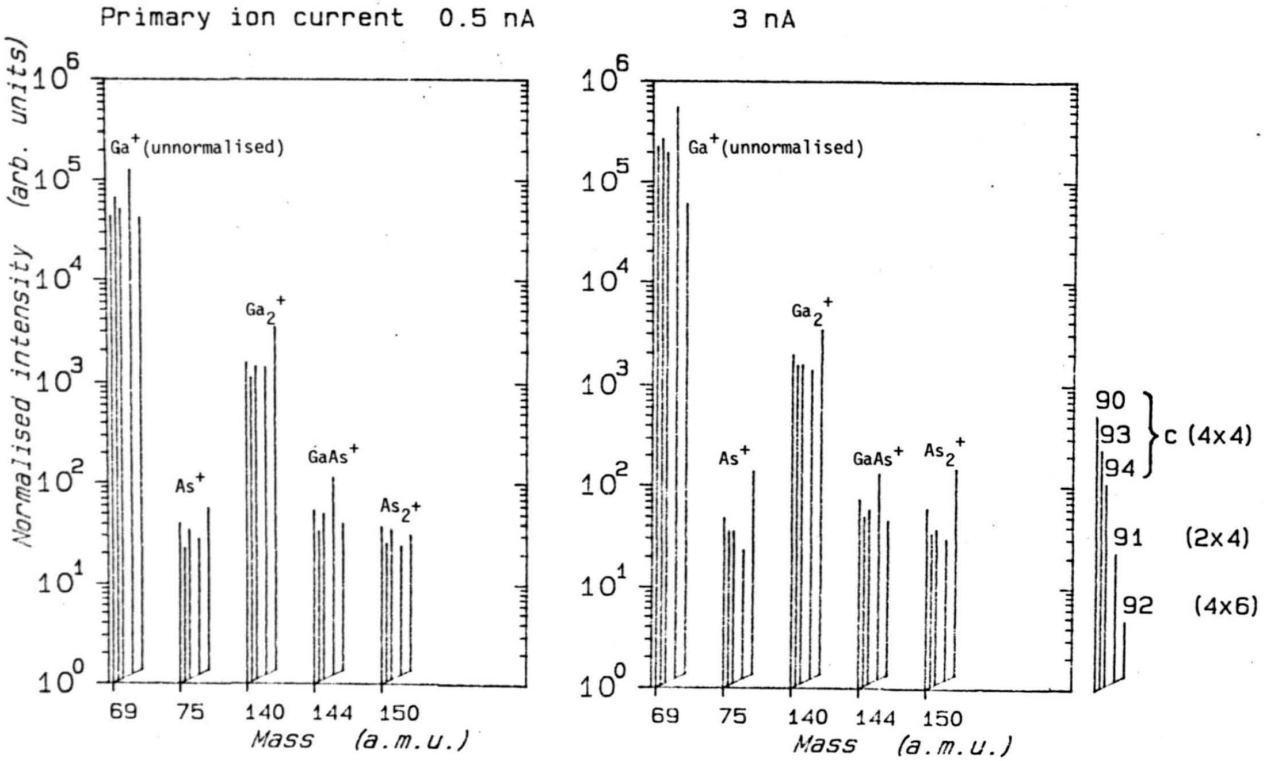

Figure 4.13 Comparative SIMS spectra of reconstructed GaAs surfaces.

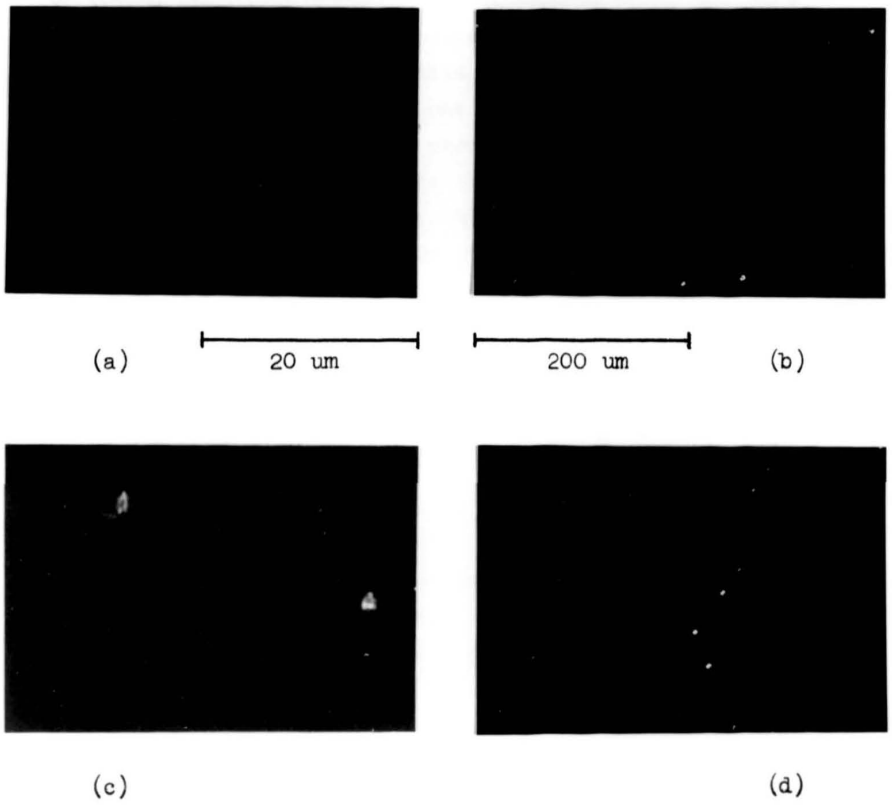

Figure 4.14 Nomarski micrographs of MBE grown surfaces used for SIMS analysis.
a&b) Epilayer 93. Epilayers 90-93 were grown sequentially on the same substrate without exposing the surfaces to air, or microscopic observation.
c&d) Epilayer 94.

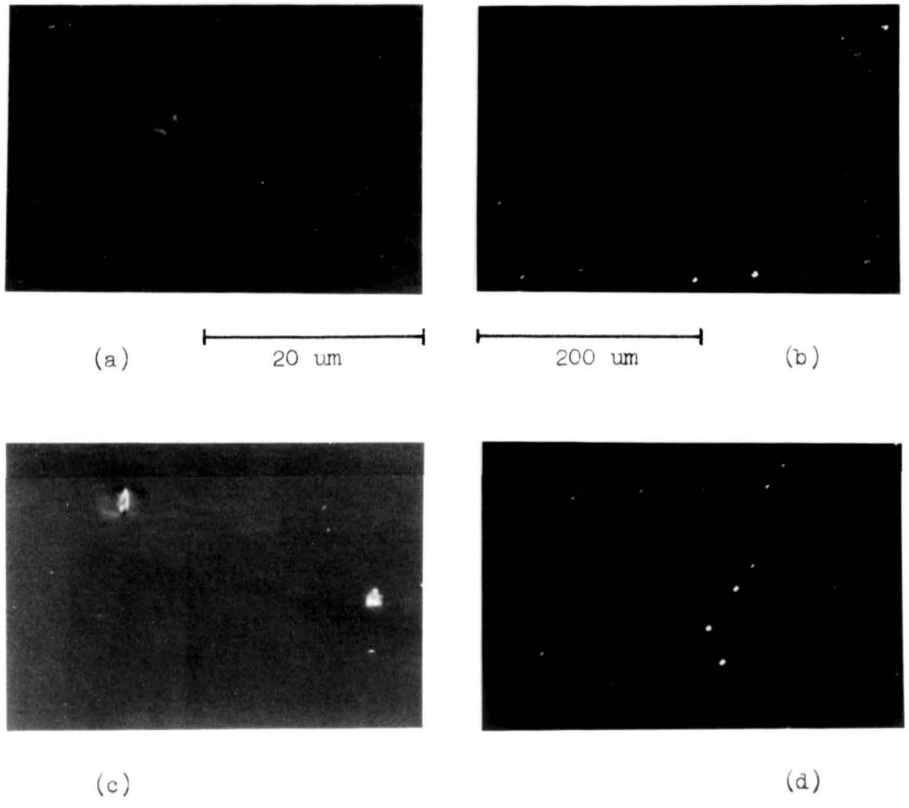

Figure 4.14 Nomarski micrographs of MBE grown surfaces used for SIMS analysis.
a&b) Epilayer 93. Epilayers 90-93 were grown sequentially on the same substrate without exposing the surfaces to air, or microscopic observation.
c&d) Epilayer 94.

Ga^+ signal was hardly changed from that measured at 0.5 nA. This may be indicative of increased sputtering of subsurface atoms at the higher current density, but why this should occur only on the (4 x 6) Ga stabilised surface is not understood.

The primary ion energy was also increased to 1 keV on one C(4 x 4) As rich surface, and here the Ga_2^+, As^+ and As_2^+ signals increased by a factor of two compared to Ga^+ and $GaAs^+$ signals. A possible explanation is increased disorder (and first order artefacts) due to the higher energy primary ion beam, coupled with increased preferential sputtering of arsenic. However, these various signals, normalised to Ga^+, changed very little with ion dose, suggesting that changes in secondary ion emission coefficient with primary ion energy are more likely to be responsible. Dawson (1976) found large but unexplained changes in relative secondary ion yields from aluminium on varying the primary ion energy in the range 150 - 1500 eV. In addition Yu (1978b) has found significant differences in the evolution of secondary ion signals with oxygen exposure of tungsten and molybdenum surfaces, dependent on primary ion energy in the range 150 - 2000 eV. These differences have been attributed to increased perturbations to the electronic structure of the surface in the vicinity of the collision cascade at higher primary ion energies. However, computer simulations [Harrison (1983), Webb & Harrison (1982), Winograd et al (1979)] of the sputtering process exhibit threshold energies for various specific sputtering mechanisms, which leads directly to changes in relative secondary ion yields at different primary ion energies. Reasonable agreement between theory and experimental results has been obtained in the limited comparisons undertaken [Winograd et al (1979)].

Barcz et al (1982) have observed changes in secondary ion yields from heavily doped gallium arsenide and other materials dependent on the instantaneous current density within the spot of a rastered ion beam, although the average current density of the rastered area was kept constant, and Wittmaack (1981), (1976) has attributed similar effects to ionisation occurring after the sputtering event. No attempt was made to identify or investigate any such dependence during this project, although the possible influence of primary ion induced disorder (see above and Section 4.2)

and the observation of annealing occurring during room temperature ion-implantation of gallium arsenide [Grimaldi et al (1981), Williams & Austin (1980)] suggests that this may be a significant effect. A more accurate means of determining the primary ion beam diameter on the sample - possibly a series of different size meshes similar to that used for focussing - would be necessary to obtain any quantitative results.

In summary the high positive secondary ion yield, and particularly high $GaAs^+$ signal from the (2 x 4) As stabilised reconstruction have been confirmed. Other differences have been observed but further work is required to determine their cause.

4.3.3 Ion Dose Effects

As already mentioned, the spectra of selected secondary ion species were repeated cyclically to obtain a variation with ion dose, but one of the most surprising results of this investigation compared with the initial results was the minimal change observed with ion dose at the initial 0.5 nA primary ion current and ion dose per cycle of $\sim 1 \times 10^{12}$ cm^{-2}. The primary ion current was therefore increased to 3 nA and the positive ion dose dependences shown in figures 4.15 - 4.17 were obtained. Higher ion doses of up to $\sim 10^{15}$ cm^{-2} were obtained at higher ion current densities but no significant changes with ion dose were observed. The largest changes were dependent on primary ion current density and will be discussed in Section 4.3.4.

The most obvious and surprising result is that, unlike the initial results, no great variation of Ga_2^+ secondary ion signal with ion dose is found. The changes that do occur appear to be correlated with changes in the Ga^+ secondary ion signal although the relative Ga_2^+: Ga^+ signal does increase slightly with ion dose in all cases. This considerable change from the previous results was, at first, interpreted as being due to the presence of adsorbed arsenic on the initial reconstructed surfaces due to inadequare preparation and/or their subsequent storage within the predominantly arsenic residual gas background of the MBE chamber. Whilst this may be relevant for some of the layers it was not so in all cases and cannot, therefore, be confirmed as the cause of these differences. In addition, as already discussed, there is no comparable change in any other matrix signals, which would be expected if this were due to changes in surface composition alone.

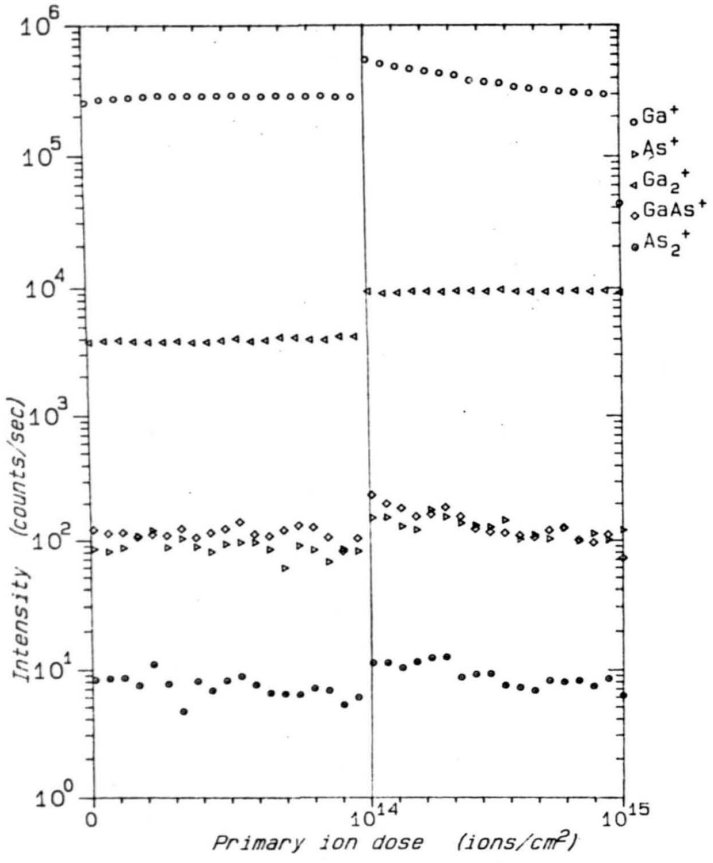

Figure 4.15 Secondary ion dose dependence c(4x4) As rich surface.

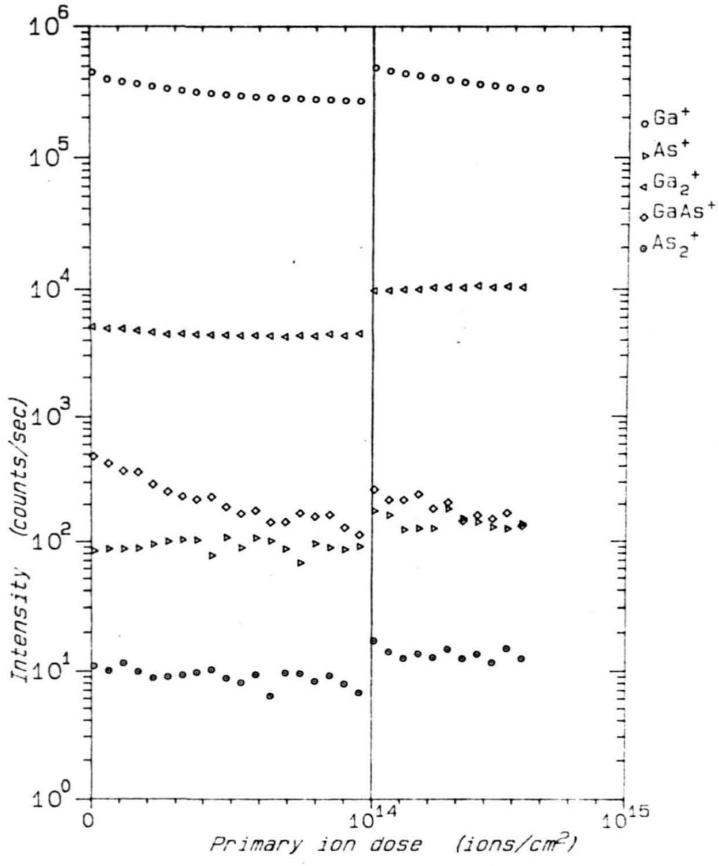

Figure 4.16 Secondary ion dose dependence (2x4) As stabilised surface.

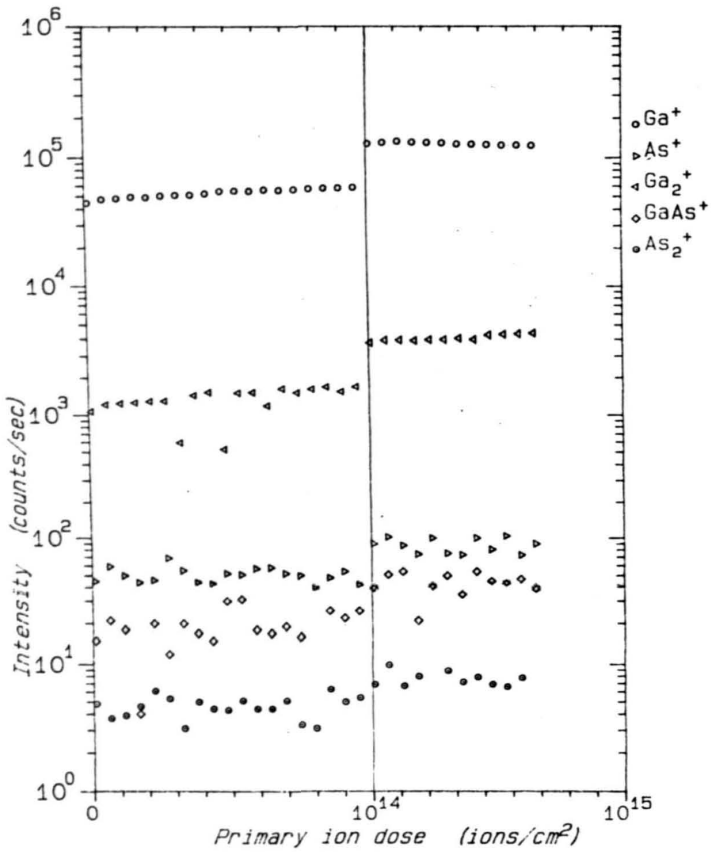

Figure 4.17 Secondary ion dose dependence (4x6) Ga stabilised surface.

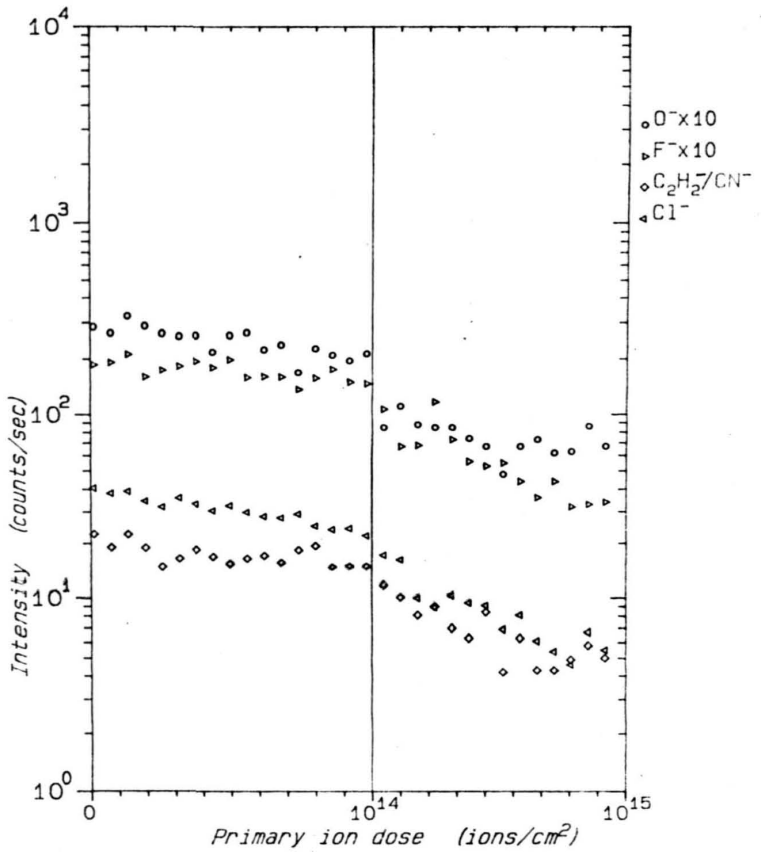

Figure 4.18 Secondary ion dose dependence c(4x4) As rich surface.

Another aspect, which cannot be overlooked, is that the increase in Ga_2^+ with ion dose always occured when the primary ion beam was incident along the [$\bar{1}$10] azimuth, whilst the later results, which did not show this increase, were obtained with the substrate holder unintentionally misaligned by ~5°. It is therefore possible that the reduced initial Ga_2^+ signal is a consequence of the primary ion beam alignment - channelling between (110) atom planes seems a probable cause of such an effect - and that this Ga_2^+ secondary ion signal increases when the local alignment is lost either by local damage caused by the ion bombardment itself or due to a macroscopic misalignment of the sample.

It is evident that further work using surfaces with deliberately adsorbed arsenic layers, which may be reexamined after desorption of the excess arsenic by the procedures described in Section 3.3, and a range of different incident angles for the primary ion beam, is necessary to answer the problems raised by these results.

The Ga^+ signals themselves slowly increase or decrease as appropriate towards an intermediate value, presumably characteristic of the ion bombarded surface with an equilibrium Ga:As concentration, and these changes confirm the variation in Ga^+ ion yields of the different surface reconstructions. This did not occur with the initial results shown in fig 4.6, but these early results are confused by the malfunctioning photon counter. It is interesting that the Ga_2^+ signal, and to a lesser extent As^+ and As_2^+, tend to show the same variation with primary ion dose as the Ga^+ signal, suggesting that some common property - perhaps surface work function - is a major factor influencing all secondary ion signals.

The other major result from these ion dose measurements is the rapid decrease of the $GaAs^+$ signal observed from the (2 x 4) As stabilised surface, which again confirms that the previously observed high $GaAs^+$ yield from this reconstruction is a real effect. The data indicates a cross section for desorption or destruction of ~1 x 10^{-14} cm^2 for this signal, similar to that previously found, and also similar to that for the Ga_2^+ signal from the earlier C(4 x 4) As rich surfaces. No correction has been made for the simultaneous but smaller decrease of Ga^+ and other secondary ion signals. The decrease of this $GaAs^+$ signal with ion dose, and the fact that it remained fairly constant on the other surface reconstructions, indicates that it is probably sputtered as an intact cluster and not formed by recombination of Ga and As species during the sputtering process.

If this species were formed by recombination then, since the (2 x 4) As stabilised surface is intermediate in composition between the other two surfaces studied, one would expect an initial increase in this signal from one of the other surfaces as its surface composition passed through the optimum value for generation of $GaAs^+$, before reaching that characteristic of the ion bombarded surfaces. However, it is always possible that the atomic configuration of this surface reconstruction is such as to promote the correlated emission of Ga and As atoms such as to favour the formation of $GaAs^+$ by recombination, similar to the results of Winograd et al (1978), Garrison et al (1978) and Holland et al (1980) for generation of metal dimers, until the surface becomes disordered by ion bombardment. Thus exactly why the (2 x 4) As stabilised reconstruction should produce more $GaAs^+$ secondary ion clusters is not understood, but it probably indicates a more 'bulk-like' surface with a predominance of Ga-As bonding over Ga-Ga or As-As bonds, which is consistent with the stability of this reconstruction and its consequent use for MBE growth.

4.3.4 Primary Ion Current Density Effects

The results discussed so far were obtained with the primary ion beam rastered over a 3 mm square area of the sample. When the raster was reduced to a 1 mm square thus increasing the current density by ~10 times, it was found that most positive secondary ion signals increased by a factor of approximately two and, when the final current density was 50 nA cm^{-2}, remained fairly steady at their new values. However, with final current densities of 300 nA cm^{-2}, some of the secondary ion signals appeared to decay back to their previous values as shown in figures 4.15 - 4.17. It is noticeable that this decay is not the same for the different surface types, and the increase in As^+ and As_2^+ signals, relative to Ga^+, from the (4 x 6) Ga stabilised surface has already been noted.

This variation of secondary ion signals at the higher current densities is indicative of the fact that these changes are directly related to primary ion current density and not to lower collection efficiencies from the edges of the sampled area. This is further supported by the absence of any such effects in the negative secondary ion spectra, as shown in figure 4.18, where the change in

slope is the only noticeable effect of changing the primary ion current density. Neither does there appear to be the same effect apparent in the positive secondary ion signals from impurity species, but this is less certain because of the larger random variation present in these low intensity signals.

The effective aperture of the secondary ion detection system was measured using the unrastered primary ion beam and noting the variation in Ga^+ signal as the beam was manually swept across the sample. The results are shown in figure 4.19. Ideally this should be repeated for each of the species of interest but it shows that secondary ions can be collected from a larger area than the 3 mm square used in these experiments, and that decreasing the sample area from 3 mm to 1 mm square should increase the secondary ion signal by only ~10% due to the increased collection efficiency from the central area. This result confirms that the observed variations are due directly to the changing primary ion current density.

Another effect of the secondary ion optical system was that the mass resolution of SIMS spectra obtained with an unrastered primary ion beam was consistently higher than when the raster was operating. This indicates that the mass filtering of ions is dependent on their point of origin within the sampled area and is another aspect of the system which may require further investigation.

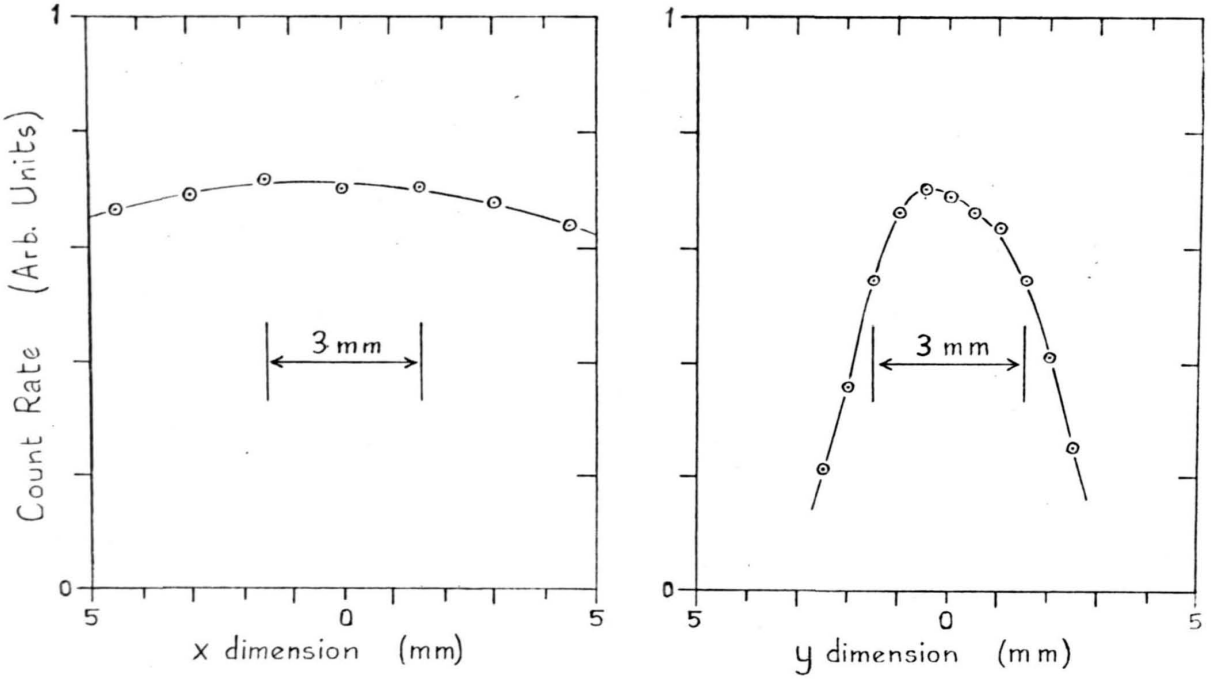

Figure 4.19 Sensitivity of Ga^+ secondary ion detection over sample area. The data are for the two orthogonal axes of the sample surface, and the edge of the usual 3mm square sample area is indicated.

4.4 Discussion of SIMS Results

Various aspects of the results have already been considered in the preceeding sections, and this section is intended to widen the discussions to additional aspects of theory and related experiments away from the details of this particular investigation.

The first aspect considered is that of sputter ion yield from a particular surface. Prediction of this yield is not straightforward and several theories have been proposed with different levels of success, for different situations (see eg Joyes (1973), Blaise & Nourtier (1979), Schroeer et al (1973), Sroubek (1974), (1981), Cini (1976), Plog et al (1977), Jurela (1973), Andersen & Hinthorne (1973), Morgan & Werner (1976), (1977), Yu (1982), (1983), Williams (1979), (1981), Williams et al (1980), (1978), Wittmaack (1981), (1976), Murray & Rabalais (1981), Coles (1979), Lin & Garrison (1982), Winograd (1982), Slodzian (1982). One relationship which is fairly well established, both experimentally and theoretically under certain conditions, although there are exceptions, is an exponential dependence of sputter ion yield on the difference between work function and ionisation energy or electron affinity, for positive and negative secondary ion species respectively, ie

$$Y^+ \propto \exp(\phi - I)/\varepsilon \qquad (4.1)$$

$$Y^- \propto \exp(A - \phi)/\varepsilon \qquad (4.2)$$

where ε may be related to details of the ionisation process or simply to an effective temperature $T_e = \varepsilon/K$. Massies et al (1979) have measured the work function of variously reconstructed GaAs (001) surfaces and find it to be largest by ~300 meV on the (2 x 4) As stabilised surface. As already mentioned these two results are consistent with the larger positive ion yields measured from this surface. Unfortunately no negative ion matrix species could be detected to see whether a complementary variation existed.

Massies et al (1979) also found that the work function for a given (001) surface reconstruction was independent of the doping level, showing the Fermi level to be pinned at the surface. However the well cleaved (110) surface is known to be free of surface states within the band gap so that the position of the Fermi level is determined by bulk doping, although defects in the cleave may lead to

Fermi level pinning near mid-gap [Huijser& Van Laar (1975), Mönch & Clemens (1979)]. This suggests that the SIMS measurements could be profitably extended to cleaved (110) surfaces of n- and p-type material where the work function will differ by up to 1400 meV, depending on the quality of the cleave, with minimal change of other parameters, thus permitting examination of the SIMS signal dependence on work function with the minimum of interference from other effects. Incorporation of a Kelvin probe or other means of determining work function would also be useful, particularly since Bauer et al (1984) maintain that work function changes dominate changes in SIMS spectra.

A second aspect is the dependence of secondary ion species on the atomic configuration of the surface and, conversely, the deduction of atomic configuration from the SIMS spectra. Although several studies have shown changes in SIMS spectra to be correlated with known changes in surface configuration [Dawson (1978), (1977), Dawson & Tam (1979b), (1980), Hopster & Brundle (1979), Fleisch et al (1978), (1979), Benninghoven et al (1978), Yu (1977), (1978)] the deduction of surface configuration from the SIMS spectra is not straightforward even with additional data from eg thermal desorption, Auger electron spectroscopy, electron induced desorption, LEED, work function changes, electron energy loss spectroscopy, photoelectron spectroscopy or ion scattering spectroscopy.

Most of these studies are concerned with changes occuring on oxidation or adsorption of other gases and it seems more appropriate to discuss them in Chapter 5. However, in the absence of additional experimental information, any deduction of surface structure from SIMS spectra can only be made using what has come to be known as the direct emission or fragmentation model. First proposed by Benninhoven (1973) this model assumes that molecular secondary ions are sputtered as intact clusters from the ion bombarded surface. However, various investigations (eg Oechsner (1982), Winograd (1982), Colton (1981), Hopster & Brundle (1979), Dawson & Tam (1980), Fleish et al (1978), (1979), Holland et al (1980), Slusser (1979), Honda et al (1979), Taylor & Rabalais (1978), Snowdon et al (1981)) have shown that this model cannot adequately describe the secondary ion species obtained from a variety of surfaces, and the phenomenon of recombination of sputtered atoms must be invoked. Oechsner (1982) has reviewed the conditions under which the direct emission and recombination models are valid and

and concludes that direct emission is possible with strong (ionic) bonds and large difference in mass numbers of a sputtered pair, whilst atomic recombination dominates for weak (metallic or covalent) bonds and comparable atomic masses. Similarly Winograd (1982) concludes that direct emission of clusters is only likely if the cluster has an inherent molecular identity within the solid. It is apparent that direct emission is unlikely to apply to the clean gallium arsenide surface although it may be relevant to the oxidised surface. Computer simulations (eg Winograd (1982), Harrison & Delaplain (1976), Foley & Garrison (1980), Winograd et al (1978), (1979), Heyes et al (1981), Garrison et al (1978), Foley et al (1984), also show considerable rearrangement and recombination in the formation of sputtered molecules, for example Cu_2^+ dimers sputtered from a copper target are produced mainly from next nearest neighbour atoms in the surface and not from adjacent pairs, although production of nearest neighbour pairs increases as the angle of incidence of the primary ion beam is reduced. It is also shown that species generated by the initial impact, generally with fairly high energies, are more influenced by the surface structure than the majority of secondary ions produced with lower energies near the end of the collision cascade when the surface may be considerablydisturbed. Although these calculations cannot yet be applied to directionally-bonded materials, such as III-V compounds, it would seem that the measurement of secondary ion distributions both in energy and emission direction, and their variation with experimental conditions, may be more important than intensity variation at the peak of the distribution as measured in this project.

Returning to the present experimental results these show little variation of the relative proportions of different secondary ion species with atomic composition of the surface, and the large proportion of Ga_2^+ present indicates that considerable recombination is occuring or that disorder in the different surfaces dominates the molecular secondary ion species. Although the surfaces of epi-layers 93 and 94 show considerably different visible defect densities it is not known whether these, or other less apparent defects, have any effect on the SIMS spectra. It is known, however, that growing epilayers using As_2 in place of As_4 gives different, generally lower, levels of defects on an atomic scale [Neave et al (1983a), (1980), Künsel et al (1982), (1980a)] and comparing epilayers grown

by the two methods would be a useful exercise. Comparison of cleaved and MBE grown (110) surfaces might also prove interesting, as would alternative measurements of the defects by eg Henzler's (1983) method of LEED spot profile analysis or Hsu et al (1983) method of reflection electron microscopy. However, defects will certainly alter the electronic surface states and fields at the surface, which may have a large effect on SIMS spectra, and they may also be reactive sites for the adsorption of contaminants [Croydon (1979), Croydon & Parker (1981), Ranke (1983)] which are well known [Winograd (1982), Wittmaack (1979), (1980), Williams (1979), Blaise & Nourtier (1979)] to increase the secondary ion yield of clean metals, often by several orders of magnitude. It therefore seems possible that the SIMS spectra may in fact be dominated by secondary ion emission in the region of surface defects and that further effort is required to quantify and reduce the defects inherent in the MBE grown surfaces. If the defect density on the epilayer surface and the primary ion spot size can both be sufficiently reduced, it may be possible to 'ion image' the surface using this system, and thus obtain a direct measurement of the influence of surface defects on secondary ion emission. Alternatively a direct imaging SIMS system, with resolution ~1 μm, could be used, provided that the necessary primary ion dose is not excessive.

With regard to the similarity of SIMS spectra from the differently reconstructed surfaces it is also possible that the relatively open nature of the (001) surface enables significant sputtering of sub-surface atomic layers, which could mask any differences due to changes in composition of the surface atomic layer, or alternatively, since variable sub-surface compositions have been reported [Neave & Joyce (1978), Gant et al (1983)] could explain some of the variation between different surfaces with the same reconstruction. Furthermore Salmon & Rhodin (1983) concluded from photoemission measurements of MBE grown GaAs surfaces and germanium overgrowths on these surfaces that measurement of LEED and RHEED patterns alone was not sufficient to uniquely define the reconstructed GaAs (001) surface. SIMS spectra of cleaved (110) surfaces may be useful in that the atomic configuration of these surfaces is well understood [Duke et al (1983), Croydon (1979),

Croydon & Parker (1981) & references therein] and there is good reason to believe that there is no Ga-Ga or As-As bonding in this surface, the surface atomic layer being formed entirely of alternating Ga and As atom chains. SIMS spectra of the (111) and $(\bar{1}\bar{1}\bar{1})$ surfaces may also be revealing because of the higher atom density in these layers than in the (001) surface, which may reduce the probability of sputtering from subsurface layers, particularly for the (111) surface which is believed to approximate the ideal surface, whilst the various reconstructions present on the $(\bar{1}\bar{1}\bar{1})$ surface may show significant differences from or similarities to the (001) surface reconstructions.

However, in suggesting these extensions of the technique to additional, equally complex, surfaces it must not be forgotten that static SIMS is, in this application, still essentially an empirical technique. It must be considered whether or not it might be more profitably applied either to surfaces that have been more completely characterised by other techniques as a critical test of static SIMS, or for those purposes, such as qualitative identification of atomic and adsorbed molecular contaminants, where it has already proved to be a useful technique. In either case it is apparent that the SIMS system must be further characterised and optimised for the static SIMS application, which may well preclude its present highest priority use for depth profiling in the dynamic SIMS mode.

I consider that a new sample holder is necessary for the static SIMS application to enable additional movements of the sample, locking of unwanted movements and operation of additional, well characterised, analysis methods. Rotation of the sample about its surface normal should be included so that variation of secondary ion yield with azimuthal angle of the incident primary ions or emitted secondary ions can be investigated. During this project all samples were analysed with the primary ions incident along the $[\bar{1}10]$ azimuth (within $\sim 5°$ and at $20°$ to the surface plane) and with no deliberate variation in the geometry for collection of secondary ions. However, Winograd and co-workers [Winograd (1982), Holland et al (1979), (1980), Foley et al (1980), (1984), Gibbs et al (1981)] have shown that variation of secondary ion signals with these parameters can be indicative of specific surface geometries, but better understanding of the basic sputtering processes is probably necessary before any

such results obtained from gallium arsenide could be confidently interpreted. Provision for heating the sample should also be included to enable the rapid, sequential generation of different surface reconstructions on the same sample, and the ability to cool to liquid nitrogen temperatures would be useful to investigate the effects of damage caused by the primary ion beam.

4.5 Summary of Clean Surface Measurements

Two major consistent results appear from the clean surface measurements on variously reconstructed (001) GaAs surfaces. Firstly a higher positive secondary ion yield from the (2 x 4) As stabilised surface which may be correlated with the higher work function of this surface, and secondly a proportionately higher $GaAs^+$ signal from the same surface. The reason for this latter effect is not clear, but since it appears to be sputtered as an intact cluster it is presumably indicative of additional Ga-As bonding present in this surface reconstruction, and a more 'bulk-like' surface structure is consistent with the predominant use of this reconstruction for MBE growth.

A large Ga_2^+ signal is also observed from all surfaces, although Ga-Ga bonding is only anticipated on the (4 x 6) Ga stabilised surface. Initial measurements indicated that this could be due to ion induced disorder in the surface but this has not been confirmed by later results. Sputter removal of a variable, adsorbed surface layer may be responsible for changes in this signal, but again is not consistent with all results, and unintentional changes in the incident primary ion beam direction near the $[\bar{1}10]$ azimuth may well be important. Changes in matrix signal intensities have been observed dependent on primary ion energy and current densities and appear to be due to changes in secondary ion emission coefficients. Various adsorbed impurity species have been observed but any dependence on surface reconstruction could not be confirmed.

CHAPTER 5

SIMS Analysis of GaAs (001) Initial Oxidation

5.1 Existing Knowledge of GaAs Oxidation

The GaAs (001) surface was chosen for this investigation partly because of the lack of understanding of this technologically important surface, as already mentioned in the introduction. The oxidation of GaAs has been recently reviewed [Croydon (1979), Croydon & Parker (1981), Ranke & Jacobi (1981)] and the relevant results, generally obtained from electron spectroscopies - AES, ESCA and ELS - are summarised here.

On polar surfaces most evidence indicates Ga-O bonding in the initial stages of oxidation, often to the exclusion of As-O bonding, although there is some evidence for the latter also. Both molecular and atomic forms of adsorbed oxygen have been found, with the molecular form dissociating under electron irradiation. There is also evidence that chemisorption sites may be associated with unsaturated gallium atoms inherent in the reconstructed surface, and that additional adsorption sites may be created by loss of gallium during the adsorption process. More attention has been paid to the cleaved non-polar (110) surface where initial results suggested exclusive As-O bonding, but more careful investigation has shown similar amounts of Ga-O and As-O bonding. Residual disorder has been shown to increase the reactivity of all surfaces, suggesting that adsorption occurs at defects and it is further suggested that the energy liberated creates additional disorder and adsorption sites. The oxide itself is amorphous and no ordered chemisorption phases have been observed but it is not known whether it is essentially a mixed Ga_2O_3/As_2O_3 oxide or a two-dimensional $GaAsO_4$ analogue, and Su et al (1982) have recently suggested that an adsorbed oxygen molecule dissociates to give a structure of the form:

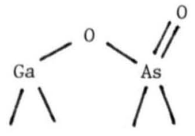

Bonding arrangements are deduced from chemical shifts of Ga and As derived peaks in the electron spectra and the ambiguities are caused

both by the small chemical shifts expected on the Ga peaks and the influence of charge transfer between surface atoms giving similar shifts for very different bonding geometries. Ludeke (1983), in fact, interprets the results of Su et al (1982) as showing sub-surface oxidation to have occured. Recent results (eg Proix & Houzay (1981), Su et al (1982), Ranke (1983)) have confirmed the influence of surface defects on the adsorption, and suggest that adsorption at defects may be significantly different from adsorption on perfect regions of a cleaved surface.

It was expected, on the basis of the direct emission model of sputtering, that SIMS would be able to provide data to enable distinction of these various states of chemisorption and oxidation.

both by the small chemical shifts expected on the Ga peaks and the influence of charge transfer between surface atoms giving similar shifts for very different bonding geometries. Ludeke (1983), in fact, interprets the results of Su et al (1982) as showing sub-surface oxidation to have occured. Recent results (eg Proix & Houzay (1981), Su et al (1982), Ranke (1983)) have confirmed the influence of surface defects on the adsorption, and suggest that adsorption at defects may be significantly different from adsorption on perfect regions of a cleaved surface.

It was expected, on the basis of the direct emission model of sputtering, that SIMS would be able to provide data to enable distinction of these various states of chemisorption and oxidation.

5.2 Experimental Procedures

The various gallium arsenide surfaces were prepared as described in Chapters 3 and 4 and transferred to the SIMS chamber whilst maintaining UHV conditions. Oxygen exposures were carried out on the three surfaces used for the initial surface studies described in Chapter 3, following up to two days exposure to the UHV background. It should be noted that all these surfaces showed an increase in the Ga_2^+ secondary ion signal with primary ion dose, unlike most of the surfaces subsequently studied, and this may indicate that they have a partial monolayer of adsorbed arsenic, in excess of that required to generate the surface reconstruction. BOC Research Grade oxygen (99.995% purity) was used for the exposures and was admitted via a UHV leak valve. The oxygen pressure was measured using an ion gauge which was left on throughout the exposure so that excited oxygen was present. No opportunity was available to repeat the measurements using unexcited oxygen, without the ion gauge, to see whether this caused appreciable differences in the speed or products of adsorption, as found by Piametta et al (1978) on cleaved surfaces. The oxygen was pumped out after each exposure and the SIMS spectra obtained after the system pressure had fallen below 10^{-8} Torr. Higher background noise levels were apparent in the negative ion spectra after oxygen exposure. This is attributed to increased secondary electron emission from oxygen adsorbed surfaces in the region of the mass filter, and was reduced by positioning a magnet near the exit from the mass filter to deflect these electrons away from the channeltron multiplier as is evident in figure 5.1(b). All SIMS analyses were carried out using a 0.5 nA, 500 eV primary ion beam rastered over a 3 mm square sample area. Stepped mass spectra covering the full range from 1 - 250 amu with a total ion dose of 1×10^{13} cm^{-2} were used for all analyses.

5.3 Results from Individual Mass Spectra

Various interesting results were obtained from individual secondary ion mass spectra of the oxidised surfaces. Some of these results are essential to the correct interpretation of the exposure data whilst others may be considered as interesting asides, and both types will be considered in the following subsections.

5.3.1 Gallium Oxide Mass Interferences

As is evident in figures 5.1 - 5.3 and listed in Appendix I several different ion species are apparent in the vicinity of both GaO^+ and GaO_2^+, many of which, because of the two Ga isotopes, give mass interferences with each other eg $^{71}GaO^+$ and $^{69}GaOH_2^+$. If this were the only mass interference then it would be a simple matter to count the $^{69}GaO^+$ and $^{71}GaOH_2^+$ peaks; however, other species provide further mass interferences and the effect of tails from high intensity mass peaks on adjacent low intensity peaks has to be considered. If all the interfering species can be identified then it should be possible to separate the counts due to individual species by solution of simultaneous linear equations, provided the statistical errors inherent in the data are not exaggerated in the process. (Inclusion of the effect of the ^{18}O isotope would complicate matters further, but this can probably be safely neglected at only 0.2% abundance.) Such a comprehensive procedure has not been implemented for this study, the relevant interfering peaks have been apportioned by comparison with other peaks of the major species present, neglecting any minor species, and the various isotopes of each species summed to maximise the total count.

The data processing programme SSPROC does contain routines for summing isotopes of any particular gallium containing species and comparing the actual distribution of isotope counts with that expected from the known isotopic abundances. Large deviations indicating the presence of mass interferences can then be investigated, and summing the counts reduces the effect of the statistical errors present in lower intensity signals.

The mass interferences present in these regions of the spectra show the importance of using all available information to positively identify peaks in the mass spectra, before attempting to reduce total ion dose by sampling only selected peaks.

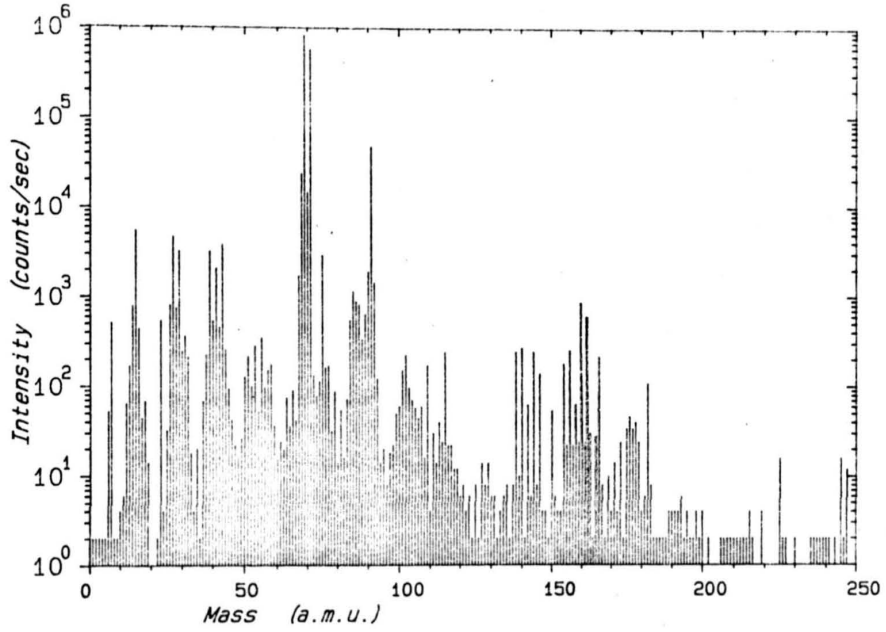

Figure 5.1(a) Positive ion SIMS of oxidized c(4x4) As rich surface

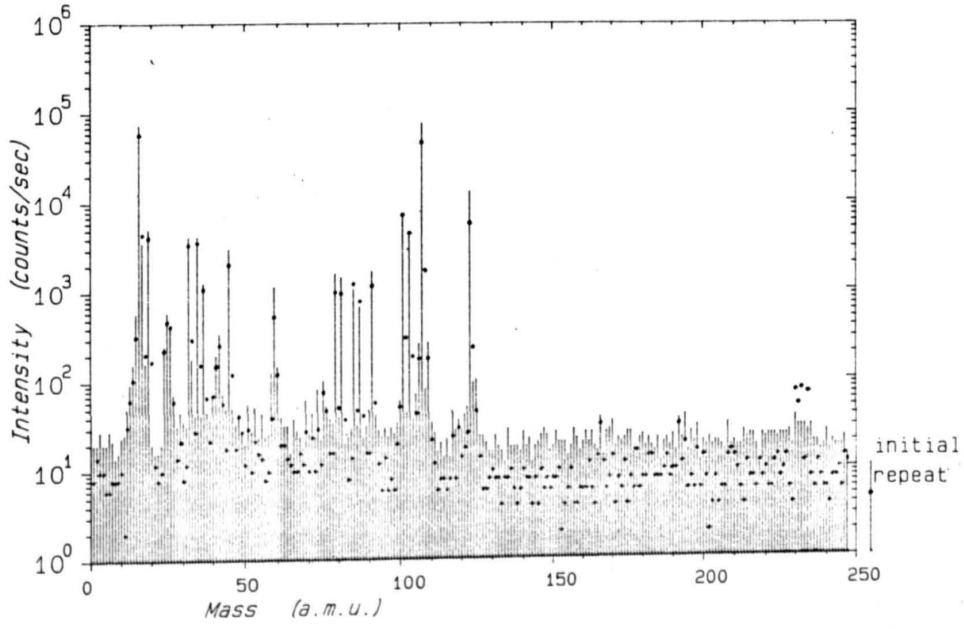

Figure 5.1(b) Negative ion SIMS of oxidized c(4x4) As rich surface

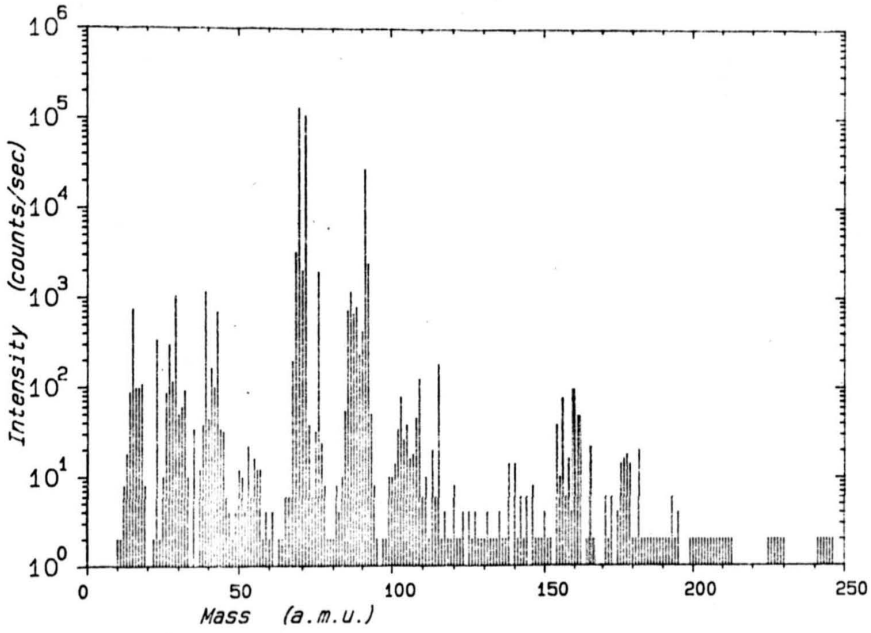

Figure 5.2(a) Positive ion SIMS of oxidized (2x4) As stab. surface

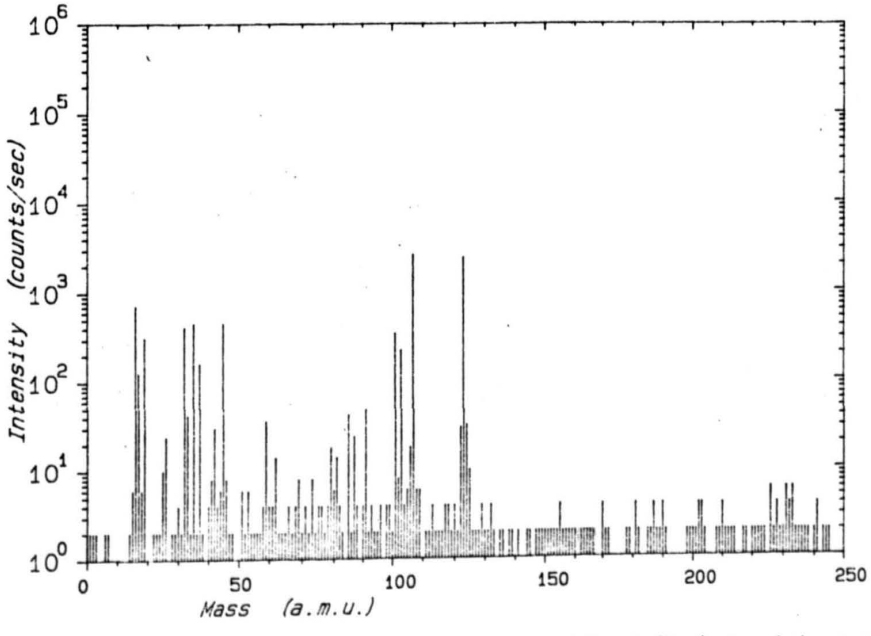

Figure 5.2(b) Negative ion SIMS of oxidized (2x4) As stab. surface.

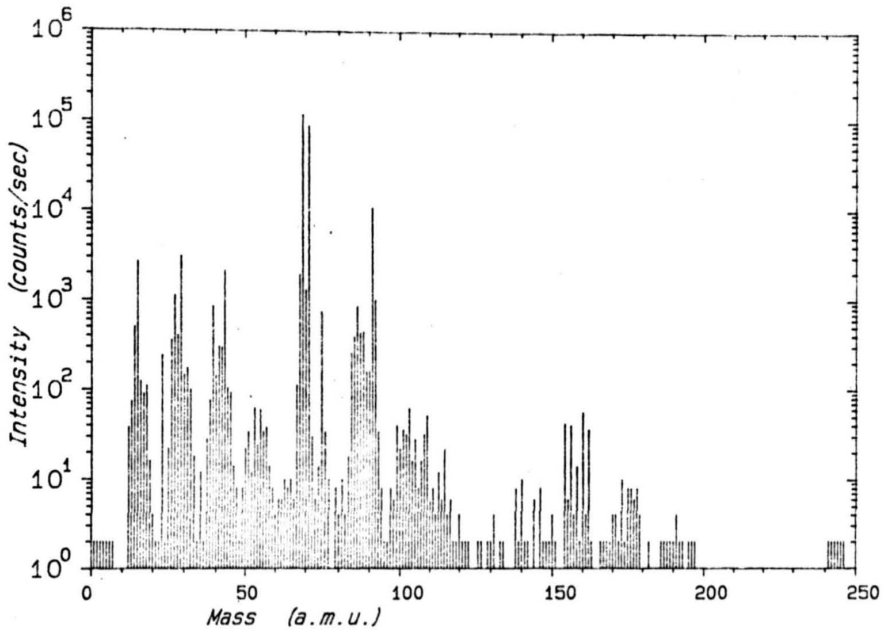

Figure 5.3(a) Positive ion SIMS of oxidized (4x6) Ga stab. surface.

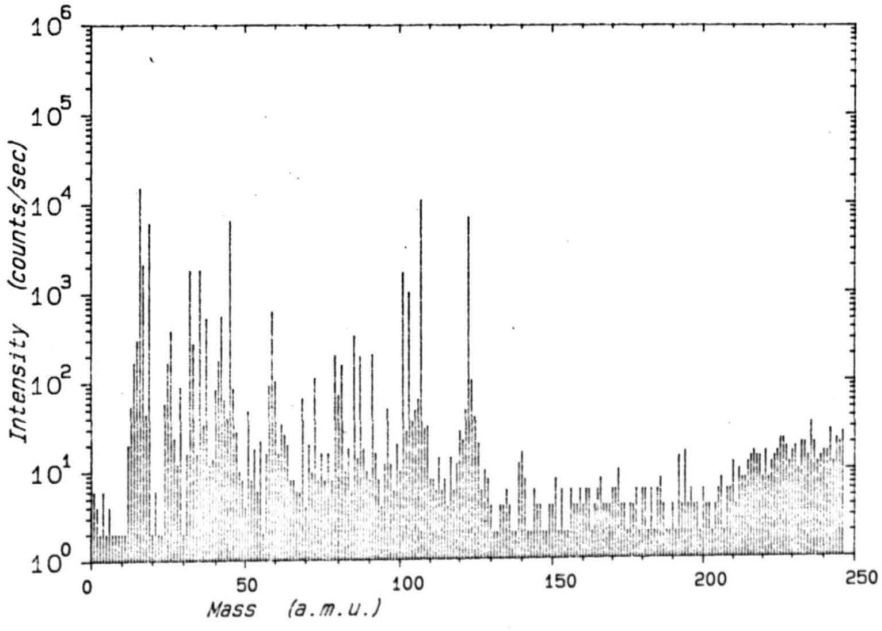

Figure 5.3(b) Negative ion SIMS of oxidized (4x6) Ga stab. surface.

5.3.2 Isotope Fractionation

The gallium isotope ratio present in the detected secondary ions was consistently found to differ slightly from the normally accepted values (see eg Kaye & Laby (1975)). Whilst at first this effect was attributed to a possible change in isotope ratio between different naturally occuring sources or on evaporation from the MBE source cell, it is well known that the peak transmission of quadrupole mass filters is not mass-independent (see eg Lawson & Todd (1972), and both sputtering and ionisation processes may be influenced by the differing isotope masses. These effects have been studied by Slodzian et al (1980), (1982) and Zinner & Grasserbauer (1982) who found mass fractionations of a few percent per amu, which varied with the element, matrix and instrumental conditions. Quantification of the effect in this investigation was hampered by the onset of saturation in the channel electron multiplier at high count rates or statistical variations at lower counts (longer sampling times should be used for a deliberate investigation of the effect) but generally showed mass fractionation of $^{39,41}K^+$, $^{69,71}Ga^+$, $^{113,115}In^+$, $^{35,37}Cl^-$, $^{79,81}Br^-$, $^{69,71}GaO^-$ and $^{69,71}GaO_2^-$ in the range +5 to -10% per amu. There were consistent variations, within this range, between results obtained at different times, which suggests that the major effect is caused by variations in instrumental sensitivity and emphasises the need for a reliable means of repeatably setting the SIMS instrument.

5.3.3 Ion Bombardment Induced Species

The problem of background noise on the negative ion mass spectra and its reduction by means of an additional magnetic field to deflect stray electrons has already been mentioned. As well as demonstrating this effect figure 5.1(b) also shows additional species present at 230 - 236 amu on the second mass scan of the sample area. The triplet of peaks is characteristic of a species with two Ga atoms and thus identifies Ga_2AsOH^-, whilst the remaining single peak at 231 amu is identified as $As_2O_5H^-$. The presence of hydrogen in these secondary ions suggests that they are formed as a result of ion bombardment induced reaction of the substrate with residual water molecules, or possibly hydrogen, either in the residual gas or already adsorbed on the substrate. Why these particular complex secondary ions were generated and their relation to the surface atomic structure is not understood, particularly confusing is the

fact that GaOH, but not AsOH, containing species are abundant in the positive ion mass spectra without any additional ion bombardment. A second positive ion mass scan of the same sample area of the oxidised surface produced higher Ga_2^+ and $GaAs^+$, as would be expected from the dose dependence curves of figure 5.6, and also mass peaks corresponding to $Ga_3O_2^+$ not originally observed in the spectrum of figure 5.1(a). Similar effects should be sought at higher mass numbers in case these species are fragments of a more complex structure, and after different oxygen exposures to determine whether any dramatic changes occur which may elucidate the problems of oxidation and other surface reactions. The ability of MASTEP2 to provide repeated cyclic measurements over a selected mass range should simplify the collection of such data.

The initial spectrum presented shows a distinctly resolved $^{75}As^{16}O^{18}O^-$ peak at ~0.4% of the $^{75}As^{16}O_2^-$ peak intensity as expected for 0.2% atomic abundance of ^{18}O, together with a less well resolved isotopic satellite for AsO_3^-, but the second spectrum shows large counts corresponding to hydrogenated species after these and other large mass peaks. These may be additional hydroxide species induced by the ion bombardment, but it is also possible that this effect has been caused by a small shift in the mass scale, causing the high mass side of the large peaks to be sampled at the next higher mass number. This latter possibility is supported by a second pair of similar spectra where the species at 230 - 236 amu were observed, but not the other hyroxide species suggested above. It is apparent that additional spectra, with a smaller mass increment, are needed to determine whether these are distinct masses or tails from the adjacent high intensity mass peak. It may be worthwhile modifying MASTEP to include measurements at half integer mass numbers as a routine check on the mass tuning.

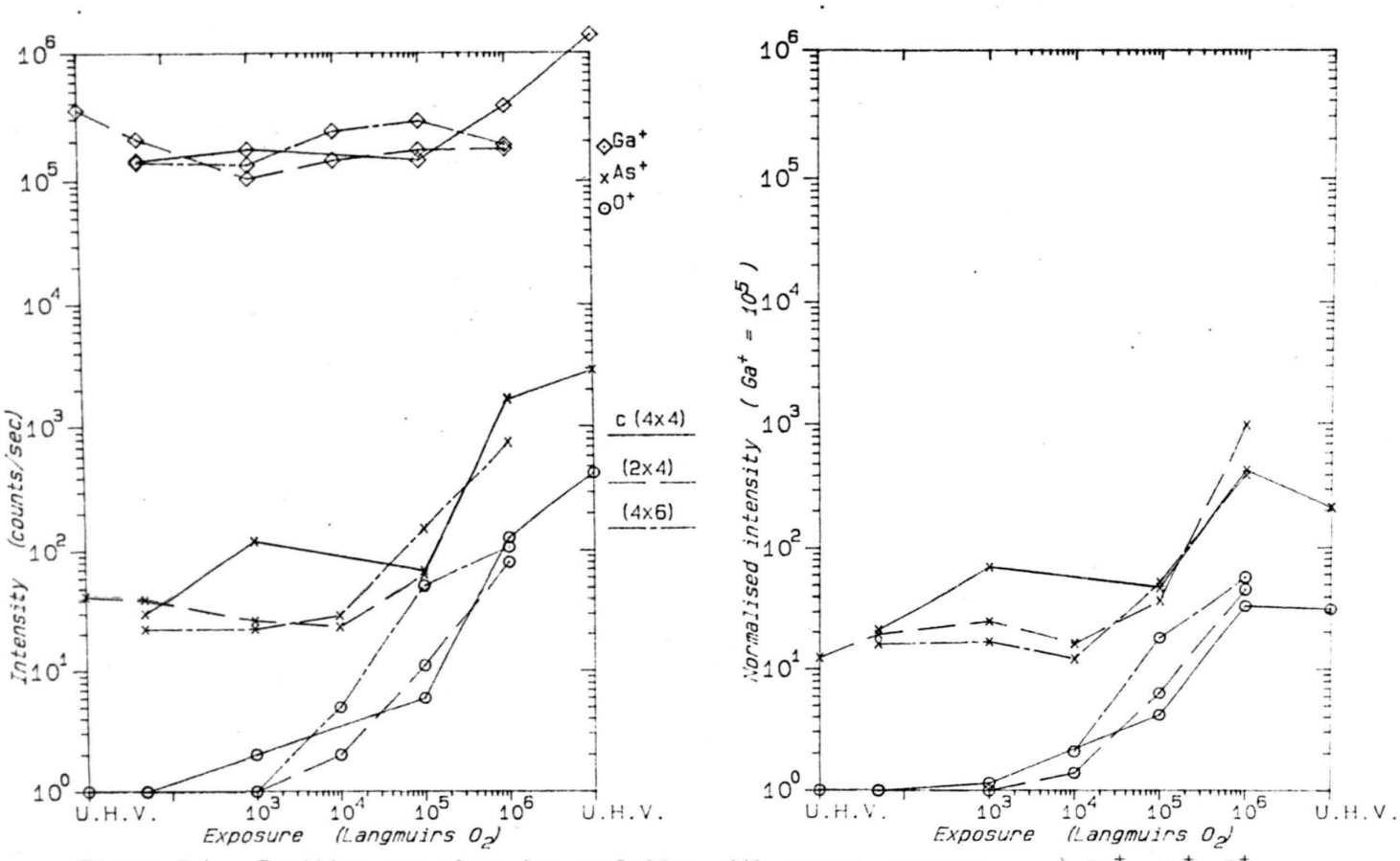

Figure 5.4 Positive secondary ion evolution with oxygen exposure. a) Ga^+, As^+, O^+.

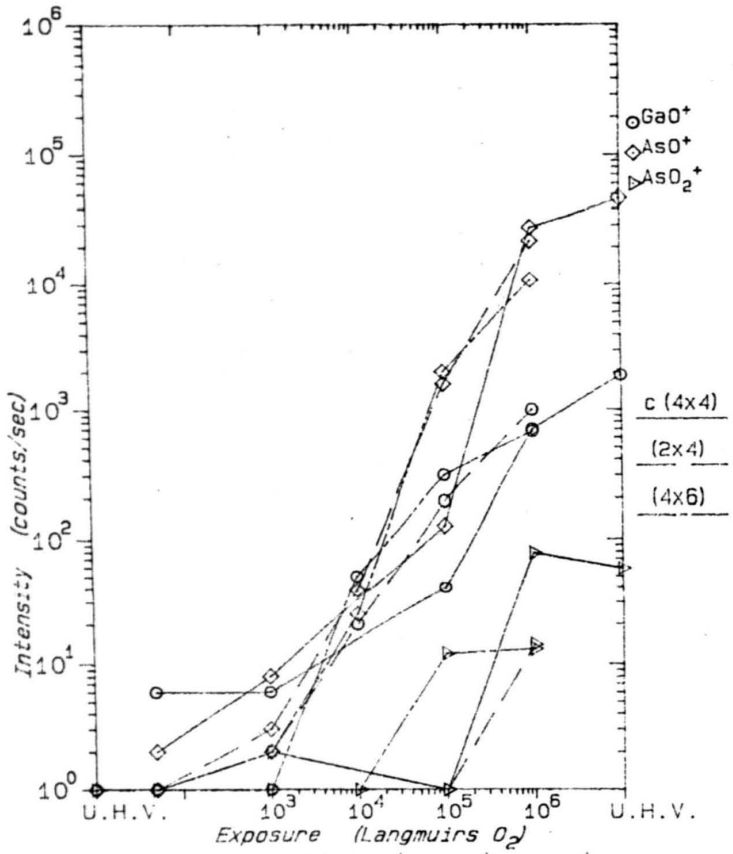

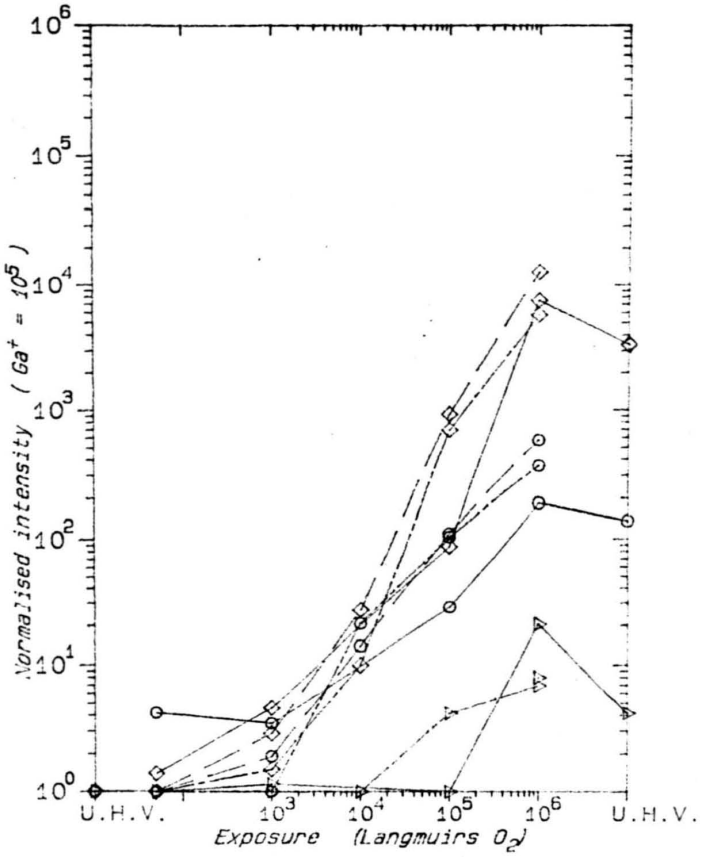

Figure 5.4 b) GaO^+, AsO^+, AsO_2^+.

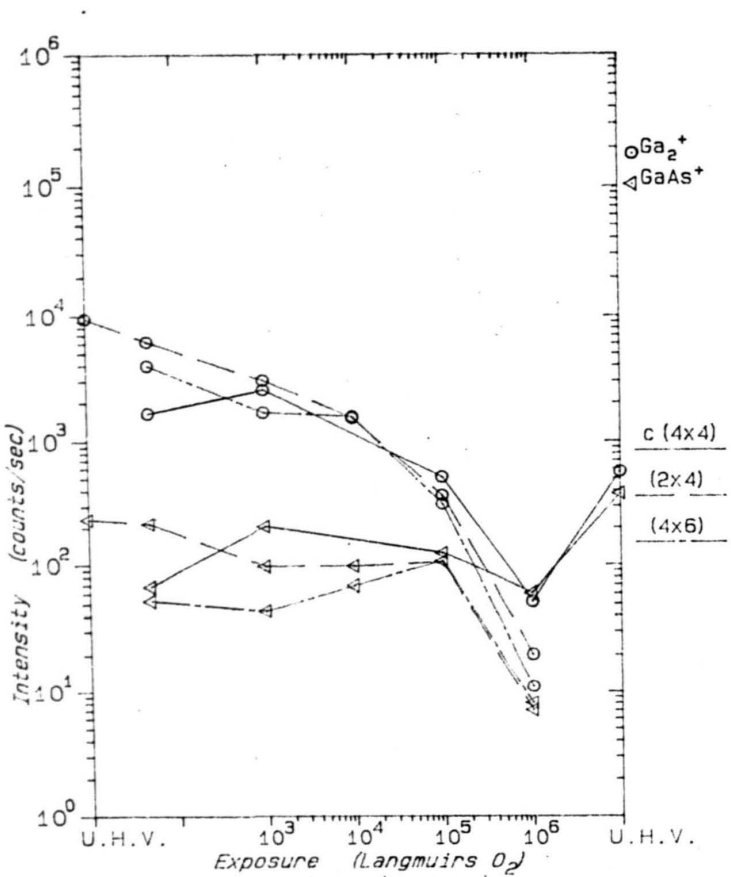

Figure 5.4 c) Ga_2^+, $GaAs^+$.

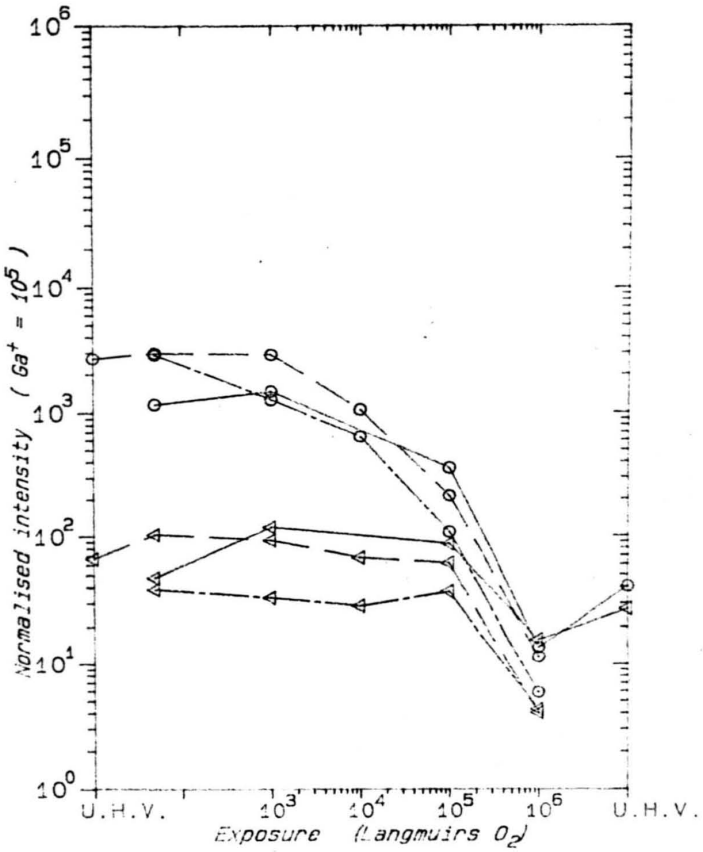

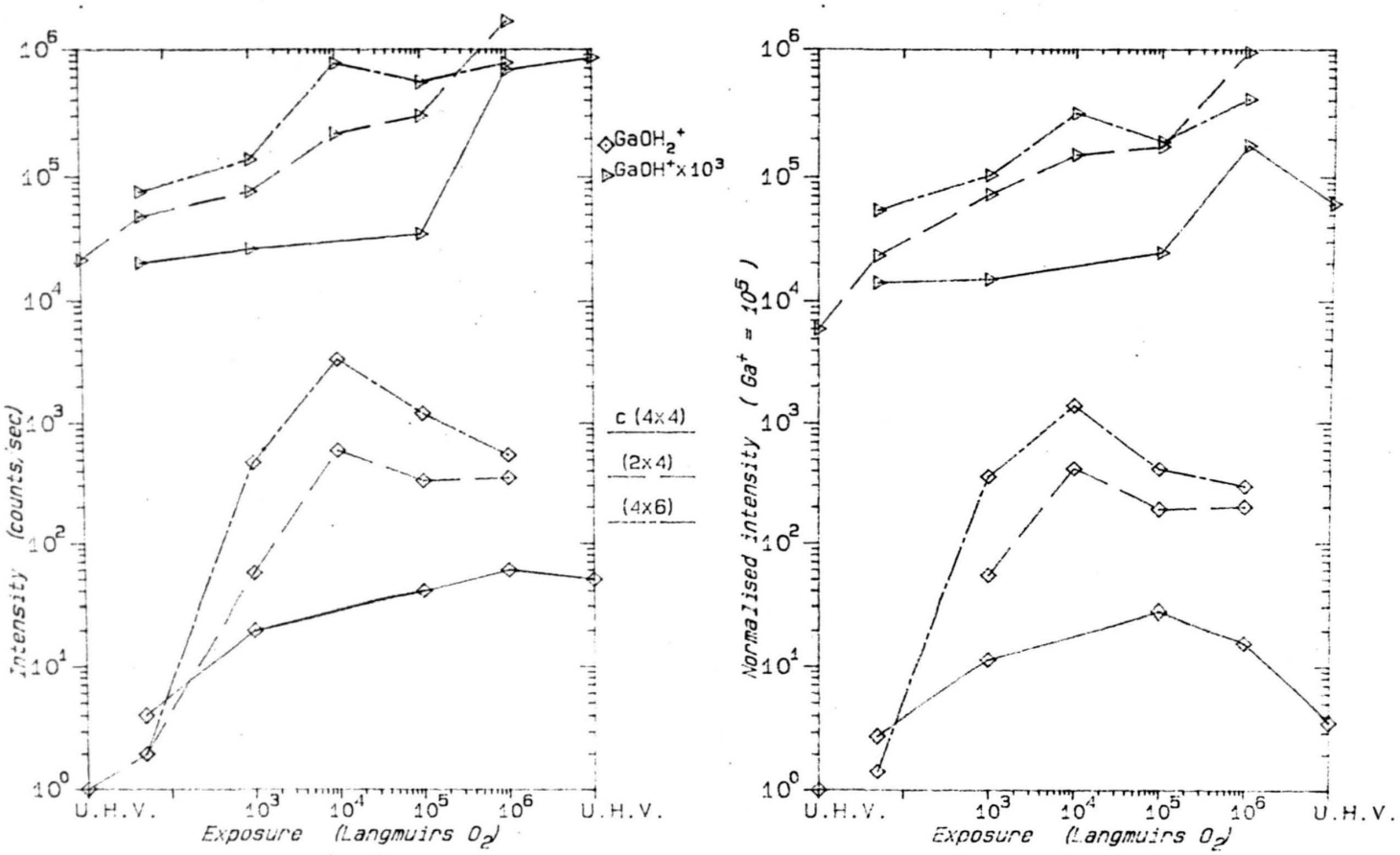

Figure 5.4 d) $GaOH^+$, $GaOH_2^+$.

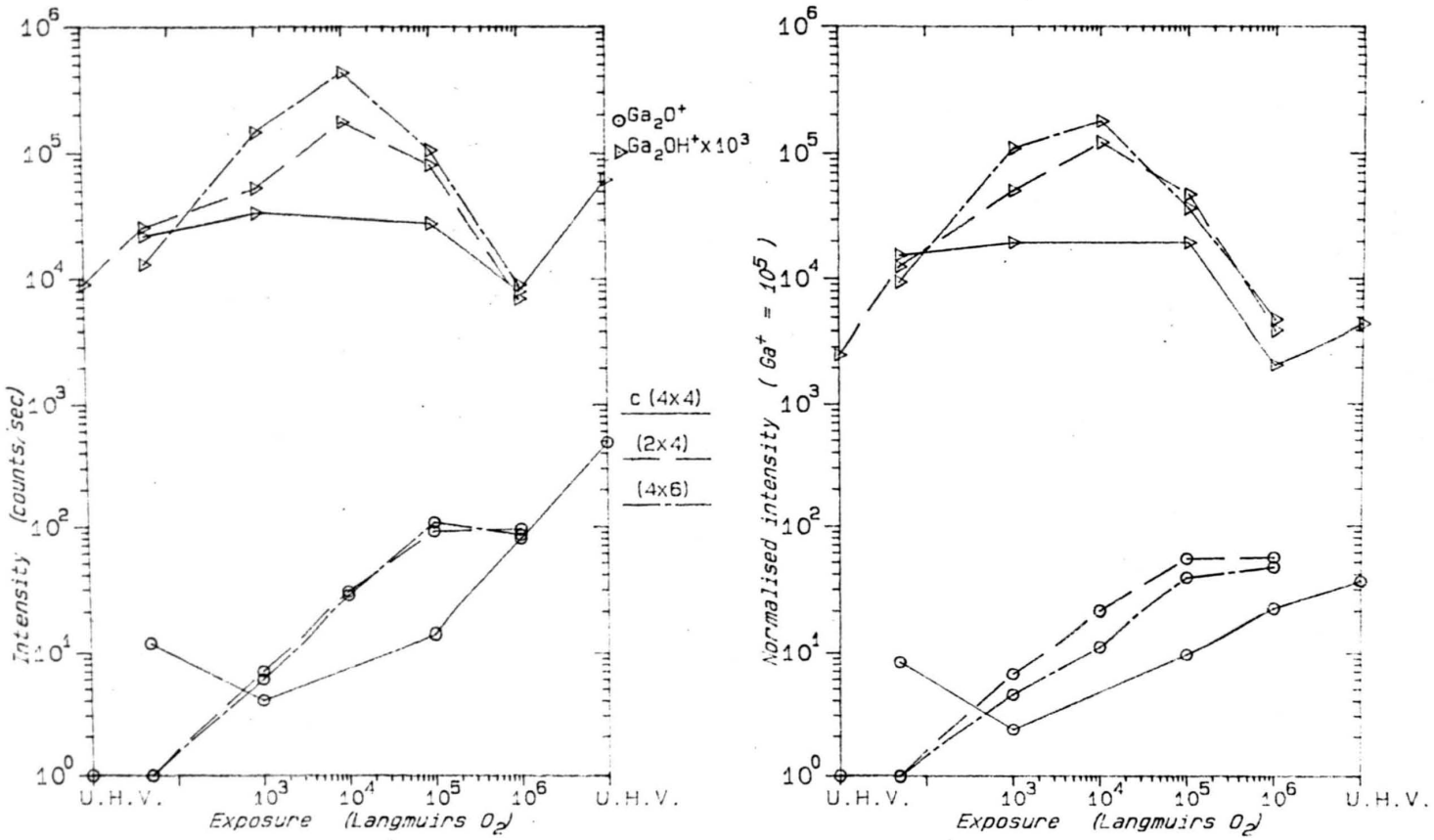

Figure 5.4 e) Ga_2O^+, Ga_2OH^+.

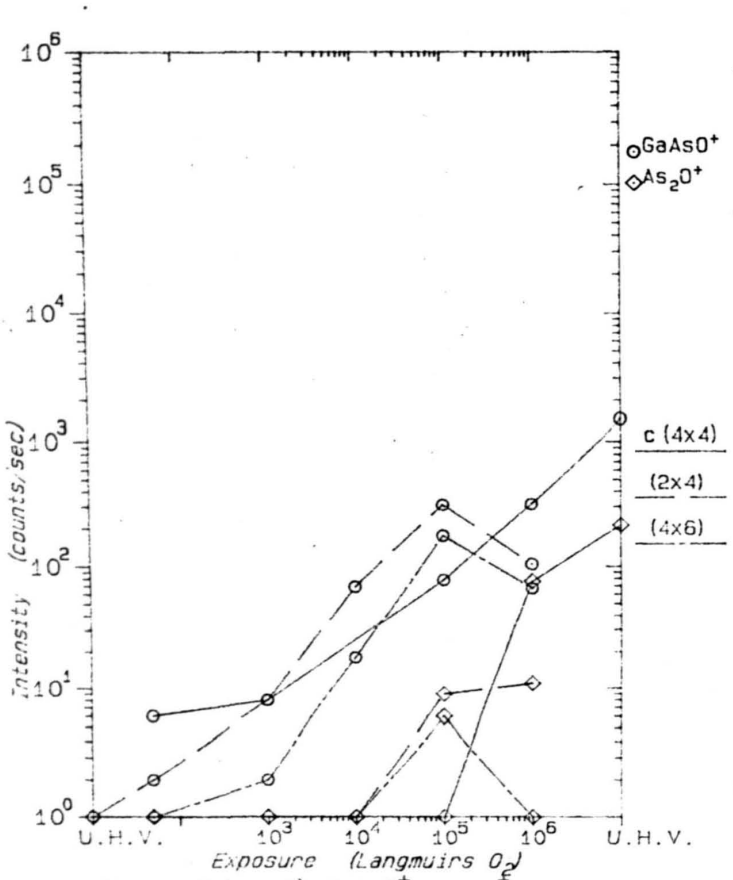

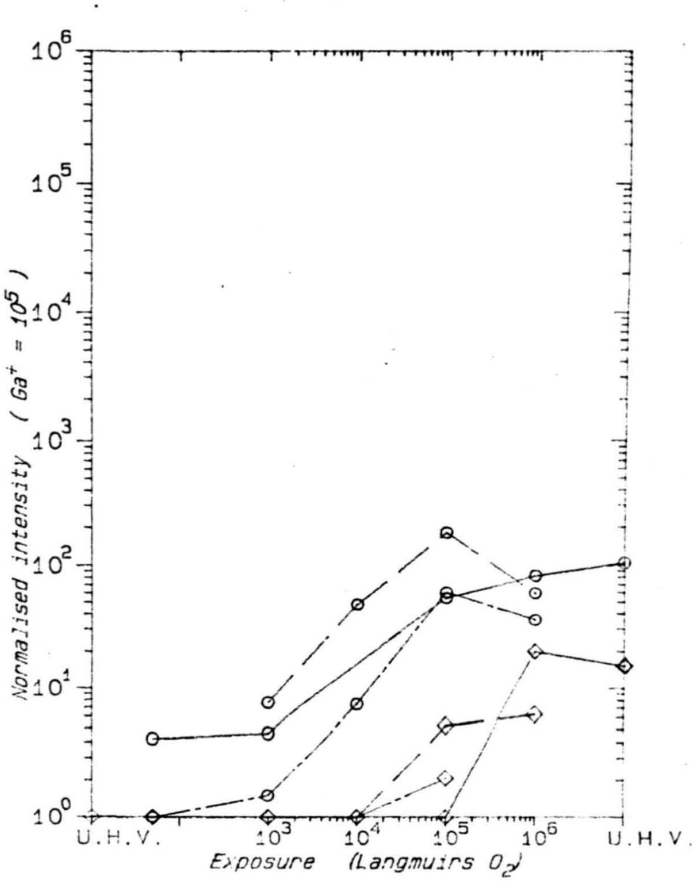

Figure 5.4 f) $GaAsO^+$, As_2O^+.

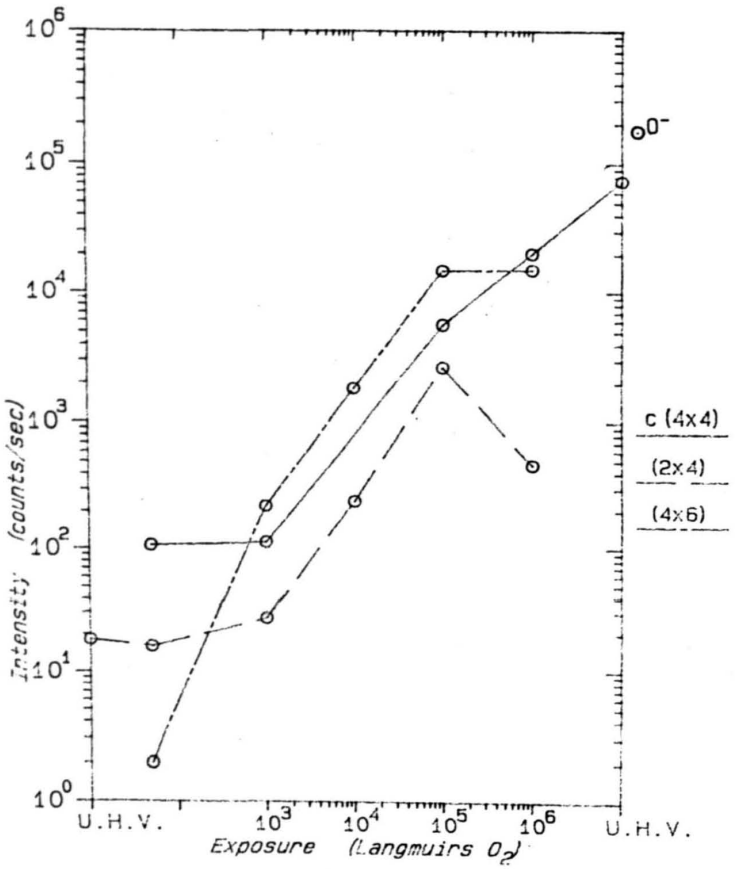

Figure 5.5 Negative secondary ion evolution with oxygen exposure.
a) O^-.

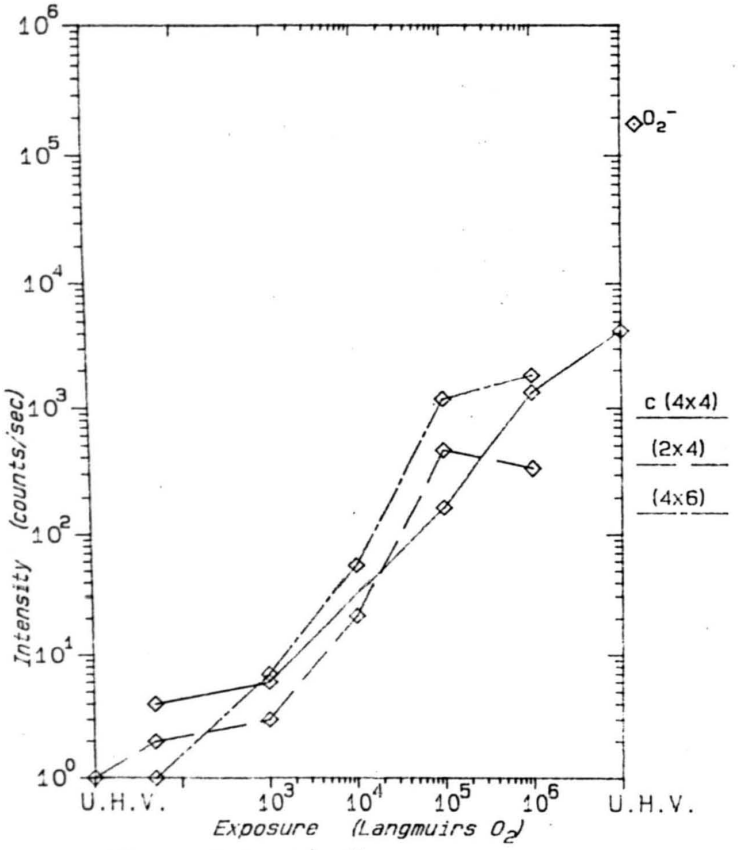

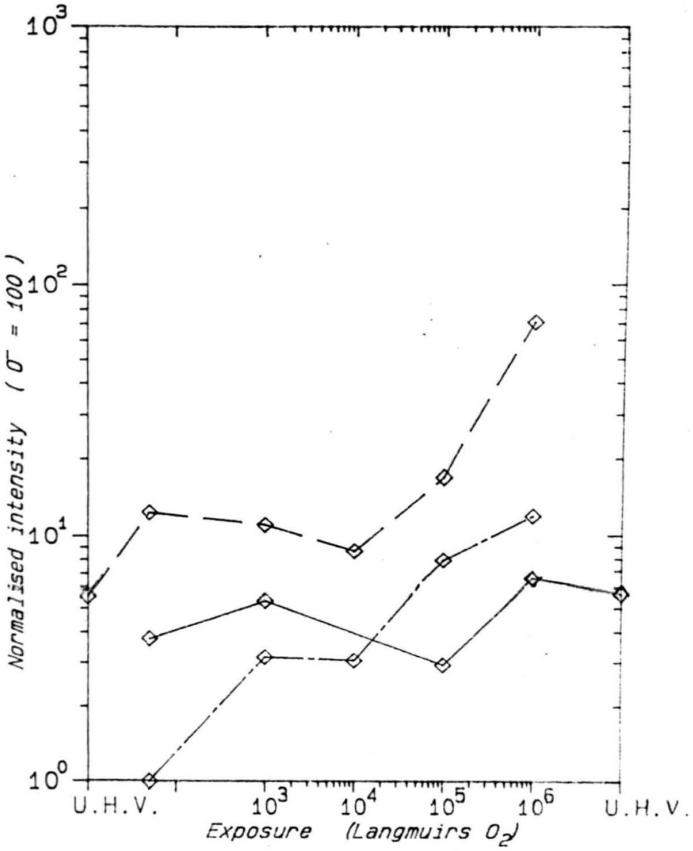

Figure 5.5 b) O_2^-.

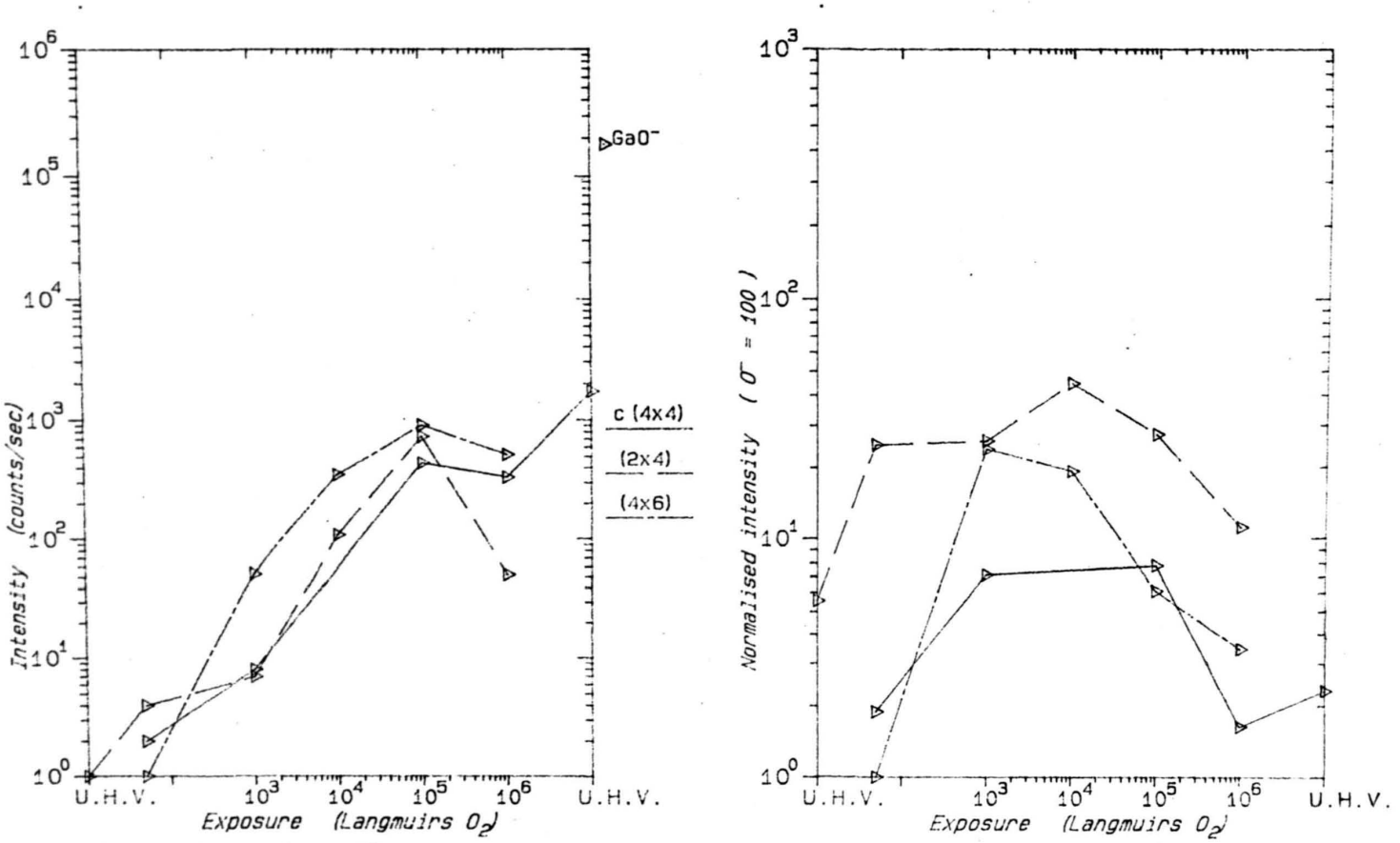

Figure 5.5 c) GaO^-.

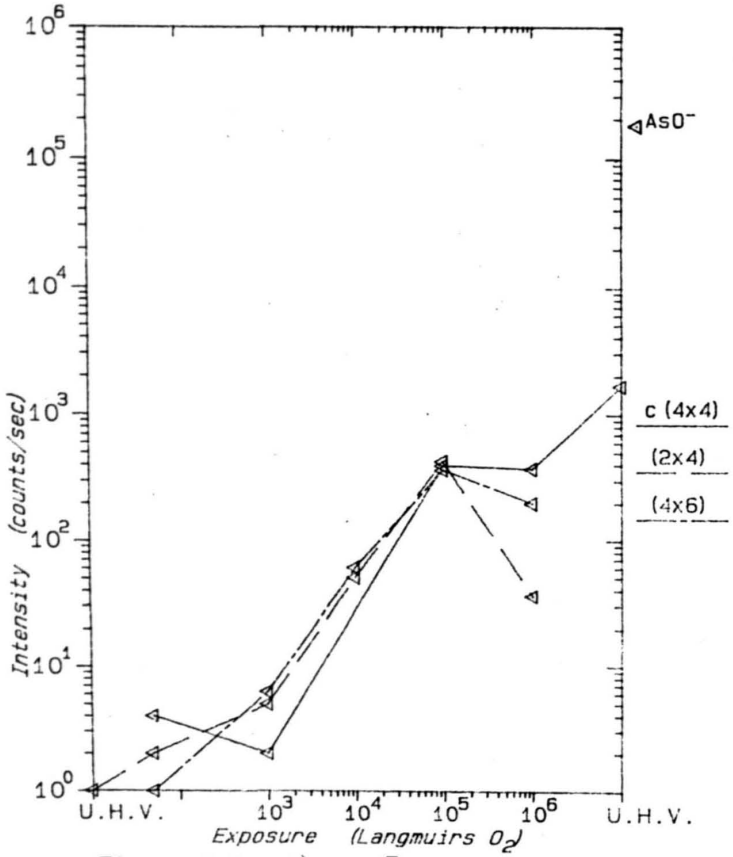

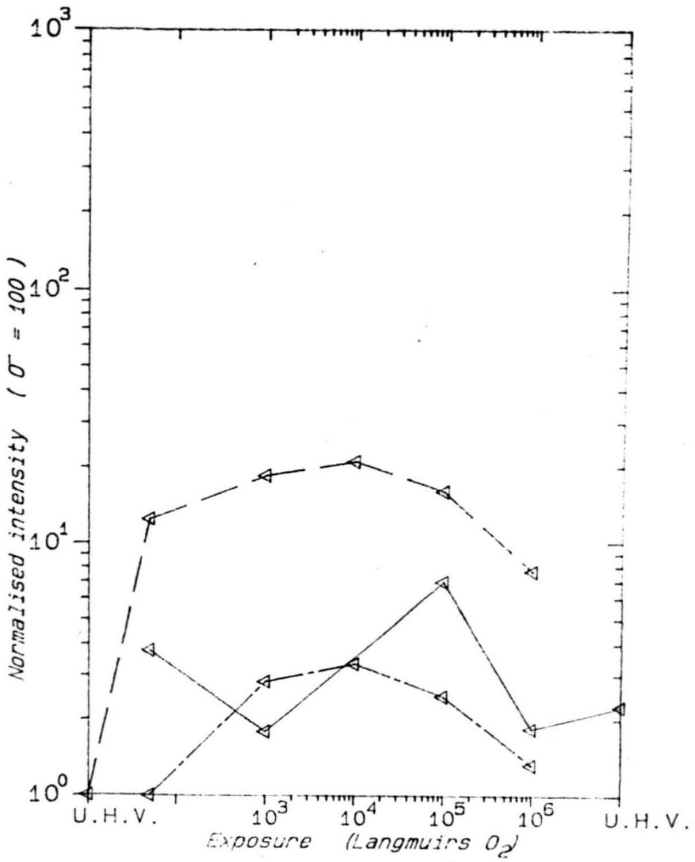

Figure 5.5 d) AsO^-.

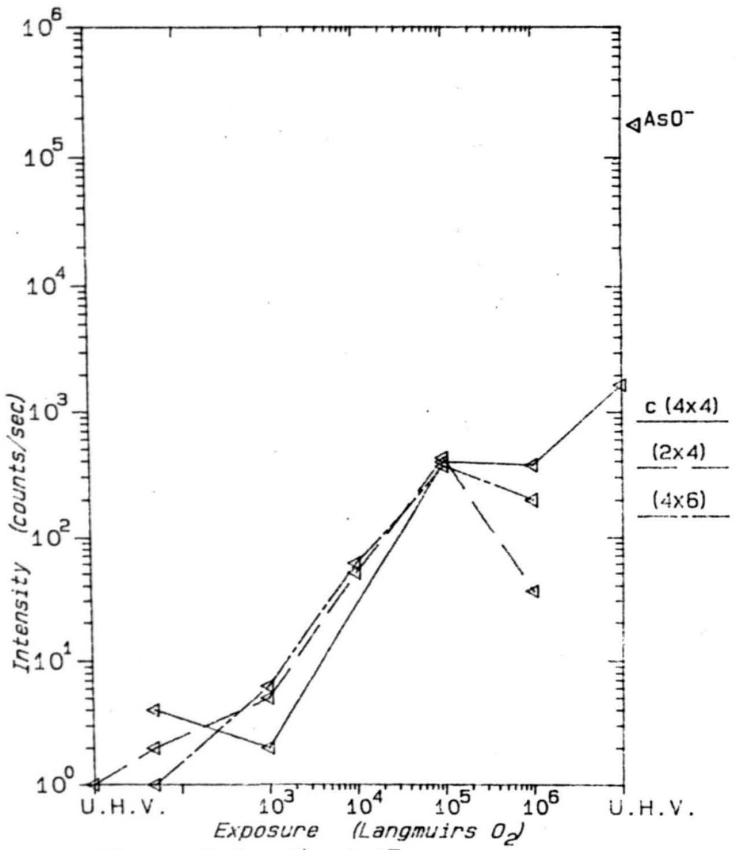

Figure 5.5 d) AsO^-.

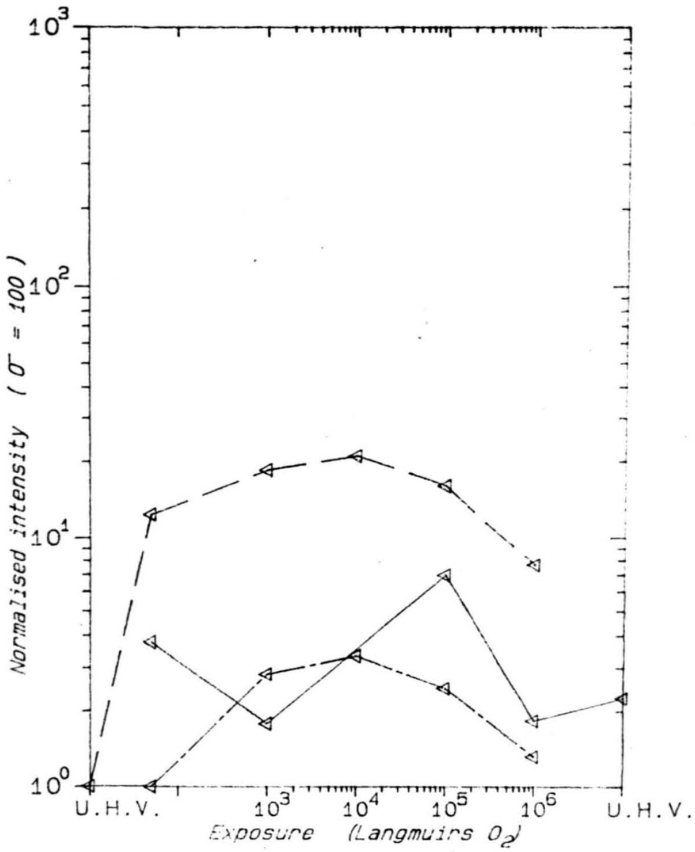

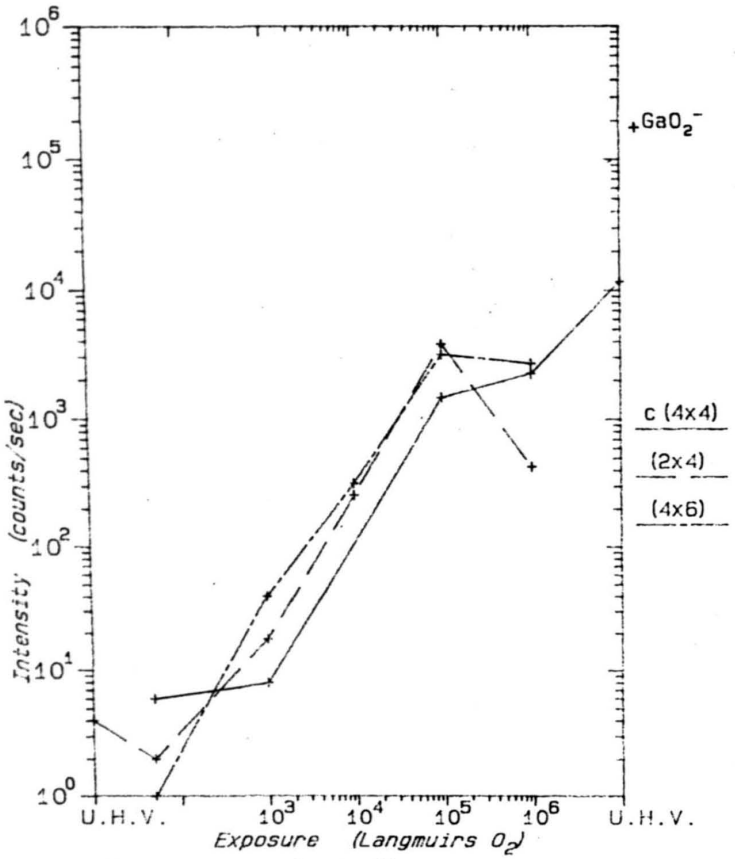

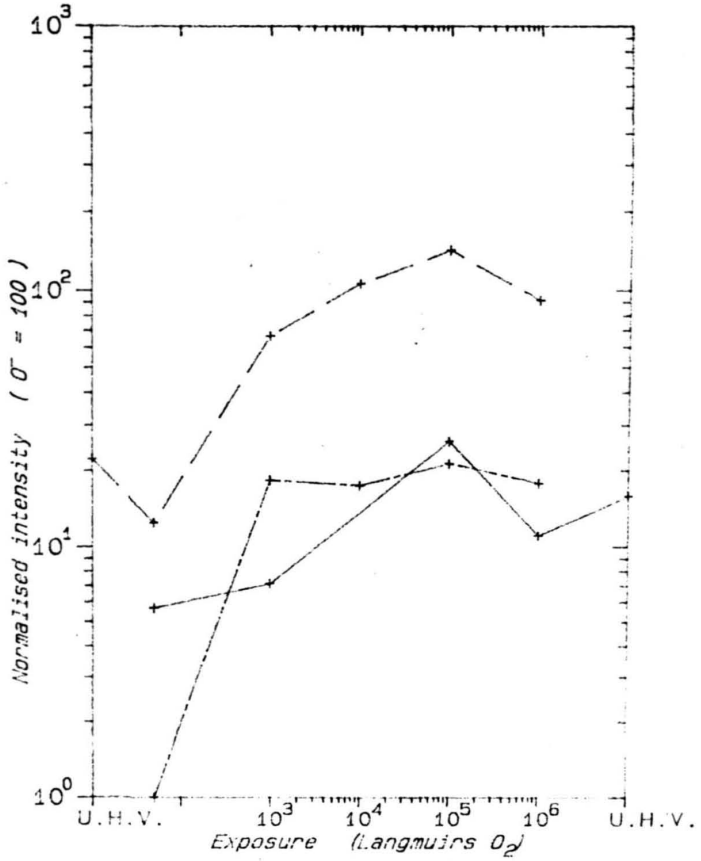

Figure 5.5 e) GaO_2^- .

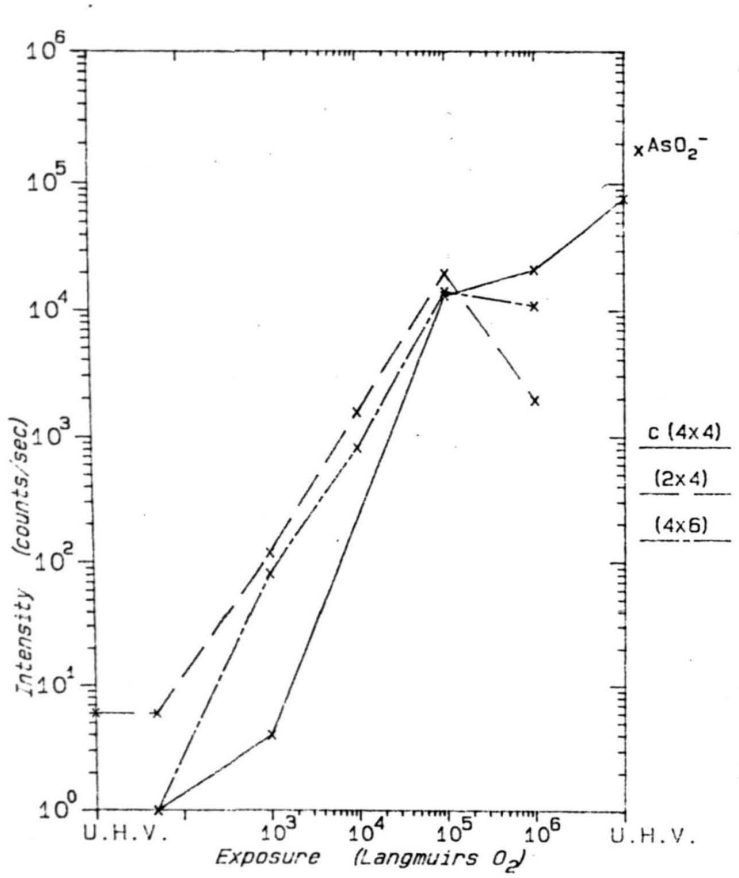

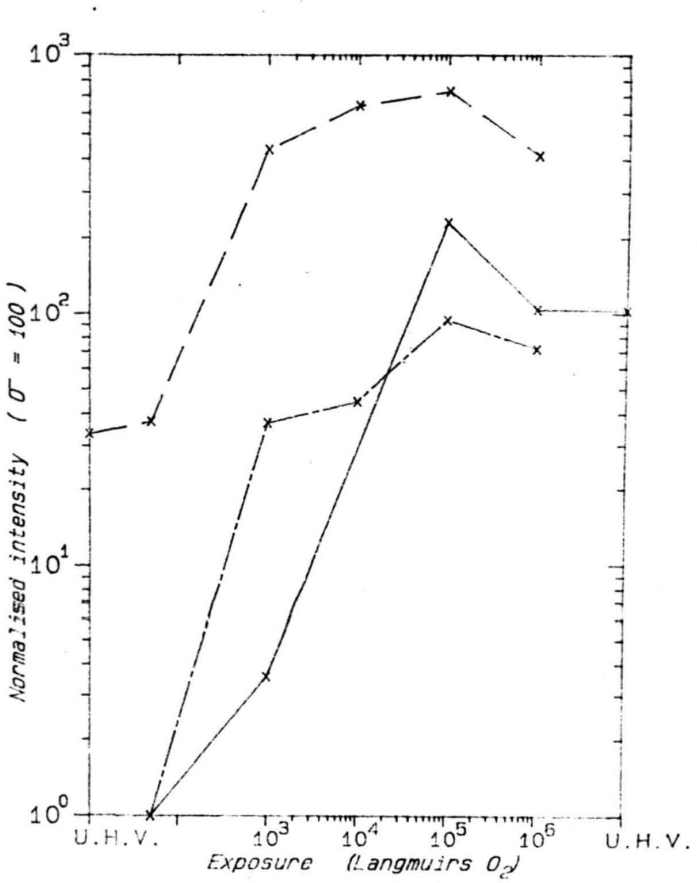

Figure 5.5 f) AsO_2^-.

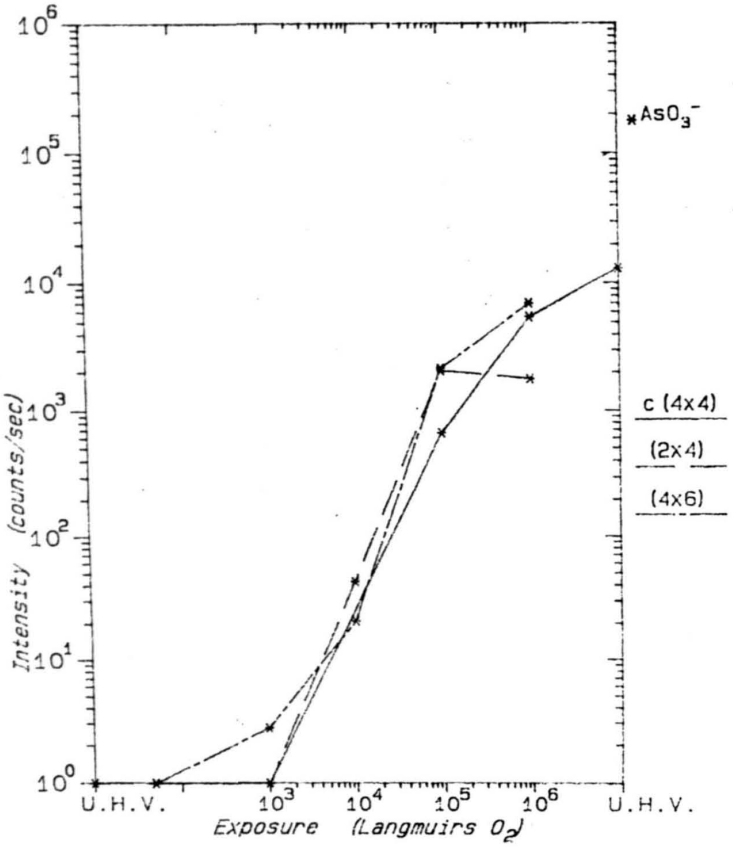

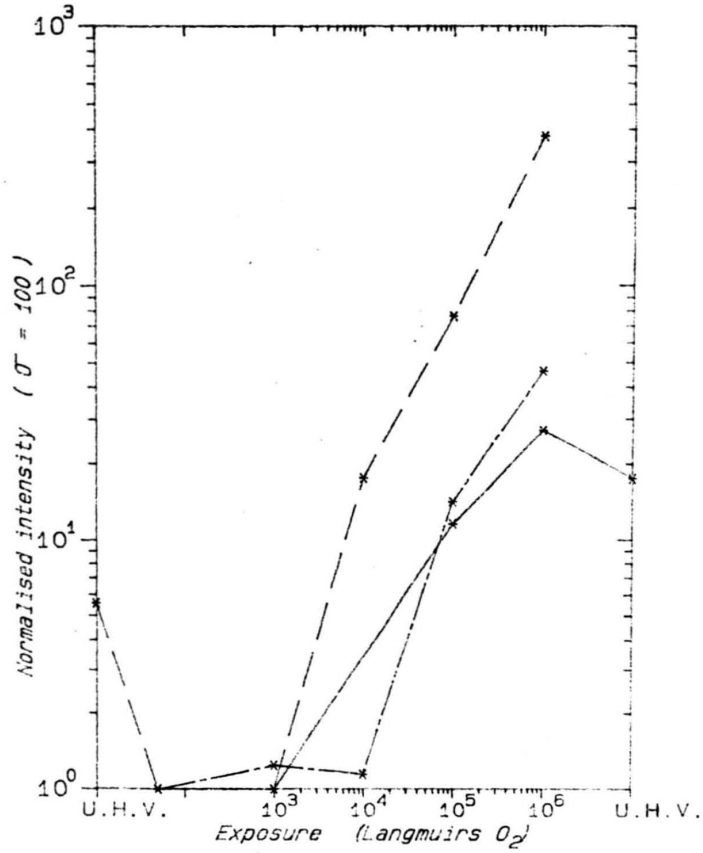

Figure 5.5 g) AsO_3^-.

5.4 Results from Oxygen Exposures

Secondary ion mass spectra of the three different surfaces examined after oxygen exposure are shown in figures 5.1 - 5.3. They may be compared with the spectra of figures 4.2 - 4.4 obtained from the same surfaces before oxygen exposure, and show a considerable increase in secondary ion yields. The evolution with oxygen exposure of selected positive and negative secondary ion signals from the three surface types are shown in figures 5.4 and 5.5.

Various SIMS investigations of oxidation and adsorption on metals and semiconductors have indicated that the O^+ [Yu (1978a), Reuter & Wittmaack (1980)], O^- [Ganschow et al (1979)], MO^+ [Dawson & Tam (1979b)], or MO^+/M^+ ratio [Marien & De Pauw (1982)] (where M is the substrate atom) is proportional to the oxygen surface coverage, at least in the sub-monolayer range. However Ganschow et al (1979) have shown that these proportionalities are not generally true, and that the actual relation must be determined for each particular case. (See also Dawson (1976), Hopster & Brundle (1979), Fleisch et al (1978), Dawson & Tam (1979b)). Yu (1978b) has also found significant differences in the form of such relationships between secondary ion signals and oxygen coverage dependent on the energy of the primary ion species in the range 150 - 2000 eV. However, it was found in this present investigation that there was no species which gave a monotonic increase with oxygen exposure for all three surface types over the range of exposures studied, and could therefore be identified with oxygen coverage.

At a slightly more general level Wittmaack (1979a) has determined a reversible dependence of SIMS signals from a molybdenum surface on oxygen exposure and ion bombardment, and similar SIMS results were obtained from thin thermally grown oxides on silicon and after sputter erosion of thicker layers [Wittmaack (1977)]. Marton (1980) has obtained a simple, but quantitative, theory of this type which has been applied to the oxidation of both silicon and [Marton & Csanady (1982)] aluminium. Due to problems with the photon counter already discussed reliable measurements of the variation of secondary ion signals with primary ion dose were only obtained for the (2 x 4) As stabilised surface, and these results are shown in figure 5.6. They will be fully discussed in Section 5.5, but at present we should note that although some species (O^-,

AsO_n^-, O^+, AsO^+, Ga_2^+) show indications of this reversible behaviour with oxygen exposure and ion bombardment, the (non-linear) scale equivalence of oxygen exposure and ion bombardment is different for the different species, and other species (GaO_n^-, Ga^+, As^+, Ga_2O^+) are definitely at variance with this interpretation. Such effects are probably attributable both to the disordering effect of the ion bombardment and incorporation of oxgyen below the surface layer. Further investigation of the possible reversibility of oxygen exposure and ion bombardment may be worthwhile if secondary ion data were available at more closely spaced oxygen exposures to more clearly define the form of secondary ion signal dependence on oxygen exposure. However, anticipating results yet to be discussed, it is difficult to envisage the precise nature of this relationship if oxygen adsorption is also dependent on the pressure at which the exposure is performed.

The interpretation of these secondary ion dependences on oxygen exposure is also complicated by the variation in absolute intensity observed between spectra from adjacent areas of the sample. This variation could be by up to a factor of two although 20% variation was more usual. Many consequences of such a variation can be avoided by normalising to a suitable large and fairly constant signal - Ga^+ is the obvious reference for the positive ions and in the absence of a more suitable signal O^- has been used for the negative ions. These normalised secondary ion dependences on oxygen exposure are also presented in figures 5.4 and 5.5 alongside the non-normalised results.

Examination of these plots of the dependence of secondary ion signals on oxygen exposure produces only two obvious systematic differences in results from the different surface reconstructions. In fact the similarity of the results from the different surface reconstructions is itself an important, and perhaps surprising result. The differences are:

(1) An increased O^-, and to a lesser extent O^+, O_2^-, and GaO^-, secondary ion signals from the (4 x 6) Ga stabilised surface. The larger O^- signal is emphasised by the generally smaller normalised negative ion signals from this surface. This correlates with the higher sticking coefficients observed for oxygen on this surface [Ludeke & Koma (1975), Ranke &

Jacobi (1981)], but it is difficult to understand why there is no comparable increase in any matrix related secondary ions, although the increased GaO^- signal may indicate that this oxygen is bound predominantly to Ga atoms.

(2) A reduction of most negative and some positive secondary ion signals from the (2 x 4) As stabilised and (4 x 6) Ga stabilised surfaces after the 10^6 L oxygen exposure. These exposures were carried out overnight at pressures of $\sim 2 \times 10^{-5}$ Torr O_2 whilst the C(4 x 4) As rich surface was exposed for 1000 sec at 10^{-3} Torr, and the most likely explanation is that this different exposure regime is the cause of the reduced signals. Dependence of adsorption on pressure as well as total dose of gaseous exposure has previously been observed with oxygen adsorption on InP [Dowsett & Parker (1979)] and PbTe [McGlashan (1982)] so this may well be a real effect which can only be investigated by repeating the exposures for a range of oxygen pressures.

Changes of secondary ion spectra obtained from the oxygen exposed C(4 x 4) As rich surface after leaving in UHV also indicate that some modification to the oxide occurs after its initial formation. This could be due to loss of volatile species from the surface, and the acquisition of SIMS spectra during or after controlled temperature cycling of the sample would be useful in elucidating this point.

Other differences appear to be comparatively small and could be due to differences in the relative sensitivity of the SIMS system or to statistical errors, particularly at the lower count rates, and speculating on other possible causes does not appear to be worthwhile at present. It is apparent that the oxygen exposures need to be repeated using smaller exposure increments and the same exposure regime and SIMS parameters for each surface type to distinguish between various possible causes of the variations in SIMS spectra so far observed.

We must now progress to some deductions about the oxidation process from the similarities apparent in these spectra obtained from the different surfaces. Taking various points in order we have:

(1) The O_2^- and AsO_3^- secondary ion signals increase more rapidly, relative to other negative secondary ion signals at the higher exposures. In terms of the direct emission model this would indicate the adsorption of molecular O_2, at the higher exposures onto an already oxidised As atom site. If we consider recombination processes to occur then this result may indicate recombination of AsO with molecular adsorbed O_2 species, or simply recombination of As and O with a much higher adsorbed O concentration being reflected in the production of multimers. The absence of any GaO_3^- is easily explained by the likely instability of such an ion with Ga in a formal valance state of +5. It is probable that molecularly adsorbed O_2 would only be weakly bound to the surface, and may also be mobile, and this could be investigated by thermal desorption or controlled temperature cycling as mentioned above. Measurement of secondary ion energy spectra may also provide information on the binding energy of various species.

AsO^+ and As^+ secondary ions also increase more rapidly than other positive secondary ion species (particularly GaO^+) and AsO_2^+ is only apparent at the higher exposures, which suggests that they may be derived from the same parent structure, and this is supported by results from ion bombardment to be discussed in Section 5.5. Thus there are strong indications that AsO_3^-, O_2^-, AsO_2^+, AsO^+ and As^+ secondary ions are all produced from a single parent structure, but it is not known whether these species are produced as intact clusters by the direct emission process with possible rearrangement and fragmentation from an excited state of a large molecular species, or by recombination reactions with a common initial or intermediate stage.

(2) Matrix dimers Ga_2^+ and $GaAs^+$ both decrease with oxygen exposure. For the Ga_2^+ this is a progressive decrease, but the $GaAs^+$ signal is more nearly constant until the 10^6 L exposure. In terms of the direct emission model this can be interpreted as due to insertion of oxygen into Ga-Ga and Ga-As bonds and shows initial oxidation in defective gallium rich regions whilst breaking of Ga-As bonds only occurs at the highest exposures used. If formation by recombination is

allowed then a progressive decrease of these dimers would be expected merely due to the reduced concentration of matrix atoms in the surface layer. These results may therefore be interpreted as supporting the view that Ga_2^+ is formed by recombination rather than sputtering from defective regions of the lattice, and that $GaAs^+$ is sputtered as an intact cluster, as was proposed in Chapter 4 for the clean (2 x 4) As stabilised surface.

(3) The absence of any significant $GaAsOH^+$ species. The presence of $GaO_nH_m^+$ where n = 1, 2 and m = 0, 1, 2 but only AsO_n^+ can easily be explained by the direct emission model as showing that hydroxyl groups, and adsorbed water, are only bound to surface Ga atoms, and applying this simple argument to the absent $GaAsOH^+$ ions implies that hydroxyl groups only bond to those Ga atoms which are not incorporated in the GaAs lattice but forming Ga microdroplets or other defects. Such a scenario does not seem inherently likely, particularly in view of the strong chemical interaction of water vapour with gallium arsenide surfaces reported by Koval et al (1981), Webb & Lichtensteiger (1982) and Mokwa et al (1984). The latter authors deduce that initial adsorption on the (110) surface is to the surface arsenic atoms. Another approach to this problem is to question the stability of the secondary molecules - perhaps, for example, ions containing AsOH groups are unstable and fragment before reaching the mass spectrometer - but such arguments can, of course, be applied to any particular species and, in the absence of basic calculations of molecular binding energies, must remain very speculative. Koval et al (1980), in fact, detected significant quantities of $GaAsOH^+$ from GaAs exposed to water vapour during ion bombardment. A time of flight mass spectrometer could be used to detect metastable ions as used by Ens et al (1983) to resolve the anomolies present in the series of $(CsI)_nCs^+$ peaks obtained in SIMS spectra of CsI.

Finally we can consider the general form of development with oxygen exposure of all positive and negative secondary ion signals as a further indication of the general progress of adsorption and

oxidation. After 10^3 L exposure the positive ions generally show a slight increase, except for matrix signals from the (2 x 4) As stabilised surface which decrease slightly - probably due to changes in work function as already discussed. Negative ion species also increase somewhat, the increase being noticeably larger from the (4 x 6) Ga stabilised surface. Except for positive -OH and $-OH_2$ containing ions which reach a maximum after the 10^4 L exposure, the trends at 10^4 and 10^5 L exposure are similar with a decrease of positive ion matrix dimers, but an increase in positive and negative ion oxide species. Ga^+ and As^+ ions, however, decrease from the C(4 x 4) As rich surface but increase in the other two cases. After 10^6 L exposure there is a noticeable difference between the C(4 x 4) As rich surface which received a short, high pressure exposure and the other two surfaces where an overnight low pressure exposure was used. For the C(4 x 4) As rich surface only positive ion matrix dimers decrease and there is a particularly large increase of the AsO^+ signal and the appearance of more complex oxide species than observed at lower exposures. The negative ions GaO^- and AsO^- show a slight decrease but all other negative ion species increase, particularly those with a high oxygen content. After further exposure of this oxidised surface to UHV all positive and negative ion signals increase further except $GaOH_2^+$ and AsO_2^+. The other two surfaces, after the overnight 10^6 L exposure, show generally smaller increases in positive ion signals and all negative ion signals decrease except for the highly oxidised AsO_3^-.

These results are generally consistent with a scenario in which the 10^3 L exposure leads to adsorption on the surface principally at defect sites with relatively little effect on general surface ion yields, and also on sites associated with surface gallium atoms. After 10^4 and 10^5 L exposure there is adsorption and general breaking of bonds in the surface, with an oxygen rich surface layer enhancing predominantly the yield of negative secondary ions. At 10^6 L exposure chemical reaction has occurred breaking back-bonds of surface atoms and oxygen is incorporated beneath the surface layer leading to enhancement of both positive and negative ion yields, and multimer species characteristic of the oxide layer rather than the original substrate. Further chemical reaction occurs with time, the surface oxygen moving into the lattice producing a thicker, but less highly oxidised, surface oxide layer,

responsible for reduced enhancement of negative ion yields.

This interpretation can only be tentative because of the many effects which may influence the early stages of oxidation and secondary ion production. One aspect not yet mentioned is the influence of the initial exposure to the UHV background (which was not measurable due to failure of the SIMS residual gas analyser at this time) on the subsequent oxygen exposures, and continued effects in conjunction with the oxygen exposure. Hopster & Brundle (1979), for example, found that the formation of hydroxide species on nickel surfaces was dependent on simultaneous exposure to O_2 and H_2O (the latter possibly present in the residual gas), but was not formed with independent or sequential exposures to either species. It should be noted that the greatest differences between the different GaAs surface types occur after the 10^3 L O_2 exposure at 10^{-6} Torr where differences in the simultaneous and previous exposure to residual gas will be a maximum, and after the 10^6 L O_2 exposure where different O_2 pressures were used and simultaneous residual gas exposure will also be different due to partial throttling of the main vacuum pump.

It is also conceivable that a surface oxide may be formed which is in equilibrium with the oxygen overpressure and that subsurface oxidation (beneath the outermost monolayer) is by a diffusive process from this surface reservoir. On removal of the oxygen overpressure subsurface oxidation could then continue with reduction of the heavily oxidised surface until equilibrium is established, and the surface itself may also lose oxygen by desorption of weakly bound species. A series of rapid measurements after exposures at different pressures would be necessary to examine such a possibility.

The generally fairly constant O_2^-/O^-, GaO_2^-/GaO^- and AsO_2^-/AsO^- ratios at least for exposures of below 10^6 L and bearing in mind the low count rates involved, may be interpreted as an indication of localised oxidation occuring by a nucleation and growth process, so that oxygen atom concentration in oxidised areas is fairly constant until 10^6 L exposure when a noticeably higher level of oxidation is achieved.

In summary SIMS analyses of the oxidation process of differently reconstructed GaAs surfaces allow some interesting but tentative

deductions about the oxidation process to be made, since interpretation of the results is hampered by several interfering effects. It is evident, however, that additional measurements with more closely spaced exposure increments would help to eliminate and quantify the effects of variable surface defect density, residual gas, pressure of exposure, additional reactions after terminating oxygen exposure, and possible changes of SIMS parameters.

deductions about the oxidation process to be made, since interpretation of the results is hampered by several interfering effects. It is evident, however, that additional measurements with more closely spaced exposure increments would help to eliminate and quantify the effects of variable surface defect density, residual gas, pressure of exposure, additional reactions after terminating oxygen exposure, and possible changes of SIMS parameters.

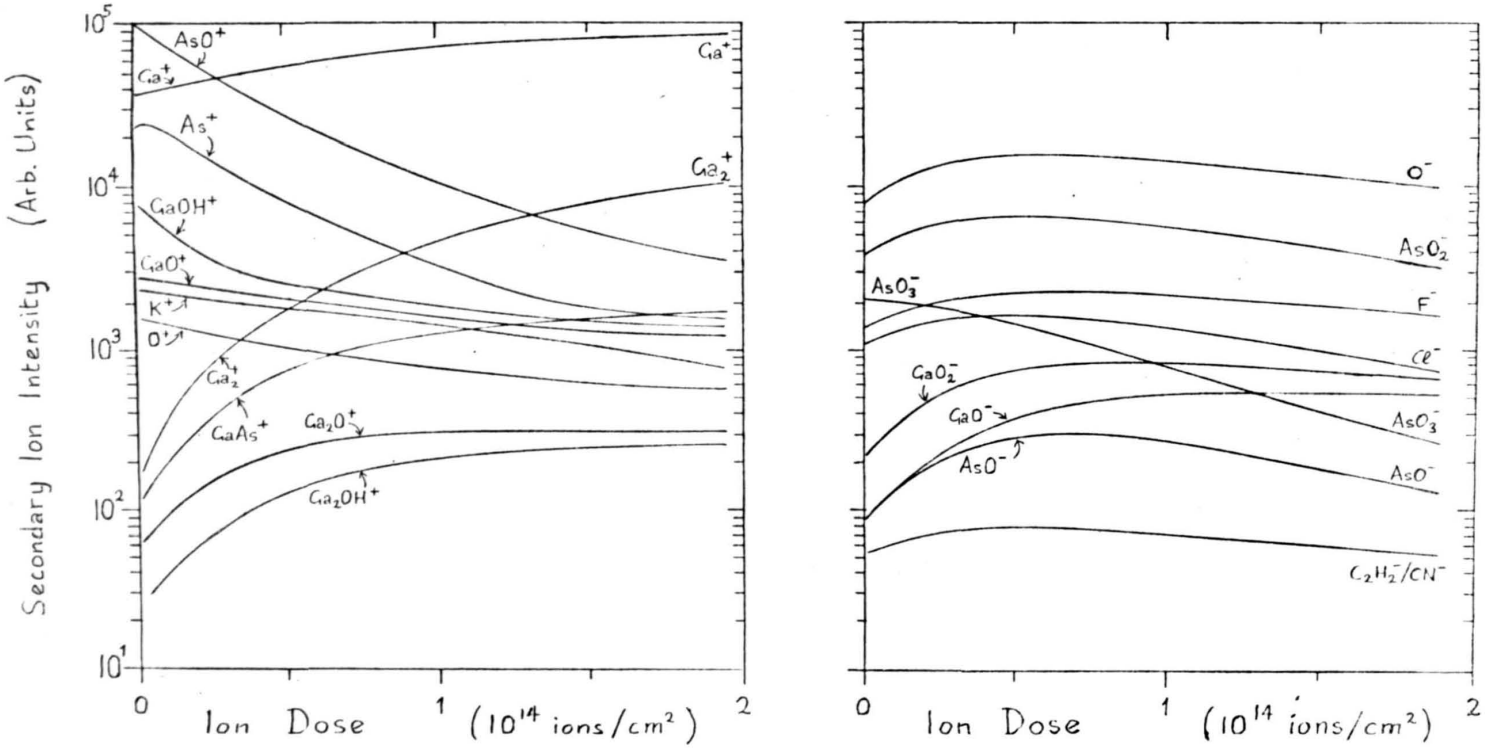

Figure 5.6 Ion dose dependence of secondary ion species from oxidized (2×4) As stabilised surface.

5.5 Ion Dose Dependence

The variation with cumulative ion dose of secondary ion signals from the clean reconstructed GaAs surfaces has been discussed in Section 4.3.3, and results from the oxidised surfaces already mentioned in connection with a possible reversibility of oxygen exposure and ion bombardment. Results from the (2 x 4) As stabilised surface are shown in figure 5.6 but similar measurements from the other surface reconstructions after oxidation are not accurate due to problems with the photon counter. Consideration of the measurement sequence for the negative secondary ion signals indicate that there should, however, be relatively little interference between the various species, and the results from the (4 x 6) Ga stabilised surface are quite similar to those obtained from the (2 x 4) As stabilised surface but no equivalent results were obtained for the C(4 x 4) As rich surface.

The positive ion results, on the other hand, do allow considerable scope for interference between different species and it is impossible to draw any definite conclusions apart from a rapidly decreasing AsO^+ signal (with cross section for desorption or destruction of $\sim 3 \times 10^{-14}$ cm^2) but the results do not indicate any gross differences in the real secondary ion signals generated from the different oxidised surfaces, and this is supported by a full SIMS spectrum obtained from the ion bombarded surface.

The most intriguing result from these measurements is the initial increase of all negative secondary ions except AsO_3^-. This strongly suggests that AsO_3, or its parent species, on the surface is rapidly destroyed by the ion beam and that the products of this destruction are causing a general enhancement of negative secondary ion yields which more than compensate for reduction caused by sputtering or destruction of all other species. It would be very interesting to see whether any similar effect occurs on less highly oxidised surfaces where the AsO_3^- signal is proportionately much lower.

The positive ion results show similar reductions in AsO^+ and As^+ species with ion dose which suggests that these may be from the same parent surface species as the AsO_3^- ions. However a careful examination of the As^+ signal shows a small initial portion of constant signal not present in the AsO^+ signal which may indicate that the former signal is produced predominantly from some inter-

mediate stage in the destruction of the parent species. GaO^+, $GaOH^+$, O^+ and the contaminant species K^+ are all seen to decrease slightly during the ion exposure, whilst all other species (Ga^+ and matrix dimers including those with additional O or OH atoms) increase substantially. This latter effect can be attributed in part to the removal of a surface oxide shielding the underlying substrate, but the increase of oxide and hydroxide species suggests that they may be formed by a recombination process, possibly in the case of Ga_2OH involving reaction with water vapour from the residual gas.

It is noticeable that at the total dose of $\sim 2 \times 10^{14}$ ions/cm^2 the As^+ and $GaAs^+$ signals are similar to those obtained from the ion-bombarded clean surface, whereas Ga^+ and Ga_2^+ are still considerably reduced and all oxide signals at a comparitively high level. In future work a much larger total ion dose should be accumulated to determine how the various secondary ion signals return to levels characteristic of the ion-damaged substrate as the surface oxide layer is sputtered away. However it should be noted that Taglauer et al (1979) report that recoil implantation may produce substantial effects in signals characteristic of the adsorbed species when they have been reduced by sputter desorption to about one tenth of the initial coverage.

5.6 Discussion of SIMS Results

As with the corresponding section of Chapter 4, this section is intended to widen the discussion of the SIMS results from details already considered in the previous sections to a more general comparison with additional aspects of theory and related experimental work. Many of the points made in this previous discussion regarding the fundamental processes of secondary ion emission from the clean reconstructed surfaces are equally applicable to the oxidized surfaces.

One related topic is the applicability of the direct emission model to sputtering of oxidized alloys and pure metals. Most results for alloys appear to be limited to the high dose dynamic SIMS mode, but Slusser (1979) has reported low dose results from adsorption of CO on a PdAg alloy where IR spectroscopy has shown that the CO molecule is bonded to Pd, whilst no AgCO bonding occurs with pure Ag. SIMS results show a rapid increase in the $AgCO^+/Ag^+$ intensity ratio to a constant value whilst the $PdCO^+/Pd^+$ ratio continues to rise more slowly comparable with the general saturation of secondary ion intensities with increasing CO exposure. These results are consistent with CO bonding to Pd only if $AgCO^+$ is formed by a recombination process dominated by the availability of Ag. Also of relevance are the theoretical results of Garrison et al (1978) who found that for oxygen adsorbed on copper, where the oxygen is bonded to a single copper atom in the surface, it is more likely for the copper atom to escape from beneath the oxygen atom without ejecting it than for both atoms to desorb. Furthermore, increasing the strength of the Cu-O bond used in the calculations decreases the CuO yield. Both of these results are inconsistent with the direct emission model, but difficult to directly verify experimentally.

We may also note that $NiCO^+$ and Ni_2CO^+ in SIMS spectra were initially correlated with linear and bridge bonded CO on a nickel surface, but that more recent results by Dawson & Tam (1980), Hopster & Brundle (1979) have shown no such correlation. In this present investigation the appearance of $GaAsO^+$, Ga_2O^+ and Ga_2OH^+ may be correlated with bridge bonded oxygen, insertion of oxygen atoms into lattice bonds or simply recombination after sputtering, but it is not possible to determine which is the major influence. The formation of molecular cluster ions by recombination processes

is discussed by eg Winograd (1982) and Garrison et al (1978) with reference to oxidized nickel surfaces and Yu (1981a), (1981b) has applied these concepts to oxidized titanium, niobium and vanadium with limited success. The experimental methods used involve rather complex correlations between the intensities of different secondary ion species over a range of conditions, and are open to argument until a definite positive correlation of experimental results with a particular recombination reaction is achieved (see also Wittmaack (1979b) and Winograd et al (1979)). It is apparent that a considerable amount of work is required to unambiguously determine the method of formation of any particular molecular secondary ion and, until this is done, any deductions of local surface structure from such molecular secondary ions are necessarily somewhat speculative. It may be noted that Hopster & Brundle (1979) in their work on oxidized nickel surfaces were, unlike Fleish et al (1978), unable to detect any direct evidence for SIMS sensitivity to changes in surface structure as followed by LEED. They were, however, able to distinguish between adsorbed O and OH species.

In contrast to these results other work (eg Buhl & Preisinger (1975), Dowsett et al (1978), Dowsett & Parker (1979)) has been used as evidence in support of the direct emission model of cluster formation. However these works often ignore mass interferences in the spectra or assign them on the basis of the known substrate structure with other peaks attributed to defects or contamination, thus assuming the validity of the direct emission model and forming a circular argument showing no more than that the results are generally consistent with this interpretation.

Correlations of SIMS spectra with surface structure are based on the idea that different structures will produce different, characteristic, "fingerprint" spectra. However, various structures eg oxygen on W(110) [Bauer & Prigge (1984), Bauer & Engel (1978) and refs therein] give no correlation between SIMS spectra and known changes in composition. Other surfaces eg oxygen on beryllium [Kraus & Grun (1979), (1980)] have only provided such information in the energy spectra of the different secondary ions, and we have already mentioned the inability of Hopster & Brundle (1979) to reproduce the change in O_2^-/O^- relative intensity found by Fleish et al (1978) on the structural change of the oxidized nickel surface.

In view of these results it is perhaps not surprising that no obvious, abrupt changes in SIMS signal intensities have been observed from the oxidized gallium arsenide surfaces where only gradual changes and the growth of an amorphous oxide have ever been reported. If these investigations are continued it is obviously essential, in addition to obtaining data at smaller exposure increments, to measure the energy distribution of various secondary ion species to see whether this can give any information about changes in surface chemistry. Furthermore, if the surface oxide is formed by a process of nucleation and lateral growth then it is essential to minimise the concentration of defects present on the initial surface which could act as nucleation centres and may dominate the early stages of oxide growth. Again it would be useful to obtain results from (110) surfaces so that they could be compared with the measurements and theories of Spicer and co-workers (eg Su et al (1982) and refs therein) for this surface. In view of the range of sticking coefficients reported for this system, and the possible large effect of defects on SIMS signals, some independent means of measuring oxygen coverage would now appear to be essential.

The desirability of a new sample holder designed for the static SIMS application has already been discussed in terms of the clean surface measurements. This will also be necessary for measurement of variation of oxide secondary ion intensities with azimuthal angle, and inclusion of a heating stage would permit the use of thermal desorption and temperature cycling of the sample to investigate different adsorption states. This could also be used in an investigation of the process of heat cleaning used preparatory to MBE growth of epilayers.

5.7 Summary of Oxidized Surface Measurements

The results obtained do not show any major differences in the response of the three surface reconstructions studied to oxygen exposure, although the sticking coefficient on the (4 x 6) Ga stabilised surface does appear to be slightly larger than the other two surfaces, as indicated by previous work. The results suggest that after initial adsorption, possibly at defect sites, the oxide is formed by a process of nucleation and lateral growth, involving oxidation of both gallium and arsenic atoms, followed by the development of a more highly oxidized surface layer at larger oxygen exposures.

Various problems have been overcome in obtaining these results and several other interesting aspects, which merit further study, have been observed. The studies were not, however, as extensive as those carried out on the clean surfaces and, with the continuing paucity of complimentary data on the (001) surface and its chemistry, further evaluation of the oxidation process involving SIMS requires the incorporation of additional well characterised techniques.

CHAPTER 6

Overview and Conclusions

A molecular beam epitaxy system has been designed and constructed and used for the growth of silicon doped gallium arsenide. Following the identification and elimination of various problems, high electron mobilities, close to Poth's universal curve, have been obtained for electron concentrations between $\sim 5 \times 10^{15}$ cm^{-3}, where residual impurities become significant limiting 77K electron mobility to < 30,000 cm^2/Vs, and a solubility limit at $\sim 7 \times 10^{18}$ cm^{-3}. Unintentionally doped layers are high mobility p-type ($\sim 10^{15}$ cm^{-3}, 8,000 cm^2/Vs at 77K) with carbon acceptors as the major impurity. The major source of this carbon is identified as the high temperature graphite source cells which should be replaced with pyrolytic boron nitride cells, and additional cryopanelling fitted to reduce further the flux of impurity species incident on the growing epilayer. Water-vapour and other impurities in the residual gas, which create deep traps in the epilayers, are significantly affected by carry-over from the loading chamber, and a separate UHV pump should be fitted to the load lock to overcome this problem.

Surface morphology of the epilayers has been monitored using Nomarski phase constant microscopy. Gross imperfections in the epilayers have been associated with inadequate surface preparation, and generally eliminated. The cause of various minor imperfections in the layers has not been established although residual contamination of the substrate or impurities in the residual gas seems likely, and the routine use of additional surface analysis equipment is considered highly desirable for the elimination of such contamination. Further investigation of the epilayers using established techniques such as preferential defect etching, transmission electron microscopy and X-ray topography is called for to help characterize and ultimately reduce extended defect densities in the surface and thereby give increased confidence that such surfaces are suitable for fundamental studies of low dose SIMS, and measurement of the intrinsic properties of the gallium arsenide surface. Further work is also required to ensure the reproducible production of the range of different gallium arsenide surface structures - particularly in the gallium rich composition region -

and their preservation on cooling to room temperature. The results of this and other investigations suggest that reflection electron diffraction is not sufficient to define uniquely the reconstructed surface.

However, the final epilayers are the best yet grown in this laboratory and, although not of the best quality obtained elsewhere, they are, apart from the carbon contamination, believed to be comparable with those routinely grown in other laboratories in the UK and elsewhere.

Surface properties of three stable reconstructions of the gallium arsenide surface have been investigated with low-dose SIMS, following their preparation by MBE and transfer to the SIMS analysis chamber under UHV conditions. Secondary ion mass spectra covering the range of 1 to 250 amu have revealed several mass interferences and shown the necessity for a positive identification of the mass peaks from isotopic abundances or other data before sampling only selected mass peaks to reduce the total primary ion dose required. The initial results showed a considerable rise in the Ga_2^+ secondary ion signal with ion dose, comparable with known damage cross sections from ion-implantation studies, and as a consequence computer control programmes were modified to reduce considerably the ion dose required to obtain SIMS spectra, by sampling only the maxima of selected mass peaks. One disadvantage of reducing the primary ion dose in this way, but which only became apparent later, is the possibly large effect on the measured intensities of small drifts in the mass scale which are not immediately apparent in the data. This should be avoided in future either by checking the mass tuning by using a much smaller mass increment or, possibly, by routinely monitoring half-integer masses also. However the final results showed a much reduced dependence of Ga_2^+ on ion dose, and it is thought that this difference may be associated with variable quantities of arsenic adsorbed from the background gas, defective regions initially present on the gallium arsenide surface, or the effect of ion bombardment close to the $[\bar{1}10]$ azimuth and possible channelling effects. Further work with deliberately adsorbed arsenic layers and a range of incident angles of the primary ion beam, together with better characterisation of the initial surface defects, is required to elucidate the effect.

Comparative SIMS measurements of the differently reconstructed, clean gallium arsenide surfaces have shown reproducible differences only in the detection of higher positive secondary ion yields from the (2 x 4) As stabilised surface, which may be correlated with the higher work function of this reconstruction, and a higher relative $GaAs^+$ ion yield from this same surface although spectra have been obtained with a primary ion dose of as low as 5×10^{11} ions/cm^2. The precise reason for the increased $GaAs^+$ ion yield is not known but it is believed to be associated with a more 'bulk-like' surface with a predominance of Ga-As bonding over Ga-Ga or As-As bonds, which is consistent with the stability of this reconstruction and its use for MBE growth. Some effects dependent on primary ion energy and current density were also apparent, and these should be investigated to attain a better understanding of the processes involved in secondary ion emission. Negative secondary ion spectra of the as-grown surfaces were remarkable in showing only contaminant species.

Changes in secondary ion spectra on oxidation of gallium arsenide surfaces were not easily interpretable, but they do not show any great differences in oxygen uptake on the different surface reconstructions. Those differences apparent in the spectra can be attributed to differences in the details of the oxygen exposure used at different times, although there is indication of a higher initial sticking coefficient on the (4 x 6) Ga stabilised surface. A tentative deduction from the results is that after initial adsorption, possibly at defect sites, the oxide is formed by a process of nucleation and lateral growth, involving oxidation of both gallium and arsenic atoms, followed by the development of a more highly oxidised surface layer at large oxygen exposures. However the repetition of these experiments with smaller increments of oxygen exposure and more nearly identical treatment of the differently reconstructed surfaces is considered essential to confirm the results and their interpretation. Several interesting effects such as mass fractionation and ion bombardment induced species have been observed in the secondary ion spectra and their further investigation may lead to a better understanding of the secondary ion emission process.

It has become apparent during this investigation that the low-dose or static SIMS technique is not as yet sufficiently well

understood to be able to determine unambiguously the surface properties of a complex and little understood surface, such as that of oxidised gallium arsenide, without the use of additional well established surface analysis techniques. Further investigations with this system must be directed as much towards understanding the secondary ion emission process as in applying it to the problem of determining the gallium arsenide surface structure. Various possible experiments have been suggested in Chapter 4 and 5, and the importance of optimising the SIMS system for static rather than dynamic measurements, as originally intended, and also measuring secondary ion energy spectra, cannot be overemphasised.

Amongst the more important modifications to the SIMS system as it currently exists is the fitting of additional surface analysis equipment for comparison with SIMS results and measurement of surface composition. A combined LEED/AES/ESCA system is probably one of the most versatile and readily available systems which could be fitted to the analysis chamber. Work function is a controversial parameter in SIMS measurements and this should also be monitored, probably by a vibrating probe technique since electron bombardment of oxidised gallium arsenide is known to cause changes in the oxidation state, and such effects must not be forgotten when using the electron spectroscopies mentioned above. The sample holder should allow rotation of the sample about its surface normal, to permit investigation of the variation in secondary ion yield with azimuthal angle of the primary ion beam, and also include facilities for heating and cooling the sample. In addition the computer control and analysis programmes will require modification, both to deal with these requirements and to extract useful results from the large quantities of raw data which will inevitably be produced.

In summary, an MBE system has been successfully constructed and used to produce high quality gallium arsenide epilayers. Some of these epilayers have been transferred to a second UHV chamber and subjected to SIMS analysis. The results of these analyses have provided some interesting, and in some respects surprising, data on the gallium arsenide surface and its reaction with oxygen. Further investigations should incorporate additional surface analysis techniques and be directed as much towards understanding the process of secondary ion emission as in applying the results to understanding the gallium arsenide surface.

Acknowledgments

I wish to express my thanks to all those who have assisted in the production of this thesis. In particular I must thank my academic supervisor Dr E H C Parker for stimulating discussions and advice on all aspects of the work, and Dr M G Dowsett for obtaining the initial SIMS data and instruction in the use of the SIMS system. For electrochemical C-V measurements I am indebted to Dr W Y Leong of CLP, for PL spectra to Dr J Medland of GEC Hirst Research Centre, and for DLTS and additional PL spectra to Mr J Nicholas of UMIST. I also wish to thank my industrial supervisor Dr D K Wickenden and Dr J D Grange of GEC Hirst Research Centre, and Drs R M King, R A Kubiak, W Y Leong and D S McPhail of CLP for assistance at various stages of the project. Thanks are also due to the CLP technical staff A Aldridge, G Burton, K Burton, P Driscoll, R Elam, J Heal, W Hugkulstone and V Manning for assistance in the construction and operation of the system, and to Miss P Hunter for typing the manuscript. For financial support I am grateful to the Science and Engineering Research Council and the General Electric Company for the provision of a CASE research studentship.

REFERENCES

Abrahams M S, Buiocchi C J (1965) J Appl Phys 36, 2855; Etching of dislocations on the low index faces of GaAs.

Adachi S, Oe K (1983) J Electrochem Soc 130, 2427; Chemical etching characteristics of (001) GaAs.

Adkins C J (1968) Equilibrium Thermodynamics, McGraw Hill.

Akimoto K, Dohsen M, Arai M, Watanabe N (1983) Appl Phys Lett 43, 1062; As_4/Ga flux ratio dependence on Si incorporation in MBE GaAs.

Akimoto K, Dohsen M, Arai M, Watanabe N (1984) Appl Phys Lett 45, 922; Infrared absorption and photoluminescence spectra of GaAs grown by MBE.

Andersen C A, Hinthorne J R (1973) Anal Chem 45, 1421; Thermodynamic approach to the quantitative interpretation of sputtered ion mass spectra.

Arthur J R (1974) Surf Sci 43, 449; Surface stoichiometry and structure of GaAs.

Ashen D J, Dean P J, Hurle D T J, Mullin J B, White A M, Green P D (1975) J Phys Chem Sol 36, 1041; The incorporation and characterisation of acceptors in epitaxial GaAs.

Aspnes D E, Studna A A (1981) Appl Phys Lett 39, 316; Chemical etching and cleaning procedures for Si, Ge and some III-V compound semiconductors.

Bachrach R Z, Krusor B S (1981a) J Vac Sci Technol 18, 756; Morphological defects arising during MBE growth of GaAs.

Bachrach R Z, Bauer R S, Chiaradia P, Hansson G V (1981b) J Vac Sci Technol 19, 335; Reconstructions of GaAs and AlAs surfaces as a function of metal to As ratio.

Bafleur M, Munoz-Yague A, Rocher A (1982) J Cryst Growth 59, 531; Microtwinning and growth defects in GaAs MBE layers.

Ballingall J M, Wood C E C (1982) Appl Phys Lett 41, 947; Crystal orientation dependence of silicon autocompensation in MBE GaAs.

Barcz A, Croset M, Mercandalli L M (1980) IOP Conf Ser 54, 124; Quantitative analysis of III-V compounds using low-energy ion-scattering spectrometry.

Barcz A, Domanski M, Wojtowicz-Natanson B (1982) SIMS III proc Springer Verlag p 134; Current density effects on secondary ion emission from multicomponent targets.

Bauer E, Prigge S (1984) SIMS IV proc Springer Verlag p 201; Single crystal surface structure studies with static SIMS.

Bebb H B, Williams E W (1972) in Semiconductors and Semimetals Ed Willardson & Beer Academic Vol 8 Chap 4; Photoluminescence I: Theory.

Bedrick W, Koch B, Mai H, Seidenkranz U, Syhre H, Voigtmann R (1982) SIMS III proc Springer Verlag p 81; Distortion of secondary ion extraction due to sample surface irregularities.

Benninghoven A (1973) Surf Sci 35, 427; Surface investigation of solids by the statical method of secondary ion mass spectroscopy.

Benninghoven A (1975) Surf Sci 53, 596; Developments in secondary ion mass spectroscopy and applications to surface studies.

Benninghoven A, Muller K H, Schemmer M, Beckmann P (1978) Appl Phys 16, 367; SIMS and flask desorption studies of nickel oxygen interaction.

Beyer J, Kruger P, Masur A, Pollmann J, Schmeits M (1982) J Vac Sci Technol 21 358; Vacancies and hydrogen adsorption at GaAs (110): Theoretical studies of the electronic structure.

Bhattacharya R S, Pronko P P, Yeo Y K, Rai A K, Park Y S, Narayan J (1982) J Appl Phys 53, 4821; Fluence dependence of displacement damage, residual defects and electrical properties of high temperature annealed Se+-implanted GaAs.

Blaise G, Nourtier A (1979) Surf Sci 90, 495; Experimental and theoretical approaches to the ionization process in secondary ion emission.

Blood P, Harris J J (1984) J Appl Phys 56, 993; Deep states in GaAs grown by MBE.

Boyle W J O (1984) PhD Thesis, CNAA, City of London Polytechnic; The application of low dose SIMS to surface studies on compound semiconductors.

Briones F, Collins D M (1982) J Electron Mat 11, 847; Low temperature photoluminescence of lightly Si doped and undoped MBE GaAs.

Buhl R, Preisinger A (1975) Surf Sci 47, 344; Crystal structures and their secondary ion mass spectra.

Buonaquisti A D, Wang Y X, Holloway P H (1983) J Vac Sci Technol A1, 776; Interfacial chemistry of electrical contacts on GaAs and AlGaAs.

Calawa A R (1978) Appl Phys Lett 33, 1020; Effect of H_2 on residual impurities in GaAs MBE layers.

Casey H C, Cho A Y, Lang D V, Nicollian E H, Foy P W (1979) J Appl Phys 50, 3484; Investigation of heterojunctions for MIS devices with oxygen doped (AlGa)As on n-type GaAs.

Cerezo A, Grovenor C R M, Smith G D W (1985) Appl Phys Lett 46, 567; Pulsed laser atom probe analysis of GaAs and InAs.

Chai Y G (1980) Appl Phys Lett 37, 379; Effect of accelerated growth rate (1 - 5 μm/hr) on MBE GaAs using Si as a dopant.

Chai Y G, Chow R (1981a) Appl Phys Lett 38, 796; Source and elimination of oval defects on GaAs films grown by MBE.

Chai Y G, Chow R, Wood C E C (1981b) Appl Phys Lett 39, 800; The effect of growth conditions on Si incorporation in MBE GaAs.

Chandra A, Wood C E C, Woodard D W, Eastman L F (1979) Sol St Electron 22, 645; Surface and interface depletion corrections to free carrier-density determinations by Hall measurements.

Chang C A, Heiblum M, Ludeke R, Nathan M I (1981) Appl Phys Lett 39, 229; Effect of substrate surface treatment in MBE on the vertical electronic transport through the substrate interface.

Chang C A (1982) J Vac Sci Technol 21, 663; Thermal removal of surface carbon from GaAs substrate used in MBE.

Chiang T C, Ludeke R, Aono M, Landgren G, Himpsel F J, Eastman D E (1983) Phys Rev B27, 4770; Angle resolved photoemission studies of GaAs (100) surfaces grown by MBE.

Cho A Y, Arthur J R (1975) Prog Sol St Chem 10, 152; Molecular Beam Epitaxy.

Cho A Y (1976) J Appl Phys 47, 2841; Bonding direction and surface structure orientation on GaAs (001).

Cho A Y, Di Lorenzo J V, Hewitt B S, Niehaus W C, Schlosser W O, Radice C (1977) J Appl Phys 48, 346; Low noise and high power GaAs microwave FET's prepared by MBE.

Cho A Y, Casey H C, Radice C, Foy P W (1980) Electron Lett 16, 72; Influence of growth conditions on the threshold current density of double-heterostructure layers prepared by MBE.

Chuang T J, Brundle C R, Wandelt K (1979) J Vac Sci Technol 16, 797; An XPS study of the chemical changes in oxide and hydroxide surfaces induced by Ar^+ ion bombardment.

Cini M (1976) Surf Sci 54, 71; A new theory of SIMS at metal surfaces.

Coles J N (1979) Surf Sci 79, 549; A study of the feasibility of a surface plasma influencing secondary ion and photon emission under medium energy ion bombardment.

Colton R J (1981) J Vac Sci Technol 18, 737; Molecular secondary ion mass spectrometry.

Comas J, Cooper C B (1967) J Appl Phys 38, 2956; Mass-spectrometric study of sputtering of single crystals of GaAs by low energy A ions.

Covington D W, Meeks E L (1979) J Vac Sci Technol 16, 847; Unintentional dopants incorporated in GaAs layers grown by MBE.

Croydon W F (1979) MSc Thesis, CNAA, City of London Polytechnic; Dielectric films on GaAs by oxidation and other processes.

Croydon W F, Parker E H C (1981) Dielectric Films on GaAs, Vol 2, Electrocomponent science monographs, Gordon & Breach.

Davies G J, Andrews D A, Heckingbottom R (1981) J Appl Phys 52, 7214; Electrochemical sulfur doping of GaAs grown by MBE.

Davies G J, Andrews D A (1984) Vacuum 34, 545; The growth of high purity GaAs by MBE in diffusion pumped systems.

Daw M S, Smith D L (1980) J Vac Sci Technol 17, 1028; Energy levels of semiconductor surface vacancies.

Dawson P H (1976) Surf Sci 57, 229; The oxidation of aluminium studied by SIMS at low energies.

Dawson P H (1977) Phys Rev B15, 5522; Oxygen adsorption on molybdenum studied by low energy SIMS and EID.

Dawson P H (1978) Surf Sci 71, 247; The adsorption of CO on MO studied by low energy SIMS and EID.

Dawson P H, Tam W C (1979a) Surf Sci 81, 164; A comparison of low energy SIMS and AES in a study of the interaction of oxygen with polycrystalline nickel.

Dawson P H, Tam W C (1979b) Surf Sci 81, 464; The interaction of oxygen with polycrystalline niobium studied using AES and low energy SIMS.

Dawson P H, Tam W C (1980) Surf Sci 91, 153; The use of low energy SIMS to study the chemisorption of CO on Ni (100) and polycrystalline nickel.

Dean P J (1977) Electroluminescence (Ed J I Pankove) Springer Verlag p 63; III-V Compound Semiconductors.

Dingle R, Weisbuch C, Stormer H L, Morkoc H, Cho A Y (1982) Appl Phys Lett 40, 507; Characterization of high purity GaAs grown by MBE.

Dobson P J (1984) private communication.

Dowsett M G (1977) PhD Thesis, CNAA, City of London Polytechnic; Development of a SIMS apparatus and its application to the analysis of insulating and other surfaces.

Dowsett M G, King R M, Parker E H C (1978) Surf Sci 71, 541; Static SIMS analysis of the mica surface.

Dowsett M G, Parker E H C (1979) J Vac Sci Technol 16, 1207; Study of low coverage adsorption on cleaved (110) InP surfaces using SIMS.

Drathen P, Ranke W, Jacobi K (1978) Surf Sci 77, L162; Composition and structure of differently prepared GaAs (100) surfaces studied by LEED and AES.

Duke C B, Richardson S L, Paton A, Kahn A (1983) Surf Sci 127, L135; The atomic geometry of GaAs (110) revisited.

Ens W, Beavis R, Standing K G (1983) Phys Rev Lett 50, 27; Time of flight measurements of CsI cluster ions.

Faktor M M, Stevenson J L (1978) J Electrochem Soc 125, 621; The detection of structural defects in GaAs by electrochemical etching.

Fleish T, Winograd N, Delgass W N (1978) Surf Sci 78, 141; Chemisorption of oxygen on Ni (100) by SIMS and XPS.

Fleisch T, Ott G L, Delgass W N, Winograd N (1979) Surf Sci 81, 1; Chemisorption of CO on Ni (100) by SIMS and XPS.

Foley K E, Garrison B J (1980) J Chem Phys 72, 1018; Mechanisms of particle ejection from Cu (001) induced by the relative orientation of the bombarding primary ion.

Foley K E, Winograd N, Garrison B J, Harrison D E (1984), J Chem Phys 80 5254; A SIMS and classical dynamics study of the chemisorption of CO on Ni {7 9 11}.

Foxon C T (1983) J Vac Sci Technol B1, 293; MBE growth of GaAs and III-V alloys.

Fynn G W, Powell W J A (1979), The cutting and polishing of electro-optic materials, Adam Hilger.

Ganschow O, Wiedmann L, Benninghoven A (1979) SIMS II proc, Springer Verlag p 263; Combined SIMS, AES and XPS investigations of oxygen covered 3d transition metal surfaces.

Gant H, Koenders L, Bartels F, Mönch W (1983) Appl Phys Lett 43, 1032; Anion inclusions in III-V semiconductors.

Garrison B J, Winograd N, Harrison D E (1978) Phys Rev B18, 6000; Atomic and molecular ejection from ion-bombarded reacted single crystal surfaces. Oxygen on copper (100).

Gibbs R A, Holland S P, Foley K E, Garrison B J, Winograd N (1981) Phys Rev B24, 6178; Image potential and ion trajectories in SIMS.

Gonda S, Matsushina Y, Makita Y, Mukai S (1975) Jpn J Appl Phys 14, 935; Characterization and substrate temperature dependence of crystalline state of GaAs grown by MBE.

Grange J D (1980) PhD Thesis, CNAA, City of London Polytechnic; Studies of InAs and GaAs layers prepared by MBE.

Grange J D, Parker E H C (1979) Phys Bull 30, 20; Device fabrication for the future?

Greene L I (1977) J Appl Phys 48, 3739; A new defect-revealing etchant for GaAs.

Grimaldi M G, Paine B M, Nicolet M A, Sadana D K (1981) J Appl Phys 52, 4038; Ion implantation and low temperature epitaxial regrowth of GaAs.

Harrison D E, Delaplain C B (1976) J Appl Phys 47, 2252; Computer simulation of the sputtering of clusters.

Harrison D E, Kelly P W, Garrison J, Winograd N (1978) Surf Sci 76, 311; Low energy ion impact phenomena on single crystal surfaces.

Harrison D E (1983) Rad Effects 70, 1; Sputtering models - a synoptic view.

Harrison W A (1979) J Vac Sci Technol 16, 1492; Theory of polar semiconductor surfaces.

Hasegawa F, Majerfeld A (1975) Electron Lett 11, 286; Majority carrier traps in n- and p-type epitaxial GaAs.

Hasegawa F, Majerfeld A (1976) Electron Lett 12, 52; Effect of heat treatment on the nature of traps in epitaxial GaAs.

Heiblum M, Mendez E E, Osterling L (1983a) J Appl Phys 54, 6982; Growth by MBE and characterization of high purity GaAs and AlGaAs.

Heiblum M, Wang W I, Osterling L E, Deline V (1983b) J Appl Phys 54 6751; Heavy doping of GaAs and AlGaAs with Si by MBE.

Heim U, Hiesinger P (1974) Phys Stat Sol B66, 461; Luminescence and excitation spectra of exciton emission in GaAs.

Henzler M (1983) Surf Sci 132, 82; Spot profile analysis (LEED) of defects at silicon surfaces.

Heyes D M, Barber M, Clarke J H R (1981) Surf Sci 105, 225; The use of sputtering as a method for analysing surface chemical composition: a molecular dynamics study.

Hilsum C (1974) Electron Lett 10, 259; Simple empirical relationships between mobility and carrier concentration.

Holland L (1956) Vacuum deposition of thin films, Wiley.

Holland S P, Garrison B J, Winograd N (1979) Phys Rev Lett 43, 220; Surface structure from angle resolved SIMS: Oxygen on Cu (001).

Holland S P, Garrison B J, Winograd N (1980) Phys Rev Lett 44, 756; Azimuthal anisotropies of dimer ions ejected from ion bombarded Ni (001).

Honda F, Fukuda Y, Rabalais J W (1979) J Chem Phys 70, 4834; Clustering distances critical to metal dimer formation in the secondary ion mass spectra of CsCl.

Honig R E, Kramer D A (1969) RCA Review 30, 285; Vapourpressure data for the solid and liquid elements.

Hopster H, Brundle C R (1979) J Vac Sci Technol 16, 548; Use of SIMS for studies of adsorption on well-defined metal surfaces (1) Combined LEED/XPS/SIMS studies of O_2, CO, H_2O and H_2 on Ni (100).

van Hove J M, Lent C S, Pukite P R, Cohen P I (1983) J Vac Sci Technol B1, 741; Damped oscillations in RHEED during GaAs MBE.

Hsu T, Iijama S, Cowley M (1984) Surf Sci 137, 551; Atomic and other structures of cleaved GaAs (110).

Huijser A, van Laar J (1975) Surf Sci 52, 202; Work function variations of GaAs cleaved single crystals.

Hwang J C M, Brennan T H, Cho A Y (1983a) J Electrochem Soc 130, 493; Initial results of a high throughput MBE system for device fabrication.

Hwang J C M, Temkin H, Brennan T M, Frahm R E (1983b) Appl Phys Lett 42, 66; Growth of high purity GaAs layers by MBE.

Iida S, Ito K (1971) J Electrochem Soc 118, 768; Selective etching of GaAs crystals in H_2SO_4 - H_2O_2 - H_2O system.

Ilegems M, Dingle R (1975) IOP Conf Ser 24, 1; Acceptor incorporation in GaAs grown by MBE.

Ilegems M (1984) in The Technology and Physics of MBE, Ed E H C Parker, Plenum.

Jensen E W (1973) Sol St Technol 16, 49; Polishing compound semiconductors.

Joyes P (1973) Rad Effects 19, 235; Theoretical models in secondary ion emission.

Jurela Z (1973) Int J Mass Spectrom 12, 33; The application of non-equilibrium surface ionization to the emission of secondary ions.

Kaye & Laby (1975) Tables of physical and chemical constants, 14th edition, Longman.

Kern W, White J P (1970) RCA Review 31, 771; Interface properties of CVD silica films on GaAs.

Kirchner P D, Woodall J M, Freeouf J L, Pettit G D (1981a) Appl Phys Lett 38, 427; Volatile metal oxide incorporation in layers of GaAs, (GaAl) As and related compounds grown by MBE.

Kirchner P D, Woodall J M, Freeouf J L, Wolford D J, Pettit G D (1981b) J Vac Sci Technol 19, 604; Volatile metal oxide incorporation in layers of GaAs and (GaAl) As grown by MBE.

Kittel C (1971) Introduction to solid state physics, 4th edition, Wiley.

Honig R E, Kramer D A (1969) RCA Review 30, 285; Vapourpressure data for the solid and liquid elements.

Hopster H, Brundle C R (1979) J Vac Sci Technol 16, 548; Use of SIMS for studies of adsorption on well-defined metal surfaces (1) Combined LEED/XPS/SIMS studies of O_2, CO, H_2O and H_2 on Ni (100).

van Hove J M, Lent C S, Pukite P R, Cohen P I (1983) J Vac Sci Technol B1, 741; Damped oscillations in RHEED during GaAs MBE.

Hsu T, Iijama S, Cowley M (1984) Surf Sci 137, 551; Atomic and other structures of cleaved GaAs (110).

Huijser A, van Laar J (1975) Surf Sci 52, 202; Work function variations of GaAs cleaved single crystals.

Hwang J C M, Brennan T H, Cho A Y (1983a) J Electrochem Soc 130, 493; Initial results of a high throughput MBE system for device fabrication.

Hwang J C M, Temkin H, Brennan T M, Frahm R E (1983b) Appl Phys Lett 42, 66; Growth of high purity GaAs layers by MBE.

Iida S, Ito K (1971) J Electrochem Soc 118, 768; Selective etching of GaAs crystals in H_2SO_4 - H_2O_2 - H_2O system.

Ilegems M, Dingle R (1975) IOP Conf Ser 24, 1; Acceptor incorporation in GaAs grown by MBE.

Ilegems M (1984) in The Technology and Physics of MBE, Ed E H C Parker, Plenum.

Jensen E W (1973) Sol St Technol 16, 49; Polishing compound semiconductors.

Joyes P (1973) Rad Effects 19, 235; Theoretical models in secondary ion emission.

Jurela Z (1973) Int J Mass Spectrom 12, 33; The application of non-equilibrium surface ionization to the emission of secondary ions.

Kaye & Laby (1975) Tables of physical and chemical constants, 14th edition, Longman.

Kern W, White J P (1970) RCA Review 31, 771; Interface properties of CVD silica films on GaAs.

Kirchner P D, Woodall J M, Freeouf J L, Pettit G D (1981a) Appl Phys Lett 38, 427; Volatile metal oxide incorporation in layers of GaAs, (GaAl) As and related compounds grown by MBE.

Kirchner P D, Woodall J M, Freeouf J L, Wolford D J, Pettit G D (1981b) J Vac Sci Technol 19, 604; Volatile metal oxide incorporation in layers of GaAs and (GaAl) As grown by MBE.

Kittel C (1971) Introduction to solid state physics, 4th edition, Wiley.

Klein P B, Nordquist P E R, Siebenmann P G (1980) J Appl Phys 51, 4861; Thermal conversion of GaAs.

Koschell W H, Smith R S, Heisinger P (1981) J Electrochem Soc 128, 1336; Optical and electrical characterisation of chemical defects in GaAs grown by MBE.

Koval' A G, Mel'nikov V N, Man'kovski N K (1981) Russ J Phys Chem 55, 92; Study of the interaction of water vapour with a GaAs surface.

Kraus A R, Gruen D M (1979); (1980) Surf Sci 90, 564; 92, 14; Secondary ion emission from beryllium surfaces parts I & II.

Kubiak R A (1983) PhD Thesis, CNAA, City of London Polytechnic; MBE studies of InAs, GaAs and (InGa) As.

Kubiak R A, Driscoll P, Parker E H C (1982) J Vac Sci Technol 20, 252; A simple source cell design for MBE.

Künzel H, Ploog K (1980a) Appl Phys Lett 37, 417; The effect of As_2 and As_4 molecular beam species on photoluminescence of MBE grown GaAs.

Künzel H, Fischer A, Ploog K (1980b) Appl Phys 22, 23; Quantitative evaluation of substrate temperature dependence of Ge incorporation in GaAs during MBE.

Künzel H, Knecht J, Jung H, Wünstel K, Ploog K (1982) Appl Phys A28, 167; The effect of As vapour species on electrical and optical properties of GaAs grown by MBE.

Lang D V, Cho A Y, Gossard A L, Ilegems M, Wiegmann W (1976) J Appl Phys 47, 2558; Study of electron traps in n-GaAs grown by MBE.

Lang D V, Logan R A, Kimmerling L C (1977) Phys Rev B15, 4874; Identification of the defect state associated with a gallium vacancy in GaAs and (AlGa) As.

Larsen P K, van der Veen J F, Mazur A, Pollmann J, Neave J H, Joyce B A (1982) Phys Rev B26, 3222; Surface electronic structure of GaAs (001) - (2 x 4): Angle resolved photoemission and tight binding calculations.

Larsen P K, Neave J H, van der Veen J F, Dobson P J, Joyce B A (1983) Phys Rev B27, 4966; GaAs (001) - C(4 x 4): A chemisorbed structure.

Laurence G, Simondet F, Saget P (1979) Appl Phys 19, 63; Combined RHEED-AES study of the thermal treatment of (001) GaAs surface prior to MBE growth.

Lawson G, Todd J F J (1972) Chem Brit 8, 373; Radiofrequency quadrupole mass spectrometers.

Lin J H, Garrison B J (1983) J Vac Sci Technol A1, 1205; Charge transfer at surfaces: A model for ionization in SIMS.

Low T S, Stillman G E, Cho A Y, Moroç H, Calawa A R (1982) Appl Phys Lett 40, 611; Spectroscopy of donors in high purity GaAs grown by MBE.

Ludeke R, Koma A (1975) CRC Crit Rev Sol St Sci 5, 259; Surface studies on clean and oxygen exposed GaAs and Ge surfaces by low energy electron loss spectroscopy.

Ludeke R (1983a) Surf Sci 132, 143; The formation of interfaces on GaAs and related semiconductors: A reassessment.

Ludeke R, Chiang T C, Eastman D E (1983b) Physica 117/118B, 819; Core level photoemission studies of MBE grown semiconductor surfaces.

Lum W Y, Wieder H H, Koschel W H, Bishop S G, McCombe B D (1977) Appl Phys Lett 30, 1; Thermal degradation of homoepitaxial GaAs interfaces.

Lum W Y, Messick L, Zeisse C R (1978) J Appl Phys 49, 3602; Evidence of damage at GaAs - insulator interfaces.

Marien J, De Pauw E (1982) SIMS III proc Springer Verlag p 377; Study of the adsorption of water on titania by SIMS.

Martin G M, Mitonneau A, Mircea A (1977) Electron Lett 13, 191; Electron traps in bulk and epitaxial GaAs crystals.

Marton D (1980) Appl Surf Sci 5, 65; A SIMS study of the adsorption of oxygen adsorption on aluminium and its alloys.

Marton D, Csanady A (1982) SIMS III proc Springer Verlag p 383; SIMS studies of oxygen adsorption on aluminimum and its alloys.

Massies J, Devoldere P, Linh N T (1979) J Vac Sci Technol 16, 1244; Work function measurements on MBE GaAs (001) layers.

Massies J, Etienne P, Dezaly F, Linh N T (1980) Surf Sci 99, 121; Stoichiometry effects on surface properties of GaAs {001} grown in-situ by MBE.

Masterov V G, Samorukov B E (1978) Sov Phys Semicond 12, 363; Deep centers in III-V compounds.

Meggitt B T (1979) PhD Thesis, CNAA, City of London Polytechnic; Structural and electrical properties of InAs layers on (100) GaAs substrates prepared by MBE.

Menezes S, Miller B (1983) J Electrochem Soc 130, 517; Surface and redox reactions at GaAs in various electrolytes.

Metze G M, Calawa A R (1983) Appl Phys Lett 42, 818; Effects of very low growth rates on GaAs grown by MBE at low substrate temperatures.

Miller D C, Rozgonyi G A (1980) in Handbook on Semiconductors, Ed T S Moss & S P Keller, North Holland; Defect characterization by etching, optical microscopy and X-ray topography.

Mittoneau A, Martin G M, Mircea A (1977) Electron Lett 13, 666; Hole traps in bulk and epitaxial GaAs crystals.

Mokwa W, Kohl D, Heiland G (1984) Surf Sci 139, 98; TDS and LEED studies of H_2O adsorption on GaAs (110).

Mönch W, Clemens H J (1979) J Vac Sci Technol 16, 1238; Surface states at clean, cleaved GaAs (110) surfaces.

Morgan A E, Werner H W (1976) Anal Chem 48, 699; Quantitative analysis of low alloy steels by SIMS.

Morgan A E, Werner H W (1977) Anal Chem 49, 927; Test of a quantitative approach to SIMS on glass and silicate standards.

Morkoç H, Cho A Y (1979) J Appl Phys 50, 6413; High purity GaAs and Cr doped GaAs epitaxial layers by MBE.

Munoz-Yague A, Piqueras J, Fabre N (1981) J Electrochem Soc 128, 149; Preparation of carbon-free GaAs surfaces: AES and RHEED analysis.

Murray P T, Rabalais J W (1981) J Am Chem Soc 103, 1007; Ejection dynamics and electronic processes governing secondary particle emission in SIMS.

McClintock J A, Wilson R A, Byer N E (1982) J Vac Sci Technol 20, 241; UV-Ozone cleaning of GaAs for MBE.

MacFadyen D N (1983) J Electrochem Soc 130, 1934; On the preferential etching of GaAs by H_2SO_4 - H_2O_2 - H_2O .

McGlashan (1982) PhD thesis, CNAA, City of London Polytechnic; The growth of PbTe thin films and a study of their dopant and electron beam induced surface reactions.

Neave J H, Joyce B A (1978) J Cryst Growth 44, 387; Structure and stoichiometry of {100} GaAs surfaces during MBE.

Neave J H, Blood P, Joyce B A (1980) Appl Phys Lett 36, 311; A correlation between electron traps and growth processes in n-GaAs prepared by MBE.

Neave J H, Joyce B A, Dobson P J, Norton N (1983a) Appl Phys A31, 1; Dynamics of film growth of GaAs by MBE from RHEED observations.

Neave J H, Dobson P J, Harris J J, Dawson P, Joyce B A (1983b) Appl Phys A32, 195; Silicon doping of MBE grown GaAs films.

Neave J H, Larsen P K, van der Veen J F, Dobson P J, Joyce B A (1983c) Surf Sci 133, 267; Effect of arsenic species on the crystallinity and electronic structure of MBE grown GaAs (001) reconstructed surfaces.

Nomarski G, Weill A R (1955) Rev Metall (Paris) 52, 121; Application to metallography of interference methods with two polarised beams.

Nottenburg R, Buhlmann H J, Frei M, Ilegems M (1984) Appl Phys Lett 44, 71; Compensation effects in Si doped GaAs grown by MBE.

Oda T, Sugano T (1976) Jpn J Appl Phys 15, 1317; Studies on chemically etched Si, GaAs and GaP surfaces by AES.

Oeschner H (1982) SIMS III proc Springer Verlag p 106; Molecule formation in oxide sputtering.

Oeschner H (1984) SIMS IV proc Springer Verlag p 291; Quantitative depth profile analysis by secondary neutral mass spectrometry.

Palmateer S C, Schaff W J, Galuska A, Berry J D, Eastman L F (1983) Appl Phys Lett 42, 183; Heat treatment of semi-insulating Cr-doped GaAs substrates with converted surface removed prior to MBE growth.

Parker E H C, Kubiak R A, King R M, Grange J D (1981) J Phys D 14, 1853; An investigation into silicon doping of MBE (100) GaAs.

van der Pauw L J (1958) Philips Res Rpts 13, 1; A method of measuring specific resistivity and Hall effect of discs of arbitrary shape.

Perry (1963) Chemical Engineers handbook, McGraw Hill.

Pianetta P, Lindau I, Garner C H, Spicer W E (1978) Phys Rev B18, 2792; Chemisorption and oxidation studies of the (110) surfaces of GaAs, GaSb and InP.

Plog C, Wiedmann L, Benninghoven A (1977) Surf Sci 67, 565; Empirical formula for the calculation of secondary ion yields from oxidised metal surfaces and metal oxides.

Ploog K (1980) in Crystals, growth, properties and applications, Vol 3 p 75 (Springer Verlag); MBE of III-V compounds.

Poth H, Bruch H, Heyen M, Balk P (1978) J Appl Phys 49, 285; Electron mobility in vapour grown GaAs films.

Prigge S, Bauer E (1981) Adv Mass Spectr 8, 543; Static SIMS studies of metal covered W(110) surfaces.

Prior K A, Davies G J, Heckingbottom R (1984) J Cryst Growth 66, 55; The thermodynamics of oxygen incorporation into III-V semiconductor compounds and alloys in MBE.

Proix F, Houzay F (1980) J Phys C 13, 1845; Interaction of oxygen with cleaved GaAs: influence of the cleavage defects.

Pukite P R, van Hove J M, Cohen P I (1984) Appl Phys Lett 44, 456; Sensitive RHEED measurement of the local misorientation of vicinal GaAs surfaces.

Ramsey N F(1963) Molecular Beams, Clarendon Press

Ranke W, Jacobi K (1981) Prog Surf Sci 10, 1; Structure and reactivity of GaAs surfaces.

Ranke W (1983) Physica Scripta T4, 100; Oxygen adsorption on a cylindrical GaAs single crystal prepared by MBE.

Reuter W, Wittmaack K (1980) Appl Surf Sci 5, 221; An AES-SIMS study of silicon oxidation induced by ion or electron bombardment.

Rode D L, Knight S (1971) Phys Rev B3, 2534; Electron transport in GaAs.

Rode D L (1975) in Semiconductors and Semimetals, Ed Willardson & Bear, Academic Vol 10 p 1; Low field electron transport.

Rode D L, Wolfe C M, Stillman G E (1982) IOP Conf Ser 65, 569; Magnetic field dependence of the Hall factor of GaAs.

Rodway D C, Cullis A G, Webber H C (1980) Appl Surf Sci 6, 76; Laser Cleaning of GaAs surfaces in vacuo.

Salmon L G, Rhodin T N (1983) J Vac Sci Technol B1, 736; Angle-resolved photoemission study of GaAs (100) surfaces grown by MBE.

Schiøtt J E (1970) Rad Effects 6, 107; Approximations and interpolation rules for ranges and range stragglings.

Schroeer J M, Rhodin T N, Bradley R C (1973) Surf Sci 34, 571; A quantum mechanical model for the ionisation and excitation of atoms during sputtering.

Shaw D W (1981) J Electrochem Soc 128, 874; Localised GaAs etching with acidic hydrogen peroxide solutions.

Shiota I, Motoya K, Ohmi T, Miyamoto N, Nishizawa J (1977) J Electrochem Soc 124, 155; Auger characterisation of chemically etched GaAs surfaces.

Singer I L, Murday J S, Cooper L R (1981) Surf Sci 108, 7; Surface composition changes in GaAs due to low energy ion bombardment.

Singer K E, Nicholas D J (1984) GaAs consortium MBE working party, GaAs round robin exercise initial report.

Slodzian G, Lorin J C, Havette A (1980) J de Phys Lett 41, L555; Isotopic effect on the ionisation probabilities in secondary ion emission.

Slodzian G (1982) SIMS III proc Springer Verlag p 115; Dependence of ionisation yields upon elemental composition; isotopic variations.

Slusser G J (1979) SIMS II proc Springer Verlag p 26; Cluster formation in SIMS: CO on PdAg.

Smith K K (1981) Thin Solid Films 84, 171; Photoluminescence of semiconductor materials.

Snowdon K J, Heiland W, Taglauer E (1981) Phys Rev Lett 46, 284; Molecule formation during sputtering by two body associative ionisation with diabatic curve crossing.

Spicer W E, Lindau I, Skeath P, Su C Y (1980) J Vac Sci Technol 17, 1019; Unified defect model and beyond.

Sroubeck Z (1974) Surf Sci 44, 47; The theoretical and experimental study of the ionisation processes during the low energy ion sputtering.

Sroubek Z (1981) in Inelastic particle surface collisions, Ed Taglauer & Heiland, Springer Verlag p 277; Theory of charge states in sputtering.

Stall R A, Wood C E C, Kirchner P D, Eastman L F (1980) Electron Lett 16, 171; Growth parameter dependence of deep levels in MBE GaAs.

Stillman G E, Wolfe C M, Dimmock J O (1977) in Semiconductors and Semimetals, Ed Willardson & Beer, Academic Vol 12 p 169; Far-infrared photoconductivity in high purity GaAs.

Stirland D J, Straughan B W (1976) Thin Solid Films 31, 139; A review of etching and defect characterisation of GaAs substrate material.

Stringfellow G B, Stall R, Koschel W (1981) Appl Phys Lett 38, 156; Carbon in MBE GaAs.

Su C Y, Lindau I, Chye P W, Skeath P R, Spicer W E (1982) Phys Rev B25, 4045; Photoemission studies of the interaction of oxygen with GaAs (110).

Suzuki Y, Seki M, Horikoshi Y, Okamoto H (1984) Jpn J Appl Phys 23, 164; Surface defects on MBE grown GaAs.

Tabor D (1969) Gases, Liquids and Solids, Penguin.

Taglauer E, Heiland W, Macdonald R J (1979) Surf Sci 90, 661; The study of sputtering effects in oxides and metal-adsorbed gas systems using combined analytical techniques.

Taylor J A, Rabalais J W (1978) Surf Sci 74, 229; Molecular rearrangement and cluster formation in SIMS of fluoride salts.

Temkin H, Hwang J C M (1983) Appl Phys Lett 42, 178; Undoped semi-insulating GaAs layers grown by MBE.

Townsend P D, Kelly J C, Hartley N E W (1976) Ion implantation, sputtering and their applications, Academic.

Tuck B (1975) J Mater Sci 10, 321; The chemical polishing of semiconductors.

Uebbing J J (1970) J Appl Phys 41, 802; Use of AES in determining the effect of carbon and other surface contaminants on GaAs-Cs-O photocathodes.

Vasquez R P, Lewis B F, Grunthaner F J (1983) Appl Phys Lett 42, 293; XPS study of the oxide removal mechanism of GaAs (100) MBE substrates in in-situ heating.

Walsh R J, Herzog A H (1965) US Patent No 3,170,273 ; Process for polishing semiconductor materials.

Walukiewcz W, Lagowski J, Gatos H C (1982) J Appl Phys 53, 769; Electron mobility in n-type GaAs at 77K; determination of the compensation ratio.

Webb C, Lichtensteiger M (1982) J Vac Sci Technol 21, 659; Formation of alternative surface oxide phases on GaAs by adsorption of O_2 or H_2O; A UPS, XPS and SIMS study.

Webb R P, Harrison D E (1982) J Appl Phys 53, 5243; Near threshold sputtering mechanisms from a computer simulation of argon bombarded clean and oxygen-reacted copper single crystals.

Wiley J D (1975) in Semiconductors and Semimetals, Ed Willardson & Beer, Academic Vol 10 p 91; Mobility of holes in III-V compounds.

Williams E W, Bebb H B (1972) in Semiconductors and Semimetals, Ed Willardson & Beer, Academic Vol 8 Chap 5; Photoluminescence II: Gallium Arsenide.

Williams J S, Austin M W (1980) Nucl Inst Meth 168, 307; Ion beam induced annealing effects in GaAs.

Williams P, Evans C A (1978) Surf Sci 78, 324; Anomolous enhancement of negative sputtered ion emission by oxygen.

Williams P (1979) Surf Sci 90, 588; The sputtering process and sputtered ion emission.

Williams P, Katz W, Evans C A (1980) Nucl Inst Meth 168, 373; Towards a universal model for sputtered ion emission.

Williams P (1981) Phys Rev B23, 6187; Ion stimulated desorption of positive halogen ions.

Winograd N, Harrison D E, Garrison B J (1978) Surf Sci 78, 467; Structure sensitive factors in molecular cluster formation by ion bombardment of single crystal surfaces.

Winograd N, Foley K E, Garrison B J, Harrison D E (1979) Phys Lett 73A, 253; Evidence for a recombination mechanism of cluster emission from ion bombarded metal surfaces.

Winograd N (1982) Prog Sol St Chem 13, 285; Characterization of solids and surfaces using ion beams and mass spectrometry.

Wittmaack K (1976) Nucl Instr Meth 132, 381; Current density effects in secondary ion emission studies.

Wittmaack K (1977) Surf Sci 68, 118; The use of SIMS for studies of oxygen adsorption and oxidation.

Wittmaack K (1979a) Surf Sci 89, 668; Secondary ion mass spectrometry as a means of surface analysis.

Wittmaack K (1979b) Phys Lett 69A, 322; On the mechanism of cluster emission in sputtering.

Wittmaack K (1980) Nucl Instr Meth 168, 343; Aspects of quantitative SIMS.

Wittmaack K (1981) Adv Mass Spectrom 8, 503; SIMS analysis of cadmium mercury telluride.

Wittmaack K, Dowsett M G, Clegg J B (1982) Int J Mass Spectrom 43, 31; Improved secondary-ion extraction in a quadrupole-based ion microprobe.

Wood C E C (1976) Appl Phys Lett 29, 746; MBE GaAs layers for MESFETS.

Wood C E C, Rathbun L, Ohno H, De Simone D (1981) J Cryst Growth 51, 299; On the origin and elimination of macroscopic defects in MBE films.

Yu M L (1977) Appl Phys Lett 30, 654; Study of chemisorbed oxygen on tungsten using SIMS.

Yu M L (1978a) Surf Sci 71, 121; The SIMS spectrum of the O-W (100) chemisorption system.

Yu M L (1978b) J Vac Sci Technol 15, 668; Effect of primary ion energy and surface chemistry on the secondary ion yields in low energy SIMS experiments.

Yu M L (1981a) Phys Rev B24, 1147; Emission mechanisms of titanium oxide ions during sputtering.

Yu M L (1981b) Phys Rev B24, 5625; Formation of molecular ions during sputtering.

Yu M L (1982) Phys Rev B26, 4731; Matrix effects in the work function dependence of negative secondary ion emission.

Yu M L (1983) J Vac Sci Technol A1, 500; Effect of surface chemistry and work function in SIMS.

Zilko J L, Williams R S (1982) J Electrochem Soc 129, 406; AES study of GaAs substrate cleaning process.

Zinner E, Grasserbauer M (1982) SIMS III proc Springer Verlag p 292; SIMS isotopic measurements at high mass resolution.

APPENDIX I

Possible Secondary Ion Species from Oxidised Gallium Arsenide

Secondary ion species identified in the various SIMS spectra, or which may be formed from atoms beleived to be present at the surface of oxidised GaAs, are listed in ascending mass order. Where significant quantities of more than one isotopic species are naturally present (Kaye & Laby (1975)) the intensities of the peaks, calculated as a percentage of the major species, are shown in parentheses. Minor isotopes, eg ^{18}O, are not included in this table since they are detectable only under extremely favourable conditions, and hydrogenated species are generally omitted to avoid overcomplicating the table and since their position is obvious from that of other species given.

Mass No	Possible secondary ion species	
1		
2		
3		
4		
5		
6	$Li^+(8)$	
7	$Li^+(100)$	
8		
9		
10		
11		
12	$C^\pm$	$C_1H_n^\pm$
13		
14	$CH_2^\pm$	
15	$CH_3^\pm$	
16	$O^\pm$	
17	OH^-	
18	$H_2O^\pm$	
19	F^-	
20	$HF^\pm$	

Mass No	Possible secondary ion species	
21		
22		
23	Na^+	
24	$C_2^{\pm}$, Mg^+	
25		$C_2H_n^{\pm}$
26	$C_2H_2^{\pm}$, CN^-	$C_2H_n^{\pm}$
27	Al^+, $C_2H_3^{\pm}$	$C_2H_n^{\pm}$
28	Si^+, CO^+, N_2^+, $C_2H_4^{\pm}$	$C_2H_n^{\pm}$
29	$C_2H_5^{\pm}$, $CHO^{\pm}$	$C_2H_n^{\pm}$
30		
31	$C_2H_7^{\pm}$, $CH_3O^{\pm}$, CF^-	
32	$O_2^{\pm}$, S^-	
33	$O_2H^{\pm}$	
34		
35	Cl^- (100)	
36	$C_3^{\pm}$	
37	Cl^- (32)	$C_3H_n^{\pm}$
38		$C_3H_n^{\pm}$
39	K^+ (100)	$C_3H_n^{\pm}$
40	Ar^+, $NaOH^+$, Ca^+, $C_3H_4^{\pm}$, $C_2O^{\pm}$	$C_3H_n^{\pm}$
41	K^+ (7)	$C_3H_n^{\pm}$
42	$C_3H_6^{\pm}$, $C_2H_2O^{\pm}$	$C_3H_n^{\pm}$
43	$C_3H_7^{\pm}$, $C_2H_3O^{\pm}$, $AlO^{\pm}$	$C_3H_n^{\pm}$
44	CO_2^+, $C_2H_4O^{\pm}$, $AlOH^+$	
45	$C_2H_5O^{\pm}$, $COOH^{\pm}$, C_2FH^-	
46	Na_2^+, $C_2H_6O^{\pm}$	
47		
48	Ti^+, $C_4^{\pm}$, O_3^-, SO^-	
49		$C_4H_n^{\pm}$
50		$C_4H_n^{\pm}$
51		$C_4H_n^{\pm}$
52	Cr^+	$C_4H_n^{\pm}$
53		$C_4H_n^{\pm}$
54		$C_4H_n^{\pm}$
55	Mn^+	$C_4H_n^{\pm}$
56	Fe^+, Si_2^+, $C_3H_4O^{\pm}$	$C_4H_n^{\pm}$
57	KOH^+, $C_3H_5O^{\pm}$	$C_4H_n^{\pm}$
58		$C_4H_n^{\pm}$
59	KOH^+ (7), $C_3H_7O^{\pm}$	$C_4H_n^{\pm}$

Mass No	Possible secondary ion species	
60	$C_5^{\pm}$, $C_3H_8O^{\pm}$	$C_5H_n^{\pm}$
61		
62		
63	Cu^+(100)	
64		
65	Cu^+(45)	
66		
67		
68		
69	Ga^+(100)	
70		
71	Ga^+(67)	
72		
73		
74		
75	$As^{\pm}$	
76		
77		
78		
79	Br^-(100)	
80		
81	Br^-(98)	
82		
83	GaN^+(100)	
84	$GaCH_3^+$(100)	
85	GaN^+(67), $GaO^{\pm}$(100)	
86	$GaCH_3^+$(67), $GaOH^+$(100)	
87	GaH_2O^+(100), $GaO^{\pm}$(67)	
88	$GaOH^+$(67)	
89	GaH_2O^+(67)	
90		
91	$AsO^{\pm}$	
92	$GaNa^+$(100)	
93		
94	$GaNa^+$(67), AsF^+	
95		
96	$GaAl^+$(100)	
97	GaN_2^+(100)	
98	$GaAl^+$(67), $NaAs^+$	

Mass No	Possible secondary ion species
99	$GaON^+$, $GaC_2H_6^+$, $GaCH_2O^+$(100), GaN_2^+(67)
100	
101	$GaON^+$, $GaC_2H_6^+$, $GaCH_2O^+$(67), $GaO_2^{\pm}$(100)
102	GaO_2H^+(100)
103	$GaO_2^{\pm}$(67)
104	GaO_2H^+(67)
105	
106	
107	$AsO_2^{\pm}$
108	GaK^+(100)
109	$GaAr^+$, $GaNaOH^+$(100)
110	GaK^+(73)
111	$GaAr^+$, $GaNaOH^+$(67)
112	GaK^+(5)
113	In^+(4), $GaAlOH^+$(100)
114	
115	In^+(100), $GaAlOH^+$(67)
116	
117	
118	
119	
120	
121	
122	
123	AsO_3^-
124	
125	$GaArO^+$(100), $GaKOH^+$(100)
126	
127	$GaArO^+$(67), $GaKOH^+$(73)
128	
129	InO^+(4), $GaKOH^+$(5)
130	
131	InO^+(100)
132	
133	
134	
135	
136	
137	

Mass No	Possible secondary ion species
138	Ga_2^+(76)
139	
140	Ga_2^+(100)
141	
142	Ga_2^+(33)
143	
144	$GaAs^{\pm}$(100)
145	
146	$GaAs^{\pm}$(67)
147	
148	
149	
150	$As_2^{\pm}$
151	
152	
153	
154	Ga_2O^+(76)
155	Ga_2OH^+(76)
156	Ga_2O^+(100)
157	Ga_2OH^+(100)
158	Ga_2O^+(33)
159	Ga_2OH^+(33)
160	$GaAsO^+$(100)
161	
162	$GaAsO^+$(67)
163	
164	
165	
166	$As_2O^{\pm}$
167	
168	
169	
170	$Ga_2O_2^+$(76)
171	
172	$Ga_2O_2^+$(100)
173	
174	$Ga_2O_2^+$(33)
175	
176	$GaAsO_2^+$(100)

Mass No	Possible secondary ion species
177	
178	$GaAsO_2^+$(67)
179	
180	
181	
182	$As_2O_2^+$, $GaIn^+$(4)
183	
184	$GaIn^+$(100)
185	
186	$Ga_2O_3^+$(76), $GaIn^+$(65)
187	
188	$Ga_2O_3^+$(100)
189	
190	$Ga_2O_3^+$(33)
191	
192	$GaAsO_3^{\pm}$(100)
193	
194	$GaAsO_5^{\pm}$(67)
195	
196	
197	
198	$As_2O_3^+$
199	
200	
201	
202	
203	
204	
205	
206	
207	Ga_3^+(50)
208	
209	Ga_3^+(100)
210	
211	Ga_3^+(66)
212	
213	Ga_3^+(15), Ga_2As^+(76)
214	$As_2O_4^+$
215	Ga_2As^+(100)

Mass No	Possible secondary ion species
216	
217	Ga_2As^+(33)
218	
219	$GaAs_2^+$(100)
220	
221	$GaAs_2^+$(67)
222	
223	Ga_3O^+(50)
224	
225	Ga_3O^+(100), As_3^+
226	
227	Ga_3O^+(66)
228	
229	Ga_3O^+(15), $Ga_2AsO^{\pm}$(76)
230	Ga_2AsOH^-(76)
231	$As_2O_5H^-$, $Ga_2AsO^{\pm}$(100)
232	Ga_2AsOH^-(100)
233	$Ga_2AsO^{\pm}$(33)
234	Ga_2AsOH^-(33)
235	$GaAs_2O^+$(100)
236	
237	$GaAs_2O^+$(67)
238	
239	$Ga_3O_2^+$(50)
240	
241	$Ga_3O_2^+$(100), As_3O^+
242	
243	$Ga_3O_2^+$(66)
244	
245	$Ga_3O_2^+$(15), $Ga_2AsO_2^+$(76)
246	
247	$Ga_2AsO_2^+$(100)
248	
249	$Ga_2AsO_2^+$(33)
250	

APPENDIX II

Investigation of MBE-grown (001) GaAs surfaces using low-dose SIMS

W. F. Croydon, M. G. Dowsett, R. M. King, and E. H. C. Parker
Department of Physics, Sir John Cass School of Science and Technology, City of London Polytechnic, 31, Jewry Street, London EC3, England

(Received 15 September 1984; accepted 15 October 1984)

A combined SIMS-MBE UHV system has been used for growth and subsequent analysis of differently reconstructed (001)GaAs surfaces. Some small, but significant, differences are found in SIMS spectra from the different surfaces, indicating that the (2×4)As stabilized surface commonly used for MBE growth may be more "bulklike" than other reconstructions. Spectra obtained after oxygen exposure indicate involvement of both Ga and As at the initial stages of oxidation, and the different surface reconstructions showed very similar response to oxygen exposure. These SIMS analyses do not indicate large differences in either the surface composition or chemistry of differently reconstructed surfaces.

I. INTRODUCTION

The existence of different (001)GaAs surface reconstructions dependent on surface atomic composition has been known since the early days of the MBE technique[1]; however it is only recently that the atomic structure of some of these surfaces has begun to be determined.[2,3] The technique of secondary-ion mass spectrometry in the static or low-dose mode has been shown to produce molecular secondary ions sensitive to precise surface atomic bonding[4–7] and has therefore been applied to these surfaces in an attempt to better understand their atomic structure, and as a starting point for further investigations of compound semiconductor surface physics.

II. EXPERIMENT

The main features, relevant to this investigation, of the EVA 2000 combined SIMS-MBE system are shown schematically in Fig. 1. The SIMS and MBE chambers are normally operated as independent systems, but the connecting valve may be opened to transfer MBE-grown surfaces into the SIMS chamber for surface analysis while maintaining UHV conditions. The MBE loading chamber is evacuated by the main MBE pumping system using suitable UHV isolation valves, and the main chamber contains additional liquid-nitrogen cryopaneling, a miniature ionization gauge flux monitor and substrate shutter not shown on the diagram. After bakeout at 200 °C base pressures $\sim 1\times10^{-10}$ Torr are obtained. GaAs substrates are cleaned by degreasing and finally etching in 7:1:1 H_2SO_4:H_2O_2:H_2O before soldering to molybdenum mounting blocks with indium. Graphite source cells[8] are used for gallium matrix and silicon dopant species with a simpler, larger volume graphite cell for arsenic. Silicon-doped *n*-type epilayers have been grown with electron mobilities close to Poth's "universal curve"[9] over the concentration range 10^{16}–7×10^{18} cm^{-3}, but residual carbon acceptor impurities $\sim 10^{15}$ cm^{-3} limit 77 K electron mobilities to $< 30\,000$ cm^2/V s at lower doping levels. 3-keV reflection electron diffraction (RED) was used to monitor

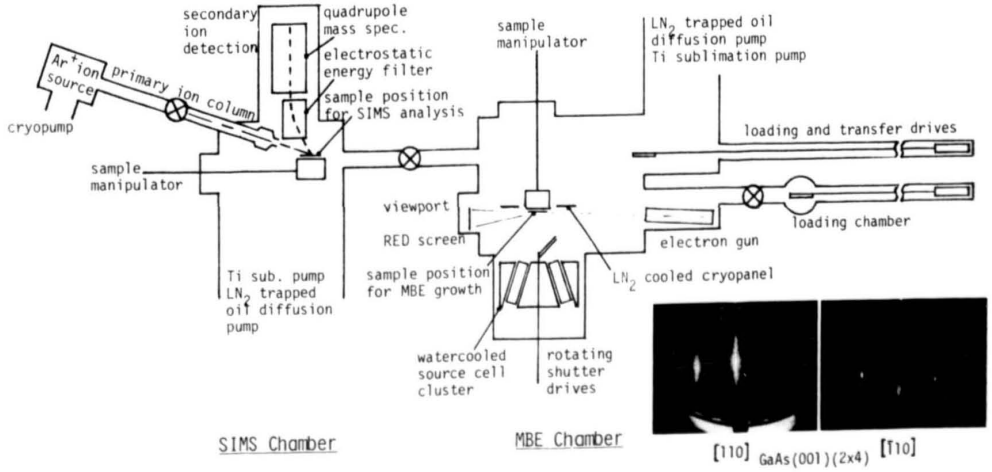

FIG. 1. EVA 2000 combined SIMS-MBE system schematic. Inset shows RED pattern from typical (2×4) As-stabilized surface.

 0734-211X/85/020604-04$01.00

surface crystallography both to ensure adequate heat cleaning of substrates prior to growth, and to generate the three differently reconstructed surfaces used for SIMS analysis. These surfaces were prepared after the arsenic background had fallen from $\sim 10^{-6}$ Torr during growth to below 1×10^{-8} Torr in order to minimize any As adsorption during transfer to the SIMS chamber. The $c(4\times4)$ As rich surface was generated by allowing the surface to cool in the residual arsenic ambient and then heating to 400 °C for 5 min to desorb excess As. The (2×4) As stabilized surface, as used for growth, was achieved by holding the substrate temperature at 500 °C, and the (4×2) Ga stabilized surface by exposing the (2×4) As stabilized surface at 550 °C to the Ga molecular beam and depositing approximately half a monolayer of Ga; however, this surface always changed to the composite (4×6) reconstruction on cooling below ~ 500 °C. RED was used to monitor the surfaces intermittently as they cooled to room temperature and to check that the surface reconstruction was maintained prior to transfer to the SIMS system. Further details of the MBE system will be presented elsewhere.[10]

The SIMS system also achieved a base pressure $\sim 1\times10^{-10}$ Torr after bakeout and has been used extensively in depth profiling studies,[11] where further details of the system may be found. The argon primary ion beam was mass filtered and focused to a spot of $\sim 100\ \mu$m diameter. The beam was incident on the sample at 70° to the surface normal and was rastered over a square area (usually 3×3 mm) during SIMS analysis, a fresh area being used for each analysis. Results were obtained from samples at room temperature using 500-eV Ar^+ primary ions and a primary ion current of 0.5–3 nA. They include both static analyses and measurement of the sensitivity of various secondary ion species to ion dose, in order to establish the range of doses permissible in a static analysis. Secondary ions, characteristic of the surface under analysis, were extracted through an electrostatic energy filter tuned to maximize the signal, into a quadrupole mass spectrometer and detected by a channel electron multiplier. Both the primary-ion beam and the secondary-ion detection system are computer controlled by a Research Machines 380Z microcomputer and, after suitable calibration, the mass spectrometer was stepped to preselected mass peaks thus minimizing the ion dose to the sample surface during the SIMS investigation, and maximizing the count of low intensity secondary ions.

III. RESULTS AND DISCUSSION

Table I shows the three surface reconstructions investigated and their approximate surface compositions as measured by Auger and photoemission spectroscopies. While all reported results agree in the compositional ordering of the major reconstructions shown in the table, there are disagreements over the absolute surface composition and the relative composition of some of the less frequently observed reconstructions. Various investigators[14–16] report that a range of surface composition could occur for a specific reconstruction, and in some cases that different reconstructions exhibited overlapping composition ranges.

TABLE I. (001)GaAs surface reconstructions.

Reconstruction	Approximate surface composition (% As) Ref. 12	Ref. 13	Ref. 14	Ref. 3
$c(4\times4)$ As rich	...	86	100	120–150
(2×4) As stabilized	50–60	61	89	100
(4×6) Ga stabilized	< 10	27	31	...

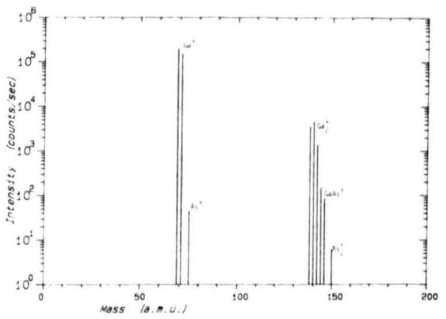

FIG. 2. Matrix species from typical positive ion SIMS spectrum of (2×4) As-stabilized (001)GaAs surface.

Figure 2 shows matrix species present in a typical positive ion SIMS spectrum from a GaAs surface. The difference in sensitivity for different elements inherent in the SIMS technique is immediately apparent, and no major changes were observed in spectra from the different surface reconstructions. Some tentative correlations between secondary ion intensities and surface composition were made from initial results. However, these have not been sustained by later measurements, although by selecting specific peaks secondary ion spectra have been obtained with a primary ion dose of less than 5×10^{11} ions/cm^2, and may be associated with the variable surface compositions of the reconstructions. This behavior is exemplified, in extreme form, by the change of the Ga_2^+ signal observed with ion dose on different $c(4\times4)$ As rich surfaces, as shown in Fig. 3. Sample A shows a large

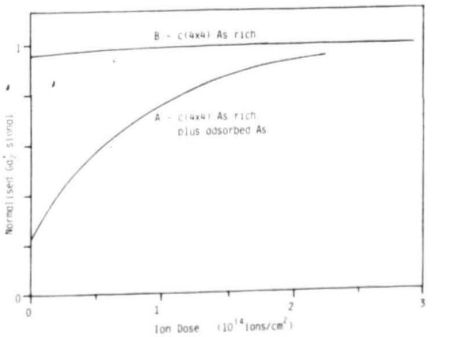

FIG. 3. Change of Ga_2^+ secondary-ion signal with ion dose for different $c(4\times4)$ As-rich surfaces.

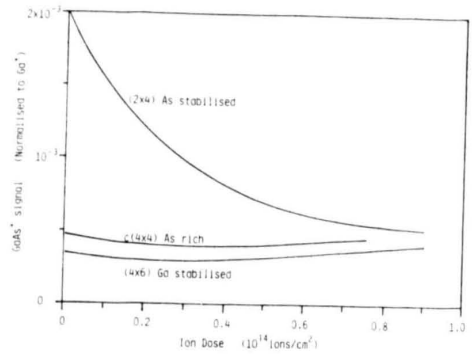

FIG. 4. Change of $GaAs^+$ secondary-ion signal with ion dose for the three surfaces studied.

and rapid increase in the Ga_2^+ signal which, since this surface is nominally arsenic covered, was initially interpreted as due to damage caused by the primary-ion beam and renewed efforts to reduce even further the primary-ion dose necessary for a SIMS analysis. However, more recent results (B) show a comparatively constant Ga_2^+ signal from a different $c(4\times4)$ surface. We have now established[10] that the method of preparing sample A (cooling in an As flux after MBE growth) will lead to additional adsorbed arsenic without altering the surface reconstruction, whereas this was removed in the case of sample B by subsequent heating to 400 °C for 5 min. The rise in Ga_2^+ signal from sample A must therefore be due to ion-induced desorption of the additional adsorbed arsenic which shields the underlying Ga atoms. Sample A also gave a detectable count of As_3^+ ions, which have not been observed from any other surface and provides additional evidence for an adsorbed As layer.

Consistent differences have been observed between the (2×4) As stabilized surface and the other two reconstructions. Firstly larger positive ion yields were always observed from this surface, which may be related to the high work function of this reconstruction compared to either of the other surfaces.[15,17] Second, the (normalized) $GaAs^+$ secondary-ion signal was larger than that obtained from the other surface reconstructions, and decreased with ion dose, whereas it remained roughly constant on the other surfaces (Fig. 4) which indicates that this is probably sputtered as an intact cluster and not formed by recombination of Ga and As species during the sputtering process. If this species were formed by recombination then, since the (2×4) As stabilized surface is intermediate in composition between the other two surfaces studied, we would expect an initial increase in this signal from one of the other surfaces, as its surface composition passed through the optimum value for generation of $GaAs^+$, before reaching that characteristic of the ion bombarded surfaces. Exactly why the (2×4) As stabilized reconstruction should produce more $GaAs^+$ secondary-ion clusters is not yet understood, but it probably indicates a more "bulklike" surface with a predominance of Ga–As bonding over Ga–Ga or As–As bonds. This is also consistent with the stability of this reconstruction and its consequent use for MBE growth.

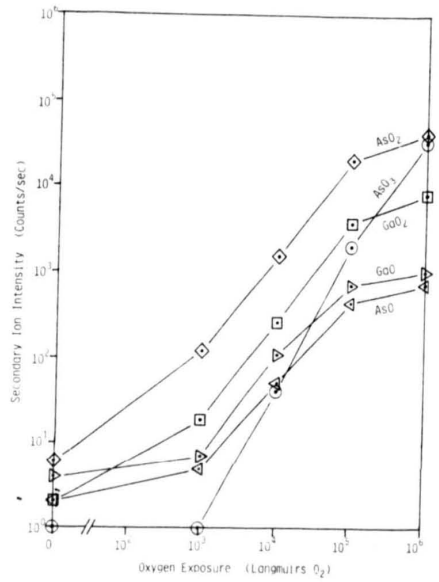

FIG. 5. Variation of oxide negative secondary ion signals with oxygen exposure observed from the (001) GaAs surfaces.

Oxidation characteristics of the various surfaces have also been investigated and some preliminary results are shown in Fig. 5. It is apparent that both Ga and As are involved in the oxidation and that no initial state of bonding to predominantly one atomic species is observed. The appearance of AsO_3^- secondary ions at larger oxygen exposures (no GaO_3^- is observed) may indicate heavy oxidation of As to the pentavalent state. Positive secondary-ion oxide species are less easily identified due to hydrogenated forms and other mass interferences not present in the negative secondary-ion spectra; however, their variation with oxygen exposure does not appear to differ significantly from the negative secondary-ion species. Each specific secondary-ion species (positive and negative) shows a similar variation with oxygen exposure for all three surface reconstructions, suggesting that the same oxidation mechanism dominates irrespective of surface reconstruction. This is easily explained if surface defects are dominant sites for oxide nucleation as suggested by Mark and Creighton.[18]

IV. CONCLUSIONS

The above SIMS results show some small but significant differences between the variously reconstructed (001) GaAs surfaces, notably that the (2×4) As stabilized surface commonly used for MBE growth appears more bulklike than the other reconstructions studied. However, the similarities in the surfaces studied and their interaction with oxygen indicates that the differences in surface chemistry are not as great as commonly supposed. This similarity can, of course, be explained by invoking defects as active sites for gas adsorption or ionization enhancement on the different

surfaces. Further work is needed to clarify these effects both in interpretation of existing data and the design of further experiments.

[1]A. Y. Cho, J. R. Arthur, Prog. Solid State Chem. **10**, 152 (1975).
[2]P. K. Larsen, J. H. Neave, J. F. van der Veen, P. J. Dobson, and B. A. Joyce, Phys. Rev. B **27**, 4966 (1983).
[3]P. K. Larsen, J. F. van der Veen, A. Mazur, J. Pollmann, J. H. Neave, and B. A. Joyce, Phys. Rev. B **26**, 3222 (1982).
[4]A. Benninghoven, Surf. Sci. **35**, 427 (1973).
[5]N. Winograd, Prog. Solid State Chem. **13**, 285 (1982).
[6]K. Wittmaack, Surf. Sci. **89**, 668 (1979).
[7]M. G. Dowsett, R. M. King, and E. H. C. Parker, J. Vac. Sci. Technol. **14**, 711 (1977).
[8]R. A. Kubiak, P. Driscoll, and E. H. C. Parker, J. Vac. Sci. Technol. **20**, 252 (1982).
[9]H. Poth, H. Bruch, M. Heyen, and P. Balk, J. Appl. Phys. **49**, 285 (1978).
[10]W. F. Croydon, PhD thesis, in preparation.
[11]M. G. Dowsett, E. H. C. Parker, R. M. King, and P. J. Mole, J. Appl. Phys. **54**, 6340 (1983).
[12]J. R. Arthur, Surf. Sci. **43**, 449 (1974).
[13]P. Drathen, W. Ranke, and K. Jacobi, Surf. Sci. **77**, L162 (1978).
[14]R. Z. Bachrach, R. S. Bauer, P. Chiaradia, and G. V. Hansson, J. Vac. Sci. Technol. **19**, 335 (1981).
[15]J. Massies, P. Etienne, F. Dezaly, and N. T. Linh, Surf. Sci. **99**, 121 (1980).
[16]J. H. Neave and B. A. Joyce, J. Cryst. Growth **43**, 204 (1978).
[17]M. L. Yu, J. Vac. Sci. Technol. A **1**, 500 (1983).
[18]P. Mark and W. F. Creighton, Thin Solid Films **56**, 19 (1979).

surfaces. Further work is needed to clarify these effects both in interpretation of existing data and the design of further experiments.

[1]A. Y. Cho, J. R. Arthur, Prog. Solid State Chem. **10**, 152 (1975).
[2]P. K. Larsen, J. H. Neave, J. F. van der Veen, P. J. Dobson, and B. A. Joyce, Phys. Rev. B **27**, 4966 (1983).
[3]P. K. Larsen, J. F. van der Veen, A. Mazur, J. Pollmann, J. H. Neave, and B. A. Joyce, Phys. Rev. B **26**, 3222 (1982).
[4]A. Benninghoven, Surf. Sci. **35**, 427 (1973).
[5]N. Winograd, Prog. Solid State Chem. **13**, 285 (1982).
[6]K. Wittmaack, Surf. Sci. **89**, 668 (1979).
[7]M. G. Dowsett, R. M. King, and E. H. C. Parker, J. Vac. Sci. Technol. **14**, 711 (1977).
[8]R. A. Kubiak, P. Driscoll, and E. H. C. Parker, J. Vac. Sci. Technol. **20**, 252 (1982).
[9]H. Poth, H. Bruch, M. Heyen, and P. Balk, J. Appl. Phys. **49**, 285 (1978).
[10]W. F. Croydon, PhD thesis, in preparation.
[11]M. G. Dowsett, E. H. C. Parker, R. M. King, and P. J. Mole, J. Appl. Phys. **54**, 6340 (1983).
[12]J. R. Arthur, Surf. Sci. **43**, 449 (1974).
[13]P. Drathen, W. Ranke, and K. Jacobi, Surf. Sci. **77**, L162 (1978).
[14]R. Z. Bachrach, R. S. Bauer, P. Chiaradia, and G. V. Hansson, J. Vac. Sci. Technol. **19**, 335 (1981).
[15]J. Massies, P. Etienne, F. Dezaly, and N. T. Linh, Surf. Sci. **99**, 121 (1980).
[16]J. H. Neave and B. A. Joyce, J. Cryst. Growth **43**, 204 (1978).
[17]M. L. Yu, J. Vac. Sci. Technol. A **1**, 500 (1983).
[18]P. Mark and W. F. Creighton, Thin Solid Films **56**, 19 (1979).